3.9 Snow and ice

PERMAFROST DEFORMATION DYNAMICS IN THE NORTHERN TIBET FROM ALOS-2

PI No.: ER2A2N030

Chao Wang ,[1,2,3], Yixian Tang [1,2,3], Bo Zhang [1,2,3], Hong Zhang [1,2,3], Lu Xu [1,2,3], Lichuan Zou [1,2,3]

[1] Key Laboratory of Digital Earth Science, Aerospace Information Research Institute, Chinese Academy of Sciences, Beijing 100094, China

[2] International Research Center of Big Data for Sustainable Development Goals, Beijing 100094, China

[2] College of Resources and Environment, University of Chinese Academy of Sciences, Beijing 100049, China

1. INTRODUCTION

The Qinghai-Tibet Plateau (QTP) is known as the Asian water tower, with an average altitude of more than 4000 meters [1]. It is bounded by the Pamir Plateau in the west, Hengduan Mountain in the east, the southern end of the Himalayas in the south and Kunlun Altun Mountain, Qilian Mountain in the north [2]. The QTP is a high terrain and thus receives more solar radiation energy than lower elevation areas [3]. The Chinese mainland climate is affected by the South Asian and East Asian monsoons, resulting in a diversity of climates in different regions, such as the rainy climate in China's southern part of the Yangtze River and drought in Northwest China [4]. In addition, the QTP has many glaciers, lakes, groundwater and surface rivers, making the QTP a super water tower in the plateau area, which affects the water system layout of all of Asia [5]. The QTP is a region with a large amount of permafrost at high latitudes [6]. As a key component of the Earth's cryosphere, permafrost plays an important role in the surface energy balance, carbon and water cycles, terrestrial ecosystem, and hydrological system [7]. In recent years, with global warming, permafrost degradation has accelerated [8], and degradation has had an impact on the environment and the energy and material balance. Therefore, it is very important to monitor the permafrost status on a large scale for a long time series [9].

Traditional measurement methods of permafrost deformation include GPS [10], leveling surveys [11], and drilling [12]. However, due to the harsh environment of the QTP, these methods cannot monitor permafrost on a large scale [8]. The multitemporal interferometric synthetic aperture radar (MT-InSAR) technique is a useful tool to map ground deformation [13]. MT-InSAR has been used to monitor the freeze-thaw cycle of permafrost [14-32], and to retrieve the thickness of the active layer [33-38] and permafrost degradation [39-42]. In these studies, some researchers have been committed to monitoring permafrost for a long time. Zhang [8] used Sentinel-1, ENVISAT and ERS-1 data to evaluate the ground deformation of permafrost and the risk along the Qinghai-Tibet Railway (QTR) from 1997 to 2018. The results show that the estimated deformation rate ranged from −20 to +10 mm/year and most of the QTR appeared to be stable. Daout [43] used ENVISAT and Sentinel-1 data to construct the spatial and temporal dynamics of permafrost deformation in the northeastern QTP from 2003 to 2019. The results show that pervasive subsidence of the permafrost of up to ~ 2 cm/year, increasing by a factor of 2 to 5 from 2003 to 2019. However, because the C-Band SAR data are easily affected by the region's vegetation and the atmosphere, the results may be affected by spatial and temporal decorrelation. The ALOS Phased Array type L-band Synthetic Aperture Rada (PALSAR) is preferred for ground subsidence monitoring in areas covered by vegetation and where there is a high rate of ground deformation [44]. Therefore, in order to improve the coherence of targets, we used L-band datasets to monitor the ground deformation of permafrost from 2007 to 2021.

The ground deformation process of permafrost is complex. With tectonic activity, erosion, and sedimentation all interacting in the QTP [45], it is difficult to accurately describe the freezing and thawing cycle of permafrost. Therefore, research has attempted to understand the deformation characteristics of permafrost. The sinusoidal model [46,47] and degree-day model [8,48] were used to describe the seasonal variation in the ground surface due to up-down deformation cycles of permafrost. However, it remains controversial which type of model is better at describing seasonal deformation [49]. To extract the temporal characteristics of permafrost directly from the SAR data, Wang [49] directly converted the network of interferograms into a deformation time series without a preset deformation model. Then, the long-term deformation velocity and seasonal deformation were extracted. However, for seasonal deformation, Wang assumed that the highest terrain elevation occurred from January–February, and the lowest elevation occurred from August–October. Wang also averaged the intra-annual deformation value. The average intra-annual deformation may smooth the features of the permafrost deformation. In addition, using prior knowledge may not be suitable for application to the QTP with spatial heterogeneity. In this study, we proposed a long-term deformation velocity and maximum seasonal deformation model without any prior knowledge to directly extract the deformation features of permafrost.

To reveal the status of the permafrost, we extracted time series deformation directly. First, we used 66 scenes of ALOS data (2007-2009), 73 scenes of ALOS-2 data (2015-2020) and 284 scenes of Sentinel-1 data (2017-2021) to reveal the spatial and temporal permafrost deformation in the northern QTP. Second, thermal collapse of permafrost were detected. Finally, we revealed the relationship between the maximum seasonal deformation and the long-term deformation velocity.

AUTOMATICALLY DELINEATING TERMINUS OF GLACIERS IN GREENLAND USING PALSAR-2 DATA

PI No. ER2A2N077

Lin Liu [1], Enze Zhang [2]

[1] The Chinese University of Hong Kong, Earth System Sciences Programme, Hong Kong, China

[2] University of Texas at Austin, Institute for Geophysics, Texas, USA

1. INTRODUCTION

The Greenland Ice Sheet has been losing mass dramatically due to the glaciers' acceleration, thinning, and retreating, increasing its contribution to sea level rise [1,2]. Glacier retreating is one of the processes that control the recent speedups of Greenland's tidewater glaciers. As a glacier retreats, it accelerates to compensate for the loss of downstream buttress.

At many marine-terminating glaciers in Greenland, their termini have been undergoing strong fluctuations at seasonal, inter-annual, and decadal timescales. A detailed, quantitative assessment of terminus variations can help to understand the mechanisms that control such variations. Conventionally, the terminus positions are delineated manually from remote sensing imagery. But manual practices can be labor-intensive and time-consuming when processing a big volume of images taken over decades and over large area such as Greenland.

This study aims to automatically delineate the terminus positions of Greenland glaciers by applying a deep learning architecture to multi-sensor and multi-temporal satellite images, including PALSAR-2 data. The L-band SAR images from PALSAR-2 promise high enough spatial resolution for delineating glacier termini and the penetration through clouds.

2. RESEARCH ACHIEVEMENTS

Our key achievement was to integrate seven remote sensing datasets (including ALOS-1 & -2) into a single deep learning network, DeepLabv3+. The network architecture is illustrated in Figure 1. We automated the delineation of the calving fronts of the Jakobshavn Isbræ, Kangerlussuaq, and Helheim glaciers using Envisat, TerraSAR-X, Landsat-8, Sentinel-1 & -2, and ALOS-1 & -2 images. We successfully applied the network to ALOS-2 images without using them to train the network. Such a successful application showed our method's generalization on L-band SAR images. We also proved the network's generalization on different glaciers and data types. The promising results for images with light cloud and shadow also attested to the robustness of our method. The integration of seven remote sensing datasets offers us sub-weekly calving front datasets. The high-temporal-resolution multi-sensor remote sensing imagery enables detailed investigations of seasonal and interannual calving front variations and large calving events. The increased accuracy, generalization, and robustness of the deep-learning method demonstrate that our method has the potential to be applied to many other tidewater glaciers both in Greenland and elsewhere in the world, using multi-temporal and multi-sensor remote sensing imagery.

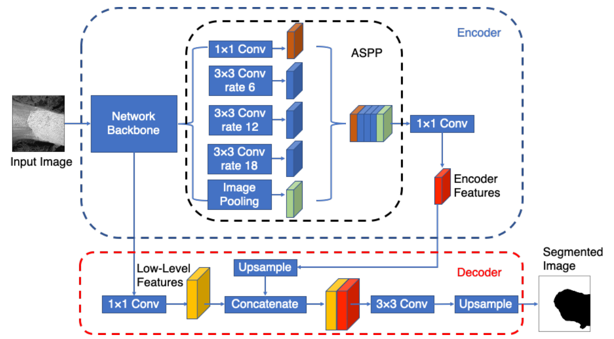

Fig. 1 Architecture of DeepLabv3+. The details of the architecture are described in [3].

3. RESULTS

The averaged uncertainty of our method is 86 meters for all the datasets used and 75 meters (7.5 pixels) for ALOS-2 images only. We produced a total of 1965 calving fronts at the three largest outlet glaciers of Greenland. Fig. 2 shows examples of network-delineated calving fronts in the test set. Most of our results show a high-degree agreement with manual delineation, even for images with light cloud coverage (e.g., Fig. 2c).

The integration of the seven datasets enabled us to produce sub-weekly calving front datasets of all three glaciers. High temporal resolution enables detailed investigations of calving front variations. For instance, we could directly obtain the number and the date of large calving events from the time series. Moreover, we could reliably capture the seasonal and interannual variations with high temporal resolution.

Jakobshavn Isbræ's two branches underwent three-phase interannual variations with strong seasonality. The time series of Kangerlussuaq's calving front variation shows strong interannual and seasonal variations, and its seasonality also changes interannually. At Helheim, the time series has two phases: 2002–2011 and 2013–2020. The retreat rate of the second phase was double the first phase, and the second phase has strong seasonal variations.

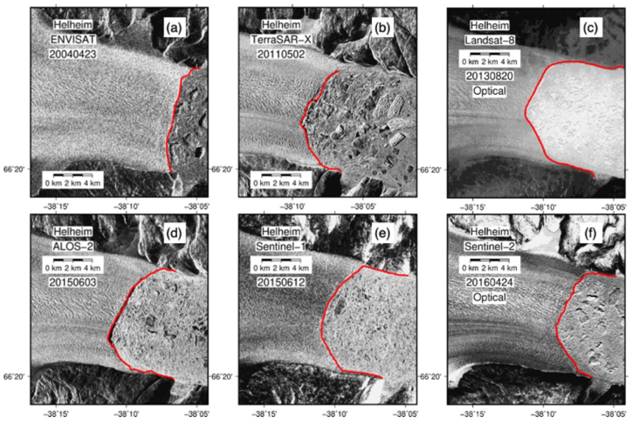

Fig. 2 Examples of deep-learning-delineated calving fronts (red line) in the test set. Background image of (d) is an ALOS-2 SAR image taken in June 2015. Modified from [3].

4. REFERENCES

[1] IPCC, "IPCC Special Report on the Ocean and Cryosphere in a Changing Climate", edited by: Pörtner, H.-O., Roberts, D. C., Masson-Delmotte, V., Zhai, P., Tignor, M., Poloczanska, E., Mintenbeck, K., Nicolai, M., Okem, A., Petzold, J., Rama, B., and Weyer, N., Cambridge University Press, Cambridge, UK and New York, NY, USA, 755 pp., 2019.

[2] IPCC, "Climate Change 2021: The Physical Science Basis. Contribution of Working Group I to the Sixth Assessment Report of the Intergovernmental Panel on Climate Change", edited by: Masson-Delmotte, V., P. Zhai, A. Pirani, S.L. Connors, C. Péan, S. Berger, N. Caud, Y. Chen, L. Goldfarb, M.I. Gomis, M. Huang, K. Leitzell, E. Lonnoy, J.B.R. Matthews, T.K. Maycock, T. Waterfield, O. Yelekçi, R. Yu, and B. Zhou, Cambridge University Press, Cambridge, United Kingdom and New York, NY, USA, 2021.

[3] Zhang, E., Liu, L., Huang, L., and Ng, K. S., "An automated, generalized, deep-learning-based method for delineating the calving fronts of Greenland glaciers from multi-sensor remote sensing imagery", Remote Sensing of Environment, Elsevier, 254, 112265, 2021.

APPENDIX

List of published papers related to ALOS EO-RA2.

[1] Zhang, E., Liu, L., Huang, L., and Ng, K. S., "An automated, generalized, deep-learning-based method for delineating the calving fronts of Greenland glaciers from multi-sensor remote sensing imagery", Remote Sensing of Environment, Elsevier, 254, 112265, 2021.

MAPPING PERMAFROST THAW SUBSIDENCE USING PALSAR-2 AND GROUND MEASUREMENTS

PI No. ER2A2N081

Lin Liu [1], Yan Hu [2]

[1] The Chinese University of Hong Kong, Earth System Sciences Programme, Hong Kong, China

[2] The Chinese University of Hong Kong, Institute of Environment, Energy and Sustainability, Hong Kong, China

1. INTRODUCTION

Rock glaciers are debris-ice landforms widely distributed in the mountainous periglacial realm worldwide [1]. They serve as important indicators for permafrost which is defined by its underground temperature and invisible in most other cases, especially for regions such as the Tibetan Plateau where in-situ observations are limited in spatial coverage due to the harsh and remote environment. Surface kinematics of rock glaciers, which manifests the characteristic permafrost creep process occurring at depth, has become an accessible and quantifiable feature with the application of remote sensing methods.

This study extends the use of Interferometric Synthetic Aperture Radar (InSAR) from measuring ground subsidence to quantifying rock glacier motions in permafrost regions in Tibet and Nepal where periglacial landforms are still not well studied. Based on the InSAR-observed surface kinematics, we further classified the geomorphological type of a puzzling landform in central Tibet and also inferred ground ice content stored in rock glaciers in Khumbu Valley, Nepal.

2. RESEARCH ACHIEVEMENTS

Through two InSAR-based studies, we have not only mapped surface motions at selected rock glaciers but also gained quantitative insights into the geomorphology and rheology of permafrost creeping.

The first study, as published in [2], aimed to address a long-standing issue concerning geomorphological classification from a kinematic perspective. A group of periglacial landforms consisting of several lobes were discovered in the East Kunlun Mountains of China 30 years ago [3] but were ambiguously classified as rock glaciers and later as gelifluction deposits [4]. We revisited the previous research question centering on the classification of the periglacial landforms near Jingxian Valley, in a way that integrates the kinematic and geomorphologic features of the landforms. We employed InSAR to ALOS-1 PALSAR and ALOS-2 PALSAR-2 images to quantify the temporal and spatial variations of the downslope creeping velocities (Figure 1). We also conducted geodetic measurements, in-situ field surveys, and excavated test pits to provide supplementary geomorphological information. By critically analyzing the influences that the mechanical processes imposed on the landform and piecing our observations together, we identified the landform as a debris-mantled-slope-connected rock glacier, with gelifluction processes occurring on the surface as small-scale and discrete events.

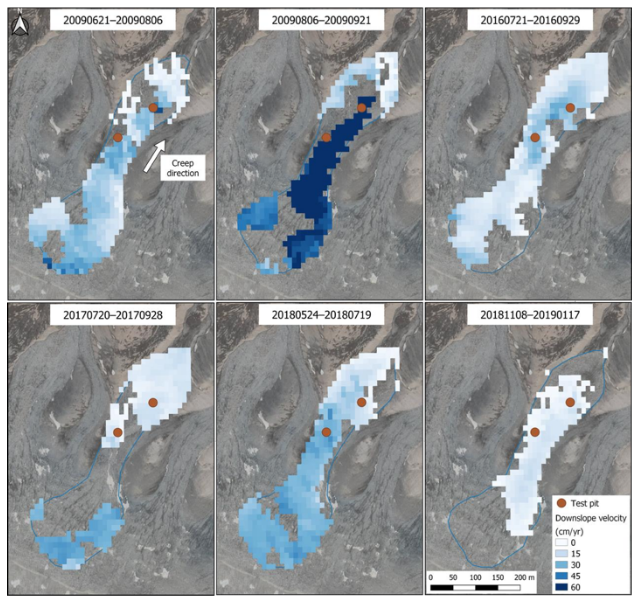

Fig. 1 Velocity maps of one lobe at the Jingxiangu Rock Glacier, showing the temporal and spatial variations of the downslope velocities as estimated from InSAR. The brown circles mark the locations of the two test pits. Figure modified from [2].

The second study, published as a discussion paper and still under review in [5], investigated the potential water storage of the rock glaciers situated in Khumbu Valley, Nepal by developing a velocity-constrained model to infer their ice contents. We adopted a rheological model based on adaptations of Glen's flow law and assumed a homogeneous two-layer structure for rock glaciers that consists of an ice-free active layer and an ice-rich permafrost core. The velocity constraints applied to the model were derived from InSAR measurements using ALOS-1/2 PALSAR-1/2 images (Figure 2). The inferred ice fraction of the studied rock glaciers in Khumbu Valley ranges from 71.0% to 75.3%. Extrapolating from our findings in Khumbu Valley, the total amount of water stored in rock glaciers could be ~10 billion m^3 over the Nepalese Himalayas.

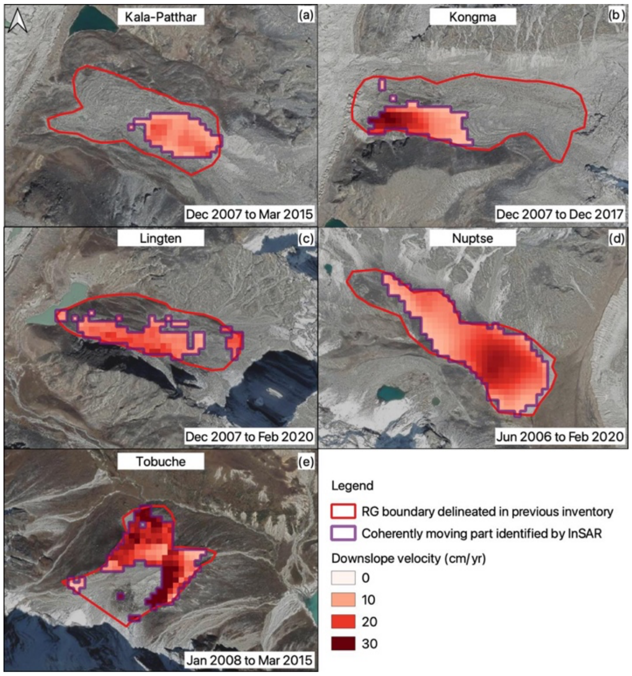

Fig. 2 Velocity field maps show the average movement rate of the coherently moving parts of five rock glaciers (purple outlines) in Khumbu Valley. The boundaries of the landforms delineated in previous inventorying work are in red polygons. The background is the Google Earth Images. RG: rock glaciers. The figure is modified from [5].

3. REFERENCES

[1] Ballantyne, C.K., "Periglacial geomorphology", Wiley-Blackwell, 2018.

[2] Hu, Y., Liu, L., Wang, X., Zhao, L., Wu, T., Cai, J., Zhu, X. and Hao, J., "Quantification of permafrost creep provides kinematic evidence for classifying a puzzling periglacial landform", *Earth Surface Processes and Landforms*, 46, 465–477, 2021.

[3] Cui, Z., "Discovery of Kunlunshan-type rock glaciers and the classification of rock glaciers", *Kexue Tongbao*, 30(3), 365-369, 1985.

[4] Harris, S. A., Cui, Z. J., and Cheng, G. D., "Origin of a bouldery diamicton, Kunlun pass, Qinghai-Xizang plateau, People's Republic of China: Gelifluction deposit or rock glacier?", *Earth Surface Processes and Landforms*, 23(10), 943-952, 1998.

[5] Hu, Y., Harrison, S., Liu, L., and Wood, J. L., "Modelling rock glacier velocity and ice content, Khumbu and Lhotse Valleys, Nepal", *The Cryosphere Discussions*, open review, 2021.

APPENDIX

List of published papers related to ALOS EO-RA2.

[1] Hu, Y., Liu, L., Wang, X., Zhao, L., Wu, T., Cai, J., Zhu, X. and Hao, J., "Quantification of permafrost creep provides kinematic evidence for classifying a puzzling periglacial landform", *Earth Surface Processes and Landforms*, 46, 465–477, 2021.

[2] Hu, Y., Harrison, S., Liu, L., and Wood, J. L., "Modelling rock glacier velocity and ice content, Khumbu and Lhotse Valleys, Nepal", *The Cryosphere Discussions*, open review, 2021.

SAR データ等を用いた豪雪地域の積雪深分布プロダクトの開発

PI No.: ER2A2N135

永井裕人 [1, 2], 山口悟 [2], 上石勲 [2], 河島克久 [3], 佐藤匠 [3, 4]

[1] 早稲田大学
[2] 防災科学技術研究所
[3] 新潟大学
[4] 国際航業株式会社

1. はじめに

地方自治体にとって豪雪は非常に大きな経済的負担を与えている。新潟県管理道路の除雪費は年間 100 億円を超えるなど、除雪車の運用は多額の税金が投入されるが、その運用計画（ルート選択や運用回数）には作業領域全体の積雪の空間分布が客観的に反映されていない。しかも年によって降雪の頻度や量が変わるため、同じ計画を毎年実施することは合理的でない。

このような背景を踏まえ、広域の積雪深分布把握技術は、積雪地域のレジリエンス向上のために不可欠な技術である。合成開口レーダー（SAR: Synthetic Aperture Radar）を用いた衛星観測では、積雪の深度に応じたレーダー反射強度の減衰が確認されている[1]。積雪にマイクロ波を放射した場合に後方散乱として受信する反射波は露出面での表面散乱、地面での表面散乱、積雪層内における体積散乱の 3 通りに分類できる[1]。

積雪が液体の水分を含むと、積雪粒子と水の誘電率の違いによって、後方散乱が著しく減少する[2], [3]。従来の SAR による積雪量推定は C-バンドを用いたものが多く、波長が短いことにより、液体水分を含む積雪層への適応が大きなハードルとなっていた[1]‐ [5]。C-バンドより波長の長い L-バンドマイクロ波は、積雪内部構造のより深い部分まで浸透するという特徴がある[5]。L-バンドを用いた既存研究では、積雪深 250 cm 程度まで感度があり、積雪深と後方散乱強度差分との間に、負の相関関係が確認された[6]。また干渉 SAR 解析よりも後方散乱強度差分の方が有用であることも示されている。
本研究「SAR データ等を用いた豪雪地域の積雪深分布プロダクトの開発」は SAR（Synthetic Aperture Radar 合成開口レーダー）を利用した、湿雪にも対応する積雪深マップの開発を目的とする。地上計測点網や積雪深モデルでは達成できなかった高解像度な空間分布を実現し、ALOS-4 を利用した積雪深情報提供サービスの構築に必要な基礎的知見を得ることをねらいとする。

2. 対象地域

本研究対象地域は新潟県長岡市付近の平野部から山間部にかけての地域である（Fig. 1）。信濃川流域圏の一部であり、沿岸域から標高 1520 m まで含まれる。コシヒカリ生産で有名な魚沼も含まれる。

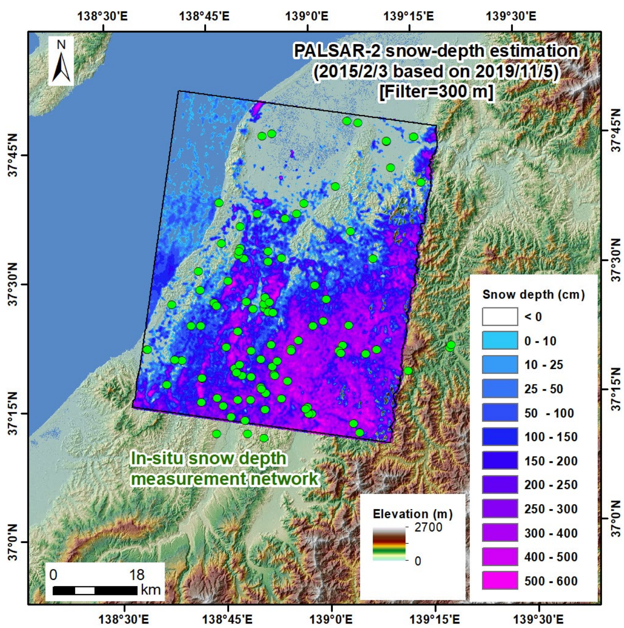

Fig. 1) Location of in-situ snow-depth measurement and spatial distribution of SAR-based snow-depth estimation in the study site.

3. データ

陸域観測技術衛星「だいち２号」に搭載された L-バンド合成開口レーダーである PALSAR-2 のデータについて、研究対象地域を観測したものを入手し、解析に用いた。全て Stripmap モード（HH 単偏波；空間分解能３ m）であり、2015 年以降の 11 月から 3 月にかけて Descending または Ascending 軌道から観測したものである。詳細は Table 1 に示した。11 月のデータは無雪時の状況を参照するために用い、その他の時期は全て積雪域が広く含まれるものである。

Table 1) Orbit and acquisition dates of PALSAR-2 data

Orbit	Date	Local Time	Referential snowless day
Descending	2015/2/3	11:30	
Descending	2016/3/1	11:30	
Descending	2017/2/28	11:30	
Descending	2017/11/7	11:30	YES
Descending	2018/1/30	11:30	
Descending	2018/2/27	11:30	
Descending	2019/2/26	11:30	
Descending	2020/2/25	11:30	
Ascending	2015/3/15	23:30	
Ascending	2015/11/22	23:30	YES
Ascending	2018/1/28	23:30	
Ascending	2018/3/25	23:30	
Ascending	2019/2/24	23:30	
Ascending	2020/2/23	23:30	

積雪深の現地計測値は、新潟大学災害・復興科学研究所が公開する準リアルタイム積雪深分布図（https://platform.nhdr.niigata-u.ac.jp/~snow-map/）の作成に使用されているものを用いた[7]。１日おきの現地計測値と現地計測地点の位置（Fig .1）が記録されたものであり、PALSAR-2 観測日を全て含む。
現地計測地点周辺の土地被覆を把握するため、JAXA 日本域高解像度土地利用土地被覆図（10m 解像度【2018～2020 年】(ver.21.11)）を入手した[8]。また現地計測地点周辺の標高と地形を把握するため、JAXA ALOS 全球数値地表モデル (DSM) "ALOS World 3D - 30m (AW3D30)" (ver. 3.2)を入手した[9]。さらに気象条件が推定精度に与える影響を検討するため、気象庁が公開する「長岡」における PALSAR-2 観測日の当日と前日について、降水量、積雪深、気温の各情報を入手した（Table 2）。

Table 2) Meteorological data provided by the Japan Meteorological Agency

相関係数	Date	Orbit	降雪積雪深 (cm)		全層積雪深 (cm)			降水量 (mm)		最低気温 (°C	最高気温 (°C
			前日	当日	前日	当日	変化量	前日	当日		
-0.793	2015/2/3	Desc	2	2	67	62	-5	0.5	0	-0.2	2.4
-0.781	2018/1/28	Asc	9	3	58	55	-3	5.5	0.5	-1.2	10.3
-0.712	2016/3/1	Desc	2	13	2	12	10	22.5	6	-1.1	3.8
-0.617	2020/2/23	Asc	0	0	0	0	0	4.5	11.5	3.7	6.9
-0.597	2019/2/24	Asc	0	0	0	0	0	1.5	0	1.9	2.4
-0.539	2017/2/28	Desc	0	0	0	0	0	0	0	-2.9	-1.2
-0.527	2018/1/30	Desc	18	45	55	94	39	16.5	25.5	-3.3	8.2
-0.52	2015/3/15	Asc	0	0	13	9	-4	4	0	-1.8	15.8
-0.411	2019/2/26	Desc	0	0	0	0	0	0	0	1.2	11.7
-0.361	2018/3/25	Asc	0	0	0	0	0	0	0.5	4.8	9.1
-0.208	2018/2/27	Desc	1	0	87	85	-2	3.5	0	-3.1	7.6
-0.033	2020/2/25	Desc	0	0	0	0	0	3	9	4.1	9.7

4. 手法

SAR データの解析結果を積雪深現地計測値で校正することにより、積雪深空間分布を導出する（Fig. 2）。まず積雪時・無雪時それぞれの PALSAR-2 データを後方散乱強度の物理量（dB）に変換し、それぞれに共通の平滑化フィルタを実施する。平滑化フィルタとはある半径の円内に含まれる画素値の平均を中心画素に与え直す画像処理であり、半径を大きくするほどスペックルノイズの影響が軽減され、見た目がぼやけた画像になる。そして積雪時と無雪時の差分値を求める。積雪深現地計測地点における差分値（dB）と積雪深実測値（cm）の関係を単回帰式として求め、この式から強度差分画像（dB）を積雪深マップ（cm）へ変換する。

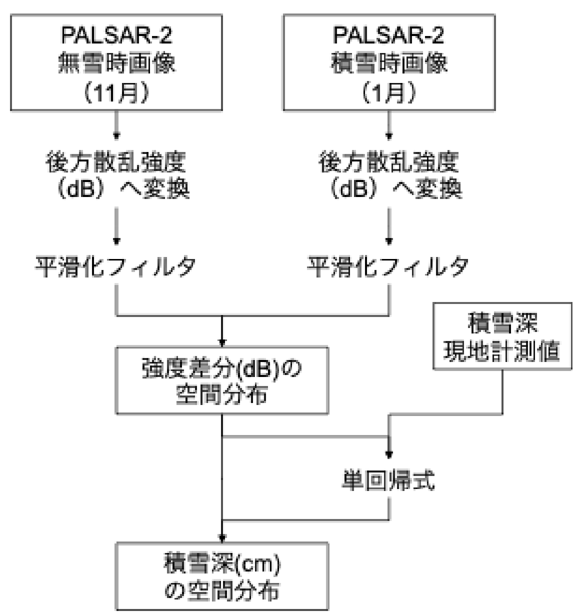

Fig. 2) Processing flow of SAR-based snow-depth estimation

5. 結果と考察

まずスペックルノイズを除去し、空間代表性を考慮した相関関係の導出のために、平滑化フィルタを最適化する必要がある。Figure 3 を見てわかる通り、積雪深と後方散乱係数変化量は負相関であり、平滑化フィルタの半径が大きいほど、より強い相関の分布を示す傾向がある。現地積雪計測地周辺の土地被覆（半径 300 m 圏内の最尤被覆）を見ると、平滑化フィルターをかけることによって、土地被覆によるバイアスはほとんど影響がなくなる。同じ積雪深の場所では水田が比較的低い値を示す傾向が見られる。都市域で浅く、森林で深い積雪深であるのは、標高によって土地被覆に偏りが生じていることが原因である。

a)

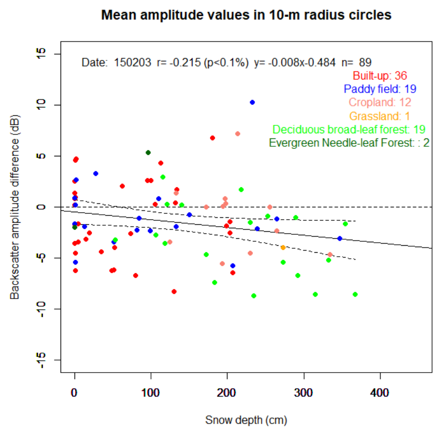

b)

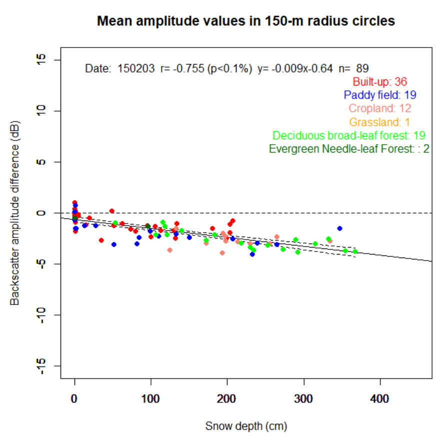

Fig. 3) Examples of scatter plot of snow depth and backscatter amplitude difference with (a) 10-m and (b) 150-m smoothing filters

Figure 3 について、どの程度の規模の平滑化フィルタを実施すれば良いかについて、設定する半径を変えていった場合の相関係数の変動を調べた（Fig. 4）。Descending/Ascending orbit それぞれについて、相関係数の大きさは観測日によって大きく異なる。強い負の相関（r< -0.5）を示し積雪推定に適した観測日のデータについては、概ね 300 m 以上の半径で平滑化フィルタを実施することによって、安定した相関係数が得られることがわかった。相関係数が 0 に近く弱相関の観測日のデータについては、平滑化フィルタに関わらず、常に弱相関である。

a)

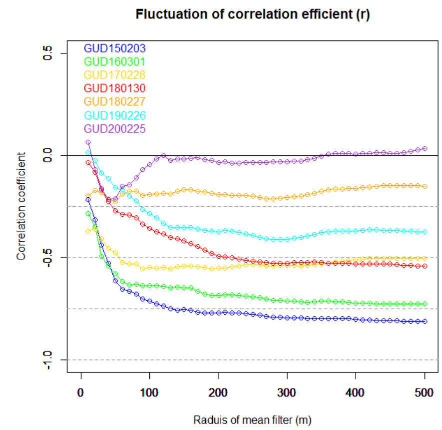

b)

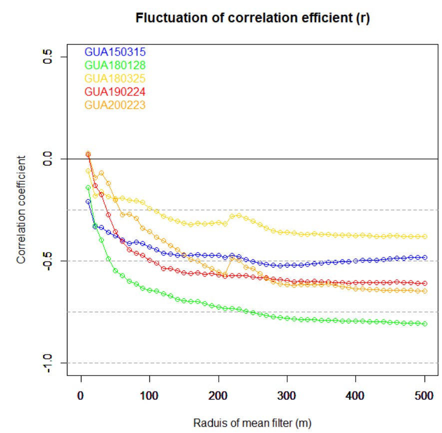

Fig. 4) Fluctuation of correlation efficient with different-scale smoothing filters in (a) descending and (b) ascending orbits.

現地計測積雪深と後方散乱係数変化量との関係性を示す単回帰式の傾きについては、観測日によって 0 から-0.01 程度の異なる値を示すこと、また平滑化フィルタを変えてもほどんど影響が及ばないことがわかった（Fig. 5）。

次に積雪深推定に誤差を生じる特性のある地点を明らかにし、除外する方法を検討する。平滑化フィルタの適応半径を 300 m に固定し、土地被覆ごとの積雪深に対する後方散乱係数差分値の分布傾向を全シーンで調べた（Fig. 6）。概ね水田と畑地が差分値の分布を引き下げている傾向が見られる。森林は回帰直線に沿って標準的な差分値を示す。相関の弱い観測日では、特定の土地被覆がばらつきを大きくし

ているわけではなく、土地被覆全てにおいてばらつきが大きい傾向がある。3 月ごろの積雪融解が進行し、相関がなくなる傾向はもちろんであるが、3 m以上など十分に積雪があっても相関が弱くなる場合がある。

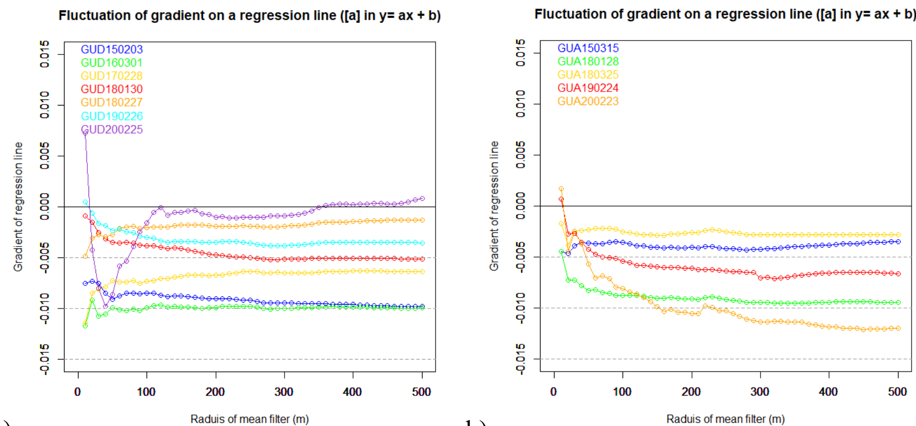

a) b)

Fig. 5) Fluctuation of regression-line gradient with different-scale smoothing filters in (a) descending and (b) ascending orbits.

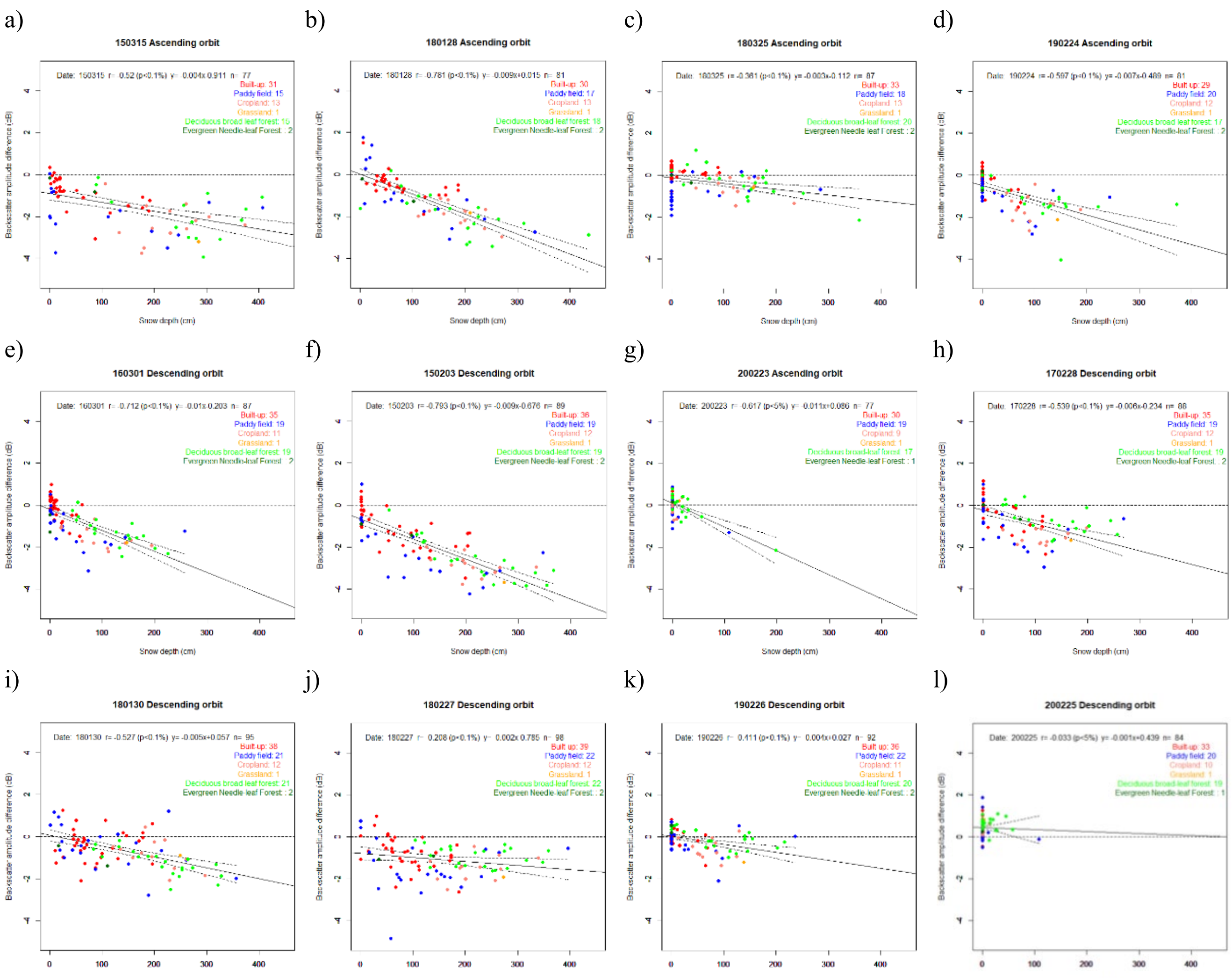

Fig. 6) Correlation of in-situ snow depth and backscatter amplitude difference in PALSAR-2 observation dates

Figure 6 の分布と Table 2 と比較すると、より直前に降雪があり前日か当日に新雪層が加わっている場合には高相関である場合が多いことがわかる。新雪層の大小が反映されている可能性がある。最低気温が 0 ℃を上回っている場合、積雪表層部分は融解水によって含水率が高いと考えられる。このような条件が期待できる日の場合、低相関であることが多い。もともと気象庁観測地点「長岡」では積雪がなくなっているため積雪深の増減がないが、高標高域では融解が進んでいる可能性がある。回帰直線の傾きについては、r= 0.5 以上の高相関の場合、-0.004 から-0.01 の値を示す。r= -0.7 よりも顕著な負相関である場合、より勾配が急になる（傾き< -0.01）特性を持つ。このように観測全シーンを俯瞰すると、積雪深と後方散乱係数差分の相関が顕著になる傾向は読み取れるが、顕著な負相関を示す上での必要条件は見出せなかった。

地形に関する分類結果を含めた積雪深と後方散乱係数差分との関係を Fig. 7 に示す。ここでは Fig. 6 の縦軸横軸を転置させて表している。標高値と斜面傾斜角について、観測地点の周り半径 300 m での AW3D30 からの平均値を現地観測地点毎に計算し、その分布の 4 分位をもとに上位 25%を赤、下位 25%を青のドットで示している。どちらも積雪深が大きいのは高標高・急傾斜の場所であることが示され、積雪が無いか低いところは低標高・緩傾斜となった。これらは山間部と平野部の観測地点に分類されていて、山間部ほど雪が深いということを示している。標高値と斜面傾斜角においては、相関関係の改善につながるようなサンプルの取捨選択方法は見出されなかった。

一方で、高標高ほど気温が低く積雪中に水分がより多く含まれるということは、今後、考慮に含めるべきである。特に高標高エリアと低標高エリアを比較すると、高標高エリアのサンプルの分布（赤ドット）が全体の単回帰式に対してより急勾配な分布であるように見える。標高値、気温減率、気象観測データ（気温）を利用して、分布の傾きが変化するような条件を見出せば、湿雪の存在が相関関係に影響を与えるかどうかも、わかるようになるかもしれない。

方位角については、Descending orbit の衛星に対して正体する斜面（東向斜面）と逆向き斜面（西向き斜面）に分類した。どちらも回帰直線に対して均一に分散していて、特定の分布傾向は見られなかった。

ある 1 箇所の観測地点の後方散乱係数が積雪深の変動によってどのように変動するかを、Descending/Ascending orbit それぞれについて、まとめた（Fig. 8）。もともと後方散乱が大きい点で積雪深による散乱減少の効果が明確にわかると考え、無雪時の後方散乱係数が-10 dB 以上のものを色付けして示している。どの点も積雪深の増加に対して緩やかに後方散乱係数が減少する傾向が見られる。加えて、同程度の積雪深であっても、観測日によって大きく後方散乱係数が変化する特徴も両軌道で共通して見られた。これらのことから、後方散乱係数の減少は積雪深の増加を反映しているものの、個別のばらつきが大きく、点レベルではなくより広域での把握・解釈が適しているという示唆が得られた。

a)

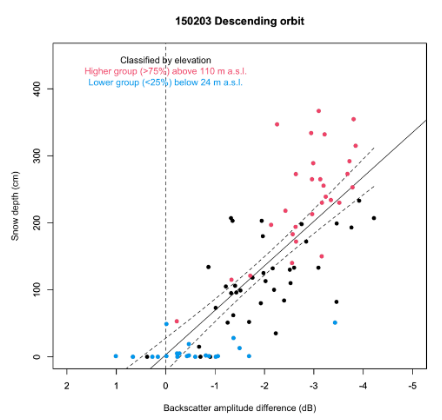

b)

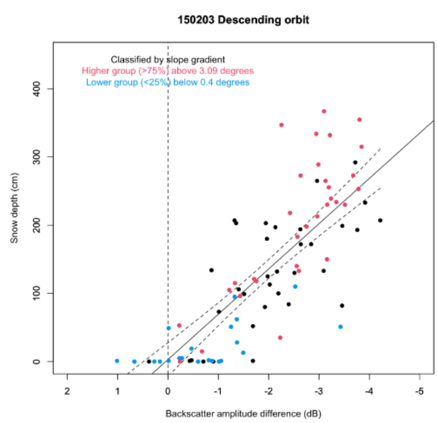

c)

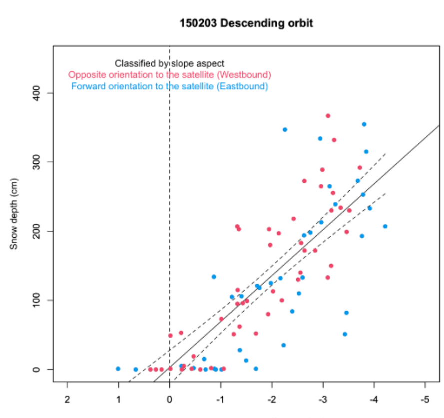

Fig. 7) Correlation of in-situ snow depth and backscatter amplitude difference in different topographic conditions of (a) elevation, (b) slope gradient, and (c) slope aspect.

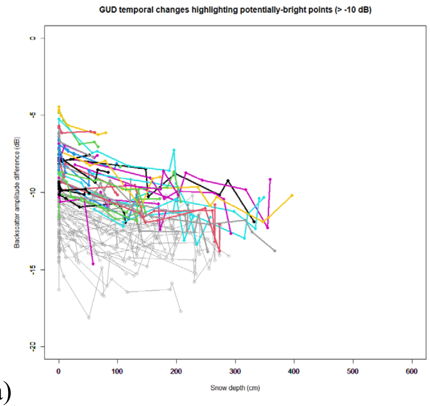

a)

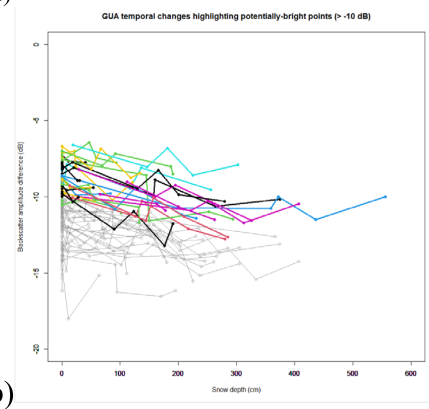

b)

Fig. 8) Temporal change of backscatter amplitude (dB) in (a) descending and (b) ascending orbits.

6. 結論

本研究では SAR からの積雪深推定について、どこまで統一的な手法やパラメータを設定し、SAR データから積雪深を高精度に推定できるかを検証した。現地観測積雪深で校正する際には、300 m 以上の半径で平滑化フィルタを実施すると、現地積雪深データに対して最もばらつきが小さな後方散乱係数差分値の分布が得られることがわかった。複数の日時における解析結果を比較すると、2015 年 2 月 3 日に最もばらつきが少なく理想的な対応関係（$r = -0.79$; $p< 0.5\%$）が得られた。同じ校正観測地点であっても日によって相関関係が弱くなり、これは積雪中に融解水が予想される日に多く見られる。地形条件（標高、斜面傾斜、斜面方位）や土地被覆によって相関係数が弱くなる影響は認められなかった。

地点毎の偶然のばらつきが大きく、PALSAR-2 データは細かな道路除雪状況モニタリングに使うには更なる精度向上が望まれる。しかしながら、流域スケールでどれくらいの積雪を貯留しているかを年々比較するなど、広域での解析にはより簡単に応用しやすいのではないかと考えられる。

謝辞

本研究を進めるにあたり、平成 30 年度内閣府・先進的な宇宙利用モデル実証プロジェクト「衛星を利用した積雪深分布把握に基づく道路除排雪システムの検討」および令和元年度新潟大学災害・復興科学研究所共同研究「衛星を活用した積雪域の広域積雪審分布把握を目指した積雪中マイクロ波反射特性の解明」で得られたデータと知見の一部を用いました。また新潟大学災害・復興科学研究所が保有・運用する準リアルタイム積雪分布監視システムのデータ提供を受けました。この場を借りて深謝いたします。

引用文献

[1] H. Li, Z. Wang, G. He, and W. Man, “Estimating snow depth and snow water equivalence using repeat-pass interferometric SAR in the northern piedmont region of the Tianshan Mountains,” J. Sensors, vol. 2017, 2017, doi: 10.1155/2017/8739598.

[2] J. Shi, J. Dozzier, and H. Rott, “Deriving snow liquid water content using c-band polarimetric SAR,” Int. Geosci. Remote Sens. Symp., vol. 3, pp. 1038–1041, 1993, doi: 10.1109/igarss.1993.322643.

[3] J. Dozier, “Corrections to ‘Inferring Snow Wetness Using C-Band Data from SIR-C’s Polarimetric Synthetic Aperture Radar,’” IEEE Trans. Geosci. Remote Sens., vol. 33, no. 6, 1995, doi: 10.1109/TGRS.1995.477195.

[4] M. Bernier, J. P. Fortin, Y. Gauthier, R. Gauthier, R. Roy, and P. Vincent, “Determination of Snow Water Equivalent using RADARSAT SAR data in eastern Canada,” Hydrol. Process., vol. 13, no. 18, pp. 3041–3051, 1999, doi: 10.1002/(SICI)1099-1085(19991230)13:18<3041::AID-HYP14>3.0.CO;2-E.

[5] E. Rignot, K. Echelmeyer, and W. Krabill, “Penetration depth of interferometric synthetic-aperture radar signals in snow and ice,” Geophys. Res. Lett., vol. 28, no. 18, pp. 3501–3504, 2001, doi: 10.1029/2000GL012484.

[6] A. Togari, S. Homma, T. Sato, K. Honda, and O. Suzuki, “Satellite SAR processing methods evaluation for snow depth estimation,” in JSSI JSSE Jt. Conf. Matsumoto, 2015, p. 210.

[7] T. Iyobe and K. Kawashima, “Development of Quasi-Real-Time Monitoring System for Regional Snow Cover by Utilizing Multiple Snow Data,” in JSSI JSSE Jt. Conf., 2020, vol. 36, no. 1, pp. 1–13.

[8] Shutaro Hashimoto, T. Tadono, Masahiko Onosato, Masahiro Hori, and Kei Shiomi, “A New Method to Derive Precise Land-use and Land-cover Maps Using Multi-temporal Optical Data,” J. Remote Sens. Sociery Japan, vol. 34, no. 2, pp. 102–112, 2014.

[9] T. Tadono, H. Ishida, F. Oda, S. Naito, K. Minakawa, and H. Iwamoto, “Precise Global DEM Generation by ALOS PRISM,” ISPRS Ann. Photogramm. Remote Sens. Spat. Inf. Sci., vol. II–4, no. May, pp. 71–76, 2014, doi: 10.5194/isprsannals-ii-4-71-2014.

MONITORING GLACIER CHANGE OVER THE TIBETAN PLATEAU BASED ON ALOS-2

PI No.: ER2A2N184

Changqing Ke[1], Guohui Yao[1], Xuening Yu[1], Yu Cai[1], Xiaoyi Shen[1]

[1] School of Geography and Ocean Science, Nanjing University

Glaciers are considered key indicators of climate change due to their sensitive reaction to even small climatic changes. The Tibetan Plateau (TP) hosts the largest glacier concentration outside the polar regions, it is the water tower of China and several countries in Asia, and glacier change in the TP play an important role in their production and daily lives.

To study the applicability of full polarimetric synthetic aperture radar (SAR) data to identify alpine glaciers in the central Himalayas, six polarimetric decomposition methods were used to obtain 20 polarimetric characteristic parameters based on the Advanced Land Observing Satellite 2 (ALOS-2) Phased Array type L-band Synthetic Aperture Radar (PALSAR) data. Object-oriented multiscale segmentation was performed on a Landsat 8 Operational Land Imager (OLI) image prior to classification, and the vector boundaries of different types of training samples were selected from the segmented results. We performed a support vector machine (SVM)-based classification on the characteristic parameters from each polarimetric decomposition. All 20 parameters were then screened and combined according to different requirements: the degree of separability of different types of training samples and the type of scattering mechanisms. The results show that the classification accuracy of the incoherent decomposition characteristics based on the covariance matrix is the best, reaching 87%, and it can exceed 91% after adding the local incidence angle to the suite of classifiers. Eventually, more than 93% accuracy was achieved using a combination of multiple polarimetric parameters, which reduced the misclassification between bare ice and rock. We also analyzed the use of controlling factors on the accuracy of alpine glacier identification and found that the polarimetric information and aspect of the glacier surface are the most important factors. The former is the main basis for identification, but the latter will confuse the feature distributions of different categories and cause misclassification.

Distinguishing debris-covered glaciers from debris-free glaciers is difficult when using only optical remote sensing images to extract glacier boundaries. According to the features that the surface temperature of debris-covered glacier is lower than surrounding objects, and higher than clean glaciers, glacial changes in the Yigong Zangbo basin was analyzed on the basis of visible, near-infrared and thermal-infrared band images of Landsat TM and OLI/TIRS in the support of ancillary digital elevation model (DEM). The results indicated that glacier area gradually declined from 928.76 km^2 in 1990 to 918.46 km^2 in 2000 and 901.51 km^2 in 2015. However, debris-covered glacier area showed a slight increase from 63.39 km^2 in 1990 to 66.24 km^2 in 2000 and 71.16 km^2 in 2015. During 25 years, the glacier length became shorter continuously with terminus elevation rising up. The area of moraine lakes in 1990 was 1.43 km^2, which increased to 1.98 km^2 in 2000 and 3.41 km^2 in 2015. In other words, the total area of the moraine lakes in 2015 is 2.38 times of that in 1990. This increase in moraine lake area could be the result of accelerated glacier melt and retreat, which is consistent with the significant warming trend in recent decades in the basin.

At the same time, by applying the method of SAR interferometry to X-band synthetic aperture radar (SAR) image of COSMO-SkyMed, detailed motion patterns of five glaciers in the Parlung Zangbo River basin, Tibetan Plateau, in January 2010 have been derived. The results indicate that flow patterns are generally constrained by the valley geometry and terrain complexity. The maximum of 123.9 m yr^{-1} is observed on glacier No.1 and the minimum of 39.4 m yr^{-1} is found on glacier No.3. The mean values of five glaciers are between 22.9 and 98.2 m yr^{-1}. Glaciers No.1, No.2, No.4 and No.5 exhibit high velocities in their upper sections with big slope and low velocities in the lower sections. A moraine lake accelerates the speed of mass exchange leading to a fast flow at the terminal of glacier No.3. These glaciers generally move along the direction of decreased elevation and present a macroscopic illustration of the motion from the northwest to the southeast. The accuracy of DEM and registration conditions of DEM-simulated terrain phases has certain effects on calculations of glacier flow direction and velocity. The error field is relatively fragmented in areas inconsistent with the main flow line of the glaciers, and the shape and the uniformity of glacier are directly related to the continuous distribution of flow velocity errors.

APPENDIX

[1] Guo-Hui Yao, Chang-Qing Ke*, Xiaobing Zhou, Hoonyol Lee, Xiaoyi Shen, Yu Cai. Identification of alpine glaciers in the central Himalaya using fully polarimetric L-band SAR data. *IEEE Transactions on Geoscience and Remote Sensing*, 2020, 58(1): 691-703. doi: 10.1109/TGRS.2019.2939430.

MONITORING TYPICAL ICE MOVEMENTS WITH ALOS-2 FOR GLACIER AVALANCHE DISASTER MITIGATION IN THE TIBETAN PLATEAU

PI No.: ER2A2N191

Jinghui Fan [1], Chuan Wang [2], QunWang [3], Weilin Yuan [2], Jienan Tu [2], Jienan Tu [2], Hongli Zhao [2], Bo Huang [4], Hongzhou Li [5], Huaguo Huang [2], Guang Liu [6]

[1] China Aero Geophysical Survey and Remote Sensing Centre for Natural Resources, Beijing, China; [2] Key Laboratory for Silviculture and Conservation of Ministry of Education, Beijing Forestry University, China, Beijing, China; [3] China Highway Engineering Consultants Corporation, Beijing, China; [4] Hebei Hydrological Engineering Geological Exploration Institute, Shijiazhuang, China; [5] Land Satellite Remote Sensing Application Center, MNR, Beijing, China; [6] Key Laboratory of Digital Earth Science, Aerospace Information Research Institute, Chinese Academy of Sciences, Beijing, China;

1. INTRODUCTION

The warming of the global climate has become an indisputable fact of climate change. Under the influence of rising global temperature, the frequency of precipitation and the melting of glaciers are accelerated, resulting in increased flow of rivers, which in turn triggers sea level rise. In China, a large number of glaciers are retreating, the frequency of glacier jumps has increased sharply, and geological disasters such as glacier collapse and glacial lake collapse have occurred frequently.

The areas where glaciers are distributed are usually steep in terrain and difficult to reach by manpower, so long-term on-site dynamic monitoring cannot be completed. The emergence of advanced remote sensing satellites can obtain glacier movement information with high resolution, global coverage and low-cost technology, and has become an important means of glacier movement monitoring. Optical images obtained by Earth observation satellites are commonly used data sets in glacier monitoring. Compared with traditional methods such as field measurements, they have a wider coverage, shorter revisit periods and lower costs. Many researchers used optical imaging early to measure surface displacement, glacier topography and velocity[1].Optical remote sensing technology is relatively mature, but it cannot overcome the limitations of weather conditions such as dependence on light and cloud and rain. In contrast, Synthetic Aperture Radar (SAR) can observe day and night without the limitation of cloud and rain in glacial regions. Currently, techniques for monitoring glacier movement based on SAR data include offset tracking, DInSAR (Differential Interferometric Synthetic Aperture Radar), and MAI (Multi-Aperture Interferometry) [2-8].

In 2016, two major natural disasters occurred near Aru lake in Tibet, China. Glacier surging occurred in two glaciers of nameless mountain on the west side of Aru Lake, and part of the collapsed ice entered Aru lake, that had caused serious damage to the lives and property of the local people and the fragile ecological environment of the surrounding areas. Some studies have shown that the collapse of the two glaciers is inconsistent with the glacier surging, which is manifested as a cycle between the stationary period and the active period[9]. This may indicate that these glaciers are now transitioning from cold bases to hotter glaciers due to warming conditions in the region. The phenomenon also threatens the stability of similar glaciers that are widely distributed on the Qinghai-Tibet Plateau. Therefore, the monitoring of glacier movement is of great significance to the monitoring and early warning of the Aru region and even the entire Qinghai-Tibet Plateau. The study intends to use ALOS PALSAR-1/2 L-band and COSMO-SkyMed-X-band SAR data, mainly using offset tracking technology, and to evaluate the surface motion characteristics of the two glaciers before and after surging, and evaluate the applicability in glacier surging monitoring.

2. 1. STUDY AREA AND DATASET

2.1.1 Study area

Aru region, located in the northern Tibetan Plateau, is an administrative division of Tibet Autonomous Region, and geographical coordinates are 78□23’40’’E-86□11′51′′E and 29 40′40′′N-35□42′55′′. Aru region is high in elevation, the altitude ranges from 3862.5 m to 6606.9 m, with an average elevation of 5450.6 m. The climatic conditions are dry and cold and the annual rainfall is small and the temperature difference between day and night is large (In august, the daytime temperature is above 10℃ while dropping below 0℃ in night-time). In July and September 2016, ice avalanche occurred in the two glaciers of nameless mountain located in the west of Aru Lake. Part of the collapsed glacier body entered Aru Lake. Figure 1 shows the location of the two collapsed glaciers.

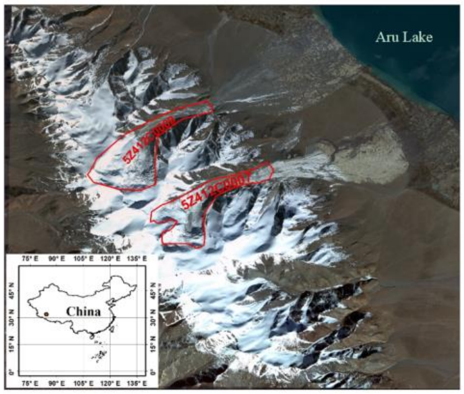

Fig.1. Google Earth image of the two glaciers next to Aru lake. (The glaciers are marked with red lines. The ID of the northern one is 5Z4120009, and the ID of southern one is 5Z412007)

2.1.2 Data

ALOS PALSAR-1/2 were launched by Japanese Space Agency in 2006 and 2014, respectively. The two satellites are equipped with L-band sensors, including single, dual and full polarization modes. In this study,5 ALOS images, collected in 2008, 2009 and 2015 - before the glacier surging-, and 2 images collected in 2018 - after the glacier surging - were used including reference and slave image. ALOS PALSAR-1 images were acquired in high-resolution mode (4.68 m in range and 3.15 m in azimuth), and the polarization mode is HH. Regarding ALOS-2 images, they were acquired in strip mode (4.29 m in range and 3.78 m in azimuth) and the polarization mode is HH. Image registration and geocoding were assisted by a 5-meter resolution DSM (digital surface model), calculated from the Chinese ZY-3 stereo images. In Table 1, the main parameters of ALOS PALSAR-1/2 data used in this paper are listed.

Table 1. Main parameters of ALOS PALSAR-1/2 data

Sensor type	Reference image date	Slave image date	Ascending/Descending	Perpendicular baseline(m)	Time baseline(d)
PALSAR1	20081126	20090111	Ascending	445.5	46
PALSAR1	20090111	20090226	Ascending	164.1	46
PALSAR2	20151008	20151217	Ascending	160.6	70
PALSAR2	20180531	20180726	Ascending	24.9	56

COSMO-SkyMed consists of four LEO low-Earth orbit medium-sized satellites launched by the Italian Space Agency (Agenzia Spaziale Italiana, ASI), each with a microwave high-resolution synthetic aperture radar X-band sensor operating at 9.6 GHz, The wavelength is 3.1 cm, and it has the function of left and right vision. It has better resolution and better ground displacement sampling rates up to 176.25 MHz than longer wavelength systems.

The scattering characteristics of the ice surface are unstable, and when two SAR images are separated for a long time, the decorrelation phenomenon is usually serious. Therefore, data with a smaller time baseline was selected to improve its coherence, and the interferometric data of 20190920-20190921 were selected for DInSAR processing.

Table 2. Main parameters of COSMO-SkyMed

Orbit direction	Reference image data	Slave image data	Perpendicular baseline(m)	Time baseline(d)
Ascending	20190920	20190921	-424.5729	1
Ascending	20190920	20190929	-899.6587	9
Ascending	20190929	20191006	719.5999	7

3. METHODS AND PROCESS

3.1 offset tracking technique

The offset tracking technique was used to obtain the movement of the glacier surface in both range and azimuth directions [10]. In general, the accuracy of offset tracking technique can reach more than 1/10 of the pixel resolution of SAR image [11]. Thus, for ALOS data with about 7 m resolution in ground range, the calculation accuracy is better than 1m.

The core algorithm of offset tracking technique is the normalized cross-correlation algorithm, which generally includes the offsets of terrain, ionosphere, orbit and glacier movement[4,12-エラー! 参照元が見つかりません。.

The ionospheric offset is related to latitude and sensor wavelength. Aru region is located in a low latitude area, and the spatial scale of ionospheric variation is small, compared with the glacier area, so it can be ignored[14]. The offset caused by the terrain is related to the time baseline and topographic relief. In this study, the terrain is steep, so the influence of topographic relief needs to be considered. Firstly, the master and slave image registration lookup table was established based on the track information of the external DEM (digital elevation model) and SAR images, and then the master image and the slave image obtained based on the initial lookup table were cross-correlated for registration. Then, the offset caused by the terrain of the study area was introduced into the lookup table to further refine it. This method can reduce the offset error caused by inaccurate track positioning and improve the accuracy of offset tracking in topographical relief areas[15-16]. The accuracy of registration can be evaluated by analysing the coherence of master-slave images with interferometric fringes. Therefore, interferograms and coherence images are generated.

7 ALOS PALSAR scenes were used. Since the area covered by the images was different, there was a need to crop them all around the location of the two glaciers. Then the external DEM was used to assist the SAR image pairs' registration. The interferograms were generated from all image pairs in order to check the reliability of the registration and analyse the possibility to detect the glacier movement with InSAR and MAI. Finally, based on cross-correlation calculation of image pair's intensity, the surface flow of the 2 glaciers in different periods were measured and analysed by creating 2-Dimensional velocity diagrams which were modulo of azimuth and range displacement based on offset tracking method.

3.2 D-InSAR

Differential Synthetic Aperture Radar Interferometry (Differential InSAR, DInSAR) is used to monitor small changes in the Earth's surface topography on the order of a few centimeters or less in the satellite line-of-sight (LOS) and provide accurate measurements related to various geophysical phenomena. kinematic data. For example, tectonic and volcanic activity, land subsidence, ice sheet and glacier movement, and landslides are involved. The two-orbit differential method is one of the most commonly used methods in differential satellite-based interferometry, which involves analyzing the phase difference between two SAR images from two separate flight trajectories and eliminating them using a digital elevation model (DEM). Terrain effects.

Ideally, the two imaging of the ground object by the antenna are located in the same spatial position, but in practice, the technology cannot achieve the exact same or repeated orbit platform and parameter settings for the two repeated imaging of the antenna. Therefore, when obtaining the interference pair of two SAR images, it is necessary to perform image registration, generate an interferogram, and obtain the upward change of the radar line of sight according to the change of the phase difference in the interferogram, so as to obtain the change of the terrain information.

4. RESULTS AND ANALYSIS

4.1 offset tracking technique

Through differential interferometry of the PALSAR-1/2 image pairs (Table.1), 4 interferograms were generated (see Fig.2). At the first glance the fringes in all interferograms were very clear. The interferometric fringes of flat terrain are straight, while the interferometric fringes of mountain area are distributed along the terrain trend, which were in line with the actual interferometric fringe characteristics. It can be stated that the registration of all the image pairs are accurate enough to be used for DInSAR, MAI and offset tracking. But the fringes disappeared on the glaciers in all interferograms, which means that the coherence on glaciers were poor and the phase based InSAR and MAI methods can’t be applied to detect glaciers’ movement.

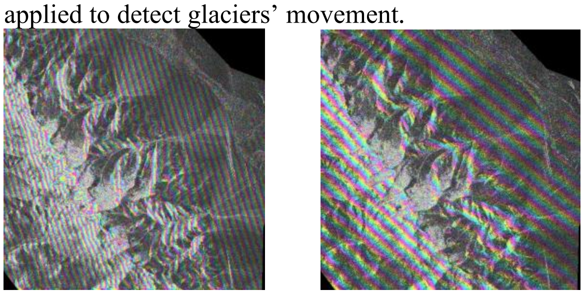

(a) 2008/11/26-2009/01/11 (b) 2009/01/11-2009/02/26

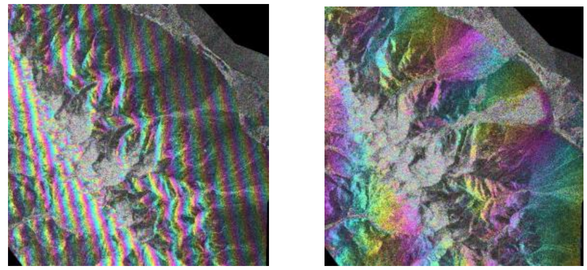

(c) 2008/11/26-2009/01/11 (d) 2008/11/26-2009/01/11

Fig. 2. The interferograms generated using PALSAR-1/2 image pairs

The differential interferogram (SAR coordinate system) of the 1-day time baseline is generated during the DInSAR process, with poor coherence and only obvious phase information at the tail of the glacier. It can be seen from the figure that the shadow situation caused by terrain fluctuations in the study area is serious, and this phenomenon occurs in the data of the ascending and descending orbits.

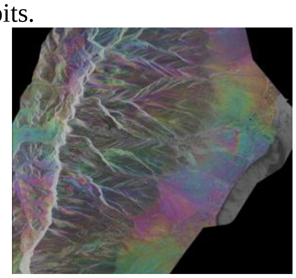

Fig.3. 20190920-20190921

4.2 Analysis of offset tracking results

4.2.1 PALSAR- 1/2 results

Based on the offset tracking technique, PALSAR- 1/2 images were used to obtain the displacement characteristics of the two glaciers from both range and azimuth direction. The two-dimensional velocity field of the 2 glaciers, in four time periods, were calculated and the results are shown in Fig.3.

From Fig.4 (a-d), it can be concluded that: (1) glacier 5Z4120009 shows a maximum movement velocity in 2008-2009, of about 5 cm/d, being the maximum movement velocity in 2015 of about 20 cm/d, and the maximum movement velocity in 2018 of about 5 cm/d; (2) glacier 5Z4120007 shows a maximum movement velocity of about 7 cm/d, in 2008-2009, and the maximum movement velocity was of about 12 cm/d, reached in 2015. In 2018 the maximum movement velocity was about 7 cm/d; (3) comparing with the velocities before the glacier surging, the ones after the glacier surging are significantly increased.

The results show that the glaciers’ movement velocity accelerate as the monitoring period approaches the ice avalanche date. After the glaciers surging in 2016, the glaciers’ movement returns to the relatively low velocity as before the surging. That’s to say the velocities before the glacier surging are significantly increased and significantly decreased after the glacier surging. These conclusions show that glaciers' movement velocity can be used as a valuable indicator to find and monitor surging glaciers.

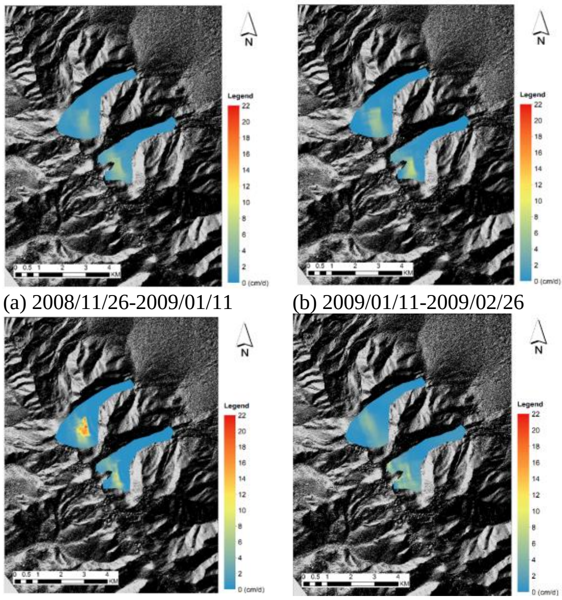

(a) 2008/11/26-2009/01/11 (b) 2009/01/11-2009/02/26

(c) 2015/10/08-2015/12/17 (d) 2018/05/31-2018/07/26

Fig.4. Representation of the 2-Dimensional velocity diagram of the 2 glaciers near Aru Lake

4.2.2 COSMO-SkyMed

The COSMO-SkyMed data is processed by the DInSAR method. After selecting the SAR image, the cross-correlation algorithm is used to perform refined registration first to generate the interferogram. A differential interferogram is generated by subtracting the topographic phase simulated by the DEM from the original interferogram.As shown in Figure3, the differential interferogram is displayed as a contour map composed of fringes, containing changes in surface motion in terms of glacier motion information. In order to suppress the decorrelation noise, a multi-view operation is performed to process the interferogram, and then a least-squares-based interferogram filter is performed. The stable rock area near the glacier is selected as the reference point, and the phase unwrapping is performed by the minimum cost flow (MCF) algorithm to generate For the results in the LOS direction, the SAR coordinate system is finally converted into geographic coordinate system data for further analysis, as shown in Figure 5.

The 20190920-20190929 interferometric pair based on DEM-assisted offset tracking technology is compared and analyzed for the daily average velocity results in the LOS direction and the 1-day displacement results of DInSAR. According to Figures 5 and 6, it can be seen that both methods detect glacier movement, and the maximum LOS velocity of the glacier detected by the offset is 25 cm/d, which is mainly distributed in the middle and upper ends of the glacier, and the glacier's maximum LOS velocity detected by the offset is 25 cm/d. The high-value area of speed fits well with the area with large terrain slope. The maximum displacement of the glacier detected by DInSAR in one day is 6 cm, and the displacement is mainly distributed at the end of the glacier, indicating that the glacier is still expanding.

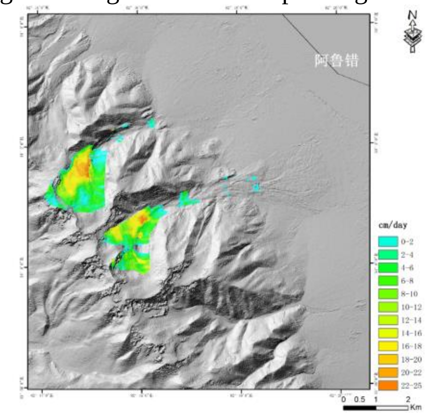

Fig.5. 20190920-20190929 offset result (LOS direction)

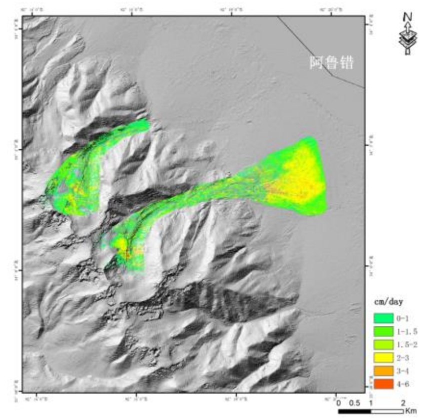

Figure 6 20190920-20190921DInSAR results

5. REFERENCES

The snow cover on the upper part of the glacier is obvious, so the ground reflection on the upper part of the glacier is strong, and its coherence is poor. Therefore, only the information of the tail end of the glacier is obvious in this DInSAR survey. The deviation of the results of the two methods is due to the fact that the offset is averaged based on the results of 9 days. Therefore, the glacier movement rate in the figure is smaller than that obtained by the DInSAR method, while the result obtained by the offset tracking technique is smaller. The detection results of the tail of DInSAR also verified that the glacier is constantly moving and flowing into Lake Alucuo. From the accumulation fan formed at the tail end and the ice blocks floating in the Alu Co Lake below it, it can be concluded that the glacier movement is very active and the flow is rapid, and the ice blocks and meltwater formed by the glacier movement enter the Alu Co Lake. Therefore, the floating ice and meltwater of the glacier become the main water source of Alu Co Lake. During the melting period of the glacier, a large amount of ice-water mixture was formed and the water flow was injected into the lake, and the water level of the lake rose.

When the water level of Alucuo Lake rose, the ice blocks in the lower part of the glacier fell off and melted, causing the glacier to melt faster and the flow rate to increase.

5. CONCLUSION

The migration tracking technique was applied to 3 ALOS PALSAR-1 and 4 ALOS-2 PALSAR-2 images to monitor the surface motion before and after the avalanche that occurred on two glaciers near Lake Aru in 2016. Two main research conclusions can be drawn:

(1) Offset tracking technology is more suitable for monitoring glacier movement than D-INSAR technology.

(2) Before the glaciers surging in 2016, the maximum movement rate of the 2 glaciers' surface increased from 5 cm/d and 7 cm/d to 20 cm/d and 12 cm/d, respectively. After the events, the movement velocity of the glaciers decreased. The maximum glacier movement velocity in 2018 decreased to 5 cm/d and 7 cm/d, close to the monitoring results of 2008 and 2009.

Based on the COSMO-SkyMed data and offset tracking technology in September-October 2019 to detect the flow velocity changes of the Alucuo Glacier, DInSAR detection was carried out on the COSMO-SkyMed data of the 1-day time baseline and the ALOS-2 data of the 14-day time baseline. The results show that the Alucuo Glacier moves at an average flow rate of 8 cm/day from late September to early October, and the highest regional movement rate can reach 22 cm/day; From the front of the glacier to the tongue of the glacier, the area with the largest flow velocity is spatially consistent with the area with the largest terrain slope.

REFERENCES

[1] Luckman A, Quincey D, Bevan S. "The potential of satellite radar interferometry and feature tracking for monitoring flow rates of Himalayan glaciers," *Remote Sensing of Environment*, 111(2-3): 172-181, 2007.

[2] Goldstein R M, Engelhardt H, Kamb B, et al. "Satellite radar interferometry for monitoring ice sheet motion: application to an antarctic ice stream," *Science*, 262(5139): 1525-1530, 1993.

[3] Gray A L, Mattar K E, Vchon P W, et al. "InSAR Results from the RADARSAT Antarctic Mapping Mission Data: Estimation of Glacier Motion using a Simple Registration Procedure," *Geoscience and Remote Sensing Symposium Proceedings. IGARSS '98*. 1998 IEEE International, 1998, 3: 1638-1640, 1998.

[4] Zhou Chunxia, Deng Fanhui, Ai Songtao, et al. "Determination of Ice-flow Velocity at the Polar Record Glacier and Dalk Glacier Using DInSAR," *Geomatics and Information Science of Wuhan University*, 39(8): 940-944, 2014.

[5] Li J, Li Z W, Wu L X, et al. "Deriving a time series of 3D glacier motion to investigate interactions of a large mountain glacial system with its glacial lake: Use of Synthetic Aperture Radar Pixel Offset-Small Baseline Subset technique," *Journal of Hydrology*, 559: 596-608, 2018.

[6] Mouginot J, Rignot E, Scheuchl B, et al. "Comprehensive Annual Ice Sheet Velocity Mapping Using Landsat-8, Sentinel-1, and RADARSAT-2 Data," *Remote Sensing*, 9(4):364, 2017.

[7] Wang Sisheng, Jiang Liming, Sun Yongling, et al. "Evaluation of methods for deriving mountain glacier velocities with ALOS PALSAR images:A case study of SKyang glacier in central Karakoram," *Remote Sensing for Land and Resources*, 28(2): 54-61, 2016.

[8] Zhang Xiaobo, Zhao Xuesheng, Ge Daqing, et al. "Motion Characteristics of the South Inilchek Glacier Derived from New C-Band SAR Satellite," *Geomatics and Information Science of Wuhan University*,44(3): 429-435, 2019.

[9]Gardelle J, Berthier E and Arnaud Y. "Slight mass gain of Karakoram glaciers in the early twenty-first century. *Nat.Geosci.*, 5(5), 322–325, 2012.

[10] Strozzi T, Luckman A, Murray T, et al. "Glacier motion estimation using SAR offset-tracking procedures," *IEEE Transactions on Geoscience and Remote Sensing*, 40(11): 2384-2391, 2002

[11] Haemmig C, Huss M, Keusen H, et al. "Hazard assessment of glacial lake outburst floods from Kyagar glacier, Karakoram mountains, China," *Annals of Glaciology*, 55(66): 34-44, 2014.

[12] Li J, Li Z, Zhu J, et al. "Deriving surface motion of mountain glaciers in the Tuomuer-Khan Tengri Mountain Ranges from PALSAR images," *Global and Planetary Change*, 101: 61-71, 2013.

[13] Deng fanghui, Zhou Chunxia, Wang Zemin, et al. "Ice-flow Velocity Derivation of the Confluence Zone of the Amery Ice Shelf Using Offset-tracking Method," *Geomatics and Information Science of Wuhan University*, 40(7): 901-906, 2015.

[14] Wegmuller U, Werner C, Strozzi T, et al. "Ionospheric Electron Concentration Effects on SAR and INSAR," IEEE International Conference on Geoscience & Remote Sensing Symposium. IEEE, 2007.

[15] GAMMA Remote Sensing. " Differential Interferometry and Geocoding Software – DIFF&GEO (Geocoding and Image Registration)," Switzerland: GAMMA Remote Sensing AG, 2008.

[16] Wang Qun, Fan Jinghui, Zhou Wei, et al. " Research on the DEM-assisted offset tracking technique applied to glaciers movement monitoring," *Remote Sensing for Land and Resources*, 30(3): 167-173, 2018.

APPENDIX

[1] Wang. C. , Fan. J. , Wang. Q. , Yuan. W. , & Sousa. J. J.. " Use of l-band sar data for monitoring glacier surging next to aru lake,"

Procedia Computer Science, 181(8), 1131-1137，2021.
[2] WANG Qun, ZHANG Yunling, FAN Jinghui, FU Yuhao. "Monitoring the Motion of the Yiga Glacier Using GF-3 Images," *Geomatics and Information Science of Wuhan University*, 45(3): 460-466, 2020.

3.10 Polar research

ADVANCING INFORMATION EXTRACTION ON ARCTIC SEA ICE USING A MULTI-SENSOR AND MULTI-TEMPORAL INTEGRATED APPROACH

PI No.: ER2A2N013
Torbjørn Eltoft[1], Malin Johansson[1]

[1] UiT The Arctic University of Norway

1. INTRODUCTION

The overall objectives of this project are:

1) *Improving sea ice type classification and geophysical parameter retrievals for operational and scientific applications. This implies studies of* synthetic aperture radar (*SAR) signature changes for different sea ice types due to variations in meteorological and environmental conditions, with focus on ALOS-2 and ALOS-4 SAR systems in comparison to Sentinel-1;*

2) *Separation of thin ice from oil slicks utilizing the good signal to noise ratio of L-band SAR*

3) *Studying the surge initiation phase of the glacier Kongsvegen on Svalbard.*

The motivation fro this study is founded in the climate changes enfolding in polar areas. In the light of a changing Arctic regime towards an environment with thinner sea ice, a longer melt season and potentially higher sea ice drift velocities with increased sea ice deformation, time series using L-band SAR are here used for seasonal sea ice studies. A changing Arctic climate regime with longer melt seasons, thinner sea ice and changes in the sea ice composition requires further studies into SAR-based sea ice classification and geophysical parameter retrievals. The longer penetration depth of L-band SAR has already been established to be beneficial in sea ice classification, where it has been shown to be of general benefit for characterizing sea ice surfaces and classifying sea ice into ice types. It improves discrimination between first year ice (FYI) and multiyear ice (MYI), and it improves detection and characterization of leads and thin ice areas. L-band SAR has also been found to be beneficial for monitoring early and advanced sea ice melt. This is in particular important for operational sea ice mapping.

In this project we have identified polarimetric and textural parameters that can help improve sea ice classification during different environmental conditions and incidence angles. During the MOSAiC drift study, overlapping C- and L-band images were acquired and the sea ice characterization capabilities compared to identify complementarity of the two frequencies.

In addition, the well monitored areas on Svalbard, and in particular Kongfjorden and the surrounding glaciers such as Kongsvegen, allow for studies of SAR capabilities of monitoring a cryosphere system from glacier to sea ice and open ocean. The satellite monitoring of the upcoming surge of Kongsvegen is of specific importance from a climate change perspective. The ongoing high resolution in-situ monitoring of the glacier and its surroundings, combined with the collection of ALOS-2 satellite data, provides a unique opportunity to observe a Svalbard glacier surge from the start for the first time.

2. DATA

Multi-channel SAR observations over ice infested areas north of Svalbard and in the Fram Strait were acquired. Thanks to a much appreciated flexibility from JAXA, we were able to acquire data over the MOSAiC sea ice drift study, and over the Belgica bank area to overlap one of the Nansen Legacy cruises in 2021. In total, 60 ALOS scenes were ordered and received for the project. These consisted of 18 quad-pol scenes, 16 dual-pol scenes and 26 ScanSAR wide-swath, dual-pol scenes. Most of the scenes were acquired during the MOSAiC cruise (September 2019 – October 2020).

In-situ data, including meteorological observations, and sea ice and snow data, was collected during the MOSAiC drift campaign, and these data was used to interpret observations made in the overlapping C- and L-band SAR images.

In-situ ground-based field data of glacier movement, meteorological and mass balance data were collected from the Kongsvegen glacier and nearby glaciers as a part of a mass-balance monitoring program conducted by the Norwegian Polar Institute. Glacier mass balance has been measured since 1987 and velocity data along the centre line of Kongsvegen started in 2004. Since the early 1990s, ice-penetrating radar surveys were conducted to complete existing bed topography maps and to document changes in the thermal structure. In 2018, an expanded monitoring system was set up, which included five continuously-logging GNSS receivers, installed at ca. 3 km intervals along the glacier centreline, a 330-m long borehole, drilled to the glacier bed and instrumented with a thermistor string, basal water pressure sensor, and cameras to monitor the front. Year-round meteorological data are also available from the Ny-Ålesund Research Station in Kongsfjorden.

3. METHODOLOGIES

A machine learning method was used in [A1, A4 and A6]. The method relies on fully polarimetric SAR images and consists of two steps; first 18 polarimetric features are extracted, and thereafter, patches for training/validation of the artificial neural network (ANN) classifier are identified. Regions of interest (ROIs) were identified manually by using in-situ data as well as overlapping optical images to find suitable areas. A detailed description of the ANN is available in [1]. The methods classify the observed sea ice scenes into four different classes, i.e., open water and nilas (OW), YI, smooth FYI(SFYI), and rough first year/multiyear ice (RFYMYI).

In [A2] the segmentation method outlined in [6,7] were used to segment the fully-polarimetric ALOS-2 PALSAR-2 images. The segments were subsequently classified by sea ice expert at the Ice Service at the Meteorological Institute of Norway.

For [A3,A5,A7,A9,A12], the ROIs were identified manually, and where possible, the first MOSAiC ice floe was included in the analysis. The sea ice types of interest here were open water and nilas (OW), YI, smooth FYI(SFYI), and rough first year/multiyear ice (RFYMYI). The evolution of the SFYI and RFYMYI ice were followed from the freeze-up to the early melt season stages, and the YI and OW classes were labelled when these were found.

For [A10-A11], were ROIs identified manually in spatially and temporally overlapping Sentinel-1 and ALOS-2 PALSAR-2 images. The ROIs are then used to retrain the method developed in [5] to classify different sea ice types in both L- and C-band SAR images.

In [A13], the InSAR module in the ESA's SNAP program was used for the interferometric study.

4. SUMMARY OF RESEARCH FINDINGS

In total, 1 scientific journal paper, 2 international conference proceeding paper, 2 conference presentations, and 4 conference posters have been published based on the research in this project. In addition, the ALOS-2 PALSAR-2 data have been a basic data source for one MSc thesis. Two ongoing publications, where data from this project has been instrumental, are soon to be submitted (incl. [A3]) and the part of this work will also be presented at the ESA Living Planet 2022 conference in May 2022. We appologice for the delay in the publications that were in part a consequence of the Covid-19 pandemic. Below are some research results, where the high-lights are pesented in terms of the paper abstracts.

The first objective of this proposal has been addressed using fully polarimetric images from the MOSAiC and N-ICE2015 expeditions as well as overlapping Sentinel-1 and ALOS-2 PALSAR-2 images from the Arctic Ocean.

In [A1], we employ an artificial neural network (ANN)-based sea ice type classification algorithm on a comprehensive data set of ALOS-2 PALSAR- 2 fully polarimetric images acquired with over a range of incidence angles and different environmental conditions. The variability of the data makes it ideal for making novel assessment of the robustness of the sea ice classification, investigating the intraclass variability, study the seasonal variations, and assess the incidence angle effect on the sea ice classification results. The images coincide with two different Arctic field campaigns in 2015: the Norwegian Young Sea Ice Cruise 2015 (N-ICE2015) and the Polarstern's (PS92) Transitions in the Arctic Seasonal Sea Ice Zone (TRANSSIZ). We find that it is essential to take into account seasonality and intraclass variability when establishing training data for machine learning-based algorithms. Moderate differences in incidence angle are possible to accommodate by the classifier during the dry and cold winter season.

An important finding was also that the incidence angle dependency for a set of different sea ice types in L-band SAR images are the same across different regions of the Arctic; including sea ice from the Canadian Arctic Archipelago [2], [3], the area north of Svalbard [A1], and the Sea of Okhotsk [4]. The implication of this is that overlapping in-situ data and satellite images from different regions of the Arctic can be used to establish training datasets. This is a cost-saving finding.

MOSAiC expedition:
In September 2019, the German research icebreaker Polarstern started the largest multidisciplinary Arctic expedition, the MOSAiC (Multidisciplinary drifting Observatory for the Study of Arctic Climate) drift experiment. Being moored to ice floes in the high Arctic for a whole year, thus including the winter season, the main goal of the expedition is to better understand and quantify relevant processes within the atmosphere–ice–ocean system that impact sea ice, ultimately leading to improved climate models. Satellite remote sensing, especially using multi-frequency synthetic aperture radar (SAR), plays a major role to achieve this goal. The expedition has two major objectives related to SAR based remote sensing of sea ice; on the one hand, to have a large coverage, and on the other hand, to make radar observations that encode as much sea ice information as possible. A comprehensive set of C- and L- band SAR images were acquired during the course of MOSAiC.

In [A3, A5, A7-A9, A12], we evaluate the effects of seasonal changes on C- and L-band backscatter from three different sea ice types, i.e., Young Ice, Smooth Ice and Rough/Deformed Ice, and study how these changes affect the performance of sea ice type retrieval of an established algorithm. Areas of deformed, smooth and young sea ice were observed in the vicinity of R/V Polarstern and were included in the year-long time series of SAR scenes. For both frequencies, a change in all polarimetric channels can be observed during the early melt season. This is first noticeable in the C-band images and later also seen in the L-band images. The later observation in L-band compared to C-band, is probably caused by the frequencies different penetration depth and volume scattering sensitivity.

An oral presentation of the work was given as a solicited talk during EGU 2021 [A5]. Here different polarimetric features and their evolution from the freeze-up to the early melt season are investigated. The MOSAiC floe consisted of two parts, one part that was deformed and had high backscatter, and another part which had a high proportion (>60%) of refrozen melt pond coverage. As has been shown before, the separation between smooth and deformed sea ice is larger in L-band compared to C-band SAR, though once the temperature approaches 0º C, the difference is reduced.

Comparing the different sea ice types, we observe that during the freezing season there is a larger difference in the co-polarization channels between smooth and deformed ice in L-band compared to C-band. Similar to earlier findings, we observe larger differences between young ice and deformed ice backscatter values in the L-band data than in the C-band data. Moreover, throughout the year the HV-backscatter values show larger differences between level and deformed sea ice in L-band than in C-band. The L-band data variability is significantly smaller for the level sea ice than for the deformed sea ice, and this variability was also smaller than that observed for the overlapping C-band data. Thus, L-band data could be more suitable to reliable separate deformed from level sea ice areas.

Within the L-band images, a noticeable shift towards higher backscatter values is observed in the early melt season compared to the freezing season for all polarimetric channels, though no such strong trend is found in the C-band data. The change in backscatter values is first noticeable in the C-band images and later followed by a change in the L-band images, probably caused by their different penetration depth and volume scattering sensitivities. This change also results in a smaller backscatter variability.

The polarization difference (PD; VV-HH on a linear scale) shows a seasonal dependency for the smooth and deformed sea ice within the L-band data, whereas for the C-band data, no such trend is observed. For the L-band data, the PD variability is reasonably small for all ice classes in the freezing season, with a significant shift towards larger variability during the early melt season. However, during the early melt season period the mean PD values remained more or less constant. However, once the temperatures reached above 0°C both the variability and the mean values increased significantly.

Overall, our results demonstrate that the C- and L-band data are complementary to one another and that through their slightly different dependencies on season and sea ice types, a combination of the two frequencies can aid improved sea ice classification. The availability of a high spatial and temporal resolution dataset combined with in-situ information ensures that seasonal changes can be fully explored. This work will also be presented on the ESA Living Planet Sympositum in May 2022 [A12], a manuscript presenting this work will soon be submitted [A3].

Newly formed sea ice and oil spills
Newly formed sea ice allow light penetration into the underlaying water and aid primary production. The good noise floor of the ALOS-2 PALSAR-2 images enabled high accuracy identification of deformed and level sea ice as well as newly formed sea ice areas. During the N-ICE2015 expedition significant numbers of ALOS-2 PALSAR-2 images were collected and this enabled a time series analysis overlapping in-situ data collected analysing the biological productivity in the water mass around the campaign. SAR images were segemented using the method outlined in [6,7] and subsequently were the percentages of the different ice types estimated and combined with the in-situ data were the effect of open water and deformed ice areas influence on the biologicaly productivity investigated and presented in [A2].

During the MOSAiC expedition had thin ice just started to form around the MOSAiC floe when the expedition started. Differences in new ice polarimetric signatures between the two frequencies are currently being investigated as, e.g., the PD show significantly different values for the C and L-band images. Improved knowledge about the polarimetric signature of newly formed sea ice is a part of addressing the objective two to supplement ongoing work first presented in [8] about separation between newly formed sea ice and oil spills.

Overlapping Sentinel-1 and ALOS-2 PALSAR-2:
In [A10, A11] overlapping Sentinel-1 and ALOS-2 PALSAR-2 images have been used to identify sea ice types for sea ice classification. The work is investigating complementarities through the use of these two frequenceies, and the work was first presented on the Arctic Science Summit Week in Tromsø in 2022 and will also be presented during the ESA Living Planet conference in May 2022.

InSAR on Svalbard:
In recent years, in-situ measurements on Kongsvegen, a surge-type glacier located in the Kongsfjorden area on Svalbard, have shown an acceleration in the flow speed of the glacier. This part of the work addresses the third

objective of the proposal. This could indicate the onset of a surging event, which in that case would present the opportunity to study the dynamics of a glacier surge using remote sensing techniques, with in-situ data for reference. In [A13] the acceleration of Kongsvegen using InSAR, Multiple-aperture InSAR (MAI) and offset tracking was investigated. Velocity measurements from the combination DInSAR - MAI are then compared to in-situ data as well as to offset tracking measurements. For image pairs, where InSAR measurements are not possible due to phase decorrelation, offset tracking is attempted as a back-up. Data from 2015, 2018 and 2019 was available, and the evolution of flow speeds over time could therefore be evaluated. The image pairs from 2018-2019 were acquired with 14 days separation in time, while the 2015 image pairs were acquired with 28 and 42 days of separation. Due to the longer separation in time, the 2015 image pairs decorrelated in time. In addition, a pair acquired in the summer of 2018 decorrelated as a result of surface melting on the glaciers.

For the image pairs from 2018-2019, the InSAR measurements were in good agreement with the in-situ data, as they also indicated an acceleration of the flow speed on Kongsvegen. The offset tracking results based on these pairs overestimated the velocity magnitudes, but also showed an increase over time. Similar to the InSAR estimates, the offset tracking failed to produce reasonable results for the images from 2015 image pairs, likely because of the large temporal baseline and the lack of surface features on Kongsvegen. Overall, InSAR could be used to measure the flow speed of Kongsvegen successfully, but more data with a short temporal baseline is needed for an in-depth analysis.

6. SUMMARY

In accordance with the described objectives, the research has contributed to improved understanding of monitoring capabilities of Arctic sea ice using C- and L-band SAR data. The multi-polarimetric, multi-sensor approach has been shown to have some complementary capabilities, which combined will improve sea ice monitoring. More specifically, the research indicates that combined C- and L-band SAR data can provide;

- Improved sea ice classification methodologies that can separate FYI and MYI, locate ridges and leads, and provide sea ice characterization of relevance to science and industry.

- Improved sea ice classification across seasons considering variations in meteorological and environmental conditions

- Efficient approaches for multi-frequency and multi-sensor data fusion with respect to sea ice classifications

The project has had participation of PhD and PostDoc scolars and in that respect been important for building competence to this exiting discipline.

7. REFERENCES

[1] Singha S., Johansson A.M., Hughes N., Munk Hvidegaard S.M., Skourup H., Arctic Sea Ice Characterization using Spaceborne Fully Polarimetric L-, C- and X-band SAR with Validation by Airborne Measurements. IEEE Transactions on Geoscience and Remote Sensing, Vol. 56, No. 7, pp. 3715-3734, 2018.

[2] J. A. Casey, S. E. L. Howell, A. Tivy, and C. Haas, “Separability of sea ice types from wide swath C- and L-band synthetic aperture radar imagery acquired during the melt season,” Remote Sens. Environ., vol. 174, pp. 314–328, 2016.

[3] M. S. Mahmud, T. Geldsetzer, S. E. L. Howell, J. J. Yackel, V. Nandan, and R. K. Scharien, “Incidence angle dependence of HH-polarized C- and L-band wintertime backscatter over Arctic sea ice,” IEEE Trans. Geosci. Remote Sens., vol. 56, no. 11, pp. 6686–6698, 2018.

[4] H. Wakabayashi, T. Matsuoka, K. Nakamura, and F. Nishio, “Polari- metric characteristics of sea ice in the sea of Okhotsk observed by airborne L-band SAR,” IEEE Trans. Geosci. Remote Sens., vol. 42, no. 11, pp. 2412–2425, 2004.

[5] J. Lohse, A.P. Doulgeris, W. Dierking, “Incident Angle Dependence of Sentinel-1 Texture Features for Sea Ice Classification”, Remote Sensing, Vol. 13, No. 4, 2021.

[6] Doulgeris, A.P. “ A Simple and Extendable Segmentation Method for Multi-Polarisation SAR Images.”, POLinSAR 2013 (Frascati, Italy), 8 pp, 2013.

[7] Doulgeris, A.P., and Eltoft, T., “Scale mixture of Gaussian modelling of polarimetric SAR data”. EURASIP J. Appl. Signal Proc., 12. doi:10.1155/2010/874592, 2010.

[8] Johansson A.M., Espeseth M.M., Brekke C., Holt B, “Can Mineral Oil Slicks Be Distinguished From Newly Formed Sea Ice Using Synthetic Aperture Radar?”, IEEE Journal of Selected Topics in Applied Earth Observations and Remote Sensing, Vol. 13, pp. 4996-5110, 2020 doi: 10.1109/JSTARS.2020.3017278

APPENDIX

List of published papers related to ALOS EO-RA2.
Journal articles:

[A1] Singha, S.*, Johansson A.M.*, Doulgeris, A.P., “Robustness of SAR Sea Ice Type classification across incidence angles and seasons at L-band”, IEEE Transactions on Geoscience and Remote Sensing, Vol. 59. No. 12, pp. 9941-9952, 2021, 10.1109/TGRS.2020.3035029. *Contributed equally

[A2] Olsen L.M., Duarte P., Peralta-Ferriz C., Kauko H.M., Johansson A.M., Peeken I., Różańska-Pluta M., Tatarek A., Wiktor J., Fernández-Méndez M., Wagner P.M., Pavlov A.K., Hop H., Assmy P., "A red tide in the pack ice of the Arctic Ocean". Scientific Reports, Vol. 9, 2019, doi: 10.1038/s41598-019-45935-0.

[A3] Johansson, M., Singha, S., Spreen, G., Howell, S., Sobue, S., and Davidson, M., "Fully-polarimetric L- and C-band Synthetic Aperture Radar data analysis from the yearlong MOSAiC expedition", IEEE JSTARS (to be submitted)

Conference proceedings:

[A4] Singha S., Johansson A.M., Spreen G., Howell S., Sobue S., Davidson M., "Year-Around C- and L- Band Observation Around the Mosaic Ice Floe with High Spatial and Temporal Resolution", 2021 IEEE International Geoscience and Remote Sensing Symposium IGARSS, pp. 5509-5512, 2021, doi: 10.1109/IGARSS47720.2021.9553062.

[A5] Johansson, M., Singha, S., Spreen, G., Howell, S., Sobue, S., and Davidson, M., "High spatial and temporal resolution L- and C-band Synthetic Aperture Radar data analysis from the yearlong MOSAiC expedition", EGU General Assembly 2021, online, 19–30 Apr 2021, EGU21-2892, https://doi.org/10.5194/egusphere-egu21-2892. (solicied)

Conference presentations:

[A6] Singha, S., Johansson, M., Doulgeris, A.P. "Arctic Sea Ice Classification Using ALOS-2 Palsar-2 L-Band SAR Images". Oral presentation at ESA Living Planet Symposium 2019, oral presentation

[A7] Johansson, M., Eltoft, T., Singha, S., Itkin, P., Spreen, G., Howell, S., Sobue, S., and Davidson, M., "L- and C-band synthetic aperture radar analysis from the yearlong MOSAiC expedition", Joint PI meeting of JAXA Earth Observation Missions FY2021, 2021, poster presentation

[A8] Eltoft, T., Johansson, M., Doulgeris, A.P., Singha, S., Itkin, P., Blix, K., "Advancing information extraction on Arctic sea ice using a multi-sensor and multi-temporal integrated approach", Joint PI meeting of JAXA Earth Observation Missions FY2020, 2020, poster presentation

[A9] Johansson, M., Singha, S., Spreen, G., Howell, S., Sobue, S., and Davidson, M., "Fully-polarimetric L- and C-band Synthetic Aperture Radar sea ice type data analysis", MOSAiC virtual conference, 2021, poster presentation

[A10] Johansson, M. and Lohse, J., " Arctic sea ice monitoring using synthetic aperture radar satellite images/data at C- and L-band frequency", Arctic Science Summit Week, 2022, poster presentation

[A11] Lohse, J., Dierking, W., Johansson, M., Doulgeris, A.P., Taelman, C., " Towards combining C- and L-band SAR imagery for operational classification of sea ice types", ESA Living Planet symposium 2022, oral presentation

[A12] Johansson, M., Singha, S., Spreen, G., Howell, S., Sobue, S., and Davidson, M., " Fully-polarimetric L- and C-band Synthetic Aperture Radar data analysis from the yearlong MOSAiC expedition", ESA Living Planet symposium 2022, oral presentation

MSc thesis:

[A13] Karlsen T., " Measuring velocities of a surge type glacier with SAR interferometry using ALOS-2 data", EOM-3901 Master's thesis in energy, climate and environment 30 SP June 2021, UiT The Arctic University of Norway

ASSESSING THERMOKARST AND FREEZE/THAW DAMAGES ON LAND USE AND INFRASTRUCTURE IN ARCTIC AND ALPINE PERMAFROST REGIONS

PI No.: ER2A2N014

Go Iwahana [1], Yoshihiro Iijima [2], Masao Uchida [3], Alexsandr Fedorov [4]

[1] International Arctic Research Center, University of Alaska Fairbanks
[2] Mie University
[3] National Institute for Environmental Studies
[4] Yakutsk Permafrost Institute

1. INTRODUCTION

The deformation process of (sub-) arctic and alpine lands underline by ice-rich permafrost caused by the melting of massive ground ice, known as thermokarst, alters the local land use and affects the local socio-economy. In order for local residents to adapt to landform changes including ground subsidence, inundation, and thermos-hydrological erosions, knowledge about the deformation rates and spatial distribution of the phenomena is essential.

This research project aims to provide information on spatio-temporal variation in thermokarst and freeze/thaw-related deformation to local stakeholders in arctic and alpine permafrost regions experiencing rapid climate warming. In order to generate the map of spatio-temporal thermokarst deformation, we employ a DInSAR (Differential Interferometry Synthetic Aperture Radar) technique, in a wide range of permafrost regions. Objectives in this project are to 1. Measure the spatial variation in seasonal and inter-annual surface displacement associated with active layer and permafrost dynamics by DInSAR, 2. Validate the spatio-temporal information on surface deformation by conducting field surveys, 3. Reduce uncertainty in radar remote sensing of permafrost degradation, and 4. Provide spatio-temporal information on thermokarst to local stakeholders.

Below, we report four case studies of the InSAR-Thermokarst analyses from Alaska, Siberia, and Hokkaido.

2. NORTH SLOPE, ALASKA

To better understand the nature of DInSAR signals over changing permafrost lands, we investigated surface displacement caused by frozen ground dynamics and thermokarst development triggered by a tundra wildfire in Alaska. The Anaktuvuk River Fire (ARF) combusted surface vegetation and organic mat of the tundra region underlain by variously ice-rich permafrost in 2002. High-precision GNSS survey, thaw depth, and surface moisture were measured along 60 – 200 m transects at three representative sites in ARF during snow-free seasons in 2017 – 2019. The three sites were located in the northernmost fire boundary, the central area, and the southernmost of the ARF burn scar underlain by differently ice-rich permafrost. High-resolution (~1 m) DInSAR signals by UAVSAR depicted enhanced seasonal thaw settlement not only in the burned area but also a liner pattern development of larger subsidence in unburned areas, which coincides with slightly concaved linear micro-topography at Site N (Fig. 1). Significant thermokarst subsidence and seasonal thaw settlement were measured along a Yedoma hill slope both by ground survey and DInSAR at Site M. The intensive permafrost degradation on the slopes was also confirmed by frozen ground coring and optical image analysis. The ground measurements of surface displacement were aligned well with DInSAR displacement using UAVSAR and ALOS2 data except for the anomaly subsidence along the troughs of ice-wedge polygons at earlier thermokarst stages. Less intensive ground surface displacement was observed at Site S, underlain by less ice-rich permafrost. Our results indicate that seasonal thaw settlement was governed mainly by spatial variation in soil frost-susceptibility and thermokarst subsidence by ground ice distribution.

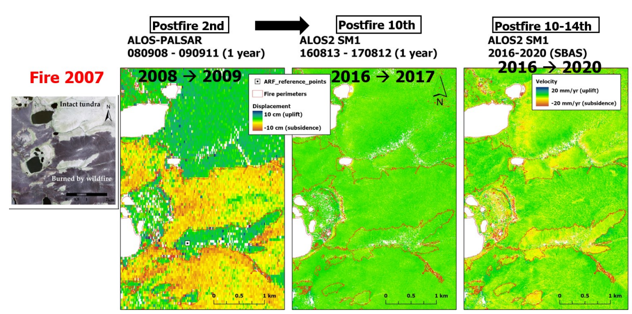

Figure 1. InSAR results of ALOS-PALSAR and ALOS2 over the northern edge of the Anaktvuk River Fire occurred in 2007 on the North Slope, Alaska. Green areas indicate stable land, while reddish color indicates thermokarst subsidence.

3. MAYYA, CENTRAL YAKUTIA

3.1 L-band SAR analysis

Mayya is located on the right bank of the Lena River and 40 km southeast of Yakutsk. Mayya area consists of forest, deforested areas for farming, mainly in the 1970s, and alasses. Alas is the final geomorphological stage of old thermokarst development. Mayya is representative of residential areas where thermokarst development has been reported in Central Yakutia.
We used ALOS/PALSAR (2007-2010) and ALOS2/PALSAR2 (2015-2018) data to investigate ground subsidence caused by thermokarst development. GAMMA software [1] was used to generate interferograms and apply stacking treatment weighted on the length of the summer period between two SAR data acquisitions. Assuming surface displacement consisted only of vertical components, the line of sight (LOS) change was converted to vertical displacement.
We detected ground subsidence with a rate of 1-4 cm/yr in both PALSAR and PALSAR-2 results (Fig. 2). Most subsidence signals are found in numerous open areas (deforested areas), and the PALSAR-2 results clearly show the spatial distribution of the subsidence corresponding to the visible observation of thermokarst development in high-resolution optical images. The subsidence rate varied with time and location.

3.2 Field observation

To validate our InSAR results, we performed leveling surveys within five 30 x 30 m areas, in which about 35 permanent survey stakes were installed and their heights were measured in September 2017 and 2018 (Fig. 3). Areas A, C, and E showed a clear subsidence trend with a

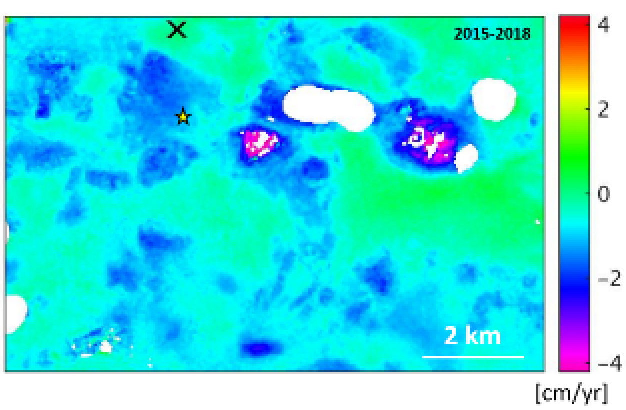

Fig. 2 Surface deformation map in Mayya derived from ALOS2/PALSAR2 data acquired from 2015 to 2018. The positive and negative values mean uplift and subsidence, respectively. The cross marks the reference point of InSAR. The star indicates the area of ground observation shown in Fig. 3.

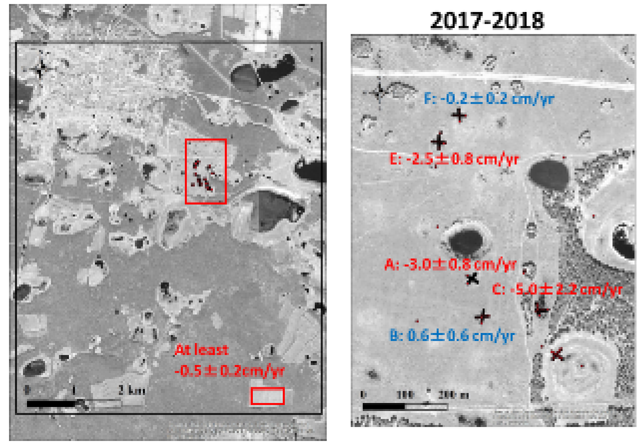

Fig. 3 (left) Locations of field surveys near Mayya; (right) Surface deformation by GPS and optical leveling in 2017 and 2018. The values show the mean and two standard errors (95 % confidence interval).

rate of 3-5 cm/yr, and we confirmed the occurrence of polygonal ground deformation that suggests thermokarst development of ice-wedge polygons. On the other hand, the other two areas (B and F) showed negligible surface displacement from 2017 to 2018. While the overall tendency of the subsidence measured in situ is in harmony with the InSAR result (Fig. 2) quantitatively, the significant subsidence signals at areas A and E were not measured by our InSAR. We revisited and repeated the same field survey in September 2019, and found significant inter-annual surface subsidence in all surveyed areas ranging from 3-10 cm/yr. InSAR analysis including 2019 SAR acquisitions is underway, and the ground truth will be compared with the InSAR in the next step.
We also visited other sites with significant subsidence signals in the interferograms at the end of September 2018. The two large subsidence signals were found in alasses. The subsidence signals could be caused by ground consolidation settlement associated with surface soil desiccation under recent dry climate conditions. However, judging from the occurrence of the polygonal ground depression at the central areas of alasses, it is possible that thermokarst subsidence is still in progress.
This study was published as a result of this project in *Planets and Space* [2].

4. BATAGAI, NE SIBERIA

Batagay is located in the midstream of the Yana River, NE of Sakha Republic. The area is underlain by at least 50-80 m thick of ice-rich permafrost as its interior structure is revealed on the headwalls of a huge thaw slump (Batagaika Megaslump; [3]). Recent wildfires burned an extensive area near Batagay, which triggered prominent thermokarst processes due to the surface disturbance by the fires. Furthermore, a heatwave with unprecedented high temperature persisted during late June 2020, resulting in substantial increases in fire activity above the Arctic Circle [4][5]. Large wildfires and following thermokarst gathered attention from residents, especially land managers and the forestry industry.

Batagay region experienced wildfires in the last decade. We set two areas of interest, AOI1 and AOI2. AOI1 includes a fire scar burned in July 2014 over 35 km^2. The 2019 fire again burned a portion of the 2014 fire scar. We set study sites B14 (381 m asl.) and U14 (254 m asl.) at burned and unburned areas with gentle slopes near the southern edge of the 2014 fire burn scar, respectively. AOI2 consists of two fire scars burned in the 2018 and 2019 summers. Sites B19 and U19 were set at burned and unburned areas in the south-eastern edge of the 2019 fire burn scar divided by a firebreak line.

4.1 Satellite remote sensing analyses

InSAR analysis to generate ground deformation maps over the post-wildfire area was performed by [6]. For this area, we used L-band HH-polarized SAR images of ALOS2/PALSAR2 (2015-2019) and C-band VV-polarized SAR images by Sentinel-1 (2017-2018). Focusing on the seasonal ground deformation in 2017-2018, we stacked Sentinel-1 interferograms to set the temporal coverages to be nearly identical with ALOS2 interferograms and compared to each other. On the other hand, to estimate the cumulative satellite LOS displacement in the post-wildfire area, we used Small Baseline Subset (SBAS)-type time-series analysis, using 50 quality ALOS2 InSAR images taken in 2015-2019.

To investigate ground surface changes, we also used optical satellite images. Five snow-free and cloud-free Landsat8 images (Collection2) acquired during 2014-2018 were used to generate the 2014 fire perimeter based on dNBR (difference normalized burn ratio; Miller and Thode, 2007). To identify newly formed gullies and active layer detachment after the 2014 fire, we used changes in the panchromatic band of Landsat8 images (Fig. 4). Pansharpened images of Pleiades-1 (7 Jun 2019), WorldView2 (6 Jun 2020), and WorldView3 (28 May 2020) were used to observe gully development and water drainage in the area of 2018 and 2019 burn scars.

4.2 Field measurements

We conducted fieldwork campaigns in three consecutive thawing seasons during 2019-2021. In late September 2019, we visited AOI1 and measured relative height, soil moisture, ground temperature, and thaw depth along a 30 m transect at B14. Additionally, thaw depths were measured at burned and unburned areas near an unburned patch within the 2014 burn scar and U14. The same field measurements at B14 were conducted at B19 and U19.

Soil pits were dug for descriptions of soil horizons, volumetric water content measurements by a TDR probe (Hydrosense, Campbell Sci.), and soil sampling for laboratory analyses from the active layer at B14, U14, B19, and U19.

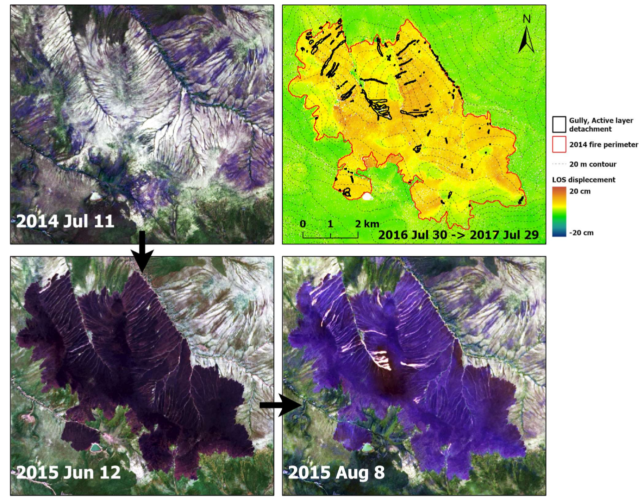

Figure 4. Time series of high-resolution optical images (Landsat8) over a burn scar by Fire 2014 (AOI1). Upper right map shows InSAR line of sight surface deformation map derived from ALOS2-PALSAR2 data acquired on 30 Jul 2016 and 29 Jul 2017 [6]. The positive (reddish colors) and negative (blueish colors) values indicate subsidence and uplift, respectively. The contours are elevation in 20 m interval. Areas of gully formations and active layer detachment during 12 Jun 2015 and 8 Aug 2015 are shown as black polygons in the upper right map.

4.3 L-band and C-band SAR analyses

We detected seasonal deformation from 2017 to 2018, whose magnitude and spatial patterns of the tendencies of subsidence and uplift were consistent in both InSAR results using different satellite data regardless of the season (Fig. 4). In particular, Sentinel-1 short-term InSAR images revealed detailed seasonal surface displacement (thaw settlement and frost heave) from the beginning of thawing to the end of freezing. L-band ALOS2 data detected long-term deformation. The results indicated that thaw settlement in the first year reached up to 15cm in the LOS direction and was continuing even three years after the fire. The calculated time series indicated that cumulative subsidence has been greater than 30 cm since October 2015 at the area of greatest deformation and the rate of subsidence decreased in the 2018 summer.

4.4 Changes in thaw depth and soil moisture

Average thaw depths at burned and unburned areas of the 2014 fire were 123-124 cm and 45-49 cm, respectively. As a 5-year cumulative consequence of the 2014 and 2019 fires, we found about 2.5 times deeper thaw depth in burned areas. Our soil pit survey at the 2014 burned site confirmed a shift of carbon accumulation in the soil profile, indicating recent active layer thickening at burned sites. The volumetric soil water content profile in late September 2019 at the burned sites was about 10-20 % higher than that at unburned.

At B19, average thaw depths in September were 78, 117, and 132 cm in 2019, 2020, and 2021, respectively, while those at U19 were 66, 71, and 80 cm. Although there was a significant (14 cm) increase in the thaw depth at the unburned site, the increase at the burned site was about fourfold (54 cm). 5-15 % higher soil moisture was recorded at B19 from late 2019 through 2020 than at U19. However, in late 2021, surface soil moisture at B19 became slighter drier than at U19, probably because of dry weather in the 2021 summer and the deepening of the active layer at the burned site.

This remarkable difference in near-surface physical conditions can be attributed to vegetation and organic mat removal due to wildfire. The impact had been prominent only about one and a half months after the fire. The difference in late-summer thaw depths between U19 and B19 kept increasing in the first two years after the fire. The complex behavior of soil moisture changes at our sites is unclear because of data gaps. However, higher soil moisture conditions in the deeper active layer persisted after the fire.

4.5 Gullies and active layer detachment

In the 2014 burn scar, more than 20 locates of gully formations or active layer detachment were identified from landsat8 images taken during the 2015 summer. The ground surface erosions were detected as significant increases in reflectance between 12 Jun and 8 Aug in 2015, about a year after the 2014 fire. Further development of the surface erosions was not noticeable. The gully formations occurred linearly along valley lines. Old gully features were prominent on the NE-facing slopes, and newly-formed gullies were found predominantly on the same slopes within the fire scar. The area of predominant gully formation coincides with the larger seasonal or interannual subsidence areas measured by ALOS2 InSAR after the fire. It is probable that the increases in soil moisture and thaw depth after the fire triggered active layer detachment leading to gully formation predominantly on the NE-facing slopes underlain by relatively ice-rich permafrost.

Unlike the natural gully formations in the 2014 burn scar, fire-fighting activities against the 2018 and 2019 fires triggered severe gully erosions. Both 2018 and 2019 fires in AOI2 were stopped by firebreak lines encompassing the burning areas. The fire suppression activities created new roads to access the burning areas by removing surface tundra and forests. The firebreak lines removed all vegetation and organic matters on the ground surface with a width of a few meters. These bare ground lines acted as drainage lines for surface water, especially during snowmelt seasons. The surface runoff, particularly parallel to the slope, rapidly eroded the firebreak lines and roads, as shown in Figure 3.

Relatively small erosions in 2020 summer escalated in the 2021 thawing season, and massive ground ice was exposed in the lower gully walls. In the 2021 fall (two years after the 2019 fire), the depth of a newly developed gully between the 2018 and 2019 burn scars was deeper than 3 meters. The massive ice layer begins at about 1.5 m depth in this area. Moreover, highly ice-rich permafrost extends more than 50 meters, as observed in Batagaika headwalls. The new erosion gullies could trigger the second Batagaika formation because the Batagaika was started from a small-scale erosion of an automobile road for forestry activities in the past.

In the high-resolution optical images, we identified a number of overflooding flows along with concaved reliefs on the slope on 28 May 2021 when the snow has completely melted. The overflow transferred a significant amount of sediment and water towards the valley bottom, where we found newly emerged ice-wedge polygon textures due to enhanced erosion. The combination of wildfire and fire suppression activities may cause significant changes in permafrost ecosystems through changing the natural runoff and erosion regimes.

5. DAISETSU MOUNTAINS

The occurrence of mountain permafrost has been reported at the summit areas of mountains in the Daisetsuzan National Park, Japan (e.g., [7] [8]). While some field investigations on freeze-thaw-related phenomena have been conducted in this mountain area (e.g., [9][10] [11]), wide-range investigation on ground-surface displacement, especially targeting inter-annual changes, has never been done. There is increased attention to the consequences of climate warming on the mountain environment due to the changes in frozen ground status.

As a preliminary analysis, we used 13 ALOS2 images obtained from 2014 until 2019 for the target area, and 78 interferograms were examined to further analyze ground-surface displacement. The interferograms from the pair images, including snow cover, showed significant decorrelation. Five images obtained in the late summer (Aug–Sep) were selected because they only produced high coherence (> 0.5) interferograms in the majority of the target area and were used to extract areas with marked displacement areas within the targeted national park area. The five images were stacked to calculate the average line-of-sight displacement during five years (2014-2019).

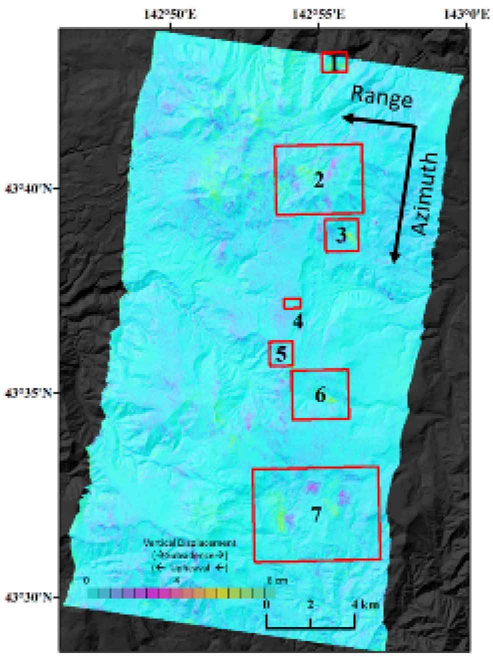

Figure 5. Stacked interferogram over the Daisetsuzan National Park. The seven rectangles are the areas of marked ground surface displacement persistently observed during 2014-2019.

Seven areas were identified as areas containing active slope movements or ground-surface displacement presumably related to permafrost changes, as shown in Fig. 5. Considering the ALOS2 observation direction and look angle, the measured displacement indicates down-slope movement of the ground. The displacement rates ranged 1-4 cm/year depending on the location and the movement persisted during the observation period. Permafrost distribution in the Daisetuzan was only confirmed at wind-swept sites on the summit areas of the mountains. However, the moving slopes we found were located at a height of a several hundred meters lower than the summit areas. Although these moving slopes are slow-moving landslides, the consistent displacement indicates occurrences of perennially frozen ground in the moving slopes, which may be interpreted as periglacial mass movement such as frozen debris lobes or rock glaciers.

To validate the InSAR-measured ground-surface displacement, we started precise GNSS surveys at some selected sites aiming a long-term in-situ observation.

6. REFERENCES

[1] Wegmüller, U., and C. L. Werner (1997), Gamma SAR processor and interferometry software, in Proc. of the 3rd ERS Symposium, European Space Agency Special Publication, ESA SP-414, Florence, Italy, 14–21 March 1997, 1686–1692.

[2] T. Abe, G. Iwahana, P.V. Efremov, A.R. Desyatkin, T. Kawamura, A.N. Fedorov, et al. "Surface displacement revealed by L-band InSAR analysis in the Mayya area, Central Yakutia, underlain by continuous permafrost. Earth," *Planets and Space*, 72(1), 138. https://doi.org/10.1186/s40623-020-01266-3, 2020.

[3] Murton, J. B., et al. (2017), Preliminary paleoenvironmental analysis of permafrost deposits at Batagaika megaslump, Yana Uplands, northeast Siberia, Quaternary Research, 87(2), 314-330, doi: 10.1017/qua.2016.15.

[4] Natali, S. M., Holdren, J. P., Rogers, B. M., Treharne, R., Duffy, P. B., Pomerance, R., & MacDonald, E. (2021). Permafrost carbon feedbacks threaten global climate goals. Proceedings of the National Academy of Sciences, 118(21). https://doi.org/10.1073/pnas.2100163118

[5] Talucci, A. C., Loranty, M. M., & Alexander, H. D. (2022). Siberian taiga and tundra fire regimes from 2001–2020. Environmental Research Letters, 17(2), 025001. https://doi.org/10.1088/1748-9326/ac3f07

[6] Yanagiya, K., & Furuya, M. (2020). Post-Wildfire Surface Deformation Near Batagay, Eastern Siberia, Detected by L-Band and C-Band InSAR. Journal of Geophysical Research: Earth Surface, 125(7), e2019JF005473. https://doi.org/10.1029/2019JF005473

[7] Fukuda, M., & Sone, T. (1992). Some Characteristics of Alpine Permafrost, Mt-Daisetsu, Central Hokkaido, Northern Japan. *Geografiska Annaler Series A-Physical Geography*, *74*(2–3), 159–167.

[8] Sone, T. (1992). Permafrost environment of the Daisetsu mountains, Hokkaido, Japan. *Permafrost and Periglacial Processes*, *3*, 235–240.

[9] Matsumoto, H., Yamada, S., & Hirakawa, K. (2010). Relationship between ground ice and solifluction: Field measurements in the Daisetsu Mountains, northern Japan. *Permafrost and Periglacial Processes*, *21*(1), 78–89. https://doi.org/10.1002/ppp.675

[10] N. Takahashi. (1992). Mire development in the Daisetsuzan Mountains, Central Hokkaido, Northern Japan. *Kikan Chiri*, *44*(1), 1–17.

[11] Sone, T., & N. Takahashi. (1993). Palsa formation in the Daisetsu Mountains, Japan. In Z. Yuanlin (Ed.) (Vol. 2, pp. 1231–1234). Presented at the the sixth international conference on permafrost, South China University of Technology Press, Guangzhou, Guangdong, China.

APPENDIX

[1] T. Abe, G. Iwahana, P.V. Efremov, A.R. Desyatkin, T. Kawamura, A.N. Fedorov, et al. "Surface displacement revealed by L-band InSAR analysis in the Mayya area, Central Yakutia, underlain by continuous permafrost. Earth," *Planets and Space*, 72(1), 138. https://doi.org/10.1186/s40623-020-01266-3, 2020.

APPLICATION OF ALOS-2 FOR FIRE DANGER ASSESSMENT IN THE NORTH AMERICAN BOREAL AND ARCTIC REGIONS (EO-RA2)

PI No.: ER2A2N037

Laura L.Bourgeau-Chavez [1], Chelene Hanes[2] and Dan Thompson [2]

[1] Michigan Technological University, Michigan Tech Research Institute, 3600 Green Ct. Suite 100, Ann Arbor, MI 48105, USA

[2] Canadian Forest Service, Natural Resources Canada, Ontario, Canada

1. INTRODUCTION

The Michigan Tech Research Institute has used ALOS-1/ PALSAR-1 and ALOS-2/PALSAR-2 data acquired via the Research Agreement with the Japan Aerospace Exploration Agency for analysis of fire related variables of fuel moisture in the soil, fuel loads in the woody aboveground biomass (which are confounding factors for soil moisture retrieval) as well as mapping land cover ecotypes to determine vulnerabilities of different ecosystem types to wildfire. Research is funded by two NASA grants which are ongoing (NASA SUSMAP NRA# NNX16AN09G and NASA ABoVE NRA# 80NSSC19M0107). The work on soil moisture retrieval during the timeframe of this data grant was limited due to COVID restrictions on travel. Without travel to field sites to collect data and to download dataloggers that are deployed in both Alaska and Alberta, Canada was restrictive. Given that soil moisture is a time sensitive variable that must be matched up to satellite overpass collections, the data we have analyzed to date is small, but the work is ongoing and access to sites in Canada is now open for summer 2022 when we will be downloading our dataloggers and collecting additional data in Northwest Territories Canada (NWT) and Alberta Canada.

Work has been focused on developing L-band SAR algorithms to map and monitor soil moisture, to produce soil drainage maps from a time series of L-band SAR, to retrieve fuel loads via biomass retrievals and to understand vulnerabilities of uplands versus lowlands in wildfire vulnerability. We also created calibrations for the Campbell Scientific Hydrosense handheld CS620 probes and Datalogger probes CS616 and CS625 to the soils of our study sites in Alberta, and Northwest Territories, Canada and Alaska. The Campbell Scientific Hydrosense handheld water content reflectometer (soil moisture) probes have built in calibration to a loam mineral soil. Organic soils of the Boreal-Arctic have characteristic low bulk density and the default loam calibration typically underestimates actual soil moisture condition. For that reason, we carefully harvested soil samples of 2.5 gallon size to use in a laboratory setting to develop gravimetric based calibration algorithms specific to the boreal and arctic organic soils [after 1]. These calibrations required wetting and drying of the samples over several months as they dried to capture a range of moisture to calibrate the probes. The completed probe calibrations were then shared with the NASA Arctic and Boreal Vulnerability Experiment (ABoVE) science team for use with the SAR data collected over the ABoVE western boreal-arctic North America study area via a report. They are provided as a separate document.

2. CREATING SOIL DRAINAGE MAPS FROM SAR

Drainage maps of the boreal and arctic region are of interest for a wide range of applications including susceptibility to wildfire, fire behavior and fire effects. We focused on C-band for burned sites which no longer have forest canopy and L-band for the unburned forested areas. Using Sentinel-1 data of fire scars we used methods of [2] to map drainage in the region that had experienced canopy replacing (crown) fires, exposing the ground surface. Sentinel-1 C-band was suitable for this application, given its high repeat cover of the study area. For the forested areas, we focused the ALOS-1/PALSAR-1 data. We selected imagery over an Alaska study area to develop similar methods to map drainage in unburned forests and wetlands. The methods rely on a time series of SAR data in a principal component analysis [after 2]. The new PCA images are then used to compare the loadings of each input image date to rainfall patterns to determine which PC image appears related to moisture/drainage. The PC image most related to rainfall patterns is then level sliced to create relative drainage maps.

Applying the methods to a time series of ALOS-2 L-band data proved difficult over the NWT study area, due to a lack of time series L-band data availability for a given year in Canada. We therefore focused on Alaska where PALSAR-1 data are abundant. In our initial assessment, we found aboveground biomass as a confusing factor in the L-band PCA analysis for creating a drainage map. We

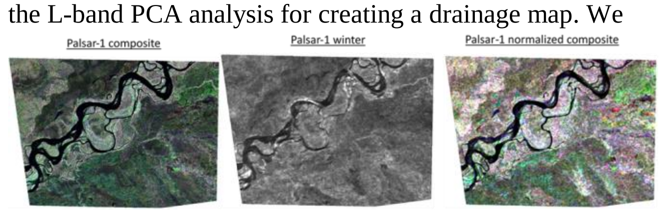

Fig. 1. Multi-date PALSAR composite (left), winter PALSAR image (center), normalized PALSAR composite (right).

1

therefore, normalized the PALSAR summer data, by ratioing it with a winter scene when the ground was frozen and backscatter should be due primarily to forest biomass (Fig. 1).

We then ran principal components analysis on the multi-date input PALSAR stack from summer 2010, each having been ratioed with the winter scene for normalization. The PC-4 normalized component appeared to be responding to 6-day cumulative rainfall from the nearby rain gauge (Fig. 2). This area is a complex of open fens, bogs, treed fens, floodplain white spruce, upland

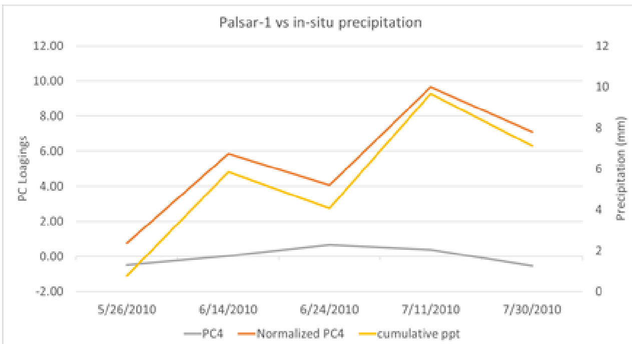

Fig. 2. Plot of PC-loadings from time series of ALOS-1 data over Bonanza Creek Alaska by date. Also shown is the 6-day cumulative rainfall leading up to each image date.

conifer, aspen and old burn scars (Fig. 3, Multi-date PALSAR and Sentinel-1 land cover classification of the Bonanza Creek study area). We then created a preliminary drainage map product from the PC-4 image (Fig. 4). The image appears to have a good deal of speckle and areas of very low biomass (e.g. sedge fens) appear to be confused as high drainage, likely due to more specular reflection in the high water, no vegetation spring stage (Fig. 4). The complex landscape of Bonanza Creek

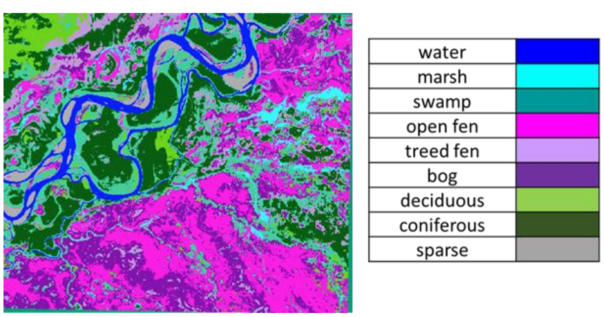

Fig. 3. Multi-date PALSAR and Sentinel-1 land cover classification of the Bonanza Creek study area

is challenging and a true test of the capability of the PCA and L-band approach. It appears that the L-band is working for capturing drainage in the forested areas (uplands and bogs), but the low biomass, herbaceous sedge fens and emergent wetlands are not captured properly. This may be due to high rainfall in one of the input images during the overpass collection. A longer time series of input images (only 5 were used for Fig. 4) may reduce speckle and improve the drainage map product.

Our next steps are to apply the methodology to a longer time series for the Bonanza Creek study area and also to apply it to a purer forested region. This work continues through the next year (April 2023), but proposals to continue beyond next year are also under review. In addition, for these more complex regions functional PCA should be analyzed to investigate the dominant modes of variation.

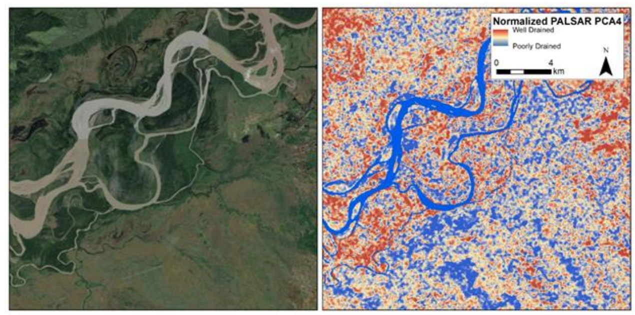

Fig. 4. Preliminary L-band derived drainage map (right) of the Bonanza Creek LTER region, near Fairbanks, AK compared to a natural color high resolution image (left).

3. MONITORING SOIL MOISTURE IN BOREAL NORTH AMERICA

For L-band, we have completed an initial algorithm development for soil moisture retrieval for the area near Fort Providence, NWT, using 25 field samples (representing 40 x 50 m areas) of burned and unburned sites. Table 1 lists the ecotypes sampled and whether there

Table 1. List of sampled sites in NWT, CA for soil moisture and biomass

Ecosystem Type	# Burned soil moisture	# Burned biophysical	# Unburned soil moisture	# Unburned biophysical
Fen	21	21	8	4
Bog	13	13	10	5
Upland	9	9	5	4
Lowland Conifer	15	15	1	0
Total	58	58	24	13

was soil moisture or biophysical data collected.

Using polarimetric decompositions and parameters allows for the dominant scattering mechanisms to be

2

isolated to better retrieve soil moisture from a surface under a vegetation canopy than backscatter alone [3]. For the L-band soil moisture retrieval we focused on two of the polarimetric decompositions used for C-band by [3]: Cloude-Pottier (CP) [4] and the non-negative eigenvalue decomposition NNED decomposition [5]. In addition, we evaluated the Neumann decomposition [6]. We used the NNED decomposition [5] because it corrects the overestimation of volume scatter of the Freeman Durden decomposition due to negative eigen

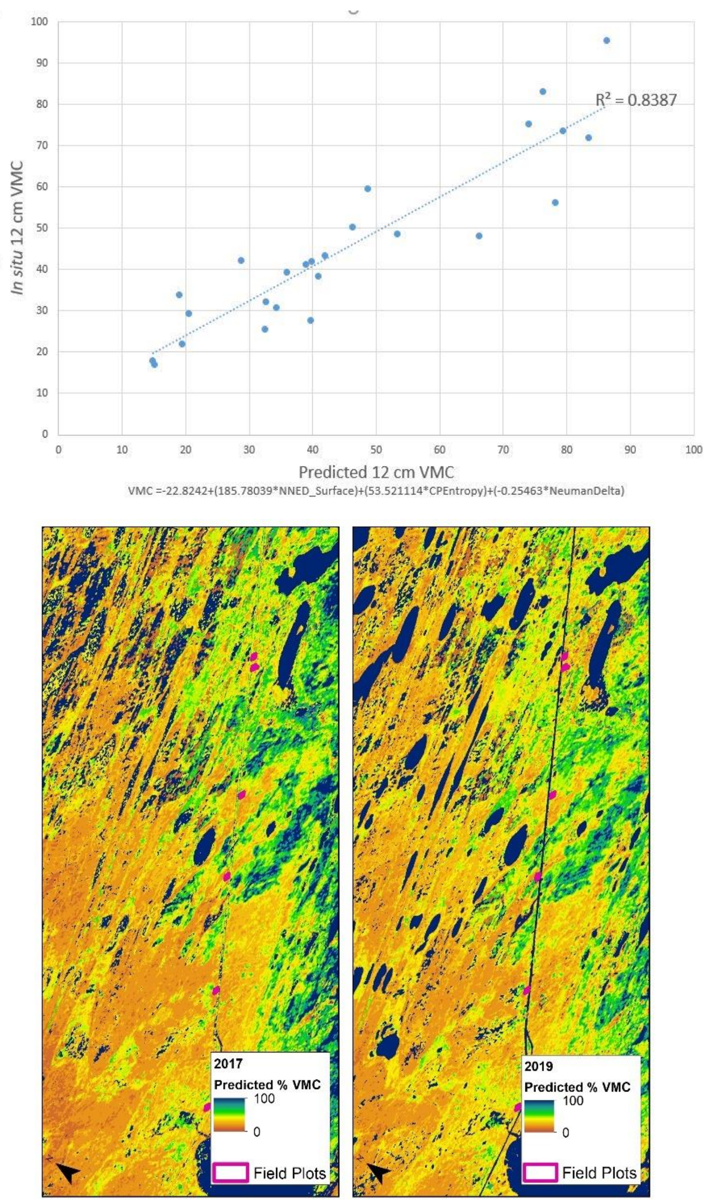

Fig. 5. Predicted vs. actual soil moisture plot for L-band SAR at burned and unburned NWT sites (top). Application of the polSAR algorithm to the 2017 and 2019 image dates for the Fort Providence study area (bottom).

values. NNED produces estimates of surface, double bounce and volume scatter. CP produces entropy (H), anisotropy (A) and alpha (α) parameters, which are not assigned to any given dominant scattering component but are representative of the complexity of the targeted area. The Neumann decomposition was developed for describing the morphological characteristics of vegetation for crop classification and has three polarimetric parameters ($|\delta|$, τ, φ_δ). It is similar to the Cloude-Pottier (CP) decomposition in that it produces 2 outputs that have similar physical meaning to CP-H and CP-α. However, [6] uses a generalized volume scattering model to describe the morphological vegetation traits; the particle scattering anisotropy δ and the degree of orientation randomness τ. The third parameter, the phase of the particle scattering anisotropy φ_δ, is related to the particle orientation direction. τ is an indicator of the degree of scattering randomness, similar to CP-H. These polarimetric parameters were used in a multi-linear regression to retrieve 12 cm surface volumetric soil moisture (VMC), we found the best fit for the model using the parameters CP-H, Neumann – δ and Van Zyl surface with an adjusted R2 of 0.84:

VMC = 22.8242 + (185.78039(NNEDsurface) + (53.521114*CP-H) + (0.25463* Neumannδ)

A plot of the predicted vs. actual soil moisture is presented in Fig. 5, along with the output maps from application of the model to the 2017 and 2019 UAVSAR data collections. This analysis shows great promise and we have many more images to evaluate. The L-band data from UAVSAR and PALSAR-2 are under further investigation. We recently received soil moisture data from September 2019 from colleagues at Canadian Forest Service, that are coincident to the NASA UAVSAR September 2019 airborne campaign. Our field data from August 2019 were of little value since soil moisture is time sensitive. The results of the L-band and C-band soil moisture analyses will be reported at the NASA ABoVE Science Team Meeting (STM8) in May 2022 and the NISAR conference this fall (August 30-September 2, 2022).

4. L-BAND ANALYSIS OF UAVSAR AND PALSAR-2 FOR BIOMASS MAPPING

This biomass work was done in cooperation with P. Siquiera, NASA ABoVE Co-I on grant 80NSSC19M0107. As mentioned in the introduction, field data have been limited due to COVID. Using 14 of the field collected biomass sites in 2019 in NWT, we used the *in situ* biomass data (Fig. 6) to relate to the co- and cross-polarized radar cross-section (RCS) plotted over time. This was done for both UAVSAR and PALSAR-2. The pre-processing of the UAVSAR RCS data was a non-trivial process. Measures of the RCS collected in terms of

σ^0, were converted into units of γ^0 [7] in order to remove the effects of area projection and to normalize for the effects of incidence angle in the UAVSAR data, before they could be compared to PALSAR-2.

Results from the time series dependencies for these varying areas, over the time of observation are shown in Fig. 7. In this figure it can be seen that there is variation in the RCS, mostly likely due to changes in soil moisture, and time of year (early through late summer). Because the

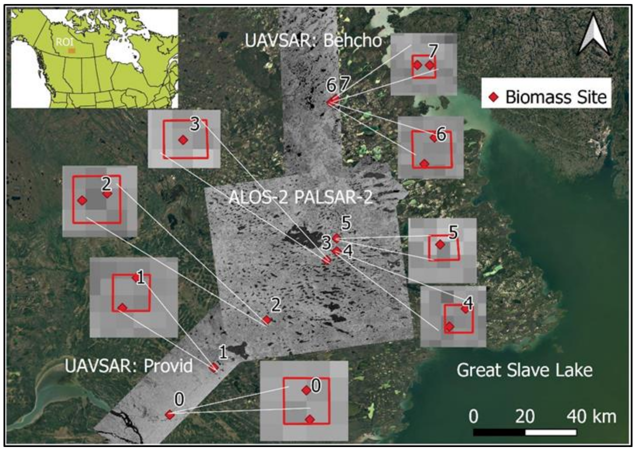

Figure 6. Map of study area plots near Great Slave Lake, NWT. UAVSAR 2019 flightlines and ALOS-2 PALSAR-2 imagery are shown for comparison.

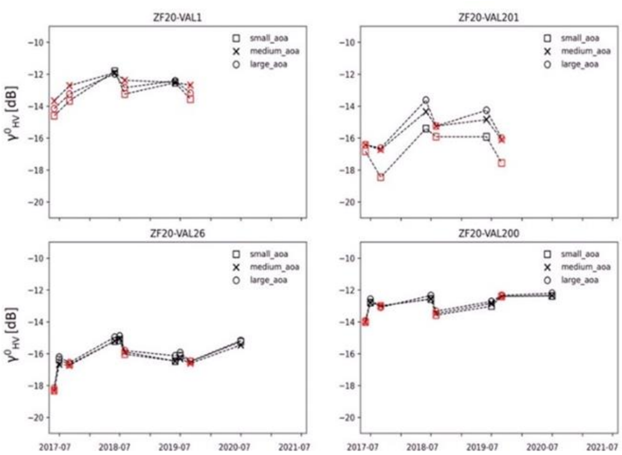

Figure 7. Time-series of RCS values for 4 areas showing both UAVSAR (red) and ALOS-2 (black) data.

vegetated areas of the Great Slave Lake region of the NWT are relatively sparse, the variations in conditions of the ground surface have a greater effect on RCS than they would be in higher biomass areas. This makes the region more challenging for remote sensing of aboveground biomass (AGB), but is a good test-site for low biomass analysis with microwave sensors such as ALOS-2 or NISAR.

Table 2. Summary of L-band SAR data collected for the Great Slave Lake region. The first six rows of the table refer to ALOS-2 data collections with the bottom two rows being from UAVSAR.

Tile ID	2017	2018	2019	2020	2021
001000	13 Jul	12 Jul	11 Jul	9 Jul	
001001	3 Jul	2 Jul	1 Jul	29 Jun	31 May
001002	13 Jul	12 Jul	11 Jul	9 Jul	
001003	4 Jul			30 Jun	
001004		24 Jun	23 Jun		
001005		24 Jun	23 Jun		
Behcho	14 Jun, 9 Sep	22 Aug	5 Sep		
Provid	14 Jun, 9 Sep	21, 22 Aug	4, 5 Sep		

For biomass retrieval algorithm development, we have explored different methods for dealing with the variability of RCS due to varying soil moisture. We found that simple averaging made the best relationships between RCS and ground validation measures of AGB (Fig. 8).

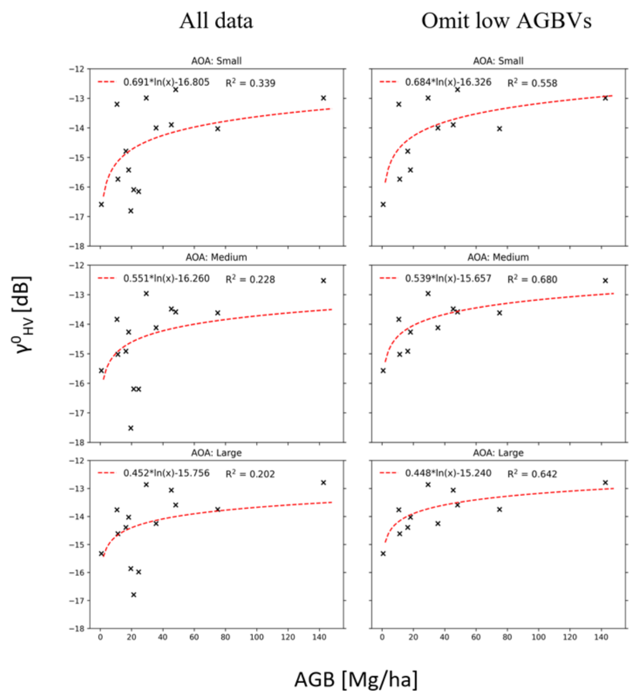

Fig. 8. Examples of the empirical curve-fit relating AGB (x) to the radar cross section, γ^0, for the different sized Areas of Aggregation (0.1, 2.5 and 14 ha) for varying combinations of the ground validation data collected for the Great Slave Lake region.

While polarimetric data could likely result in an improved model, given the likelihood of dual polarization data into the future on a global scale, the 2-band algorithm provides a coefficient of determination of 0.68, with outliers removed. Outliers from the fit can be attributed to particularly low regions of AGB (and hence a heightened sensitivity to surface roughness and soil moisture). After removing those regions from the parameterization of the model and the assessment, the overall curve fit that relates AGB to γ^0 is much improved, with the best fit appearing for regions that had a medium-sized Area of Aggregation (2.5 ha).

With the analyzed data thus far, and using the empirical relationship between AGB and γ^0 derived from this study, the parameterized curve was applied to collected data by ALOS-2 data specified in Table 2. Using a mosaic of collected scenes averaged over time, a map of AGB was created for the region (Fig. 9). The methods and map are in review at JSTARS [8]. These data are being uploaded onto the ABoVE science cloud so that other researchers can access the provided estimates of AGB and it will be archived on the NASA ORNL DAAC.

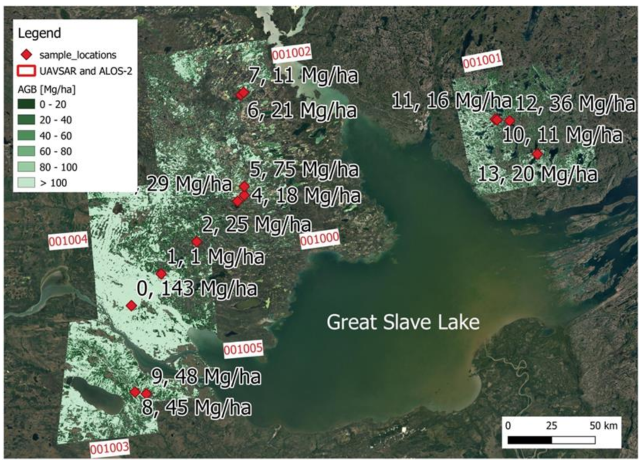

Figure 9. A map of AGB values derived from ALOS-2 data and sorted into 20 Mg/ha bins for the Great Slave Lake region of Canada's Northwest Territories. Shown too are the location and values of AGB for the 14 test sites used in the analysis [8].

Estimating Carbon Storage from Peatland Biomass

We assessed using the map of [8] versus field data in estimating C storage in AGB for the study area peatland sites. As a comparison in our calculations of C content from field data vs. the map of [8] (fig. 9), Above ground C estimates for treed fen were 8.87 Mg/ha from the field data and 9.77 MG/ha from the model, for bog estimates were 9.74 Mg/ha from the field data and 6.36 Mg/ha from the model, and for shrub/open fen were 1.81 Mg/ha from the field data and 35.17 Mg/ha from the model. While the model worked well in peatland classes with high biomass (e.g. treed fen and bog), the model was greatly overpredicting in areas with low biomass (e.g. shrub/open fen) where soil moisture is most strongly influencing backscatter, as mentioned above. Fen peatlands are very wet. This is a limitation in the biomass model that will be further assessed with data collected in 2022. A separate biomass retrieval algorithm may be needed for wetlands, but it may also be a limitation of SAR in the summer. Winter data when the ground is frozen may be a better time to estimate biomass. One thing to note is that in Fig. 9, the first set of sites on the x-axis were burned in 2014 or 2015 (label starting "BS-"), thus the PALSAR-2 model is measuring dead standing biomass in comparison to field measurements of the dead standing biomass. Most of the biomass is in the remaining boles, but they are no longer transpiring/living. All site names that do not start with "BS-" on the x-axis were unburned.

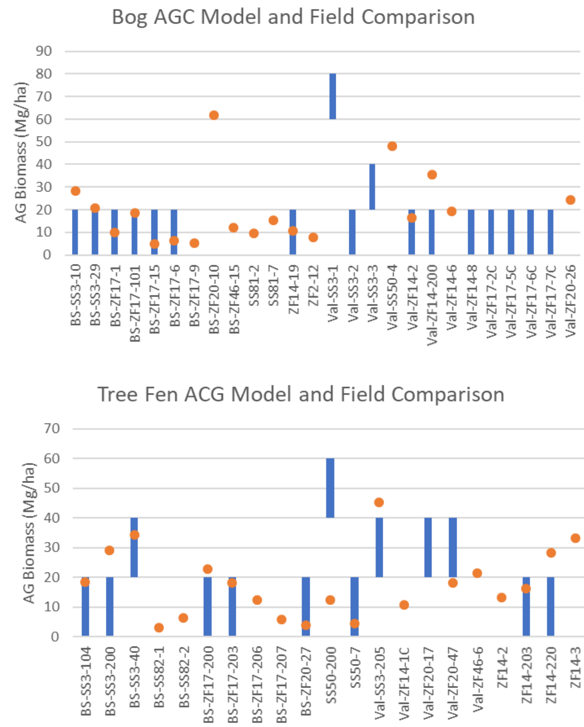

Figure 13. Comparison of [8] modeled biomass (flue bars) with high biomass classes treed fen and bog showed a close match between field estimates (orange dots) and the ALOS-2 biomass model. Note that the sites labeled "BS-" are burned sites and the biomass map of [8] is measuring dead standing tree biomass.

5. BROADSCALE ASSESSMENT OF ECOSYSTEM VULNERABILITY TO WILDFIRE

The broadscale assessment of 136 wildfires that affected 3.3 M hectares in 2014 and 2015 in the Great Slave Lake area of NWT, CA was made possible by the integration of L-band ALOS-1 and 2 data in mapping land cover ecotypes provided via this data grant (Fig.14 (top left [9, 10]). This map was then intersected with a burn severity map (Fig. 14 (bottom left) [11,12]) produced for the organic soil layer (since all fires are crown fires) to understand the effects of fire to the organic soil layer and resulting seed beds. This allowed us to assess the vulnerability of different ecosystems to wildfire across gradients of ecoregion: *Taiga plains ecoregion vs Taiga shield*; permafrost status: *discontinuous vs. sporadic*; by fire year: *2014 vs. 2015*; and season of fire (using a fire progression map from MODIS after [13]): *early, middle and late* (Fig. 14). It also allows us to understand the consumption and C loss from the wildfires via modeling, such as CanFIRE [14].

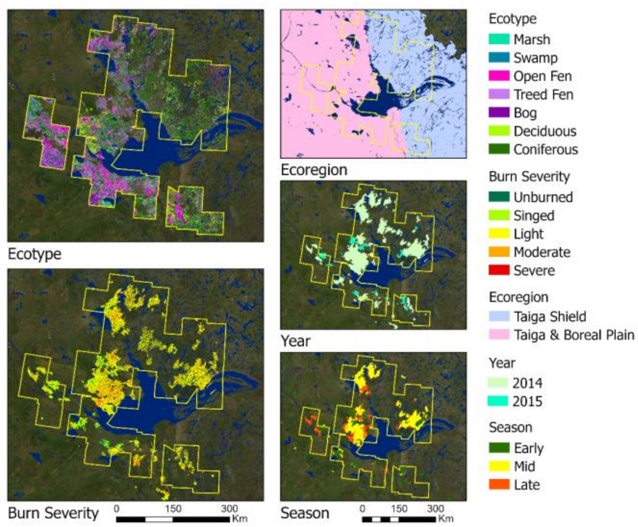

Fig. 14. Study parameters were parsed by ecoregion consisting of Taiga plains and Taiga shield, year by the 2014 and 2015 wildfire perimeters, season by early, middle, and late season fires, and by ecotype.

Wildfire and climate are drivers of change in boreal ecosystems. Understanding the tipping point of drought conditions at which the landscape becomes connected, and peatlands are susceptible to wildfire with deeper burning of the organic soil layers is important for understanding the potential future effects of climate change and projected increases in wildfire on peatlands.

In this study, we used empirical field data and remote sensing to assess the vulnerability of the landscape [as 15] to wildfire by exposure (defined by areas burned and unburned islands by ecotype) and susceptibility (assessed by evaluating severity of burn to the soil organic layers).

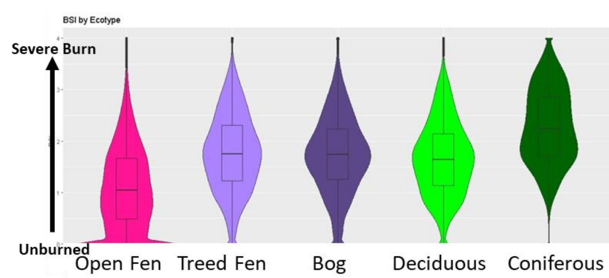

Figure 15. Violin plot of burn severity by ecotype across all 136 wildfires in the Great Slave Lake area of NWT, CA.

While overall, we found open fens to be burning the least severely and upland conifer the most severely (Fig. 15), we found great differences in ecotypes burning and at what severities within fire perimeters on the Taiga shield and plains, which both reside in the same fire regime. The rocky landscape, with greater topographic gradients and shallow soils of the Taiga shield seemed to have reached the threshold of drought conditions in 2014, where the landscape became connected, and all ecotypes had high susceptibility to wildfire. Everything was burning on the Taiga shield in these extreme years, even emergent wetland marshes. Despite having fragmentation by 42% of the area by unburnable (water/exposed bedrock) cover on the Taiga shield, there were few unburned islands and on average >92% of the area within fire perimeters burned. There was also consistency across ecotypes in proportional area burned at the various fire severities (Fig. 16), with a dominance of light fire severity across ecotypes, in all seasons and in both 2014 and 2015. In contrast the wildfire on the Taiga plains affected large areas, but fire severity within fire events was much patchier than on the shield, and larger differences were observed across seasons of fire (Fig. 16) and years of fire.

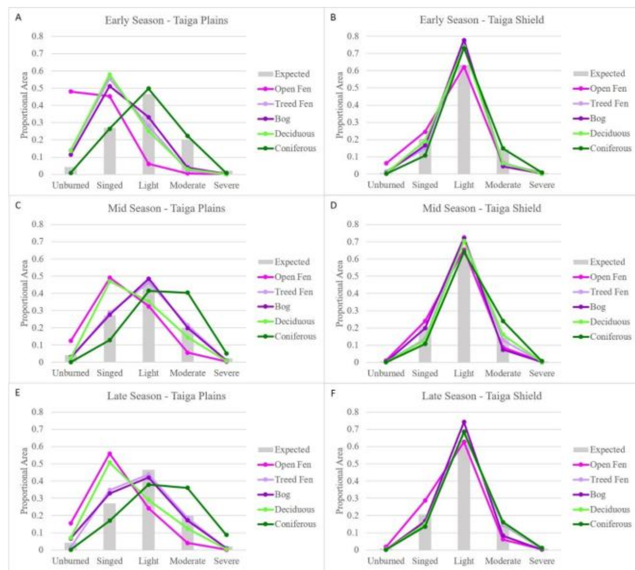

Figure 16. Plots of expected (grey bars) and actual proportional area of each burn severity for each ecotype by (A) Early season on the Taiga plains; (B) Early season on the Taiga shield; (C) Mid-season on the Taiga plains; (D) Mid-season on the Taiga shield; (E)Late season on the Taiga plains; and (F) Late season on the Taiga shield.

6. REFERENCES

[1] Bourgeau-Chavez, L.L., Garwood, G.C., Riordan, K., Koziol, B.W., and Slawski, J. 2010. Calibration algorithm development for selected water content reflectometers to burned and non-burned organic soils of Alaska. International Journal of Wildland Fire, Vol. 19:961-975.

[2] Bourgeau‐Chavez, L.L., Kasischke, E.S., Riordan, K., Brunzell, S., Nolan, M., Hyer, E., Slawski, J.,

Medvecz, M., Walters, T. and Ames, S., 2007. Remote monitoring of spatial and temporal surface soil moisture in fire disturbed boreal forest ecosystems with ERS SAR imagery. International Journal of Remote Sensing, 28(10), pp.2133-2162.

[3] Bourgeau-Chavez, L.L., Leblon, B., Charbonneau, F. and Buckley, J.R., 2013. Evaluation of polarimetric Radarsat-2 SAR data for development of soil moisture retrieval algorithms over a chronosequence of black spruce boreal forests. Remote Sensing of Environment, 132, pp.71-85.

[4] Cloude, S.R. and Pottier, E., 1997. An entropy based classification scheme for land applications of polarimetric SAR. IEEE transactions on geoscience and remote sensing, 35(1), pp.68-78.

[5] Van Zyl, J.J., Arii, M. and Kim, Y., 2011. Model-based decomposition of polarimetric SAR covariance matrices constrained for nonnegative eigenvalues. IEEE Transactions on Geoscience and Remote Sensing, 49(9), pp.3452-3459.

[6] Neumann, M., Ferro-Famil, L., Jäger, M., Reigber, A. and Pottier, E., 2009, July. A polarimetric vegetation model to retrieve particle and orientation distribution characteristics. In 2009 IEEE International Geoscience and Remote Sensing Symposium (Vol. 4, pp. IV-145). IEEE.

[7] Small, D., "Flattening gamma: Radiometric terrain correction for SAR imagery," IEEE Trans. Geosci. Rem. Sens., 49(8), 3081-3093, 2011.

[8] Kraatz, S., L. Bourgeau-Chavez, M. Battaglia, A. Poley, and P. Siqueira. "Mapping and scaling of in situ Above Ground Biomass to regional extent with SAR in the North American Boreal Region," *Submitted to* IEEE J. Selec. Top. Appl. Rem. Sens., 11 pp., 2022 in review.

[9] Bourgeau-Chavez, L.L., Endres, S., Powell, R., Battaglia, M.J., Benscoter, B., Turetsky, M., Kasischke, E.S. and Banda, E., 2017. Mapping boreal peatland ecosystem types from multitemporal radar and optical satellite imagery. Canadian Journal of Forest Research, 47(4), pp.545-559.

[10] Bourgeau-Chavez, L.L., J.A. Graham, S. Endres, N.H.F. French, M. Battaglia, D. Hansen, and D. Tanzer. 2019. ABoVE: Ecosystem Map, Great Slave Lake Area, Northwest Territories, Canada, 1997-2011. ORNL DAAC, Oak Ridge, Tennessee, USA. https://doi.org/10.3334/ORNLDAAC/1695

[11] French, N.H., Graham, J., Whitman, E. and Bourgeau-Chavez, L.L., 2020. Quantifying surface severity of the 2014 and 2015 fires in the Great Slave Lake area of Canada. International journal of wildland fire, 29(10), pp.892-906.

[12] FRENCH, N., GRAHAM, J., BOURGEAU-CHAVEZ, L.L. and WHITMAN, E., 2020. ABoVE: Burn Severity of Soil Organic Matter, Northwest Territories, Canada, 2014-2015. ORNL DAAC.

[13] Loboda, T.V. and Csiszar, I.A., 2007. Reconstruction of fire spread within wildland fire events in Northern Eurasia from the MODIS active fire product. Global and Planetary Change, 56(3-4), pp.258-273.

[14] De Groot, W.J., Pritchard, J.M. and Lynham, T.J., 2009. Forest floor fuel consumption and carbon emissions in Canadian boreal forest fires. Canadian Journal of Forest Research, 39(2), pp.367-382.

[15] Bourgeau-Chavez, L.L., Grelik, S.L., Billmire, M., Jenkins, L.K., Kasischke, E.S., and Turetsky, M.R., 2020. 'Assessing Boreal Peat Fire Severity and Vulnerability of Peatlands to Early Season Wildland Fire', Frontiers in Forests and Global Change, 3. doi: 10.3389/ffgc.2020.00020

APPENDIX

[1] Kraatz, S., L. Bourgeau-Chavez, M. Battaglia, A. Poley, and P. Siqueira. "Mapping and scaling of in situ Above Ground Biomass to regional extent with SAR in the North American Boreal Region," *Submitted to* IEEE J. Selec. Top. Appl. Rem. Sens., 11 pp., 2022 in review.

[2] Bourgeau-Chavez, L.L, Graham, J.A., Vander Bilt, D.J., and Battaglia M.J. 2022 in submission soon. Assessing the broadscale effects of wildfire under extreme drought conditions to Taiga plains and Taiga shield peatlands. *Frontiers in Forests and Global Change*

[3] Bourgeau-Chavez, L.L., A.F. Poley, and K. Bosse. 2019. Probe calibration document report. Report to NASA Arctic and Boreal Vulnerability Experiment.

MONITORING PERMAFROST ACTIVE LAYER DYNAMICS WITH PALSAR

PI No.: ER2A2N058

Sang-Eun Park [1], Yoon Taek Jung [1], and Hyun-Cheol Kim [2]

[1] Department of Geoinformation Engineering, Sejong University, 209 Neungdong-ro, Gwangjin-gu, Seoul 05006, Korea.

[2] Center of Remote Sensing and GIS, Korea Polar Research Institute, 26 Songdomirae-ro, Yeonsu-gu, Incheon 21990, Korea.

1. INTRODUCTION

Permafrost, which accounts for 24% of the land area in the Northern Hemisphere, exhibits great variability due to repeated thawing and freezing depending on climate. The seasonal freeze/thaw process of the permafrost active layer has been a sensitive indicator of changes in climate conditions. To understand the changes in the active layer, spatially detailed monitoring methods such as optical and Synthetic Aperture Radar (SAR) remote sensing technologies have been extensively applied to the observation of the permafrost environments.

Optical remote sensing has been mainly used to monitor permafrost-related land cover information [1]. Optical remote sensing has also been used to monitor changes in the permafrost ecosystem. However, high-altitude areas where permafrost is located are difficult to obtain optical images except during the summer period. Synthetic Aperture Radar, which enables continuous acquisition of a wide range of images in all weather conditions, is capable of effective monitoring of permafrost areas, so in this study, topographic, geologic and hydrological characteristics of permafrost can be identified and monitored through the development of technologies using optical data and polarimetric SAR data.

SAR observations have been actively used to observe permafrost local environments and spatiotemporal changes in the active layer. Due to the advantages of periodic observations independent of cloud coverage and solar elevation, early SAR applications focused on the identification and detection of freeze/thaw states of the active layer ecosystem with seasonal SAR backscatter timeseries [2], [3].

Although both optical and SAR remote sensing techniques have been widely used to retrieve and monitor the unique ecological and periglacial features of permafrost area, each method has its own challenges or limitations. Permafrost regions have a long winter season with low solar intensity and angle and a short and rapidly progressing summer season. The geographical constraints limit the acquisition of optical remote sensing data, and as a result, it is often difficult to obtain appropriate data corresponding to the regions and timing of interests. On the other hand, SAR remote sensing has the advantage of being able to continuously acquire data for high latitude regions regardless of the season. Therefore, this study aims to explore the possibility of combined interpretation of optical and SAR data for identifying and understanding spatiotemporal details of the short- and long-term changes occurring in the permafrost active layer.

2. STUDY AREA AND DATA SETS

The selected study area is central Yakutian lowlands, eastern Siberia (Fig. 1). The alluvial terraces of the Lena River in eastern Siberia are composed of silty and sandy loams, which has high ice content, and the study area has been highly affected by thermokarst due to ice wedges [4]. The study site is covered with forests, shrublands, and thermokarst landforms. Particularly, one of the distinct features of the central Yakutian lowlands is the abundance of thermokarst lakes. The red and black rectangle in the Fig. 1 indicates Landsat and ALOS-1 PALSAR-1 data coverages, respectively. and the white box is the location of the main study area.

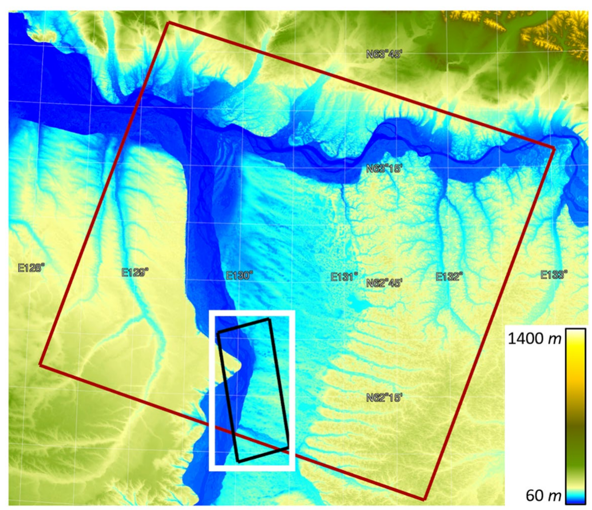

Fig. 1. Location of the study area and the topography obtained from the Copernicus 30-meter global digital elevation model (GLO-30).

3. ECOSYSTEM CHANGES IN OPTICAL DATA

In order to examine both land cover changes and cryogenic processes throughout the thawing and freezing periods, two Landsat data acquired during the summer season in August 2006 (LS1) and 2007 (LS2). Previous studies were focused only on the detection and area change of thermkarst lake, but the study area has a regional characteristic that it is very difficult to identify changes in the ecosystem due to changes in the soil environment unless changes in other land covers are comprehensively considered. The method of using the vegetation index of optical images is not easy to specify temporal and spatial changes in the active layer ecosystem, and thus, this study used the support vector machine (SVM) classification approach that can appropriately classify various topographical features and changes in the region based on the spectral characteristics of optical images. The change detection of Landsat data between 2006 and 2007 summer period was carried out to minimize the effects of atmospheric or phenological conditions in the interpretation of the bi-temporal data to understand land cover changes as shown in Fig. 2(a) and (b). To reduce errors related to classification performance in the analysis of land cover changes, five classes with distinct spectral characteristics in both data were selected including dense forest (DF), sparse forest or shrub (SF), grassland (Gr), barren or bare surface (BS), and water (Wa).

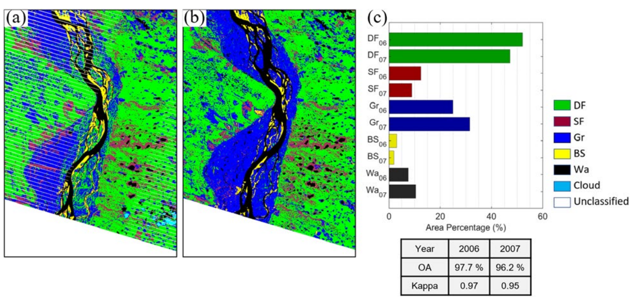

Year	2006	2007
OA	97.7 %	96.2 %
Kappa	0.97	0.95

Fig. 2. SVM-based classification results for (a) LS1 (2006) and (b) LS2 (2007) data, and (c) areal percentage of different land cover classes of the study area.

Overall accuracy (OA) and Cohen's kappa index (Kappa) were used to evaluate the accuracy of each Landsat data as shown in Fig. 2 (c). In order to assess the spatial pattern of changes in these four main classes, a grid-based analysis of the areal fraction of changes was applied as shown in Fig. 3.

Fig. 3 shows the spatial change distributions for the four main classes, D_{DF}, D_{SF}, D_{Gr}, and D_{Wa}, per 1 km^2 grid cell. In the change analysis, riverine lowland areas with the elevation below 100 m were masked to exclude land cover changes related to the fluvial regime of the Lena River. The gridded change distribution for DF class exhibits that there were specific areas where the forest areas were primarily reduced, and in some areas, the forest coverage within the grid cell was rather expanded. The DF class mainly decreased in the thermokarst terrace on the right bank of the Lena River, while the SF class increased in this region, which indicates that a significant part of the dense forests was changed to the sparse forests or shrublands in this area.

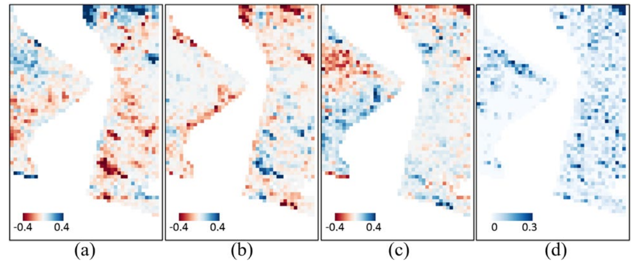

Fig. 3. Grid-based spatial class changes (km2/ km2/yr) over 2006-2007 for (a) DF, (b) SF, (c) Gr, and (d) Wa classes.

4. CHANGES IN POLARIMETRIC SAR DATA

The data obtained in September 2006 (PA1) can be said to have been obtained at the end of the thawing period, and the data obtained in November 2006 (PA2) can be said to have been obtained at the beginning of the freezing period. The data obtained in March (PA3) and May 2007 (PA4) can be said to be the end of freezing period and the beginning of the thawing period, respectively. The status of acquiring ALOS-1 PALSAR-1 data is shown in Fig. 4, and is shown with meteorological data from the global atmospheric reanalysis ERA-5 data of European Center for Medium-Range Weather Forecasts (ECMWF).

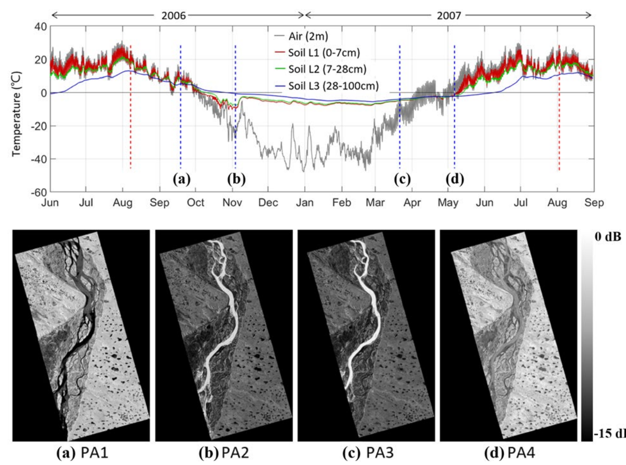

Fig. 4. Overall meteorological conditions during the study period (red: Landsat, blue: PALSAR) and PALSAR images of the main study area.

The polarimetric SAR data with radiometric and geometric correction can be represented in the form of the covariance matrix [C]. In order to better clarify the change in scattering processes associated with the frost actions during winter, we have adopted additional polarimetric parameters called HHVV correlation coefficient $\gamma(HH,VV)$ that can provide additional information on the microwave scattering mechanism. The magnitude ρ_{HHVV} can be a good indicator of signal depolarization that varies from 0 for a completely random signal to 1 for a pure single scattering. On the other hand, the phase Φ_{HHVV} can be used to distinguish surface and double-bounce scattering mechanisms [5] and can indicate dielectric properties of subsurface-layer of dry soil [6]. In addition to $\gamma(HH,VV)$, the polarimetric correlation defined in the right (R) and left (L) handed circular polarization basis has been also used as another indicator of scattering characteristics. The magnitude of $\gamma(RR,LL)$, i.e., ρ_{RRLL}, has been proved to be an effective parameter for estimating the roughness of scattering surfaces regardless of the dielectric properties of the scatterer [7]. On the other hand, the phase term ϕ_{RRLL} has been found to be directly related to the local orientation angle of the scattering surface [8].

The changes of HHVV correlation and RRLL correlation are shown in Fig. 5, and the Pearson correlation coefficients between polarimetric parameters and optical data and between polarimetric parameters and meteorological data are summarized in Table 1.

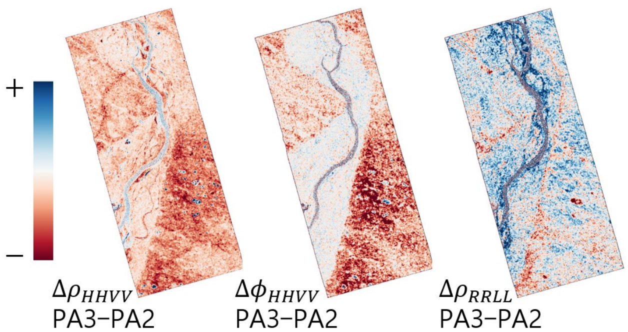

Fig. 5. Changes of $\Delta\rho_{HHVV}$, $\Delta\phi_{HHVV}$, and $\Delta\rho_{RRLL}$.

Table 1. Pearson correlation coefficients for the relation of land cover changes in three polarimetric parameters ρ_{HHVV}, ϕ_{HHVV}, and ρ_{RRLL}.

	Landsat-based land cover changes			
	D_{DF}	D_{SF}	D_{Gr}	D_{Wa}
$\Delta\rho_{HHVV}$	0.24	-0.24	-0.06	-0.04
$\Delta\phi_{HHVV}$	0.25	-0.33	-0.06	-0.05
$\Delta\rho_{RRLL}$	-0.20	0.39	-0.05	0.06

A decrease of ρ_{HHVV} in Fig. 5 indicates an increase in the level of depolarization in the signal [9]. The scattering properties could be changed from single dominant surface scattering in the early freezing period to an increase of the stochastic scattering process from the frozen active layer in the late freezing period. The decrease in ϕ_{HHVV} during the freezing period can be interpreted as a decrease in the effective dielectric constant of the active layer scatterers [10]. Soil cryogenic process, such as increased frozen ice content and the development of ice lenses, can be one of the ground characteristics resulting in an increase in signal depolarization. On the other hand, the increase in ρ_{RRLL} during the freezing process indicates an increase in the roughness of the scattering surface independently of the change in dielectric properties of the scatterer. Consequently, experimental results illustrate that polarimetric SAR timeseries data acquired in the freezing period may indicate the areas where the soil cryogenic process actively occurred, and such areas can be linked with changes in the ecosystem, such as reduction of forest and expansion of shrub.

5. DISCUSSIONS

Changes in both the land cover and the winter scattering characteristic, which can be experimentally identified through Landsat and PALSAR data, showed distinctive spatial patterns between the left and right terraces of the Lena River as shown in Fig. 6. Fig. 6 (a) shows the SVM-based classification results for Landsat data in 2002 and 2010, and Fig. 6 (b) shows the changes of $\Delta\rho_{RRLL}$ between PA2 and PA3 acquisition time.

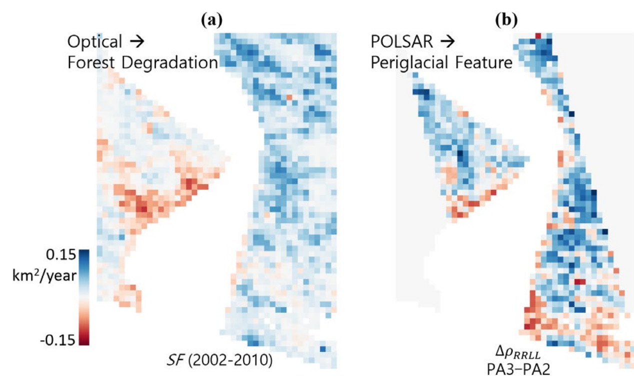

Fig. 6. (a) SVM-based classification results for Landsat data in 2002 and 2010, (b) changes of $\Delta\rho_{RRLL}$.

Among the land cover classes, increasing SF classes and decreasing DF classes were found to be related to RRLL coherence during the winter of 2006-2007 in both the left and right terraces of the Lena River. As discussed earlier, the RRLL coherence can be related to the microtopography of the scatterer that could be attributed or related to the patterned surface properties.

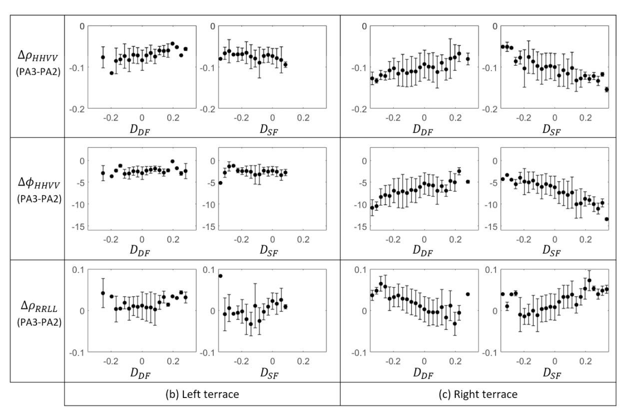

Fig. 7. Relationship between the winter changes in polarimetric parameters and the changes in DF, SF, Gr, and Wa classes for the (a) left and (b) right terraces of the Lena River.

6. CONCLUSION

In this study, we analyzed ecological and geo-cryological dynamics in the central Yakutian region throughout the summer and winter seasons between 2006 and 2007 by using Landsat and PALSAR data obtained during the summer and winter seasons, respectively. The optical data with the advantage of being able to distinguish different land covers through spectral response measurements were used to elucidate ecosystem changes between consecutive summers. The results of post-classification-based change detection using Landsat data confirmed that vegetation cover also changed significantly between 2006 and 2007 in the Yakutian lowlands, where lake area expansion had been previously reported. To understand the effect of the soil freezing process on ecosystem change, the radar scattering characteristics in winter were evaluated between the summer Landsat data acquisition period. We analyzed scattering mechanism indicators from the SAR data to highlight soil's dielectric and roughness properties. The result of analyzing the relationship between information obtained from optical and SAR sensors revealed that there was a significant correlation between winter changes in scattering properties observed in SAR data and summer land cover changes observed in optical data. The scattering characteristics of winter soil were found to be particularly related to the ecosystem changes in areas that can be explained by the thermokarst development process. Additional data from independent sources, such as elevation data, meteorological data, and long-term optical data, consistently supported the relationship between the winter SAR observations and the thermokarst-related ecosystem changes.

Based on these experimental results, information on the soil cryogenic processes related to the distribution and change of thermokarst landforms could be obtained through SAR observations during the freezing period. It is worth noting that polarimetric scattering mechanism indicators played a decisive role in deriving information about the permafrost process from the winter SAR data.

7. REFERENCES

[1] A. Bartsch, A. Höfler, C. Kroisleitner, and A. Trofaier, "Land Cover Mapping in Northern High Latitude Permafrost Regions with Satellite Data: Achievements and Remaining Challenges," *Remote Sensing*, vol. 8, no. 12, p. 979, Nov. 2016, doi: 10.3390/rs8120979.

[2] E. Rignot and J. B. Way, "Monitoring freeze—thaw cycles along North—South Alaskan transects using ERS-1 SAR," *Remote Sensing of Environment*, vol. 49, no. 2, pp. 131–137, Aug. 1994, doi: 10.1016/0034-4257(94)90049-3.

[3] S.-E. Park, A. Bartsch, D. Sabel, W. Wagner, V. Naeimi, and Y. Yamaguchi, "Monitoring freeze/thaw cycles using ENVISAT ASAR Global Mode," *Remote Sensing of Environment*, vol. 115, no. 12, pp. 3457–3467, Dec. 2011, doi: 10.1016/j.rse.2011.08.009.

[4] A. Brouchkov, M. Fukuda, A. Fedorov, P. Konstantinov, and G. Iwahana, "Thermokarst as a short-term permafrost disturbance, Central Yakutia," *Permafrost Periglac. Process.*, vol. 15, no. 1, pp. 81–87, Jan. 2004, doi: 10.1002/ppp.473.

[5] A. Freeman and S. L. Durden, "A three-component scattering model for polarimetric SAR data," *IEEE Trans. Geosci. Remote Sensing*, vol. 36, no. 3, pp. 963–973, May 1998, doi: 10.1109/36.673687.

[6] Y. Lasne, P. Paillou, T. August-Bernex, G. Ruffie, and G. Grandjean, "A phase signature for detecting wet subsurface structures using polarimetric L-band SAR," *IEEE Trans. Geosci. Remote Sensing*, vol. 42, no. 8, pp. 1683–1694, Aug. 2004, doi: 10.1109/TGRS.2004.830645.

[7] S.-E. Park, W. M. Moon, and D. Kim, "Estimation of Surface Roughness Parameter in Intertidal Mudflat Using Airborne Polarimetric SAR Data," *IEEE Trans. Geosci. Remote Sensing*, vol. 47, no. 4, pp. 1022–1031, Apr. 2009, doi: 10.1109/TGRS.2008.2008908.

[8] Y. Yamaguchi, A. Sato, W.-M. Boerner, R. Sato, and H. Yamada, "Four-Component Scattering Power Decomposition With Rotation of Coherency Matrix," *IEEE Trans. Geosci. Remote Sensing*, vol. 49, no. 6, pp. 2251–2258, Jun. 2011, doi: 10.1109/TGRS.2010.2099124.

[9] S. Cloude, *Polarisation: applications in remote sensing*, 1st ed. Oxford ; New York: Oxford University Press, 2010.

[10] Y. Lasne *et al.*, "Study of Hypersaline Deposits and Analysis of Their Signature in Airborne and Spaceborne SAR Data: Example of Death Valley, California," *IEEE Trans. Geosci. Remote Sensing*, vol. 47, no. 8, pp. 2581–2598, Aug. 2009, doi: 10.1109/TGRS.2009.2014862.

APPENDIX

S.-E. Park, Y. T. Jung, and H.-C. Kim, "Monitoring permafrost changes in central Yakutia using optical and polarimetric SAR data," *Remote Sensing of Environment*, vol. 274, 112989, Jun. 2022

InSAR BASED ICE VELOCITY AND GROUNDING LINE MEASUREMENTS IN ANTARCTICA

PI No ER2A2N107

B. Scheuchl [1], J. Mouginot [1,2], E. Rignot [1,3]

[1] Department of Earth System Science, University of California, Irvine, USA
[2] Univ. Grenoble Alpes, CNRS, IRD, Grenoble INP, IGE, 38000 Grenoble, France
[3] NASA-JPL, Pasadena, USA

1. INTRODUCTION

Ice sheets are acknowledged by WMO and UNFCCC as an Essential Climate Variable (ECV) needed to make significant progress in the generation of global climate models. Information requirements include ice velocity (IV), grounding line position (GP), Ice front position (IP), all of which can be derived using spaceborne SAR data [1,2].

We are funded through a NASA MEaSUREs project to generate high-quality Earth Science Data Records (ESDR) in Antarctica. To do so, we utilize multi-mission spaceborne SAR data and, more recently, optical data. Our primary information products are ice velocity and grounding line position, but we also provide ice front position as well as basin boundaries. Our maps are provided continent-wide, though coverage is limited by the data availability for the corresponding observation period. A list of available products is provided in section 4.

The primary objective of this report is to evaluate the utility of ALOS-2 PALSAR-2 data for ice sheet monitoring. We show the utility of L-band data for both ice velocity and grounding line measurements and evaluate limitations of the mission for this task. Our experience with L-band SAR data is based on our extensive work with ALOS PALSAR data acquired in Antarctica between 2006 and 2010 in several campaigns. We used all available data for our products.

For ALOS-2 PALSAR-2, we employed a more regional approach. The primary reason for this is more regulated access to high resolution stripmap data from the mission. We have been working with JAXA to define a number of key geographic areas for repeat pass data collection to maximize the scientific impact of the data acquisitions.

2. DATA

ALOS-2 PALSAR-2 has a 14-day repeat orbit, which is advantageous over ALOS PALSAR as data correlation is even higher, particularly for fast glaciers. The shorter repeat will reduce the signal to noise ratio for ionospheric noise, so ionospheric perturbations will have a greater impact compared to longer repeat data, especially in slow moving areas. No Antarctica-wide interferometric acquisition strategy is in place for ALOS-2, and access to stripmap data is somewhat restricted due to a limitation on data quotas. Throughout the project, we worked with JAXA to identify regions of interest where a smaller number of acquisitions has a high scientific impact given the sensor properties. We focussed on fast glaciers to optimally use our data quota. These areas are distributed around Antarctica and include the Antarctic Peninsula (from an earlier project phase), the Amundsen Sea Embayment, and the Getz Coast in West Antarctica, as well as Totten and Denman Glaciers in East Antarctica (from different RA projects). We found for early ALOS-2 PALSAR-2 data that the range displacement component is affected by strong shifts in range direction, an issue that JAXA also identified and subsequently resolved. None of the data sets delivered to us in recent years are affected.

3. METHODOLOGY

The primary method to measure ice sheet velocity from spaceborne SAR data is speckle tracking [1]. Clear advantages of the method include its robustness and the availability of 2-D measurements from a single data pair. Using the method, we have published the first continent-wide ice velocity map for Antarctica [2] and an ice sheet wide ice velocity map of Greenland [3]. Our processing infrastructure is built on well-established methods [2,5,8], more than 20 years of expertise in the field, and long term funding through the NASA MEaSUREs program to produce and provide Earth Science Data Records for Antarctica. In recent years, we started to integrate optical data processed with feature tracking [8] into our ESDR production. For this, we synergistically process SAR and optical data, automatically calibrate the resulting velocity maps and merge them to seamless, ice sheet wide products. This approach allows us to provide annual mosaics of ice motion in Antarctica (and Greenland) with all available data acquired in a particular year [8].

A detailed description of our technical approach to generate ice velocity maps is provided in [5,8]. We use single look complex images in stripmap mode (CEOS format at the processing level 1.1). To process ice velocity, we derive displacement-offset maps from successive PALSAR-2 pairs. The offset map is calculated using ampcor from JPL's ROI_PAC package. The offsets are then converted to 2D velocities. To reduce error and mitigate ionospheric artifacts, we average multiple measurements from all available sensors in the generation of the Antarctica-wide reference ice velocity map. Less averaging takes place for velocity maps covering shorter time periods, like annual maps and, more recently, monthly maps.

A second, more accurate method to measure ice velocity from spaceborne SAR is to utilize the sensitivity of the interferometric phase to displacement in rage direction [9]. This approach has a more stringent data requirement, as it requires data to be collected in both ascending and descending direction. No single mission to date provides such coverage, we achieve it by mixing data from different sensors acquired over multiple years. The resulting ice velocity product is vastly more accurate compared to speckle tracking based results, particularly in areas of slow ice flow. For fast flowing areas, the method cannot be used, so we generate a high-precision Antarctica-wide reference map by combining phase-based velocity measurements with tracking based maps. . Ionospheric perturbations do affect the L-and interferometric phase, however, the impact can be greatly reduced using a split band method [10]. A detailed description of the reference ice velocity map based on InSAR phase as well as method used to produce it is provided in [11]

The grounding line of a glacier is the boundary where the ice starts to float in ocean waters. The floating section moves up and down with rising and falling tide. The resulting vertical displacement can be measured using a spaceborne SAR using double difference interferometry [3,6,7]. The method requires the availability of two interferometric pairs (generated either with three consecutive acquisitions, or two times two consecutive acquisitions). We have previously shown the potential of ALOS PALSAR for grounding line measurements [3], however, the shorter revisit time of ALOS-2 PALSAR-2 is highly advantageous for this application.

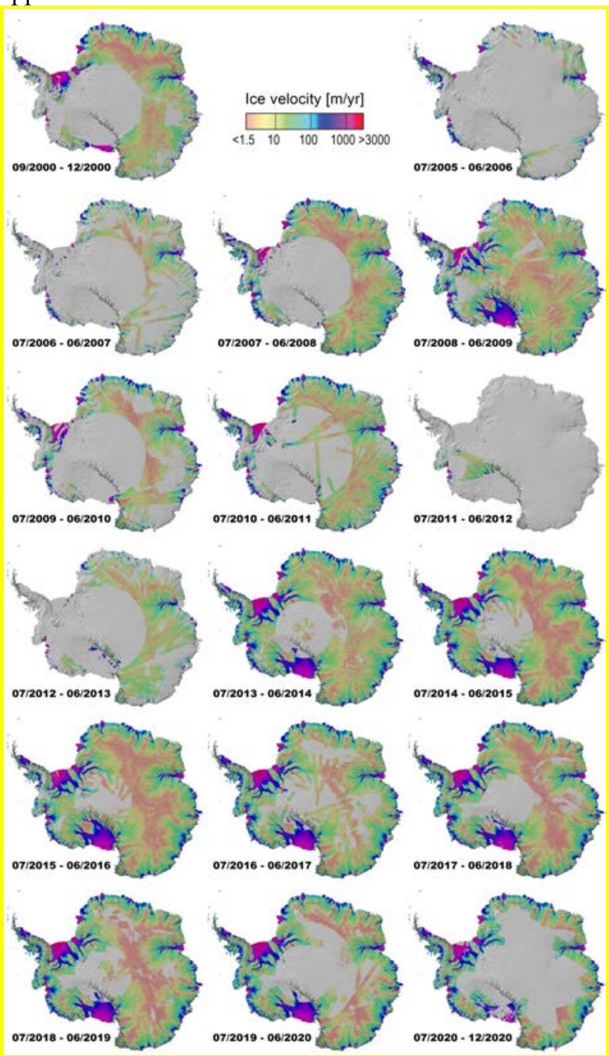

Fig. 1: MEaSUREs Annual Antarctic Ice Velocity Maps 2000-2020, V1 [8].
http://nsidc.org/data/NSIDC-0720

4. MEASURES EARTH SCIENCE DATA RECORDS

Our efforts resulted in a number of ESDR's that are freely available for use:
http://nsidc.org/data/measures/data_summaries

- MEaSUREs Multi-year Reference Velocity Maps of the Antarctic Ice Sheet, V1
  http://nsidc.org/data/NSIDC-0761
  (Note: link not yet active at the time of report submission)
- MEaSUREs Phase-Based Antarctica Ice Velocity Map, V1
  http://nsidc.org/data/NSIDC-0754
- MEaSUREs Annual Antarctic Ice Velocity Maps, V1
  http://nsidc.org/data/NSIDC-0720
- MEaSUREs Antarctic Boundaries for IPY 2007-2009 from Satellite Radar, V2
  http://nsidc.org/data/NSIDC-0709
- MEaSUREs InSAR-Based Antarctica Ice Velocity Map, V2
  http://nsidc.org/data/NSIDC-0484
- MEaSUREs Antarctic Grounding Line from Differential Satellite Radar Interferometry, V2
  http://nsidc.org/data/NSIDC-0498
- MEaSUREs InSAR-Based Ice Velocity of the Amundsen Sea Embayment, Antarctica, V1
  http://nsidc.org/data/NSIDC-0545
- MEaSUREs InSAR-Based Ice Velocity Maps of Central Antarctica: 1997 and 2009, V1
  http://nsidc.org/data/NSIDC-0525

Our original continent-wide Antarctica ice velocity map (NSIDC-0484) is based on speckle tracking of data collected using ALOS/PALSAR along with ENVISAT/ASAR, RADARSAT-1&-2, Sentinel-1a/b, ERS-1/2, TerraSAR-X and Landsat-8. Based on our expertise, we also produced a series of annual surface ice velocity maps of the Antarctic Ice Sheet between 2000 and 2021 (NSIDC-0720), as shown in Figure 1 [5]. Both data sets were processed using speckle or feature tracking and are published at the National Snow and Ice Data Center (NSIDC). The latest generation Landsat satellite (Landsat-8) proved to be a useful addition to the suite of SAR satellites providing data for our products. We process SAR and optical data in a synergistic fashion, automatically calibrate, mosaic, and integrate these data sets together into seamless, ice-sheet-wide products.

The aforementioned products are solely based on tracking methods (speckle tracking for SAR, feature tracking for optical), which limits the accuracy on the ice motion to about 10 m/yr, which impacts the determination of flow direction in slow moving areas. These limitations impact our ability to accurately define drainage basins of glaciers in the region or to model and understand the ice flow in slow moving areas.

The utilization of the InSAR phase allows us to measure ice velocity much more accurately, particularly in slow areas in the interior of the ice sheet. This advantage comes at the cost of more stringent data requirements. While speckle tracking provides 2d flow results from a single pair, InSAR phase analysis requires data acquired in ascending and descending orbits to combine two range-only velocity vectors to form a 2d flow map [9] [11]. We solved this issue by combining ascending and descending InSAR phases from ALOS-2/PALSAR-2, ALOS/PALSAR, ERS-1/2,

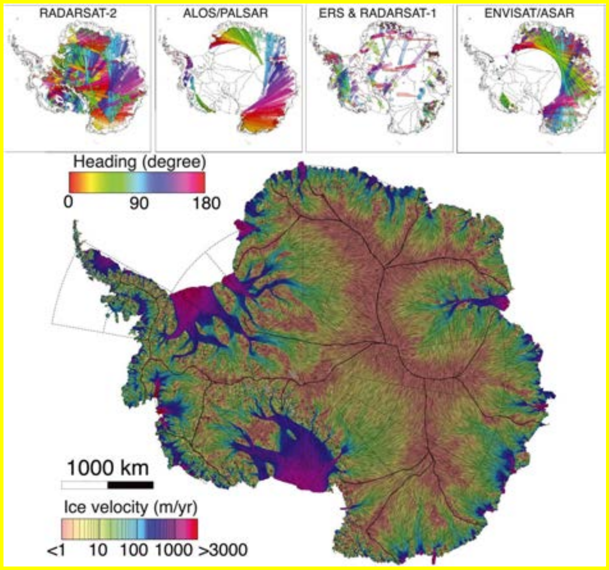

Fig. 2: MEaSUREs Phase-Based Antarctica Ice Velocity Map, V1 [11].
http://nsidc.org/data/NSIDC-0754
Contributions of the various missions are shown in the top row.

Envisat/ASAR, COSMO-SkyMed, RADARSAT-1/&-2, and TanDEM-X/TerraSAR-X and achieve phase-based ice velocity coverage for more than 71% of the area [11]. In areas of fast flow on the coast, InSAR phase analysis is no longer possible due to phase decorrelation. Due to the high signal, tracking-based results have an excellent SNR for these regions and combining tracking with phase-based results leads to the most precise ice velocity reference map of Antarctica to date (NSIDC-0754, see Figure 2).

Figure 3 shows the published grounding line product [3,6,7] divided by sensor as well as by year of data acquisition. All grounding lines were measured using double difference interferograms by utilizing the sensitivity of the interferometric phase to vertical displacement due to tide lift of the floating portion of the ice. Grounding mapping efforts are ongoing, particularly using ALOS-2 PALSAR-2, Sentinel-1, RADARSAT-2, and Cosmo SkyMED. We are also shifting to measuring multiple grounding line positions per year to account for tidal induced short term variations of the grounding line position and define a grounding zone.

5. ALOS-2 PALSAR-2 EXAMPLE RESULTS

In an effort to evaluate ALOS-2 PALSAR-2 data for ice sheet monitoring, JAXA kindly agreed to acquire, on a best effort basis, repeat pass interferometric data in several key areas, where acquisitions with limited geographic coverage still have significant scientific impact. Figure 4 shows the distribution of the areas of interest around Antarctica. We chose fast glaciers in coastal Antarctica that undergo changes as observed in [12]. Also shown in Figure 4 are ALOS-2 PALSAR-2 sample ice velocity maps, all with good correlation.
Figure 5 shows a double difference interferogram of two adjacent frames in the Denman Glacier region. Data correlation is excellent and the differential tide leads to a vertical displacement of the floating portion of the ice resulting in a dense fringe pattern that allows the delineation of the InSAR grounding line position, which is the upstream boundary of the dense fringes.

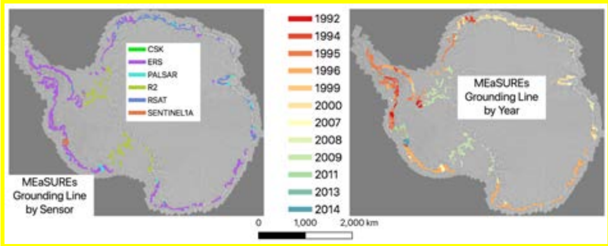

Fig. 3: MEaSUREs Antarctic Grounding Line from Differential Satellite Radar Interferometry, V2 [3,6,7].
http://nsidc.org/data/NSIDC-0498

A phase jump is visible between the two frames, because they were processed separately. The area has a complex grounding line, which was previously mapped using COSMO SkyMed X-band SAR data with 1 day repeat orbit [13]. The ALOS-2 PALSAR-2 example shows excellent correlation and a grounding line signal even on the trunk of Denman Glacier, an area that suffers from decorrelation in 6-day Sentinel-1 C-band data.

Figure 6 shows several example ALOS-2/PALSAR-2 double difference interferograms for Totten Glacier, East Antarctica. Data acquisition was on a best effort basis, so interferometric pairs are dispersed throughout the year. We use all available interferometric pairs to generate double difference interferograms, even though a preferred way of doing so is with interferograms that were acquired close in time (less than 6 months apart). The examples show a difference in fringe patterns depending on the acquisition dates used to form the interferograms. Similar tide level differences between the acquisitions can potentially limit the vertical displacement of the ice thus resulting in no discernable grounding line fringes.

6. SUMMARY AND CONCLUSIONS

We evaluate 14-day interferometric L-band SAR data from ALOS-2 PALSAR-2 for their utility for ice sheet monitoring. The higher correlation of L-band data compared to data with shorter wavelength and comparable temporal baseline makes PALSAR-2 an excellent instrument to monitor land ice. For the data we have available, tracking results show generally good correlation. Grounding line measurements are possible. The sensitivity of L-band data to vertical displacement is smaller compared to C- or X-band data resulting in fewer fringes for the same differential tide. The primary benefit for L-band is the higher correlation compared to higher frequency bands, however, phase decorrelation on fast flowing areas can occur for some of the areas where we have data (predominantly in West Antarctica). Another (frequency band independent) limiting factor for grounding line mapping are interferograms with similar differential tides, resulting in no discernable fringe pattern related to vertical displacement due to tide. This risk can be mitigated by acquiring multiple interferograms, not just two, the minimum needed to form a double difference interferogram. We also find that short term, tide related grounding line migration patterns can be observed if multiple grounding line measurements are available for a year. These aspects are addressed by our request to JAXA to acquire multiple interferograms in the course of a year for a given test site. The developed acquisition plan (best effort InSAR acquisitions in targeted, high-impact areas), together

with the examples shown, illustrates how ALOS-2 PALSAR-2 can be used for ice sheet monitoring under the current BOS with high scientific impact. The number of sites for acquiring multiple interferograms per year could be increased to cover the grounding lines for more glaciers around Antarctica.
ALOS-2 PALSAR-2 has the capability to collect data in left looking mode, thus making it one of the few missions able to collect data in Ross and Ronne ice shelves, particularly the grounding zone regions of these ice shelves. Collecting multiple interferograms in a given year for these regions would contribute to the sparse grounding line record for the area.
ALOS-2 PALSAR-2, under the BOS, collects stripmap data collected in right-looking mode over large portions of coastal Antarctica, geared towards geographic coverage. Few InSAR acquisitions are available outside the defined Areas of Interest defined for this and similar projects. Given the excellent correlation for tracking-based ice velocity generation, a comprehensive collection of interferometric SAR data in Coastal Antarctica would be an asset for ice velocity mapping. Such a coverage would likely require an adjustment of the BOS, but could be achieved by extending the time frame allowed to achieve a full geographic coverage with stripmap data to allow for 14-day repeat InSAR data collection thus vastly improving the scientific impact of stripmap data collected in Antarctica.

7. REFERENCES

[1] Michel R, Rignot E (1999) Flow of Glaciar Moreno, Argentina, from repeat-pass Shuttle Imaging Radar images: comparison of the phase correlation method with radar interferometry. J. Glaciol. 45(149):93–100.

[2] Rignot, E., Mouginot, J., B. Scheuchl (2011), Ice flow of the Antarctic ice sheet. Science, 1066 10.1126/science.1208336.

[3] Rignot, E., Mouginot, J., & Scheuchl, B. (2011). Antarctic grounding line mapping from differential satellite radar interferometry. Geophysical Research Letters, 38(10).

[4] Rignot E, Mouginot J (2012) Ice flow in Greenland for the International Polar Year 2008- 2009. Geophys. Res. Lett. 39, L11501:1–7.

[5] Mouginot J, Scheuchl B, Rignot E (2012) Mapping of ice motion in Antarctica using synthetic-aperture radar data. Remote Sens. 4(12):2753–2767

[6] Rignot, E., Mouginot, J., Morlighem, M., Seroussi, H., & Scheuchl, B. (2014). Widespread, rapid grounding line retreat of Pine Island, Thwaites, Smith, and Kohler glaciers, West Antarctica, from 1992 to 2011. Geophysical Research Letters, 41(10), 3502-3509.

[7] Scheuchl, B., Mouginot, J., Rignot, E., Morlighem, M., & Khazendar, A. (2016). Grounding line retreat of Pope, Smith, and Kohler Glaciers, West Antarctica, measured with Sentinel‐1a radar interferometry data. Geophysical Research Letters, 43(16), 8572-8579.

[8] Mouginot J, Rignot E, Scheuchl B, Millan R (2017) Comprehensive annual ice sheet velocity mapping using Landsat-8, Sentinel-1, and Radarsat-2 data. Remote Sensing 9(4).

[9] Joughin IR, Kwok R, Fahnestock MA (1998) Interferometric estimation of three- 1091 dimensional ice-flow using ascending and descending passes. IEEE Trans. Geosci. Remote Sens. 36(1):25–37.

[10] Liao, H., Meyer, F. J., Scheuchl, B., Mouginot, J., Joughin, I., & Rignot, E. (2018). Ionospheric correction of InSAR data for accurate ice velocity measurement at polar regions. Remote Sensing of Environment, 209, 166-180.

[11] Mouginot J., Rignot, E., Scheuchl, B. 2019 Continent-wide, interferometric SAR phase, mapping of Antarctic ice velocity. Geophysical Research Letters, 46, 9710– 9718.

[12] E. Rignot, J. Mouginot, B. Scheuchl, M. van den Broeke, J. Wessem, M. Morlighem, (2019) Four decades of Antarctic Ice Sheet Mass Balance: 1979-2017, Proc. Nat. Academ. Sci., 116 (4) 1095-1103.

[13] Brancato, V., Rignot, E., Milillo, P., Morlighem, M., Mouginot, J., An, L., Scheuchl, B., Jeong, S., Rizzoli, P., Bueso Bello, J.L. and Prats‐Iraola, P. (2020). Grounding line retreat of Denman Glacier, East Antarctica, measured with COSMO‐SkyMed radar interferometry data. *Geophysical Research Letters*, *47*(7), e2019GL086291.

SEA ICE CHARACTERISTICS DURING TRANSITION PERIODS IN THE MARGINAL ICE ZONE OF THE PACIFIC ARCTIC OCEAN UTILIZING QUAD-POL SAR DATA

PI No.: ER2A2N144

Hyangsun Han [1], Seung Hee Kim [2]

[1] Department of Geophysics, Kangwon National University, Republic of Korea
[2] Center of Remote Sensing and GIS, Korea Polar Research Institute, Republic of Korea

1. INTRODUCTION

The Arctic sea ice is very sensitive to climate change and its spatiotemporal changes influence the operation of the Northern Sea Route [1-2]. Therefore, observation of the changes in the Arctic sea ice is very important. In the high latitude region, the spatiotemporal variations of sea ice are small, whereas the variations of sea ice in the marginal ice zone are very large [3]. Various characteristics of sea ice such as size, thickness, surface roughness, and distribution of melt ponds are rapidly changing from spring to summer when sea ice melts (thaw-up phase) and from autumn to winter when sea ice freezes (freeze-up phase). Particularly, the Pacific Arctic Ocean, including the East Siberian Sea, the Chukchi Sea and the Beaufort Sea, is characterized by faster melting and freezing region than the other Arctic regions [4].

Due to recent climate change, the transition periods of Arctic sea ice is changing and the characteristics of sea ice change accordingly. Thus, characterizations of sea ice at the marginal ice zone during the transition periods in the Pacific Arctic Ocean should be performed for understanding the response of the sea ice due to the climate change and for determining more economic Northern Sea Route.

Polarimetric synthetic aperture radar (SAR) data can be effectively used for characterizing sea ice because it provides physical and structural information of the target. Many studies have been conducted to analyze sea ice using polarimetric SAR data. However, few studies for sea ice in the marginal ice zone of the Pacific Arctic Ocean during the transition periods have been performed.

This research aims to characterize sea ice in the transition periods of the previously unexplored marginal ice zone of the Pacific Arctic Ocean by using ALOS-2 polarimetric SAR dataset and develop analytical techniques for the generation of sea ice information. The objectives of this research are 1) to classify sea ice types using the ALOS-2 polarimetric backscattering signals, 2) to characterize the physical properties of sea ice such ice thickness, 3) to develop the sea ice characterization models for ALOS-2 polarimetric SAR based on machine learning approaches, and 4) to assess the accuracy of the derived sea ice characteristics with in-situ measurements.

2. CLASSIFICATION OF SEA ICE TYPES

Accurate mapping of Arctic summer sea ice is necessary to assist in safely conducting human activities and to provide meaningful information related to climate change. Since the 1970s, passive microwave sensors have made observations of sea ice distributions based on distinct microwave radiation properties between sea ice and open water and have provided sea ice concentration data every day with a grid size of ~25 km. The sea ice concentration derived from the passive microwave sensors has been used as a primary data source for ship navigation. However, significant inaccuracies occur in the summer season, especially in the marginal ice zone [5], so that exhaustive verification of the accuracy is required.

SAR has been widely used to map sea ice because it can provide high quality images regardless of weather conditions and sun altitudes. Particularly, polarimetric SAR can obtain various information on sea ice, which is extremely useful for sea ice mapping.

In this research, we developed machine learning-based sea ice classification models for ALOS-2 polarimetric SAR data in Arctic marginal ice zone. Random Forest, a rule-based machine learning approach, was used for the model development. Random Forests generates a number of bootstrapped samples from the original data and constructs multiple no-pruning classification and regression trees [6]. A series of independent trees are grown by a randomly selected subset of the training samples and splitting variables of the tree, which can solve classification and regression problems.

A total of 24 ALOS-2 polarimetric (HH and HV) SAR images over the Chukchi Sea in Arctic in September 2015. Fig. 1 shows an example of the ALOS-2 SAR images of the Arctic sea ice obtained on 15 September 2015. The HH-polarized SAR images shows higher backscattering signals for sea ice compared to the HV-polarized SAR image. In the study area, there was no multi-year sea ice and all sea ice was defined as first-year sea ice.

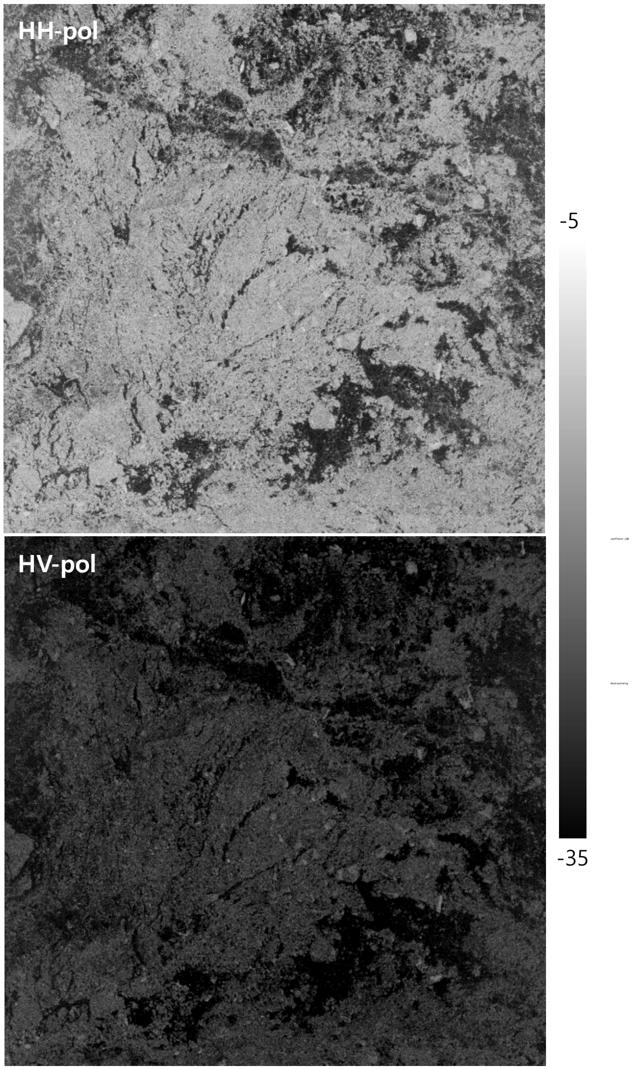

Fig. 1. ALOS-2 HH- and HV-polarized SAR images of Arctic sea ice obtained on 15 September 2015

By helicopter survey of the Arctic expedition based on ice breaking research vehicle (IBRV) ARAON operated by the Korea Polar Research Institute (KOPRI) and sea ice charts provided by the Russian Arctic and Antarctic Research Institute, we constructed the reference samples (pixels) for thick sea ice, thin sea ice, and open water from the ALOS-2 SAR images. A total of 12,600 samples (4200 thick sea ice, 4200 thin sea ice, and 4200 open water) for HH- and HV-polarized backscattering coefficient were selected. Eighty percent of the total samples (3360 samples for each class) were randomly selected and used as training samples, and the remaining samples (840 samples for each class) were used as test samples.

The HH- and HV-polarized backscattering coefficients were used as the input variables for the Random Forest-based sea ice classification model. Table 1 shows the performance of the classification model. The developed model's performance was low, with the overall accuracy of 75.2% and the Kappa coefficient of 62.9%. Fig. 2 shows the sea ice map classified from the SAR data of Fig. 1 based on the developed model.

Table 1. Performance of sea ice classification model developed by using ALOS-2 HH- and HV-polarized backscattering coefficients

Reference / Classified	Thick sea ice	Thin sea ice	Open water	Sum	User's Accuracy
Thick sea ice	533	51	60	644	83.28%
Thin sea ice	215	704	141	1060	66.41%
Open water	72	85	639	796	80.28%
Sum	840	840	840	2520	
Producer's Accuracy	65.83%	83.81%	76.07%		
Overall Accuracy			75.24%		
Kappa coefficient			62.86%		

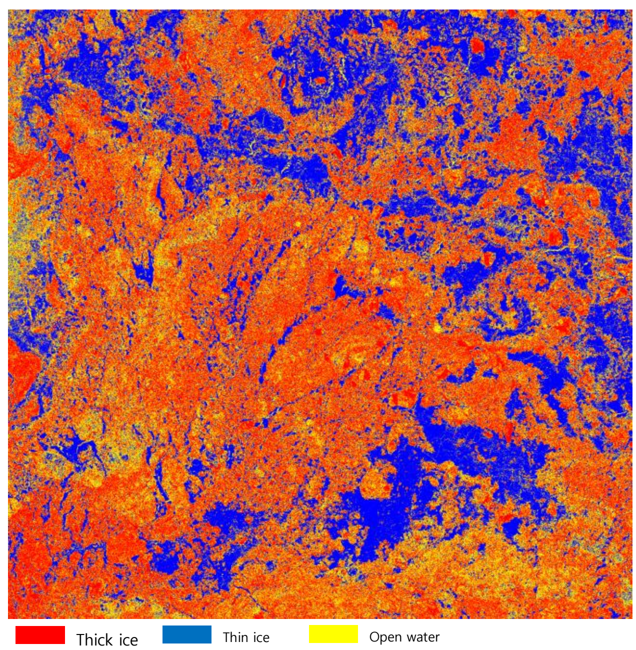

Fig. 2. A map of sea ice classification derived from the model developed by using ALOS-2 HH- and HV-polarized backscattering coefficients

We computed entropy, anisotropy, and alpha angle from the ALOS-2 SAR images by using H-Alpha dual-polarimetric decomposition method. The calculated polarimetric parameters and the backscattering coefficients were used as input variables for classification of sea ice types. The newly developed model showed much higher performance (overall accuracy of 89.8% and Kappa coefficient of 84.6%, respectively) compared to the model using only the backscattering coefficients (Table 2). Fig. 3 shows the sea ice map for the SAR data of Fig. 1, derived from the newly developed model.

Table 2. Performance of sea ice classification model developed by using ALOS-2 polarimetric parameters and backscattering coefficients

Reference / Classified	Thick sea ice	Thin sea ice	Open water	Sum	User's Accuracy
Thick sea ice	747	29	16	792	94.32%
Thin sea ice	60	729	38	827	88.15%
Open water	33	82	786	901	87.24%
Sum	840	840	840	2520	
Producer's Accuracy	88.93%	86.79%	93.57%		
Overall Accuracy			89.76%		
Kappa coefficient			84.64%		

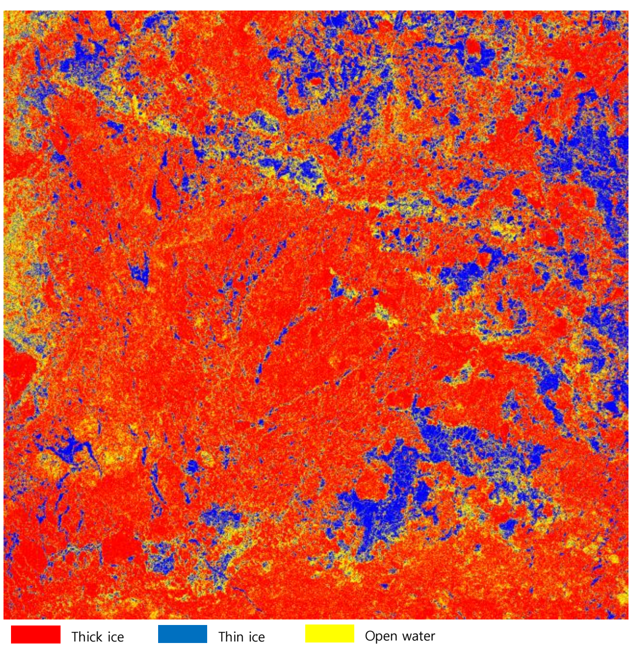

Fig. 3. A map of sea ice classification derived from the model developed by using ALOS-2 polarimetric parameters and backscattering coefficients

Table 2 and Fig. 3 demonstrates that the polarimetric parameters of ALOS-2 SAR data much improved the performance of sea ice classification compared when using backscattering coefficients only. We could not use full polarimetric ALOS-2 SAR data for developing the Arctic sea ice classification model ice because there were no full polarimetric data for the marginal ice zone during transition period. Nevertheless, if the full polarimetric ALOS-2 data is obtained, it can be expected that the sea ice mapping performance will be much better, and we think that the ALOS-2 will greatly contribute to the field of sea ice research.

3. BACKSCATTERING CHARACTERISTICS BY SEA ICE THICKNESS

Radar backscattering can vary with changes in sea ice thickness. Several studies have analyzed the variations in backscattering characteristics observed by SAR depending on sea ice thickness changes. The previous studies showed a meaningful relationship between the backscattering and sea ice thickness. However, few studies on snow-covered sea ice has been performed so far.

In this study, we collected ALOS-2 polarimetric SAR images of landfast sea ice in Barrow, Alaska, and compared the backscattering characteristics of the sea ice with its thickness. From January to April 2015, 8 dual-polarimetric (HH and HV) and 2 full polarimetric ALOS-2 SAR images for the landfast sea ice were acquired. The image acquisition period corresponded to the sea ice thaw-up phase (transition period). We used in-situ sea ice thickness measured at the sea ice mass balance site (71.37725° N, 156.55350° E) by University of Alaska Fairbanks (Fig. 4). Fig. 5 shows a HH-polarized ALOS-2 SAR image of the study site obtained on 25 April 2015. The red dot in Fig. 5 represents the location of sea ice mass balance site shown in Fig. 4.

Fig. 4. A picture of sea ice mass balance site (https://seaice.alaska.edu/gi/data/barrow_massbalance/brw_2015/)

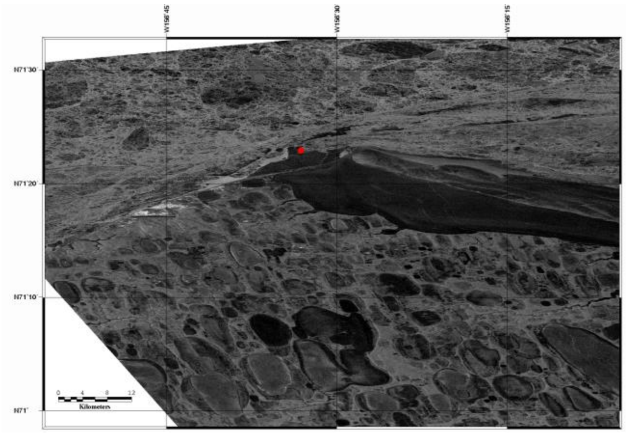

Fig. 5. ALOS-2 SAR image for the landfast sea ice in Barrow, Alaska. The red dot represents the location of sea ice mass balance site

Fig. 6 shows the scatterplot between the in-situ measured sea ice thickness and ALOS-2 backscattering coefficients at HH-polarization. The ALOS-2 L-band backscattering coefficient at HH-polarization strongly correlated with the landfast sea ice thickness, showing a R^2 value of 0.933. This represents that it can be possible to develop a model for estimating sea ice thickness from the ALOS-2 polarimetric data in the transition period.

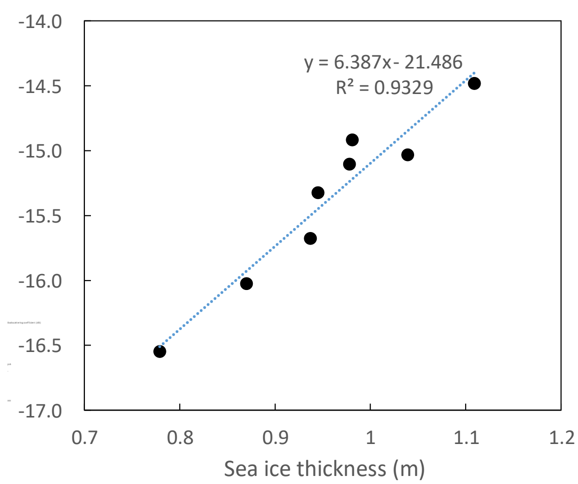

Fig. 6. Scatterplot between sea ice thickness and ALOS-2 HH-polarized backscattering coefficient

Fig. 7 show the scatterplot between the in-situ measured sea ice thickness and ALOS-2 backscattering coefficients at HV-polarization, of which the value of R^2 was 0.019. The landfast sea ice thickness could not be estimated from the ALOS-2 HV-polarized backscattering coefficient.
A model for estimating sea ice thickness from ALOS-2 polarimetric data could not be developed in this research because of a lack of ALOS-2 data capturing the sites of field observations. Nevertheless, our results showed that the ALOS-2 polarimetric data can be used to estimate accurate sea ice thickness in the transition periods.

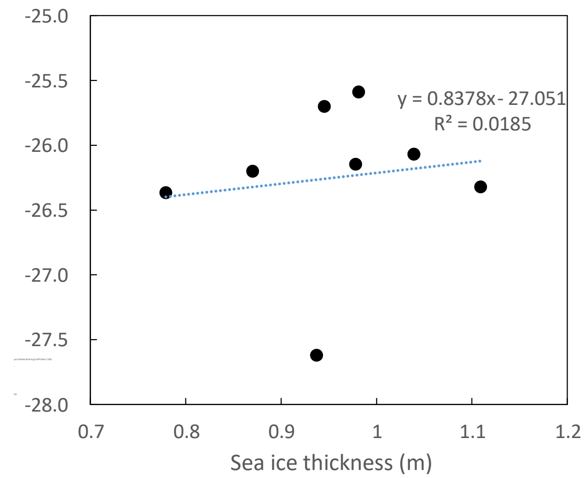

Fig. 7. Scatterplot between sea ice thickness and ALOS-2 HV-polarized backscattering coefficient

4. POSSIBILITY OF USING ALOS-2 DATA FOR ESTIMATING CHANGES IN SEA ICE PHYSICAL PROPERTIES

In this research, we analyzed the incidence angle dependence of multiyear sea ice in the marginal ice zone on the ALOS-2 L-band backscattering. We focused on the marginal ice zone of the western Beaufort Sea, north of Alaska. A sea ice drifter buoy with an integrated GNSS positioning system and Argos satellite-based data transmission system was installed on the surface of sea ice floe during the field campaign on August 12, 2019. The time and coordinates of the tracker on the ice floe were used to select ALOS-2 PALSAR2 images that capture the sea ice floe within its swath. However, there was few ALOS-2 polarimetric SAR images for the ice floe. Instead, we used Sentinel-1 dual-polarimetric SAR images, and analyzed the incidence angle dependence of the C-band backscattering coefficients of HH- and HV-polarization by using a robust linear regression model. The determinant coefficient and root mean square error between the measured and calculated backscattering coefficients were analyzed. Then, a polynomial regression model to determine a temporal trend of the normalized backscattering coefficients over the surface of multiyear sea ice during the SAR observation period was determined. Based on this result, we expect that ALOS-2 full-polarimetric SAR data can be used for analyzing the temporal changes in sea ice physical properties.

5. REFERENCES

[1] J.C. Stroeve, M.C. Serreze, M.M. Holland, J.E. Kay, J. Malanik, and A.P. “The Arctic's Rapidly Shrinking Sea Ice Cover: A Research Synthesis,” *Climate Change*, 110, pp. 1005–1027, 2012.

[2] S.R. Stephenson, L.C. Smith, and J.A. Agnew. “Divergent Long-Term Trajectories of Human Access to the Arctic.” *Nature Climate Change*, 1 (3), pp. 156–160, 2011.

[3] H. Han and H.-c. Kim. “Evaluation of Summer Passive Microwave Sea Ice Concentrations in the Chukchi Sea Based on KOMPSAT-5 SAR and Numerical Weather Prediction,” *Remote Sensing of Environment*, 209, pp. 343–362, 2018.

[4] R.A. Woodgate, T. Weingartner, and R. Lindsay. “The 2007 Bering Strait Oceanic Heat Flux and Anomalous Arctic Sea-Ice Retreat,” *Geophysical Research Letters*, 37, L01602, 2010.

[5] S. Andersen, R. Tonboe, S. Kern, and H. Schyberg. “Improved Retrieval of Sea Ice Total Concentration from Spaceborne Passive Microwave Observations Using Numerical Weather Prediction Model Fields: An Intercomparison of Nine Algorithms,” *Remote Sensing of Environment*, 104, pp. 374–392, 2006.

[6] L. Breiman. “Random forests,” *Machine Learning*, 45, pp. 5–32, 2001.

INTERACTION OF ICE FLOW AND SUBGLACIAL LAKES IN ANTARCTICA OBSERVED BY SYNTHETIC APERTURE RADAR INTERFEROMETRY

PI No.: ER2A2N164

Jihyun Moon [1], Heejeong Seo [2], Hoseung Lee [1], Da-woon Jung [1], Hoonyol Lee [1]

[1] Department of Geophysics, Kangwon National University, Republic of Korea
[2] Earthquake and Volcano Research Division, Korea Meteorological Administration, Republic of Korea

1. INTRODUCTION

Glacier flow rates are affected by changes in mass balance gradient due to snowfall on the glacier surface, changes in physical properties occurring inside and below the glacier, and basal sliding [1]. Many studies have been conducted on the observation of glacier flow rates due to changes in mass balance gradients and physical properties due to snow cover and erosion [2]. In addition, studies on flow rate changes due to the basal sliding are receiving great attention.

The flow rate change due to the basal sliding is greatly affected by the water in the base. The pressure of thick ice lowers its melting point, allowing liquid water to exist at lower temperatures between the Antarctic ice and bedrock. Molten water is an important factor in changing the flow rate of glaciers. This is because the melt water reduces friction between the ice and the bedrock, accelerating the flow of the glacier [3, 4]. Molten water travels along the topography of the bedrock, creating channels and being stored in watersheds to form subglacial lakes. [5] suggested that large subglacial lakes initiate rapid ice flow.

The study of subglacial lakes began with the discovery of elliptical depressions in the ice sheet. The first subglacial lakes were first discovered by Radio Echo Sounding (RES) from 1968 to 1979 [6]. Interactions between the ice sheet surface and subglacial lakes were unknown at the time of discovery, but were analyzed in the 1990s [7]. Most subglacial lakes were discovered using Ice-penetrating Radio Echo Sounding and Satellite Altimetry techniques [8, 9, 10]. Observations of subglacial lakes using RES showed that the intensity of the reflected signal from the subglacial lake surface was much stronger and flatter than the reflected signal from the bedrock due to the dielectric constant.

Subglacial lake detection using satellite altimeter was performed by detecting the flat surface of an ice sheet appearing from above in a large subglacial lake, or by detecting a sharp difference in altitude between the ice sheet around a subglacial lake and the ice sheet above the subglacial lake. Large subglacial lakes, such as Lake Vostok, can be detected by optical satellite imagery because the ice sheet surface is wide and flat. The difference in altitude above subglacial lakes are caused by changes in the water level below the ice sheets. The water system at the bottom of the ice sheet is pressurized by the thick ice above it. Changes in water level under these pressure conditions can change the elevation of the ice surface and can be observed from satellites [11]. The melt water below the ice sheet is driven by hydraulic pressure to discharge and rechange the subglacial lake, causing the upper ice to fall or rises as the water level changes.

[12] found a total of 124 subglacial lakes in Antarctica using the ICE-Sat radar altimeter. [12] defined an active subglacial lake as a subglacial lake in which elevation displacement occurs due to hydrological activity. However, since RES and satellite altimeters measure using lines, it is difficult to detect small subglacial lake between lines. Also, when an altimeter detects the flat surface of the upper ice sheet of a subglacial lake, the physical properties of the ice sheet can make the surface appear flat, just as the low shear stress at the bottom make the surface of the ice sheet appear flat. In addition, the upper ice surface of subglacial lakes less than 4 km in diameter may not be flat, limiting detection [13].

The satellite Synthetic Aperture Radar (SAR) is very effective for research in Antarctica, where access is limited. In addition, it has the advantage of providing high-resolution images in all conditions as it is not affected by the illuminance of the sun and weather conditions. Differential-interferometric SAR (DInSAR), one of the SAR image processing techniques, can be applied to measure ice displacement with cm accuracy. For example, [14] calculated the exact flow velocity of the Campbell Glacier Tongue using the DInSAR technique and tidal correction. Since DInSAR technique also includes vertical displacement, changes in the elevation of the glacier surface can also be observed. [15] used InSAR to observe changes in glacial surface elevation due to movement of subglacial water. [16] determined glacial subsidence due to drainage of subglacial lake, considering that displacement using InSAR is in the Line-Of-Sight (LOS) direction.

In this study, DInSAR was applied to Cook_{E2}, one of the active subglacial lakes discovered by [12], to observe discharge and recharge, and to analyze the 2D surface change accordingly. The study area and data are described in Section 2 and the study methods are presented in Section 3. The results were discussed in Section 4, and Section 5 concludes this report.

2. STUDY AREA AND MATERIALS

Stretching from the coast George V in East Antarctica to Mount Prince Albert in West Antarctica, the Wilkes Subglacial Basin of Wilkes Land is covered by an ice sheet

1,400 km long, 400 km wide and 3 km thick. The Wilkes Subglacial Basin was observed with airborne radar dataset performed in the 1970s, and the deepest part of the basin is deeper than 2100 m below sea level [17]. Of the entire basin, the area observed in this study is approximately 100 km west of Talos Dome in East Antarctica. Near this area, there is an Ice Divide that divides the direction of the ice flow into three directions, and this area is included in Cook Glacier. In particular, this area is drawing attention from many researchers as drainage progressed rapidly from 2006 to 2008.

The study area is included in the list of active subglacial lakes in Antarctica presented by [12]. [12] determined that 2.7 km3 of water drained from Cook$_{E2}$ from November 2006 to March 2008 using ICESat (Ice, Cloud and land Elevation Satellite) laser altimeter data. A decrease in height of 44 m was observed in track 227 and a decrease of 48 m in track 1325, which is approximately five times the height decrease found in other subglacial lakes [12]. [9] combined ICESat and CryoSat-2 data to construct a time series for the elevation model and observed that the height of the Cook$_{E2}$ upper surface decreased sharply from 2006 to 2008 at an average rate of 35 ± 14 m/year and then increased again to 5.6 ± 2.8 m/year. [18] observed an elevation decrease of about 70 m from November 2006 to October 2008 through ICESat. They also found that an elevation increase of about 13 m occurred when comparing the October 2008 altitude with the SPOT5 DEM obtained in February 2012 [18]. [19] show a decrease in elevation of 59.6 m from February 2006 to October 2008 due to drainage, followed by steady increase at a rate of about 1.1 m/year from January 2011 to November 2016 using ICESat and CryoSat-2 data.

This study observed Cook$_{E2}$ using satellite SAR images. Since the satellite SAR system uses an active imaging system using microwaves, it can acquire high-resolution images of a large area in all weather conditions. In previous studies, satellite altimeters were mainly used to check changes according to lines. Satellite SAR imagery allows the identification of two-dimensional structures by analyzing images of the entire scene.

In this study, images from the Advanced Land Observing Satellite (ALOS) Phased Array L-Band Synthetic Aperture Radar (PALSAR) operated by the Japan Aerospace Exploration Agency (JAXA) were used. ALOS was launched on January 24, 2006 and operated until May 12, 2011. Its primary mission is land observation, and is used for mapping, regional observation, disaster monitoring, and resource surveys. ALOS has three sensors: Panchromatic Remote Sensing Instrument for Stereo Mapping (PRISM) for digital altitude measurement, Advanced Visible and Near Infrared Radiometer type-2 (AVNIR-2) for precision land cover observation, and PALSAR with L-band SAR (1.27GHz) for all-weather land observation. As shown in Table 1., ALOS PALSAR has Fine Mode, Scan SAR Mode, and Polarimetric Mode. In this study, SAR images acquired in FBS(Fine Beam Single polarization) mode were used, and level 1.1 SLC(Slant range single look complex) products acquired in October 24, 2007, November 15, 2007, December 9, 2007, December 31, 2007, October 20, 2010, and December 5, 2010 were used.

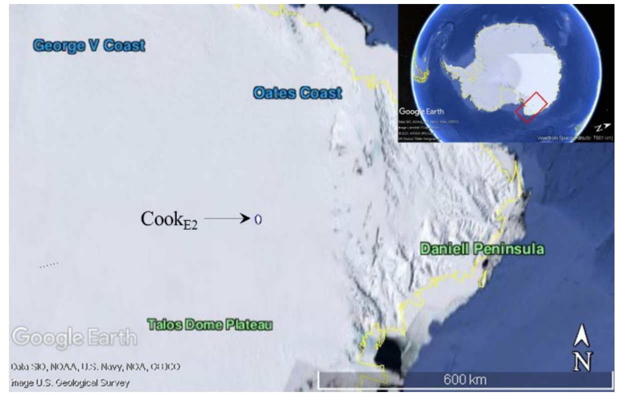

Fig. 1 Study area

Table 1 ALOS PALSAR imaging acquisition modes characteristics

Mode		Swath (km)	Spatial resolution (m)	Polarization
Fine	FBS	70	10×10	Single (HH or VV)
	FBD	70	20×10	Dual (HH+HV or VV+VH)
Scan SAR		360	71-157×100	Single (HH or VV)
Polarimetric		30	31×10	Quad-pol (HH/HV/VH/VV)

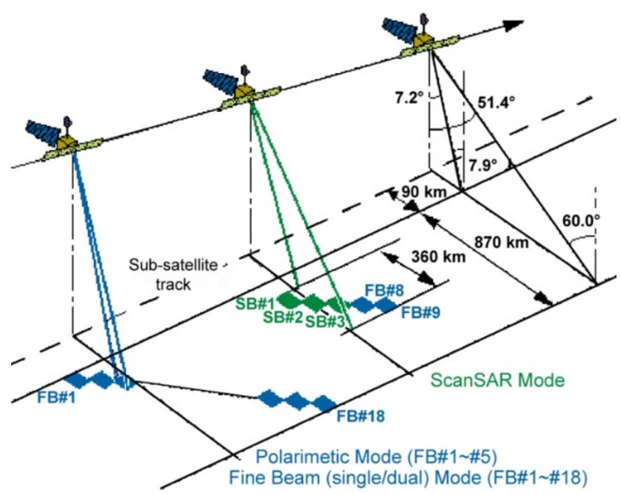

Fig. 2 ALOS PALSAR observation modes [20].

3. METHODS

A satellite SAR system can detect subtle differences by observing the same object more than once. There are two methods of observation. The first is a method of acquiring images with a time difference using the repeated orbit of a single radar mounted on a single satellite. The second way is to take images with two radars at the same time. In this method, two radars can be installed on one satellite to take images at the same time, or two satellites are equipped with radars respectively and fly together. Most satellites such as ALOS-1/2, ERS-1/2, Sentinel-1A/B, and COSMO-SkyMed use repeated orbits, while TerraSAR-X and TanDEM-X take images in parallel. In the method using the repeated orbit, the displacement is represented by fringes and can be considered as a concept of velocity. When using two radars at the same time, it is mainly used to generate global DEM by observing the altitude.

The geometry of the SAR Interferometry technique is shown in Fig. 3. InSAR configuration is usually achieved by imaging a target point P from two radar positions at S_1 and S_2. The distance between S_1 and S_2 is baseline, B. The line passing through S_2 and perpendicular to the slant range of S_1 is called $B_\perp$. The height of S_1 from the surface is H and the radius of the Earth is r_e. θ_l is the look angle, and α_B is the angle between the line perpendicular to H and baseline B. If the slant ranges from S_1 and S_2 to the target points P are R_1 and R_2, respectively, and the slant range difference between R_1 and R_2 is ΔR, the interferometric phase ϕ can be expressed as follows using the radar wavelengths λ and ΔR:

$$\phi = -\frac{4\pi}{\lambda}\Delta R \qquad (1)$$

Phase represents a displacement of 2π, and a single fringe means displacement of $\frac{\lambda}{2}$. ΔR can be expressed as follows by applying the second law of cosines:

$$\Delta R = \sqrt{R_1^2 + B^2 - 2R_1 B \sin(\theta_l - \alpha_B)} - R_1. \qquad (2)$$

The elevation Z from the surface to the target point P is calculated by the following equation:

$$z = \sqrt{(r_e + H)^2 + R_1^2 - 2R_1(r_e + H)\cos\theta_l} - r_e. \qquad (3)$$

The height sensitivity of InSAR can be expressed as

$$\frac{\partial\phi}{\partial z} \approx \frac{4\pi}{\lambda}\frac{B_\perp}{R_1 \sin\theta_l}. \qquad (4)$$

This means the change of the interferometric phase according to the amount of change in the elevation of the surface. The height ambiguity indicated by single fringe in InSAR can be expressed as follows:

$$h_a = 2\pi\frac{\partial z}{\partial\phi} \approx \frac{\lambda}{2}\frac{R_1 \sin\theta_l}{B_\perp}. \qquad (5)$$

If the perpendicular baseline becomes too large, coherence will be small, and information may not be obtained. Therefore, the perpendicular baseline should be considered when selecting the DInSAR piar. We determined the InSAR pair as shown in Table 2 by considering the perpendicular baseline.

The interferogram shows fringes that include both the phase by topographical elevation and the phase by ground displacement. To observe the displacement of the surface, it is necessary to remove the phase by topographical elevation. Therefore, the Differential Interferometric SAR (DInSAR) technique using a reference Digital Elevation Model (DEM) was applied to remove the topographic phase. Since there is very little ice flow in the study area, the DInSAR images show areas with different flow velocity than the surrounding areas. Note that one fringe in the DInSAR image means a displacement in the Line-Of-Sight (LOS) direction corresponding to half the wavelength of the band.

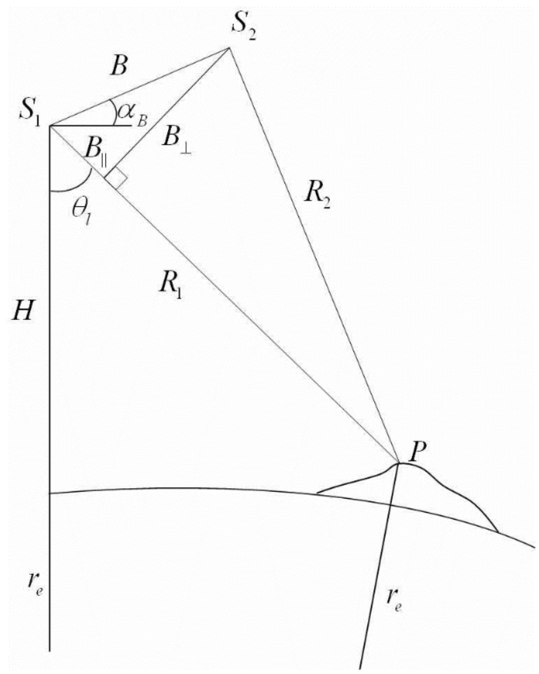

Fig. 3 InSAR geomerty

Table 2 Used data.

InSAR Pair	Perpendicular baseline (m)	Temporal baseline (days)
20071024_20071209	-791.9373168945	46
20071115_20071231	880.2124023438	46
20101020_20101205	1020.9151611328	46

4. RESULTS AND DISCUSSION

The study area is the upper part of subglacial lake Cook_{E2} included in [12], who first collected the entire Antarctic subglacial lake list. The circular fringe signal shown in the DInSAR image means the LOS displacement according to the volume change of the subglacial lake. [18] used an altimeter and a DEM to observe changes in elevation at the surface of lake Cook$_{E2}$. As a result, it was confirmed that from the end of 2006 to the end of 2008, the altitude decreased sharply by more than 60 m [18].

As a result of DInSAR processing of ALOS PALSAR images on October 24, 2007 and December 9, 2007, about 56.6 circular fringes appeared, confirming that there was a decrease in altitude of about 6.7±0.2 m. In [18], the elevation decrease during a similar period was about 5.5±1.6 m, and considering the error range, it shows a similar value to the elevation decrease obtained from the DInSAR image. Additional DInSAR processing was performed at similar times on the ALOS PALSAR images from November 15, 2007 and December 31, 2007 to observe some regions that were not acquired in the image frame of the first DInSAR pair. About 52.5 fringes appear, and it can be seen that an elevation decrease of about 6.2±0.2 m occurred during 46 days. In the DInSAR images generated from the ALOS PALSAR images on October 20, 2010 and December 5, 2010, an elevation increase of about 0.5±0.2 m was confirmed after the elevation decrease was completed. In [18], the elevation increase was 1.13±1.6 m during the same period.

The rates of elevation decrease in 2007 estimated in this study are about 53.16 m/year and about 49.2 m/year. In addition to the study of [18] compared above, the previous study had a value of from a minimum of about 21.7 m/year to a maximum of about 40 m/year, which was generally smaller than the results of this study [9, 12, 18, 19]. This can be seen as the result of calculating the initial rate of elevation decrease at which the discharge occurs rapidly in this study. Since the discharge rate can be change, additional data analysis is required until the discharge is complete in order to accurately analyze the change in the rate of elevation decrease over time.

The area of the circular anomaly observed in the DInSAR images of the discharge of a subglacial lake is much larger than the area of the circular anomaly when the water level is recharged after discharge is complete. This is thought to be because the displacement including the surrounding area occurs due to the elasticity of the ice when the altitude decreases rapidly when the lake is discharged. Considering the elevation change patterns observed in previous studies and this study, it is thought that the water level of Lake Cook$_{E2}$ is gradually being recharged after discharge occurred for about 1 year and 6 months from the end of 2006. Through comparison with previous studies, it was possible to verify that the behavior of the subglacial lake surface can be continuously observed using satellite SAR images. In addition, since the location of the circular fringes and the location of the subglacial lake are exactly the same, the SAR interferometry is being considered as a method to detect the presence and volume change of the subglacial lake.

5. CONCLUSIONS

In this study, the displacement in the LOS direction was analyzed using the SAR interferometry technique and the elevation change of the upper surface of the subglacial lake

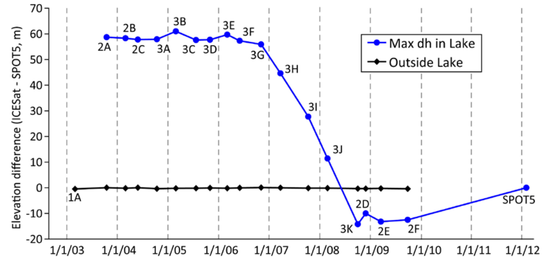

Fig. 4 time series of elevation difference at surface of Cook$_{E2}$ Subglacial Lake in [18].

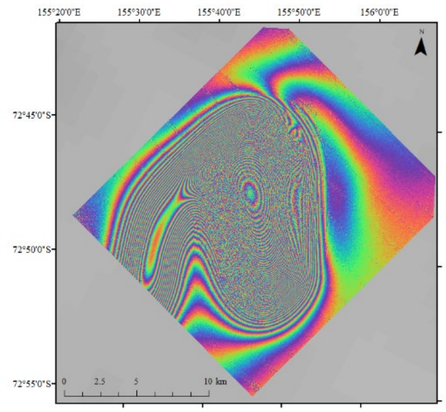

Fig. 5 20071024_20071209 ALOS PALSAR DInSAR imagery.

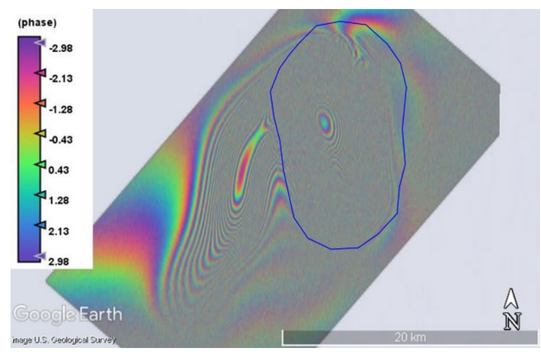

Fig. 6 20071115_20071231 ALOS PALSAR DInSAR imagery. The blue line is CookE2 in [12].

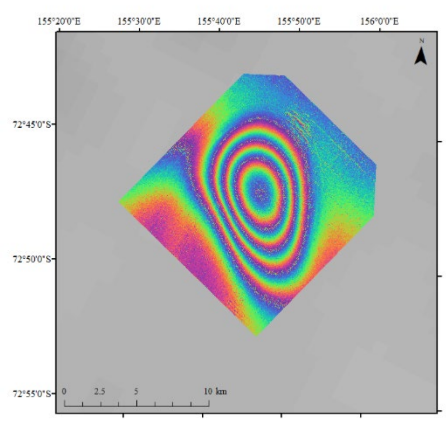

Fig. 7 20101020_20101205 ALOS PALSAR DInSAR imagery.

was estimated. Lake Cook$_{E2}$ is located in an area where glacial flow rates are slow, allowing DInSAR images to detect anomaly that differ from surrounding areas. In the DInSAR image, the flow velocity appeared as in form of circular fringes, and since there was almost no displacement in the surrounding ice, these fringes are thought to be due to vertical displacement. It is known that the subglacial lake exists in this area, so the circular fringes are thought to be due to the volume change of the subglacial lake, and it can be seen in comparison with previous studies. From the end of 2006 to the end of 2008, the elevation appears to have decreased sharply and has been increasing since then. In addition, it is judged that a more precise analysis using the SAR images is required for the increasing signal of the upper part of the subglacial lake to the present, which has been revealed in recent studies. Through this study, it was confirmed that the positions and volume changes of subglacial lakes can be observed using the SAR interferometry as well as the RES, satellite altimeter, and DEM that have been used in previous studies of subglacial lakes. Also, SAR interferometry is considered capable of detecting small subglacial lakes that have not been discovered in previous studies. Through this, it is thought that it will be helpful in site selection for subglacial lake field exploration.

6. REFERENCES

[1] R.M. Bennett, and N.F. Glasser, "Glacial Geology Ice Sheets and landforms," *John Wiley & Sons.*, pp. 65-82, 1996.

[2] E. Rignot, D.Vaughan, M. Schmeltz, T. Dupont, and D. Macayeal, "Acceleration of Pine Island and Thwaites Glaciers, West Antarctica," *Annals of Glaciology*, vol. 34, pp.189-194. 2002. doi:10.3189/172756402781817950

[3] H.J. Zwally, W. Abdalai, T. Herring, K. Larson, J. Saba, and K. Steffen, "Surface Melt-Induced Acceleration of Greenland Ice-Sheet Flow," *Science*, vol. 297, 5579, pp. 218-222, 2002. doi:10.1126/science.1072708

[4] K. Macgregor, C. Riihimaki, and R. Anderson, "Spatial and temporal evolution of rapid basal sliding on Bench Glacier, Alaska, USA," *Journal of Glaciology*, vol. 51 (172), pp. 49-63. 2005. doi:10.3189/172756505781829485

[5] R. Bell, M. Studinger, C. Shuman, M. Fahnestock, and I. Joughin, "Large subglacial lakes in East Antarctica at the onset of fast-flowing ice streams," *Nature*, vol. 445, pp. 904–907, 2007. doi:10.1038/nature05554

[6] M.J. Siegert, "Antarctic subglacial lakes," *Earth-Science Reviews*, vol. 50, pp. 29-50, 2000.

[7] G.Q. Robin, C.W.M. Swithinbank, and B.M.E. Smith, "Radio-echo exploration of the Antarctic ice sheet," *IASH Publ.*, 86 (Symposium at Hanover 1968 - Antarctic Glaciological Exploration (ISAGE)), pp. 97-115. 1970.

[8] M. Siegfried, and H. Fricker, "Thirteen years of subglacial lake activity in Antarctica from multi-mission satellite altimetry," *Annals of Glaciology*, vol. 59 (76pt1), pp. 42-55, 2018. doi:10.1017/aog.2017.36

[9] M. McMillan, H. Corr, A. Shepherd, A. Ridout, S. Laxon, and R. Cullen, "Three-dimensional mapping by CryoSat-2 of subglacial lake volume changes," *Geophysical Research Letters*, vol. 40(16), pp. 4321-4327, 2013.

[10] H.A. Fricker, M.R. Siegfried, S.P. Carter, and T.A. Scambos, "A decade of progress in observing and modelling Antarctic subglacial water systems," *Philosophical Transactions of the Royal Society A: Mathematical, Physical and Engineering Science*, vol. 374, 2016.

[11] H.A. Fricker, T. Scambos, A. Bindschadler, and R.L. Padman, "An active subglacial water system in West Antarctica mapped from space," *Science*, vol. 315, no. 5818, pp. 1544-1548, 2007.

[12] B.E. Smith, H.A. Fricker, I.R. Joughin, and S. Tulaczyk, "An inventory of active subglaical lakes in Antarctica detected by ICESat (2003-2008)," *Journal of Glaciology*, vol. 55, No. 192, pp. 573-595, 2009. doi:10.3189/002214309789470879

[13] M.J. Siegert, and J.K. Ridley, "An analysis of the ice-sheet surface and subsurface topography above the Vostok Station subglacial lake, central East Antarctica," *Journal of Geophysical Research Solid Earth*, vol. 103(B5), 1998. doi:10.1029/98JB00390

[14] H. Han, and H. Lee, "Surface strain rates and crevassing of Campbell Glacier Tongue in East Antarctica analysed by tide-corrected DInSAR," *Remote Sensing Letters*, vol. 8(4), pp. 330-339, 2017. doi:10.1080/2150704X.2016.1271158

[15] L. Gray, I. Joughin, S. Tulaczyk, and V. Spikes, "Evidence for Subglacial water transport in the West Antarctic Ice Sheet through three-dimensional satellite radar interferomery," *Geophysical Research Letters*, vol. 32, 2005.

[16] S. Palmer, M. McMillan, and M. Morlighem, "Subglacial lake drainage detected beneath the Greenland ice sheet," *Nature Communications*, vol. 6, 8408, 2015. doi:10.1038/ncomms9408

[17] F. Ferraccioli, E. Armadillo, T. Jordan, E. Bozzo, and H. Corr, "Aeromagnetic exploration over the East Antarctic Ice Sheet: a new view of the Wilkes Subglacial Basin," *Tectonophysics*, vol. 478 (1–2), pp. 62-77, 2009. doi:10.1016/j.tecto.2009.03.013

[18] T. Flament, E. Berthier, and F. Remy, "Cascading water underneath Wilkes Land, East Antarctic ice sheet, observed using altimetry and digital elevation models," *The Cryosphere*, Copernicus vol. 8 (2), pp. 673-687, 2014. doi:10.5194/tc-8-673-2014

[19] Y. Li, Y. Lu, and M.J. Siegert, "Radar sounding confirms a hydrologically active deep-water subglacial lake in East Antarctica," *Frontiers of Earth Science*, vol.8, 294, 2020. doi: 10.3389/feart.2020.00294

[20] A. Rosenqvist, M. Shimada, N. Ito and M. Watanabe, "ALOS PALSAR: A Pathfinder Mission for Global-Scale Monitoring of the Environment," *IEEE Transactions on Geoscience and Remote Sensing*, vol. 45(11), pp. 3307-3316, 2007. doi: 10.1109/TGRS.2007.901027

FINAL REPORT OF THE 2ND RESEARCH ANNOUNCEMENT ON THE EARTH OBSERVATIONS(EO-RA2) "EVALUATION OF GLACIER MOVEMENT AND CRUSTAL REBOUND IN THE GREENLAND WITH A TIME-SERIES ANALYSIS USING MULTI-TEMPORAL ALOS-2 PALSAR-2 OBSERVATIONS"

"

PI No.: ER2A2N177

Sang-Hoon Hong [1]

[1] Department of Geological Sciences, Pusan National University, Pusan, 46241, Korea

1. DATA RETRIEVAL

We have ordered and downloaded SAR images through ALOS-2/ALOS User Interface Gateway (AUIG2) until the system does not operate anymore. After the transition to Globe Portal System (G-Portal), the download system will be improved shortly. We made the mistake of losing some quota by ordering the same scene because we were unfamiliar with the new download system. We believe the system could be significantly improved by maintenance in the next EO-RA3 stage.

2. DATA ARRANGEMENT USING RSP PATH CALCULATION

Our interferometric data processing chain automatically arranges the downloaded data by calculating the path number with the orbit accumulation number from the file name notation. In the case of the ALOS PALSAR image, we found the below equation to calculate the RSP path number and used it.

RSP Path for ALOS = [46 * orbit accumulation No. + 84] MOD 671 + 1 (1)

However, we could not find yet similar equation for the ALOS-2 PALSAR-2 image. After gathering the information on the ALOS-2 orbit from the JAXA website, the below equation could be written.

RSP Path for ALOS2 = [14 * orbit accumulation No. + 24] MOD 207 (2)

So far, the above equation allows us to calculate the path information of ALOS-2 correctly from the orbit accumulation No.

3. ALOS-2 PALSAR-2 STRIPMAP DINSAR ANALYSIS IN JAKOBSHAVN ISBRAE

The polar regions play an important role in the Earth system. Monitoring the glaciers from the space-based synthetic aperture radar observations could be very useful to understand the polar regions and forecast how much sea level will increase in the near future in the global warming environment. Differential radar interferometry (DInSAR) provides a displacement map with high spatial resolution from an earthquake, volcano, water level change in the mm to cm accuracy. However, When it is covered with glaciers or snow, it is challenging to apply DInSAR because the shift in topographic altitude over time is relatively severe compared to other land topography. L-band has a longer wavelength than X- and C-band, so it has advantages for coherence analysis with relatively high coherence in applying interferometry. To observe surface displacement in Jakobshavn Isbrae, we used the L-band ALOS-2 PALSAR-2 SAR observations from Sep-16, 2014, to Mar-26, 2019. DInSAR provides more precise surface displacement than the offset tracking method. Still, the rapidly changing glacial environment also affects the decorrelation between the two images, which can cause errors and limited measurement. As for the results, it was possible to have a relatively good coherence because the area where the surface displacement was only partially observed is the glacier's bedrock. As the glacier that was pressing the crust on the earth's surface melts and the weight of the surface decreases, it is possible that the surface rebounds and the displacement is observed. We want to apply the SBAS technique to monitor possible displacement of bedrock and estimate surface displacement would be validated with a global positioning system in the near future.

4. OFFSET TRACKING VELOCITY MAP USING ALOS-2 PALSAR-2 OBSERVATIONS IN JAKOBSHAVN ISBRAE

Ice velocity is an important factor in analyzing the effects of various glaciological applications and global environmental changes. Field surveys of ice velocity along glaciers are difficult to access, time-consuming and expensive, limiting long-term observations. Synthetic aperture radar (SAR), which has been used to observe various surface displacements, is also helpful in observing glacier displacements. Differential Radar Interferometry (DInSAR) can detect relative surface displacements with high spatial resolution from mm to cm accuracies at the surface, such as ground subsidence, volcanoes, water level changes, and earthquake. However, DInSAR application is often limited by the decorrelation effect due to much larger displacements than the radar wavelength, a large temporal baseline, volume decorrelation caused by snow melting or accumulation, etc. Therefore, the DInSAR technique has limitations in measuring the displacement at high rate glaciers. Offset tracking can be applied to glaciers because it estimates a direct displacement by measuring the same feature between two images. We measured the ice velocity using intensity offset tracking with an appropriate window patch size. In Figure 2, the areas with a consistent blue color are bedrock, compared with a flowing glacier. We tried to find a proper window patch size. Jakobshavn Isbrae had limitations in measuring the velocity at the glacier’s end due to the temporal baseline and the faster ice velocity approaching the terminus. We will estimate a time series of glacier movement using the STBAS technique based on speckle tracking in the near future.

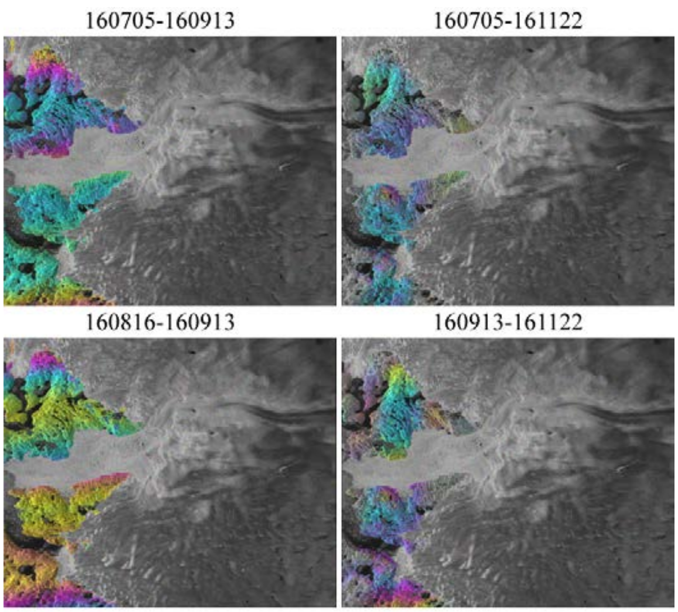

Fig. 1. Surface displacement map generated by using DInSAR. The interferograms show the displacement of a portion of the bedrock around which a fast-moving glacial region is not observed due to decorrelation.

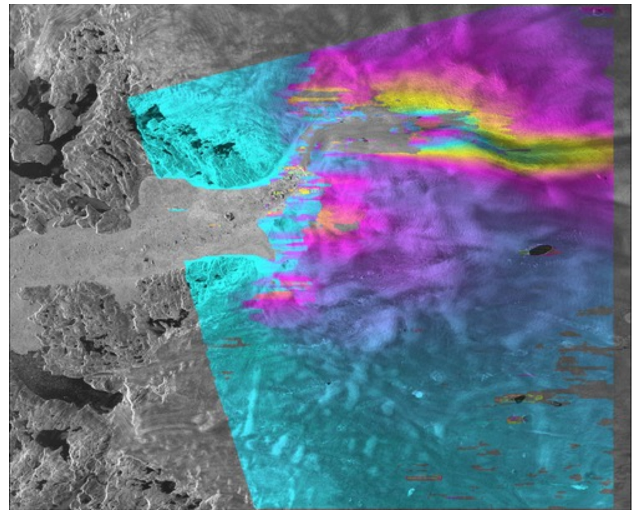

Fig. 2. Offset tracking ice velocity map of Aug 16-Sep 13, 2016, scaled from 0 to 200 m. The ice velocity is faster toward the terminus and the center of the mainstream.

3.11 Oceanography and coastal zone

SUBSIDENCE OF COASTAL RECLAMATION LAND MONITORING WITH ADVANCED INSAR TECHNIQUE

PI No.: ER2A2N082

Guang Liu [1,2], Jinghui Fan [3], Shiyong Yan [4], Jiahui Lin [1,2]

[1] University of Chinese Academy of Sciences, Beijing, China
[2] Institiue of Remote Sensing and Digital Earth, CAS, Beijing, China
[3] China Aero Geophysical Survey & Remote Sensing Centre for Land & Resources, Beijing, China
[4] China University of mining and Technology, Xuzhou, China

1. INTRODUCTION

Reclamation land has long history in human history, due to the special geographical conditions and complex geological environment of reclamation area, land subsidence always the most series problem of these areas. Due to the special geographical conditions and complex geological environment of reclamation area, land subsidence becomes most series problem of these area. It will cause elevation loss, uneven settlement and other issues which will have a direct impact on the industrial engineering, flood control, municipal pipeline roads and other facilities in the area, and indirectly threaten the stability of the construction and economic development of the region as well. The hazards of land subsidence mainly include the destruction of buildings and production facilities and the impact on the construction and resource development [1]–[3]. Interferometric Synthetic Aperture Radar (InSAR) technology integrates the principle of Synthetic Aperture Radar imaging and electromagnetic wave interference technology, and theoretically can obtain very accurate digital elevation model and surface deformation information of millimeter scale [4]–[6]. Compared with conventional methods such as GPS and level monitoring, InSAR can observe the target all day and all day. With wide coverage and high spatial resolution, continuous surface monitoring can be implemented in a large range. Compared with the accuracy it can achieve, the cost is low and it has the characteristics of stable data source. These characteristics show that if InSAR technology is used to monitor land subsidence, it can not only reduce the cost, but also monitor the land subsidence displacement in the whole radar image coverage area in a quasi-real-time and dynamic manner [7]–[9].

The research project under the ALOS Research Announcement (RA) by the Japan Aerospace Exploration Agency (JAXA), was intended to use L-band SAR data acquired from ALOS-1 and ALOS-2 satellites for earth surface subsidence monitoring [10]–[13]. Considering the phase loss correlation and atmospheric delay effect of conventional DInSAR, the time series InSAR technique which only tracks the targets with relatively stable scattering characteristics in the imaging region, while abandoning the targets with serious loss of correlation. These stable targets can maintain high coherence in a long-time interval and can also maintain high coherence when the spatial baseline distance exceeds the critical baseline distance, the interference image pairs with long baseline distance can be fully utilized to maximize the utilization of data. Therefore, by analyzing the time series of these stable points and eliminating the influence of the atmosphere, the subsidence of stable points can be accurately measured, so as to monitor the movement of the ground and accurately reflect the relative displacement of the monitored area. The studies carried out in this project mostly cover Tianjin Binghai and Zhongshan reclamation area, meanwhile we also studied the conventional InSAR and time series InSAR technique in monitoring the subsidence of mining area and landslide monitoring and some results are given in this report.

2. STUDY AREA

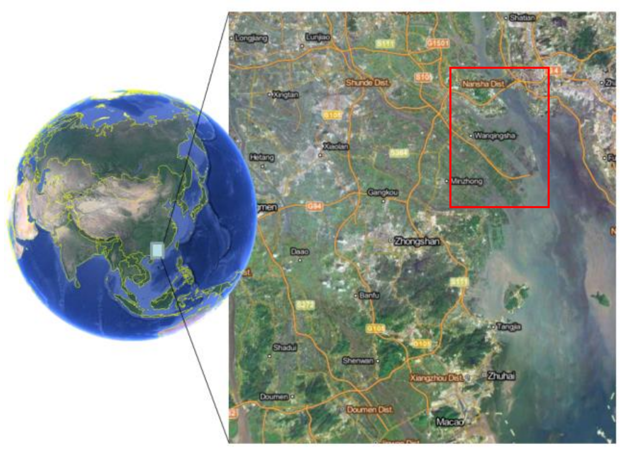

Fig. 1 The location of the study area which covers Zhongshan city area located at Pearl River Delta plain, Reclamation activities in the Pearl River Estuary can be traced back to the Song and Yuan Dynasties. From 1950 to 2014, nearly 930 km^2 was accumulated in the Pearl River Estuary area (Red rectangle).

The Pearl River Delta plain is a loose sediment accumulation plain. Under the influence of human engineering activities and natural consolidation, serious land subsidence has occurred in some areas, resulting in varying degrees of damage to houses, highways, Bridges, water conservancy facilities, embankments and underground pipe network facilities, and causing serious economic losses. A large area of soft soil is distributed in the plain area of the Pearl River Delta, and the distribution thickness is relatively large. The soft soil is mainly silt and silty soil deposited by Marine facies, followed by peat soil, silty sand, carbonized plant debris and shell fragments. Due to the low strength and high compressibility of soft soil, the soft soil foundation is particularly prone to settlement deformation under various loads, resulting in huge economic losses for engineering construction, as shown in Fig 1. The terrain in this region is relatively flat, mainly consisting of flat land, farmland, small towns, mountains, hills and platforms. From the perspective of geological structure conditions, there is a small scale fault at the southern foot of Wugui Mountain, which runs through Doumen District in a northeast-southwest direction. From the hydrogeological point of view, this area is adjacent to the South China Sea, with numerous internal river networks and abundant rainfall, which can be well supplied to the ground water.

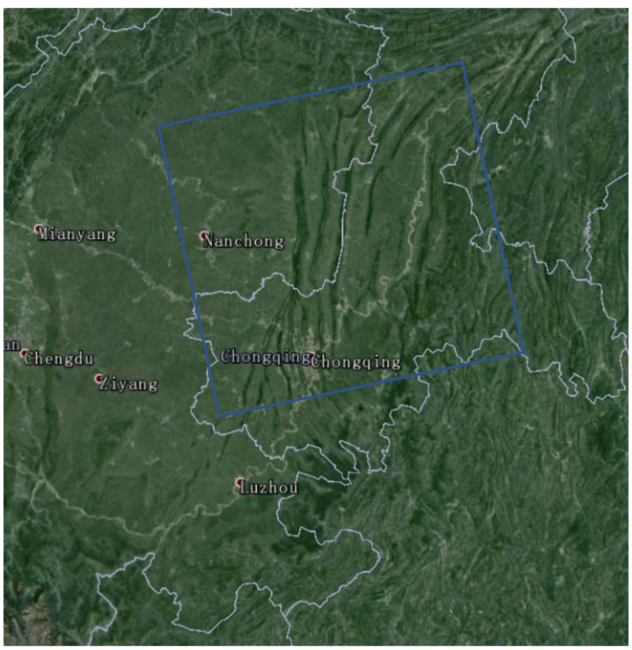

Fig. 2 The location of the study area which covers the Chongqing area. The yellow color area is about one scence of PALSAR-2 stripmap dataset.

Chongqing is one of the geological disaster areas in China with severe geological disasters such as landslides and landslides ranks first among the 70 cities in China. Chongqing is the largest industrial and commercial center in southwest China. Especially after chongqing becomes the municipality directly under the central government. Landslide, collapse and other geological disasters are mainly determined by geological structure, stratigraphic lithology, hydrology and meteorology. Chongqing is located in the eastern Sichuan basin, mountain and basin margin slope zone with deep creek, complex geological structure, the surface of the weak layer, and sometime with heavy rain, make the geological disasters in this area wide spreaded and great harm.

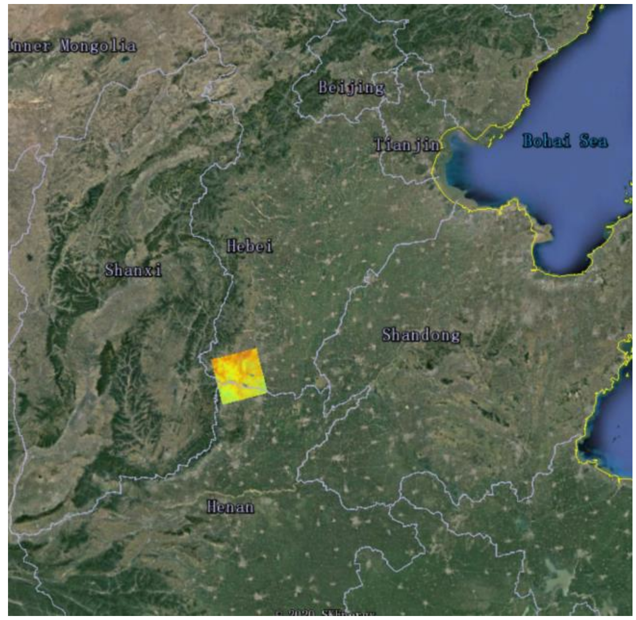

Fig. 3 The location of the study area which covers the Fengfeng mining area. The yellow color area is about one scence of PALSAR-2 stripmap dataset.

Hebei Fengfeng coal mine is an old mining area in China, with a history of more than 100 years. The west side of Fengfeng mining area is a mountain basin, and the east side is a sloping plain, with the highest elevation of 891 meters. Fengfeng mining area is located at the eastern foot of the south part of Taihang mountain, which is the transition zone between Taihang mountain and north China plain. There are more than 30 kinds of proven mineral resources in Fengfeng mining area, including coal, iron ore, China clay, bauxite, limestone, marble and gypsum. In order to reduce overcapacity in the coal industry and eliminate backward production capacity in the thermal power industry, the city have arranged the withdrawal of two coal mines and the shutdown of seven coal-fired power units. The SAR image covers the northern part of the Fengfeng mining area and part of the Wuan area. The central part is the remaining vein of the Taihang mountains, with the altitude of more than 800 meters at the highest and less than 100 meters at the lowest.

The area around bohai sea is to point to encircle bohai sea whole and yellow sea part of littoral area place forms extensive economy area. Land subsidence is one of the major environmental geological disasters in the bohai rim region, which includes tianjin, hebei and shandong provinces. Dongying City is a very serious subsidence area in this region. The coastline of Dongying City is 421 kilometers, and the coastal tidal flat area is 1159 square kilometers. The shallow underground brine reserves are about 1.16 billion cubic meters, and the estimated geological reserves of salt mines are 600 billion tons. According to the statistics of Dongying Salt Industry Association, the salt fields in Hekou District cover an area of 450,000 mu, with a raw salt production capacity of 2.55 million tons. With the strengthening of salt mining capacity and the increase of mining intensity, the ground subsidence of salt mining area is becoming more and more serious. Although there are few reports on land subsidence caused by salt mining, the cause and mechanism of subsidence have been studied clearly. With the increase of water gushing at the wellhead, the ground subsidence is intensified. When the ground surface subsidence reaches a certain degree, the cavity is gradually filled. When the stress redistribution makes it reach a new equilibrium.

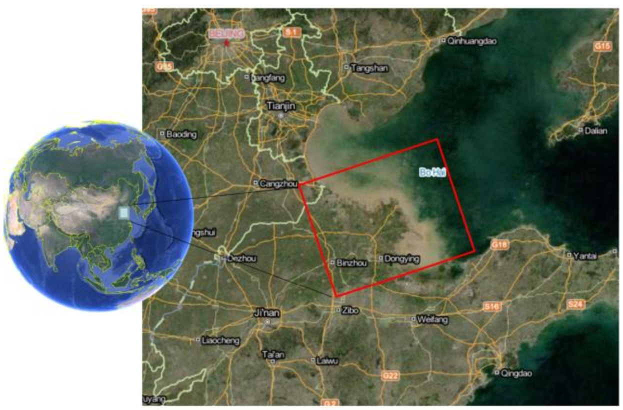

Fig. 4 The location of the study area which covers the Dongying city salt mining area.

3. DATA SET

The data set used consists of ALOS-1 and ALOS-2 SAR data, both datasets were acquired in strip map mode, part of them are bi-polarimetric dataset. The format of the single complex looking data of ALOS-1 and ALOS-2 has very small different, so most part of the code for read-out software for them are the same. This reduce lots of works to migrate code from ALOS-1 data to ALOS-2 data.

In this report, eight scences of ALOS-2 dataset acquired between Dec 2014 to May 2020 were used in Zhongshan area, the polarimetric mode is HH; nine scenes of ALOS-2 dataset acquired from 2015-Jul-11 to 2018-Oct-27 were obtained in Chongqing area, the polarimetric mode is HH, and the fly direction is ascending. While in Fengfeng area, we obtained 4 scenes of ALOS-1 data and 3 ALOS-2 data, both fly directions are ascending, and the polarimetric mode are HH. In Bohai sea area, four scenes of ALOS-2 data are obtained during 2015 to 2018 in ascending mode, and two interferogram are generated.

The external DEM used is from Shutter Radar Topography Mission (SRTM).

4. METHODOLOGY

The mining of underground coal will cause the goaf. Under the action of the gravity of the upper rock and soil layer itself, the deformation will occur in the upper part of the goaf, thus causing the subsidence of the mining area surface. Along with the mining of the long arm, the surface subsidence center will then move, in general, the fastest sedimentation generally formed in the goaf on the surface of the earth after a few months, then the sedimentation rate tends to be stable, in the initial stage, the surface subsidence may reach several centimeters every day, at this point you can ignore the influence of the atmosphere.

Since the SAR uses the synthetic method to image the surface, ideally the surface deformation of the mining area can be clearly reflected on the radar interferogram, so as to realize the monitoring of the surface subsidence or underground mining activities [13]–[16]. The SAR interferometric phase map contains information about the difference in the length of the propagation path from the radar antenna to the target during two imaging periods. The length of the propagation path is generally affected by the change of satellite measurement position, the change of measurement time and the change of atmospheric conditions. In the case of ignoring the influence of the atmosphere, the deformation interference phase can be obtained by removing the topographic interference phase caused by the change of satellite measurement position through a certain algorithm, so as to realize the monitoring of the surface deformation. For C-band radar sensors, such as the ASAR SAR sensors carried by ERS and ENVISAT satellites, the one-period variation of the deformation interference phase represents the surface variation of 2.8cm. For L-band radar sensors such as PALSAR deformation interference phase change one period corresponds to the surface change of 11.75 cm.

$$\Delta r = \frac{\lambda}{4\pi}\left(\varphi_{ifg} - \varphi_{ifg}^{simulation}\right) \qquad (1)$$

where with λ being the wavelength of the SAR sensor, φ is the phase on the interferogram and the simulated terrain phase.

There are various SBAS processing strategies. In this study we use Small BaselineSet (SBAS) method [17]–[20]. First N scenes of SAR images are coregistrated on the super master image, then the images pairs are formed so as to obtain interferograms, here we should take care that the InSAR pairs with heavy atmospheric effect should be removed from the list. For each interferogram pair, the master image acquisition time is less than the slave image acquisition time for later processing convenience. Then the first round we could select possible stable point with amplitude dispersive index, and with the selected candidates, we estimated the atmospheric and deformation together with the elevation error of the points. In common situation, the phase model could write as:

$$\varphi_{\text{model}}(x) = -\frac{4\pi}{\lambda}\left(v(x)\delta t + \frac{B_k}{r\sin\theta}\delta h\right)$$

Then stable points candidates with significant deviation are removed from the stable point's subset. The next step is to remove the height error phase of each point from its observed phase. The residual phase is then containing the spatially high pass topographic error and the noises along with the displacement phase information. After this processing we could be estimated the ensemble phase coherence so as to estimate the error of the results, and select the possible stable points, after that, the networks are established and the deformation are estimated at last. In this study we only estimated the linear deformation.

5. EXPERIMENTS AND RESULTS

Fig. 5 The SBAS deformation results of Zhongshan City, most of the area is relatively stable while the reclamation area in the upper right corner has obvious land subsidence.

In Zhongshan region, 8 scenes ALOS-2 SAR data are used and the image acquired between December 2014 and May 2020 are selected. The climate in this region is humid and the atmospheric phase screen is obvious. From the result of time series InSAR processing, the land subsidence is concentrated in the southwest corner of the thick soft soil layer and the northeast corner of reclamation. The maximum subsidence speed of this region is more than 50mm/year. This result is consistent with that of ground monitoring. From the optical image, it can be seen that the highly coherent target points of time series InSAR are mainly concentrated on the cofferdam in the reclamation area, in the reclaimed area, it is difficult to obtain the target point with high coherence because of the obvious vegetation cover.

Fig. 6 The Reclamation activities area in the Pearl River Estuary.

In Chongqing region, 9 scenes ALOS-2 SAR data are used and the image acquired in November 2017 is selected as the master image. Fig.7 shows the baseline distribution of the images, the whole period is about three years of the acquired ALOS-2 dataset, and the maximum perpendicular baseline is about 300 meters. Generally speaking, the spatial and temporal baseline distribution is relatively uniform, but the data volume is small.

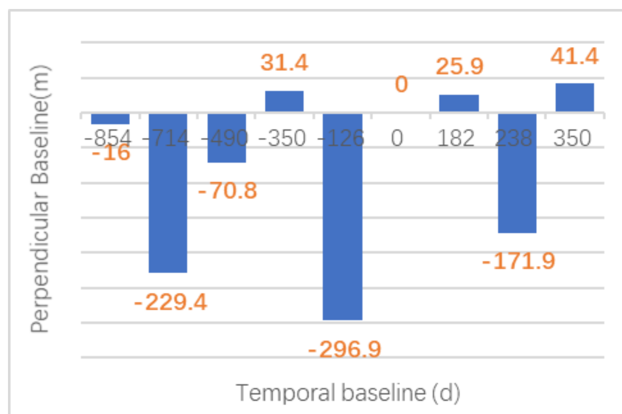

Fig. 7 The baseline distribution of the ALOS-2 images acquired in Chongqing area.

A total of 72 SAR interferogram pairs can be formed by using 9 scenes SAR images, some of which are of low quality, and 30 of which have high quality are retained after selection. To a certain extent L-band SAR can keep good coherence within ground changes in 2 to 3 years. During the process we found that although the accuracy of the orbit data is ok, due to the large time interval of the provided orbit data, it is easy to be unstable in the process of interpolation, which is easy to cause errors of the orbit, which has a certain impact on the unwrap. As the terrain in this area is not flat, it is not convenient to carry out the analysis of orbital characteristics, which may be considered in the later work.

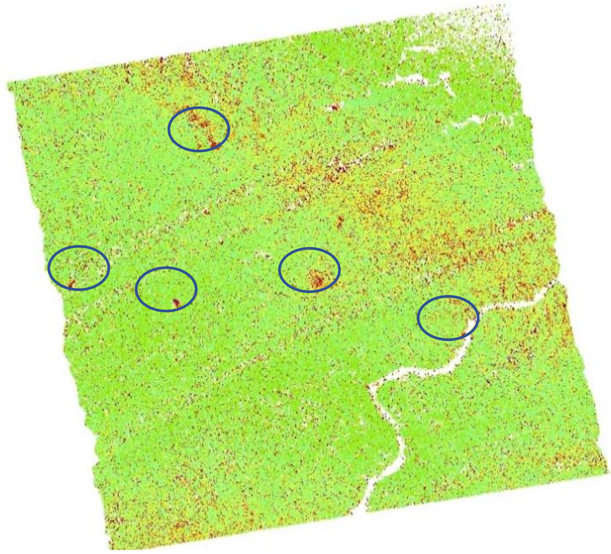

Fig. 8 The SBAS deformation results around Chongqing City, where the area is relatively stable without large area subsidence.

The whole area of the image coverage is about 60 km south-north and 60 km east to west. On the whole, the situation of the whole region is relatively stable. There are 5 obvious surface movement areas, and the movement rate is basically within 3 centimeters per year.

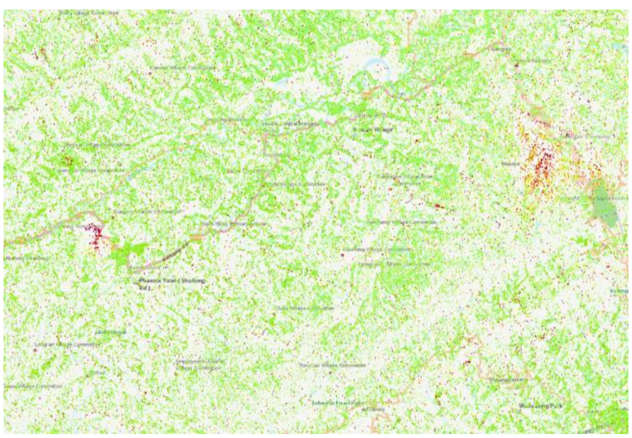

Fig. 9 The enlarge image of the middle region in the central area of image.

Figure 9 is an enlarged image of two deformation regions in the central region. The deformation region on the right is located in JiangYin village. This sliding region is mainly located on a relatively large terrace with an area of about 0.5 square kilometers. The left deformation area is XianYing village, we found that the topography in this area is flat and with an altitude difference of about 100 meters, it may not cause rapid movement and disaster.

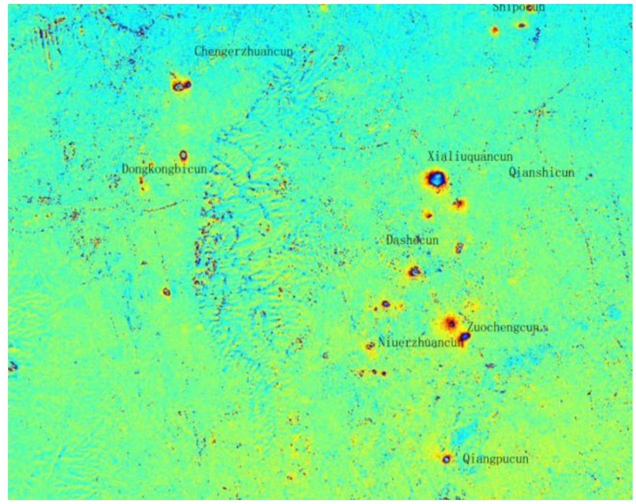

Fig. 10 (a) The DInSAR interferogram of PALSAR-1 data which acquired in 2007-Dec-15 and 2008-Jan-30 near XiangtangShan area.

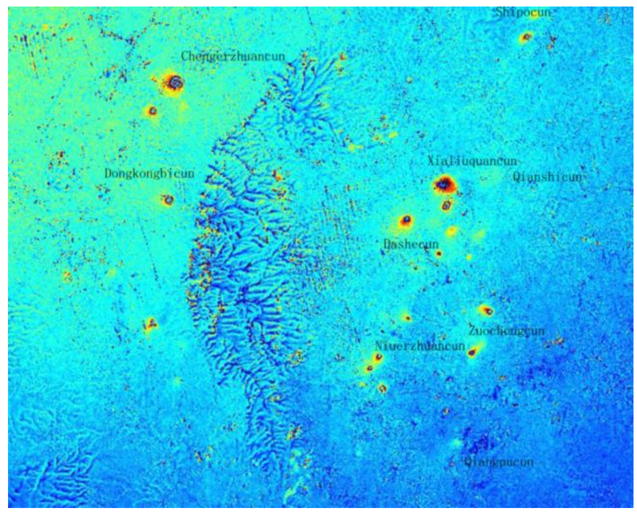

Fig. 10 (b) The DInSAR interferogram of PALSAR-1 data which acquired in 2009-Dec-20 and 2010-Feb-04 near XiangtangShan area.

In Fengfeng mine area, mining activities is relatively concentrated, we chose the northern area which located surrounding XiangtangShan in the town of Cishan, the extent of the area is about 30 kilometers east-west, and 30 kilometers north-south. On the whole, for PALSAR data, the accuracy of the orbital data is acceptable, which can remove the flat ground interference phase and topographic phase, and there is no obvious residual phase information on the whole, which provides a favorable condition for the interpretation of the mining settlement. Nevertheless, we can see that the topographic phase in figure 10 (b) is relatively obvious and has a relatively small orbital influence. Meanwhile, we can see that for figure 10 a-c with a relatively short time baseline, the coherence is significantly higher than that of figure 10 (d) with a time baseline of 5 months.

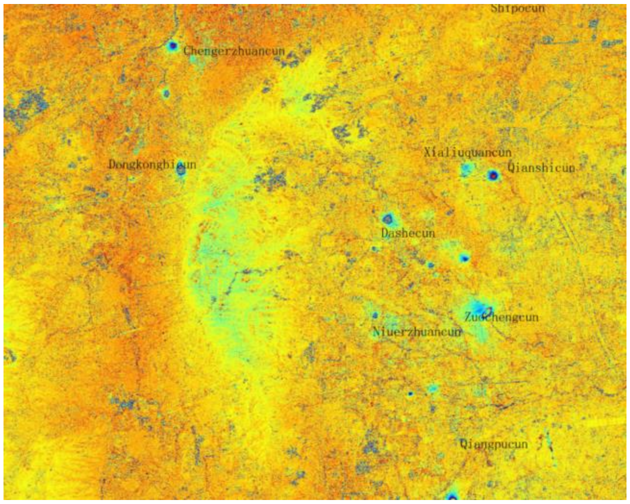

Fig. 10 (c) The DInSAR interferogram of PALSAR-2 data which acquired in 2018-Nov-04 and 2018-Dec-16 near XiangtangShan area.

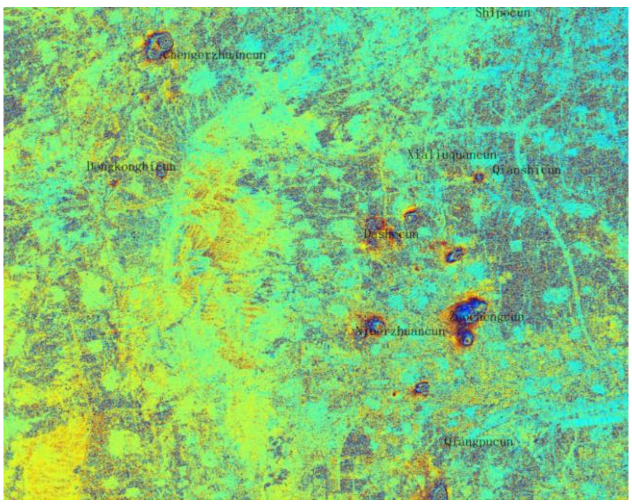

Fig. 10 (d) The DInSAR interferogram of PALSAR-2 data which acquired in 2018-Dec-16 and 2019-May-19 near XiangtangShan area.

In XiangtangShan area, the extraction activities of the overall trend are being small. From Fig.10 (a) and Fig.10 (b) about 20 active mine area or so can be clearly identified, and they are almost the same in year 2008 and 2010, the exploitation of the most rapid mining area is located in Xialiuquancun area, then the mining area in Chengerzhuancun, from Fig.10(a) and Fig.10(b) we can see that the ground subsidence of these two mine area caused by mining beyond 10 cm per month. And in 2018, from Fig.10 (c) and Fig.10 (d) we can see that the extraction activities were reduced to 10 or so, and from Fig.10 (d) we could see clear deformation pattern due to extraction, the up left area show about half a meter's deformation due to extraction. And the low right area the mine deformation of two work-plane is contacting after five months.

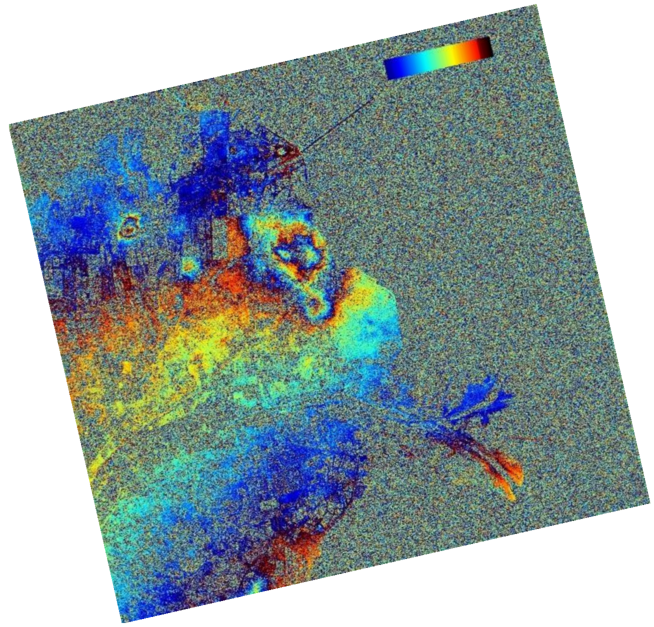

Fig. 11 (a) The DInSAR interferogram of PALSAR-2 data which acquired in 2015-Oct and 2016-Jul of Dongying.

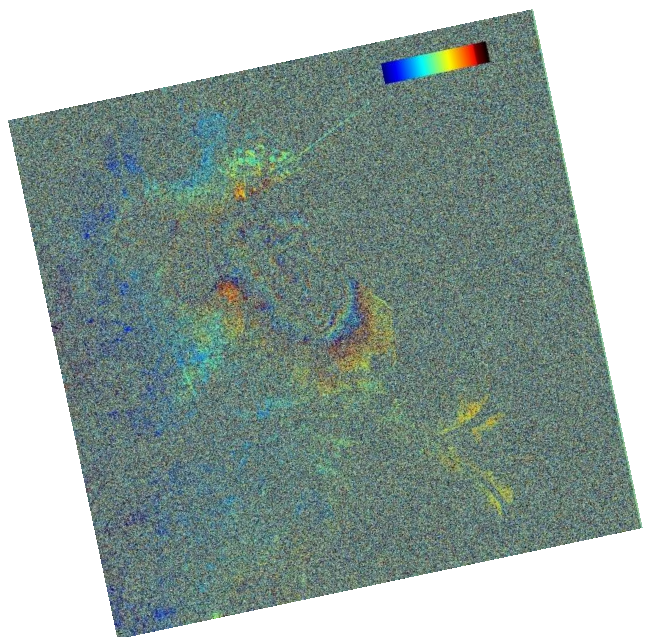

Fig. 11 (b) The DInSAR interferogram of PALSAR-2 data which acquired in 2017-Mar and 2018-Nov of Dongying.

Around bohai sea, Dongying area is focused. The main factors affecting the land subsidence in Dongying city are the long-term exploitation of oil, natural resources such as salt and gas, and deep groundwater, which makes the strata stress increase and produce compression. Neotectonic movement, global sea level rise, natural subsidence of under consolidated soil and ground load are the secondary influencing factors of land subsidence.

There are 4 scenes ALOS2 images were acquired, in 201510-201607 and 201703-201811 separately. Both the spatial baseline is about 100 m, while due to the temporal baseline is 266 days and 588 days each, we could see that not only the correlation has large different, but also the subsidence pattern. There are three obvious subsidence center large than 40cm/yr in Fig 11 (a), and due to temporal decorrelation the Fig 11 (b) show pattern not very clear, but the range of the interferogram is still visible. This shows that for large deformation the temporal baseline should be carefully select so as to make the interferogram pattern to be clear to extract information.

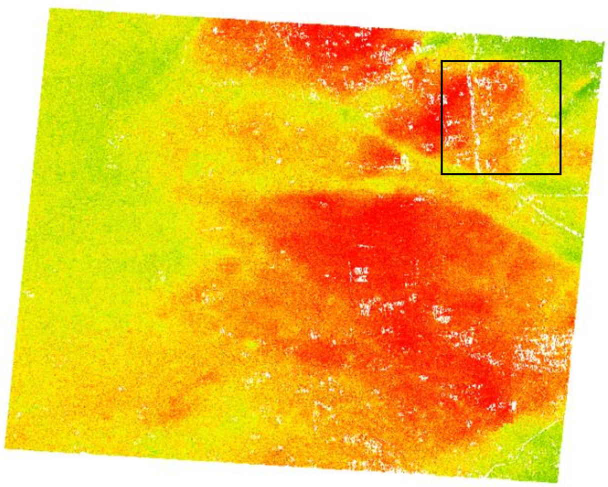

Fig. 12 (a) The SBAS deformation results at the east part of Beijing with PALSAR-2 spotlight dataset which acquired in 2014 and 2018.

Fig. 12 (b) The enlarge image of the east-north region in the area of the image.

Geohazards occur not only in remote areas but also in highly populated cities. In the framework of the Dragon-4 32365 Project, this paper presents the main results and the major conclusions derived from an extensive exploitation of Sentinel-1, ALOS-2 (Advanced Land Observing Satellite 2) , GF-3 (GaoFen Satellite 3) , and latest launched SAR (Synthetic Aperture Radar) , together with methods that allow the evaluation of their importance for various geohazards[21]. Here we will show some new results especially with ALOS-2 dataset.

There are 10 scenes ALOS2 spotlight images were acquired, in 201410-201808. All the spatial baseline is within 500 m, this combination of baselines can be relatively coherent. From the results, firstly, we find that more stable points can be obtained by using the high-resolution data of ALOS2, compared with GaoFen-3 and Sentinel-1 results, which is directly related to the high resolution of the data. Meanwhile, as can be seen from the results of Figure 12 (a), the area with large deformation is obviously divided into different parts, which may be related to the local microgeological structure. It is well known that groundwater mining in the east of Beijing has caused a certain extent of surface subsidence. Although this subsidence occurs in a large area, the deformation of different small blocks is different. And this differential deformation between the different blocks in turn reflects the boundaries between the blocks.

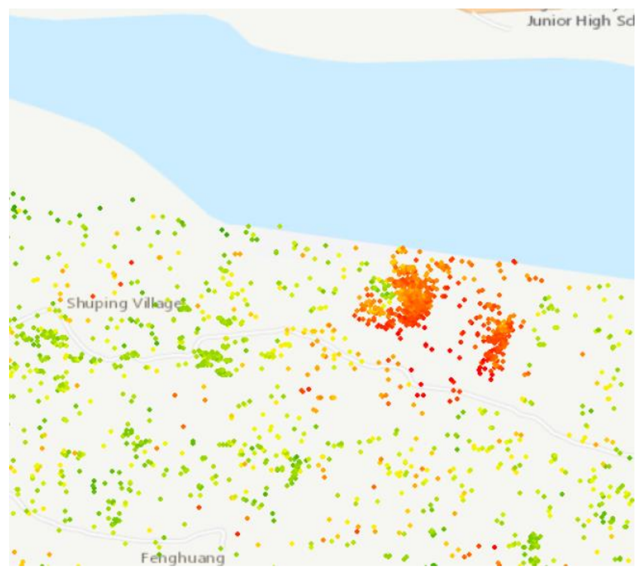

Fig. 13 The SBAS deformation results of Shuping landslide in Three Gorges Reservoir area.

As the largest water conservation project in China, the Three Gorges Reservoir has attracted a lot of attention. Shuping landslide, is located on the southern bank along the Yangtze River. The landslide belongs to Zigui County in the HuBei Province. The Shuping landslide is a large accumulation landslide with obvious deformation every flood season, posing a major threat to the Three Gorges Project and the life and property safety of local residents. To ensure safety, a landslide treatment project for the Shuping landslide began in August 2014. We have obtained TerraSAR-X data in the spring of 2012 in this area, and through time series InSAR analysis, we found that the Shuping landslide area movement speed is quite large, with the maximum movement area speed reaching 37mm/month [6]. In this report, we obtained the data of ALOS2 after treatment. From 201507 to 202105, through time series analysis, we found that the sliding speed of the landslide area has basically decreased to less than 50mm/year. The results show that the landslide control work has obtained a relatively obvious effect. We also use the sentinel-1 data for comparison, but due to the problem of de-correlation, no good results are obtained.

6. CONCLUSIONS

In this study, we used time series interferometry method to monitor land subsidence of reclamation area and some other area, in the Zhongshan region, the maximum subsidence speed of this region is more than 50mm/year, and the highly coherent target points are mainly concentrated on the cofferdam in the reclamation area. For Chongqing city, where the terrain is complicated and the elevation error is large, we found that the land subsidence in this area is not obvious, however there exists a few areas with slow subsidence, the deformation area needs further observing in the later works. In Fengfeng mine area, the land subsidence mainly comes from the coal mining, and as a result, there has been less activity after 2017 due to the regulation of mining. And around Bohai area, the Dongying city has subsidence due to salt mining extraction and has a large deformation velocity to 40 cm/yr, however the PALSAR-2 could catch the deformation pattern clearly. In general, L-band radar data can be used to obtain better results not only in mountainous areas, but also in non-urban areas. More details of the deformation can be seen from the enlarged image. In the middle of Figure 9(b) is Wenyu River. The deformation of the east side and the west side of the river are different.

7. REFERENCES

[1] J. Geertsma, “A basic theory of subsidence due to reservoir compaction: the homogeneous case,” *Verh. Van Het K. Ned. Geol. Mijnbouwkd. Genoot.*, vol. 28, pp. 43–62, 1973.

[2] G. Gambolati and R. A. Freeze, “Mathematical Simulation of the Subsidence of Venice,” *Water Resour. Res.*, vol. 9, no. 3, pp. 721–733, 1973.

[3] J. Geertsma and G. van Opstal, “A numerical technique for predicting subsidence above compacting reservoirs, based on the nucleus of strain concept,” *Verh. Van Het K. Ned. Geol. Mijnbouwkd. Genoot.*, vol. 28, pp. 63–78, 1973.

[4] L. C. Graham, “Synthetic Interferometer Radar for Topographic Mapping,” *Proc. IEEE*, vol. 62, pp. 763–768, 1974.

[5] H. A. Zebker and R. M. Goldstein, “Topographic Mapping from Interferometric Synthetic Aperture Radar Observations,” *J. Geophys. Res.*, vol. 91, no. B5, pp. 4993–4999, 1986.

[6] G. Liu *et al.*, “Monitoring the slope movement of the Shuping landslide in the Three Gorges Reservoir of China, using X-band time series SAR interferometry,” *Adv. Space Res.*, vol. 57, no. 12, pp. 2487–2495, Jun. 2016, doi: 10.1016/j.asr.2016.03.043.

[7] D. Small, F. Holecz, and D. Nüesch, “Combination of ascending/descending {ERS-1} {INSAR} data for calibration and validation,” in *International Geoscience and Remote Sensing Symposium, Florence, Italy, 10–14 July 1995*, 1995, pp. 553–555.

[8] R. Bamler and R. Hanssen, “Decorrelation Induced by Interpolation Errors in {InSAR} Processing,” in *International Geoscience and Remote Sensing Symposium, Singapore, 3–8 Aug 1997*, 1997, pp. 1710–1712.

[9] S. Usai and R. Hanssen, “Long time scale {INSAR} by means of high coherence features,” in *Third ERS Symposium—Space at the Service of our Environment, Florence, Italy, 17–21 March 1997*, 1997, pp. 225–228. [Online]. Available: http://enterprise.lr.tudelft.nl/doris/Literature/usai97.pdf

[10] J. W. Kim *et al.*, “Integrated analysis of PALSAR/Radarsat-1 InSAR and ENVISAT altimeter data for mapping of absolute water level changes in Louisiana wetlands,” *Remote Sens. Environ.*, vol. 113, no. 11, pp. 2356–2365, 2009, doi: 10.1016/j.rse.2009.06.014.

[11] C. J. Thiel, C. Thiel, and C. C. Schmullius, “Operational Large-Area Forest Monitoring in Siberia Using ALOS PALSAR Summer Intensities and Winter Coherence,” *Ieee Trans. Geosci. Remote Sens.*, vol. 47, no. 12, pp. 3993–4000, 2009, doi: 10.1109/TGRS.2009.2021469.

[12] S. Suzuki, Y. Kankaku, and Y. Osawa, *Development status of PALSAR-2 onboard ALOS-2*, vol. 8176. Spie-int Soc Optical Engineering, 2011. doi: 10.1117/12.897705.

[13] G. Liu, R. F. Hanssen, H. Guo, H. Yue, and Z. Perski, “Nonlinear Model for InSAR Baseline Error,” *IEEE Trans. Geosci. Remote Sens.*, vol. 54, no. 9, pp. 5341–5351, Sep. 2016, doi: 10.1109/TGRS.2016.2561305.

[14] S. Jonsson, H. Zebker, P. Segall, and F. Amelung, “Fault slip distribution of the 1999 M-w 7.1 Hector Mine, California, earthquake, estimated from satellite radar and GPS measurements,” *Bull. Seismol. Soc. Am.*, vol. 92, no. 4, pp. 1377–1389, 2002, doi: 10.1785/0120000922.

[15] H. Yue *et al.*, “Coal mining induced land subsidence monitoring using multiband spaceborne differential interferometric synthetic aperture radar data,” *J. Appl. Remote Sens.*, vol. 5, no. 1, p. 053518, 2011, doi: 10.1117/1.3571038.

[16] Zbigniew Perski, “Applicability of ERS-1 and ERS-2 InSAR for land subsidence monitoring in the Silesian coal mining region, Poland,” presented at the ISPRS Commission VII, Working Group 6, 1998, vol. XXXII, pp. 555–558.

[17] J. Fan *et al.*, "Monitoring the deformation of Shuping landslide with TerraSAR-x spotlight images," Jul. 2013, pp. 29–32. doi: 10.1109/IGARSS.2013.6721084.
[18] Zbigniew Perski, Freek van Leijen, and Ramon Hanssen, "Applicability of psinsar for building hazard identification. Study of the 29 January 2006 Katowice exhibition hall collapse and the 24 February 2006 Moscow basmanny market collapse," presented at the Proc. of Envisat Symposium 2007, Montreux, Switzerland, 2007.
[19] C. Y. Zhao, Q. Zhang, C. S. Yang, and W. B. Zou, "Integration of MODIS data and Short Baseline Subset (SBAS) technique for land subsidence monitoring in Datong, China," *J. Geodyn.*, vol. 52, no. 1, pp. 16–23, 2011, doi: 10.1016/j.jog.2010.11.004.
[20] L. Zhang, D. Q. Ge, X. F. Guo, Y. Wang, M. Li, and X. D. Zhang, *Seasonal Subsidence Retrieval With Coherent Point Target Sar Interferometry: A Case Study In Dezhou City*. Ieee, 2011.
[21] G. LIU *et al.*, "Land Surface Displacement Geohazards Monitoring Using Multi-temporal In-SAR Techniques," 测绘学报（英文版）, vol. 4, no. 1, pp. 77–87, 2021.

APPENDIX

LIU, G., ZBIGNIEW, P., STEFANO, S., BENNI, T., Lixin WU, Jinghui FAN, Shibiao BAI, Lianhuan WEI, Shiyong YAN, Rui SONG, Bignami CHRISTIAN, Tolomei CRIS-TIANO, Stefan SCHNEIDERBAUER, and João Sousa JOAQUIM. "Land Surface Displacement Geohazards Monitoring Using Multi-Temporal In-SAR Techniques." Journal of Geodesy and Geoinformation Science, Vol. 4, No. 1, 2021, pp. 77–87.

COMMERCIAL VESSELS DETECTION AND CLASSIFICATION USING DEEP LEARNING WITH ALOS-2 IMAGERY

PI No.: ER2A2N090

Bo Zhang [1,2,3], Xin Lin [1,2,3], Chao Wang [1,2,3], Hong Zhang [1,2,3], Tianyang Li [1,2,3], Qian Wu [1,2,3]

[1] Key Laboratory of Digital Earth Science, Aerospace Information Research Institute, Chinese Academy of Sciences, Beijing 100094, China

[2] International Research Center of Big Data for Sustainable Development Goals, Beijing 100094, China

[3] College of Resources and Environment, University of Chinese Academy of Sciences, Beijing 100049, China

1. INTRODUCTION

SAR (Synthetic Aperture Radar) is an active sensor with all-day, all-weather, high resolution and wide coverage, which has been widely used in marine resource monitoring, ship detection and other fields. As an end-to-end model, the deep network can automatically perform feature extraction and carry out detection work with far better performance than traditional detection methods, showing great application potential. Therefore, the research on SAR image ship detection based on deep learning is developing rapidly.

In recent years, researchers have done a lot of work to demonstrate the superiority of deep networks that search for potential regions containing targets by using the intersection ratio of a predefined anchor frame to a sample ship bounding box and fitting the target bounding box by the network self-learning parameter offsets. To improve the detection accuracy, the existing methods mainly include changing the feature extraction (backbone) structure [1,2], adding attention mechanism [3,4], and optimizing the loss function [5].

However, the current deep network-based detection methods are usually trained and tested on fixed data sets, with fewer experiments for open scenes, and the process of ship detection for the whole SAR image is not clear enough. Therefore, this report designs a set of detection process for the whole SAR image, and conducts preliminary experiments of cross-band simulation of open scenes using L-band ALOS data, which is useful for subsequent research The report provides a reference for the direction of subsequent research.

2. METHOD

Deep detection network is mainly divided into one-stage network and two-stage network, the two-stage network mainly performs candidate region generation first and then classifies by CNN, which has higher accuracy but higher computational cost and long inference time. The single-stage network extracts features directly in the network to predict object categories and locations, which gains a huge speed boost compared to two-stage detection and is only slightly less accurate. YOLO, as one of the representatives, is known for its light weight, flexibility, and fast detection speed. And YOLOv5 is the newer versions, has improved the detection accuracy compared to its predecessor, and at the same time, it is much faster and more flexible, and there are several versions available for different data sizes to facilitate deployment and improvement.

In summary, YOLOv5 was selected as the detection network. The specific network structure is shown in Figure 1. It consists of four main parts: Input, Backbone, Neck, and Head parts (also known as the prediction part). The input side uses random Mosaic, data enhancement techniques and adaptive anchor frame calculation and adaptive image scaling to expand the amount of sample features and improve the network robustness, and adaptive anchor frame calculation is used to automatically match different training sets. The Neck part adopts FPN+PAN structure, FPN is the feature pyramid network, which is used to extract and merge features at different levels, and PAN structure is mainly to copy the features at the bottom of FPN and perform secondary downsampling, and then fuse the extracted features. The main part is to calculate the classification and regression loss to complete the prediction.

In order to complete the ship detection for a whole SAR image, the corresponding detection system is designed, and the specific detection process is described as follows:

(1) The whole image is divided into blocks, and regional sea clutter modeling is performed for each block, with five alternative types of sea clutter: G0 distribution, K distribution, Gaussian distribution, Rayleigh distribution, and Weibull distribution.

(2) CFAR threshold segmentation is performed for different blocks to initially filter out the suspected targets with high intensity values.

(3) Slicing is performed with the suspected target as the center, and it is linearly stretched and output as JPG format image.

(4) The chips are fed into the trained YOLOv5 network for detection.

(5) The corresponding detection results are generated after intersection-and-comparison calculation and removal of overlapping detection frames.

3. EXPERIMENT AND ANALYSIS

The GF3 satellite 1-10m resolution images in C-band are used to make ship target chips, which are fed into the constructed YOLOv5 for training and retaining the best weight parameters. The test images are the provided L-band ALOS PALSAR 2 images, and a total of 2 scenes are selected, which have pure sea surface areas, and these

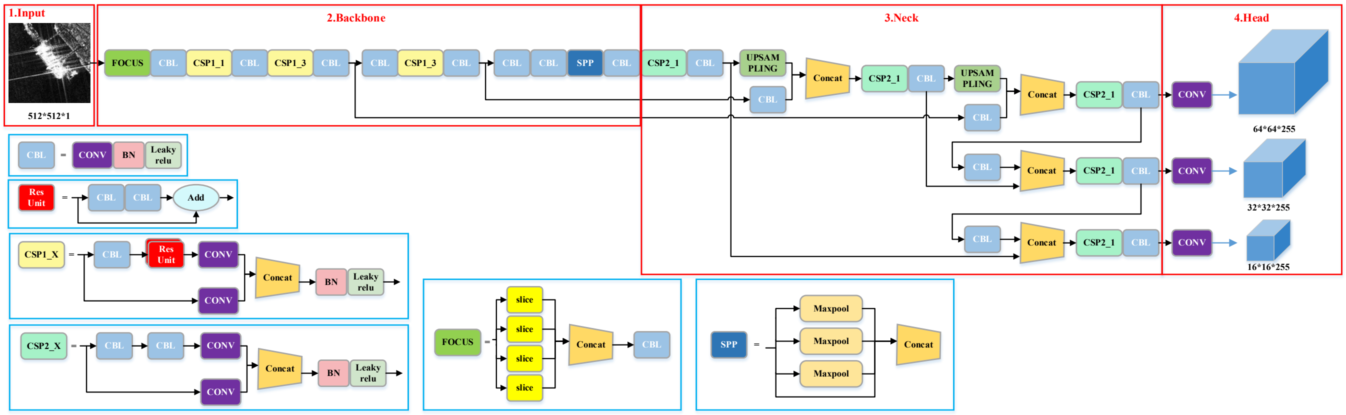

Fig. 1 Flowchart of YOLOv5.

images containing confusingly small islands, as shown in Fig. 2. The resolution of image(a) is 5m, and the resolution of image(b) is 12m. The number and location of ships in each view image are determined by visual interpretation.There are 34 ships in image(a),86 ships in image(b).

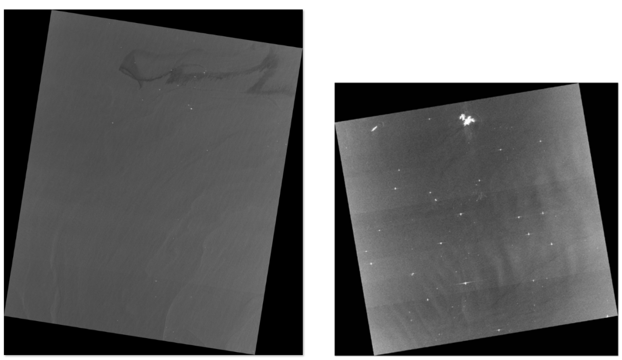

(a) (b)

Fig. 2 SAR images used in test. (a) the image containing pure sea surface (b)the image containing small islands

In order to recognize the detection effectiveness of the constructed system for each image as a whole, metrics such as recall(R) and precision(P) are introduced. They are defined as follows:

$$P = \frac{TP}{TP + FP}; R = \frac{TP}{NP} \tag{1}$$

where TP is the number of the correctly detected target, FP is the number of false alarm, and NP is the number of ground truths. These are two of the more important indicators in the detection experiments, but this report is more focused on selecting more typical regions and targets for analysis, to provide reference for subsequent research on cross-band open scenes.

The test accuracy indexes of the two images are shown in Table 1, and the detection accuracy can be above 90%, but the recall rate is low, indicating that there are more missed detections. Through observation and analysis, the ship characteristics of L-band and C-band have certain differences, which may be due to the different wavelengths of electromagnetic waves in the two bands, and there is a certain gap in the characterization ability of the target.How to migrate the network to different bands of data for detection will be one of the important aspects of cross-band detection research in the future.

TABLE I
Overview of each image indicator

	P	R
Image(a)	1	0.8235
Image(b)	0.9114	0.8372

Meanwhile, some typical targets and regions in the image are analyzed for their detection. Fig. 3 shows the slices of Image (b) in Fig. 1. after preliminary extraction by CFAR, while the detected ships are assigned detection labels. For the detection of the island in (a), a false alarm target appears, and a small part of the island is misclassified as a ship, which is due to the presence of small and poorly resolved ships in the training dataset, where the texture information is not obvious enough, but the target shape features are more similar, resulting in false detection.The small island in (b) was recognized as a suspected target during CFAR detection, but was not misdetected when fed into the network for detection, and both ships in (c) were detected, indicating that the network has some generalization capability, but further in-depth research is needed to address the problem of misdetection.

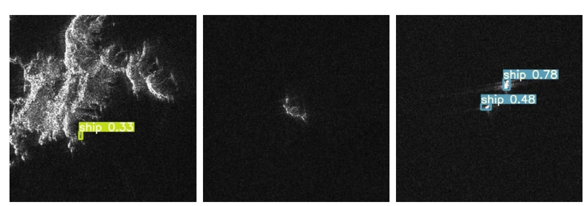

(a) (b) (c)

Fig. 3 Partial detection of slices in images. (a) the chip containing island (b)the chip containing small island (c) the chip containing ships

4. CONCLUSION

This report designs a detection process for the whole SAR image based on YOLOv5. By training the depth network on the C-band dataset and using the L-band ALOS image as the detection image, the ship detection experiments in cross-band open scenes are conducted. The improvement in detection efficiency of deep networks is considerable and the accuracy improvement is large compared to traditional methods, but the performance of networks trained and tested in the same distribution of data sets is poor for open scenarios.According to the analysis of the detection accuracy index and the detection effect of typical regions, it can be learned that just simply using the depth network for ship detection in cross-band open scenes has a low recall rate, more missed detections, and a large risk of false detection, mainly because the ship characteristics are different in different bands, and the knowledge learned by the network cannot be directly applied to open scenes, so how to combine the scattering mechanism of SAR and migrate the network Therefore, how to combine the scattering mechanism of SAR and migrate the network to the data of different bands for detection will be one of the important aspects of cross-band open scene detection research in the future.

5. REFERENCES

[1] Z. Cui, Q. Li, Z. Cao, and N. Liu, “Dense Attention Pyramid Networks for Multi-Scale Ship Detection in SAR Images,” *Journal*, IEEE Transactions on Geoscience and Remote Sensing, Vol. 57 Issue 11, pp. 8983-8997, 2019.

[2] T. Zhang, X. Zhang, and X. Ke, “Quad-FPN: A novel quad feature pyramid network for SAR ship detection,” *Journal*, Remote Sensing, Vol. 13 Issue 14, pp. 2771, 2021.

[3] Z. Wang, B. Wang, and N. Xu, “SAR ship detection in complex background based on multi-feature fusion and non-local channel attention mechanism,” *Journal*, International Journal of Remote Sensing, Vol. 42 Issue 19, pp. 7519-7550, 2021.

[4] Y. Zhao, L. Zhao, B. Xiong, and G. Kuang, “Attention receptive pyramid network for ship detection in SAR images,” *Journal*, IEEE Journal of Selected Topics in Applied Earth Observations and Remote Sensing, Vol. 13, pp. 2738-2756, 2020.

[5] J. Wang, C. Lu, and W. Jiang, “Simultaneous Ship Detection and Orientation Estimation in SAR Images Based on Attention Module and Angle Regression,” *Journal*, Sensors (Basel), Vol. 18 Issue 9, 2018.

CHARACTERISTICS OF SEA SURFACE WIND FIELDS IN THE SEAS AROUND THE KOREAN PENINSULA FROM PALSAR DATA AND AIR-SEA INTERACTION

PI No.: ER2A2N124
Kyung-Ae Park [1], Jae-Cheol Jang [2]

[1] Department of Earth Science Education, Seoul National University
[2] Department of Science Education, Seoul National University

1. INTRODUCTION

Sea surface wind is an important variable in studying air-sea interactions and oceanic phenomena in the marine-atmospheric boundary layer (MABL). Winds affect climate change and the marine environment, and as interest in climate change increases, frequent and accurate observations to increase the reliability of wind turbines have been emphasized. Satellite synthetic aperture radar (SAR) sensors have provided high-resolution observations, allowing the investigation of wind fields in coastal areas that cannot be observed by satellite scatterometers. In particular, the Korean Peninsula exhibits varied marine environmental conditions; thus, this region is suitable for evaluating the performance of SAR-measured sea surface winds and investigating various atmospheric-oceanic interactions. Therefore, many studies have used SAR to calculate sea surface wind, understand the characteristics of the wind field, and analyze ocean phenomena in the coastal areas of the Korean Peninsula [1-3].

Because the relative wind direction is necessary to examine winds using SAR, these data must obtained from an external source, such as in-situ measurements, scatterometer data, and numerical model data. Although wind direction data are frequently available, they have inherent potential aliasing errors due to their much coarser spatial resolutions than those of the SARs. Moreover, the much larger time difference between the model data and SAR data are insufficient for resolving small-scale marine phenomena in the wind field. However, if wind-induced streaks are apparent in the SAR image, the wind direction can be directly estimated using a 2-D Fourier transform spectrum, wavelet analysis, and the local gradient. However, these methods are only valid for cases in which no ambient oceanic or atmospheric features (e.g., internal waves, atmospheric gravity waves, and ship wakes) are present, and a 180° ambiguity remains. Furthermore, under-determination associated with the sensitivity of single normalized radar cross section (NRCS) measurements to both the wind speed and direction should be considered in wind interpretation.

In this study, we calculated wind fields using ALOS-2 PALSAR images and compared their accuracy with that of the Korean Meteorological Administration (KMA) ocean meteorological buoy data near the Korean Peninsula. Land masking was performed using the Shuttle Radar Topography Mission digital elevation model data. To eliminate the influence of double scattering due to ships on the wind field, a ship removal process was performed using the adaptive threshold method. To remove speckle noise in the SAR data, we preprocessed the data utilizing a moving window and applied an ensemble average. To understand the impacts of the coastal wind field on ecosystems, we collected sea surface temperature (SST) data from the National Oceanic and Atmospheric Administration, which used an advanced very-high-resolution radiometer (NOAA AVHRR); chlorophyll-a (chl-a) data from the Communication, Ocean, and Meteorological Satellite, which used a Geostationary Ocean Color Imager (COMS/GOCI); and sea surface height (SSH) data from the Archiving, Validation and Interpretation of Satellite Oceanographic data (AVISO). We subsequently analyzed the changes in SST and chl-a concentration caused by wind. In addition, atmospheric-oceanic interaction mechanisms were analyzed using atmospheric stability, which varies with SST and wind field.

2. STUDY AREA AND DATA

2.1. STUDY AREA

The study area was the coastal regions near the Korean Peninsula, as shown in Fig. 1, which includes portions of the Yellow Sea, East Sea/Japan Sea (EJS), and East China Sea. The study area is dominated by well-developed, seasonal current systems (warm and cold), shallow bathymetry, and strong tidal currents in the Yellow Sea. It is characterized by relatively deep waters but with a depth of less than 3000 m and contains diverse oceanic phenomena, such as coastal upwelling, fronts, and suspended sediment.

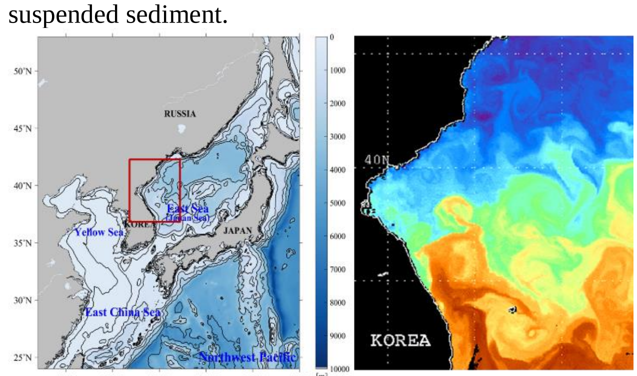

Fig. 1. (a) Bathymery (m) of the marginal seas of the Northwest Pacific around Korean peninsula: the East/Japan Sea, the Yellow Sea, the East China Sea. (b) The spatial distribution of sea surface temperature [°C] in the study region from 1-km NOAA/AVHRR data.

2.2. ALOS-2 PALSAR

ALOS-2 PALSAR-2 satellite, which was launched on May 24, 2014, is equipped with an L-band SAR instrument operated by the Japanese Aerospace Exploration Agency (JAXA) and has been continuously observing Earth's surface (Arikawa et al. 2014). PALSAR-2 data have been widely used in land, agricultural, natural resources, and oceanic applications. Oceanic observations have been utilized for detecting and monitoring sea ice, ships, oceanic currents, and sea surface winds. The factors affecting the sea surface wind errors of ALOS-2 PALSAR-2 have not been previously discussed in detail, particularly for the stripmap mode. In total, we collected 45 Stripmap mode images to assess sea surface winds; however, for eddy investigation, we used ScanSAR mode images with a wide swath, which is more suitable for comprehensive analysis than the stripmap mode because of its wide spatial coverage.

2.3. COMS/GOCI AND NOAA AVHRR

COMS/GOCI is the world's first geostationary satellite centered on the Korean peninsula and has a spatial resolution of 500 m × 500 m. It has observed the marine environment in a 2500 km × 2500 km area around the Korean Peninsula eight times daily for 7.7 years [4].
The near-polar orbiting NOAA AVHRR provides sea surface temperature data twice daily at a 1 km spatial resolution. The sensor has five spectral channels, including visible, near-infrared, and thermal infrared wavelengths; the center wavelengths are 0.6, 0.9, 3.7, 11, and 12 μm.

2.4. AVISO DATA

To investigate marine environments, we used the SSH data from AVISO (https://www.aviso.altimetry.fr/). We used Level 4 data, which contains multiple sensor-merged products, such as maps and time series reproduced by the data unification and altimeter combination system. The maps are constructed by optimal interpolation of multi-mission altimeter observations and are provided daily with a 0.25° × 0.25° resolution for the global products and a 0.125° × 0.125° resolution for regional products, such as those for the Mediterranean and Black Seas, through the Copernicus Marine Environment Monitoring Service [5].

2.5. KMA BUOYS

A total of 17 KMA oceanic meteorological buoys are located near the coast of the Korean Peninsula: six in the Yellow Sea, five in the EJS, and six in the East China Sea. The measurement interval of the buoys is 30 minutes or 1 hour, and the height of the measurements varies, from -1.2 m to -0.1 m for water temperature and from 3.6 m to 4.0 m for wind speed.

3. METHOD

3.1. RADIOMETRIC CALIBRATION

The ALOS-2 PALSAR-2 data utilize different NRCS calculations based on the data processing levels and number of conditions (Table 1). The data used in this study were L1.5 data, which is a product of the stripmap fine mode. The NRCS was calculated using the digital number for each pixel and various calibration constants for each processing level and observation mode [6]. The calibration factors vary with the software version, acquisition mode, spatial resolution, and incidence angles for the ALOS PALSAR data [7]. Table 1 summarizes the calibration factors for stripmap fine-mode data [8]. The digital number of the ALOS-2 PALSAR-2 image was converted to NRCS using these calibration factors, based on the characteristics of the data.

Table 1. Calibration factors for the ALOS-2 PALSAR data with respect to the observation mode, data processing version, and product ID.

Observation mode	ID	Processing version	
		000.001-002.022	002.023-
Stpotlight	all	-81.1	
	U2-6	-81.6	
	U2-7	-81.2	
	U2-8	-81.6	
	U2-9	-81.7	
	FP6-3	-81.0	
Stripmap	F6-4	-81.7	
	F6-5	-82.8	-83.0
	F6-6	-82.5	
	F6-7	-80.8	
	F2-5	-82.4	
	F2-6	-82.4	
	F2-7	-81.9	
ScanSAR	W2	-79.0	
Other mode	all	-83.0	

3.2. SHIP DETECTION AND REMOVAL

Single scattering on the ocean surface, as well as Bragg scattering and its backscattering coefficient (e.g., normalized radar cross section (NRCS)) all show low values. However, ships over the ocean impose various scattering characteristics, including single scattering, double scattering, and volume scattering, associated with the interactions between the ship and its internal structure. In general, due to the predominantly double scattering and volume scattering by ships, the measured NRCS becomes much larger than that of the surrounding ocean pixels. These scattering characteristics affect not only the pixels where the ship is, but also those of the surrounding ocean, causing errors when calculating the sea surface wind from SAR data. To obtain an accurate sea surface wind field, this study applied a method of detecting and removing ships for ALOS-2 PALSAR. Previous studies have used the global threshold, adaptive threshold, and artificial neural network methods to detect ships in SAR data; we applied the adaptive threshold method to calculate the threshold that influenced the characteristics of surrounding pixels.

3.3. RETRIEVAL OF L-BAND SAR WIND SPEED

Using the ECMWF reanalysis wind field data and radar azimuth look angles, the relative wind direction was calculated and subsequently used as input data for the L-band geophysical model function (GMF) [9]. Then, the preprocessed NRCS, incidence angle, and relative wind direction were utilized in the L-band GMF to retrieve high-resolution sea-surface wind fields.

The L-band GMF is an empirical model that was developed based on HH polarized data from ALOS-1 PALSAR. It is expressed as a function of NRCS, incidence angle, relative wind direction, and wind speed. The L-band GMF 2009 is calculated as follows:

$$\sigma^0 = A_0(c, u_{10}, \theta)[1 + A_1(c, u_{10}, \theta)\cos\varphi + A_2(c, u_{10}, \theta)\cos 2\varphi] \quad (1)$$

where σ^0 is the NRCS in linear units, u_{10} is the neutral wind speed at 10 m height, θ is the incidence angle, φ is the relative wind direction, and c is the constant coefficient. A_0, A_1, and A_2 are the coefficients related to and θ. The L-band GMF 2009 is capable of accurate wind retrieval for wind speeds of less than 20 m s^{-1} and incidence angles from 17° to 43°.

To understand the properties of the L-band GMF 2009 for each input data point, we ran the model with a maximum incidence angle of 43° (Fig. 2), at which, the upwind value was higher than the downwind value. The anisotropy of the upwind and crosswind values became more apparent at increasing incidence angles; however, the anisotropy of the downwind and crosswind values became more evident at decreasing incidence angles. In addition, as the wind speed increased, the variation in wind speed increased, with respect to the fluctuations in the NRCS. This effect was more pronounced at lower incidence angles. These observations imply that accurate NRCS values are more important for retrieving precise wind speeds at smaller incidence angles and higher wind speed ranges.

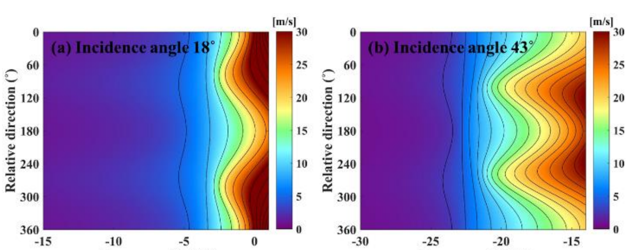

Fig. 2. Distributions of estimated wind speeds (m s^{-1}) of the L-band GMF 2009 as a function of relative wind direction (°) and NRCS (dB) at given incidence angles of (a) 18° and (b) 43°.

4. RESULTS

4.1. ACCURACY OF ALOS-2 PALSAR WIND

The estimated wind speeds derived from the ALOS-2 PALSAR-2 Stripmap Fine mode data by using the L-band GMF 2009 were compared to the 10-m neutral wind speeds converted from the in-situ measurements (Fig. 3). The accuracy of the sea surface winds using the L-band GMF 2009 showed the root-mean-square error (RMSE) of about 2.11 m s^{-1}, bias error of −1.16 m s^{-1}, and standard deviation of 1.78 m s^{-1} [10]. According to the previous study on the accuracy of ALOS-2 PALSAR-2 ScanSAR mode, the L-and ALOS-2 PALSAR-2 wind speeds showed the RMSE of 2.33 m s^{-1} and the bias error of 0.23 m s^{-1} [11]. Since the RMSE was derived from the ScanSAR mode with a much wider spatial coverage than the Stripmap Fine mode, it is not possible to compare the RMS errors directly. However, this difference implies a possibility that the Stripmap Fine mode data can be applicable to derive the wind speed with accuracy similar to that of the ScanSAR mode data.

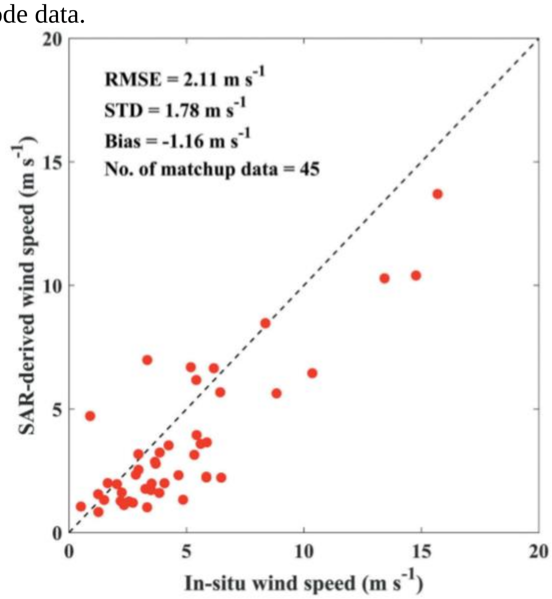

Fig. 3. Comparison of buoy wind speed with the wind speed derived from the ALOS-2 PALSAR-2 using L-band GMF 2009, where the texts indicate the accuracy of SAR-derived wind speed.

4.2. REGIONAL ACCURACY

The three seas around the Korean Peninsula have different water depths, islands, tidal currents, coastlines, and other marine characteristics. To assess the accuracy of the sea surface wind derived from the ALOS-2 PALSAR data for each sea, we classified the Yellow Sea, East China Sea, and EJS according to the criteria of the KMA, and assessed the accuracy of the sea surface winds in each area, estimated using the L-band GMF 2009 (Fig. 4). We found that ALOS-2 PALSAR underestimated sea surface winds throughout the region, which became more apparent as the wind speed increased. This tendency to underestimate was strongest in the EJS and weakest in the Yellow Sea. In general, this is because the average water depth decreases and tidal currents become strongest in the Yellow Sea, and are deeper and weaker, respectively, in the EJS [3]. Thus, because of the water depth and tidal currents, the underestimation of sea surface wind from ALOS-2 PALSAR was alleviated in the Yellow Sea. However, the standard deviation of the wind speed error was highest there; therefore, the influence of tidal current and water depth led to uncertainty in the retrieval of the ALOS-2 PALSAR-derived sea surface wind over the Yellow Sea.

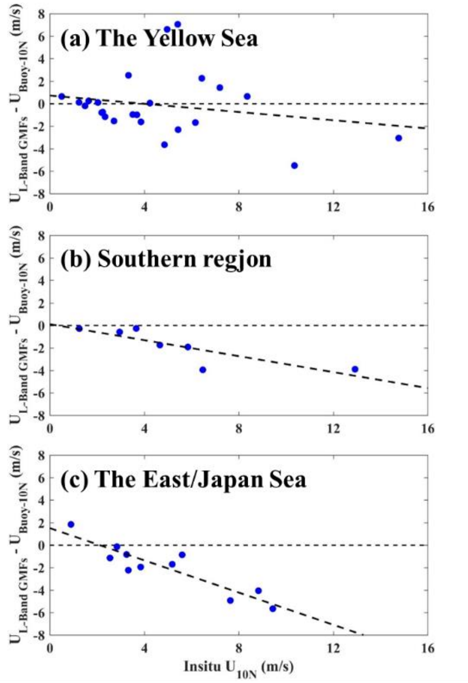

Fig. 4. Comparison of residuals (ALOS-2 PALSAR wind speed – buoy wind speed) using L-band GMF 2009 in (a) the EJS, (b) the southern region, and (c) the Yellow Sea, where the black dashed line represents a least-squared fit to a linear function.

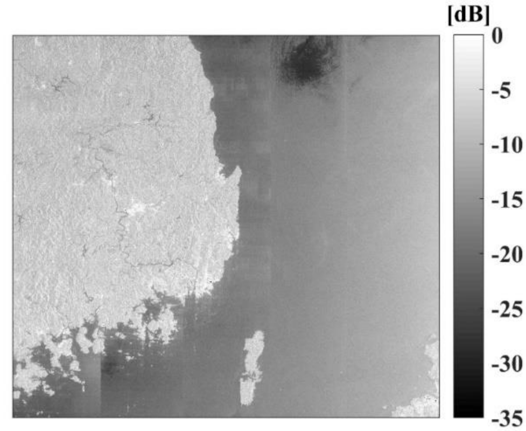

Fig. 5. Distribution of backscattering coefficient (dB) of ALOS-2 PALSAR observed on April 22, 2017, at 03:24 UTC in the EJS.

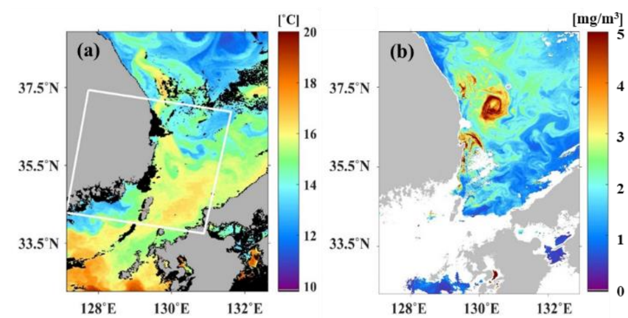

Fig. 6. Distributions of (a) SST (°C), from NOAA AVHRR, observed on April 22, 2017, at 05:59 UTC and (b) chl-a (mg m-3), from COMS/GOCI, observed on April 22, 2017, at 03:00 UTC. The white box represents the ALOS-2 PALSAR ScanSAR image.

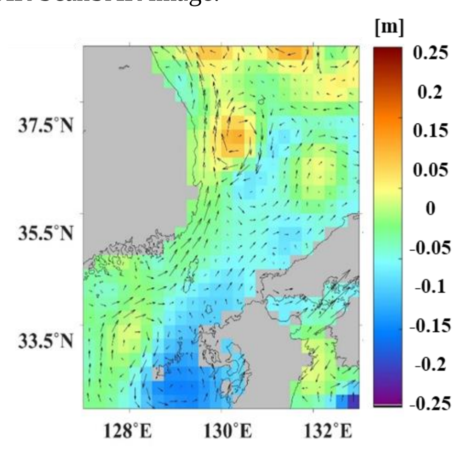

Fig. 7. Distribution of sea surface height anomaly (m) from the AVISO Level 4 data on April 22, 2017, near the Korean Peninsula.

4.3. MARINE ENVIRONMENTS OVER EDDY

Fig. 5 shows the backscattering coefficient of ALOS-2 PALSAR observed on April 22, 2017, at 03:24 UTC. These data were obtained from a ScanSAR mode image of an area with a low sea-surface wind in the EJS. In general, sea surface wind is affected by stability, which is derived from the temperature difference between SST and air temperature [1]. This difference is induced by marine phenomena, such as fronts and eddies.

To consider the spatial distributions of marine environments, we investigated the SST and chl-a data derived from the NOAA AVHRR and COMS/GOCI, respectively (Fig. 6). Fig. 6a shows the spatial distribution of SST observed on April 22, 2017, at 05:59 UTC; Fig. 6b shows the spatial distribution of chl-a observed on April 22, 2017, at 03:00 UTC. The eddy was enclosed by a high SST current; its boundary showed a high chl-a (above 5 mg m^{-3}) concentration compared with the surrounding environment, which accompanied an algal bloom.

Fig. 7 shows the spatial distribution of the sea surface height anomaly (SSHA) from the AVISO Level 4 data. As shown by the SSHA, the eddy over the EJS was an anticyclonic warm eddy; the rotation direction of the eddy can be seen in the time series of the SST and chl-a distributions. This warm-core eddy showed a positive SSHA compared to the surrounding environments. In general, warm-core eddies show low dissolved nutrient concentrations, deep mixed layer depth, and low chl-a concentrations [12]; however, this eddy showed high chl-a concentrations (Fig. 6b).

4.4. WIND FIELDS OVER EDDY

To investigate the wind field over the warm core eddy, we estimated the sea surface wind from an ALOS-2 PALSAR ScanSAR image using the L-band GMF 2009 (Fig. 8). The ECMWF reanalysis model data were used as wind direction information to retrieve the sea surface winds. The winds moved westward, and their speed decreased over the eddy.

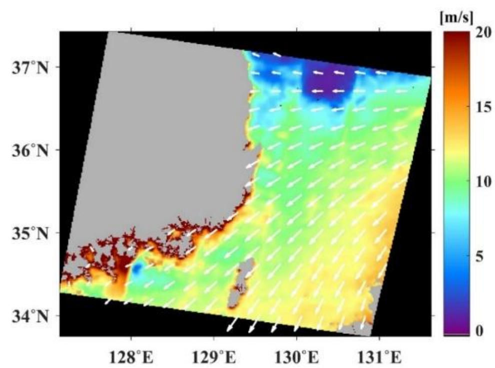

Fig. 8. Spatial distribution of sea surface winds (m s-1) from an ALOS-2 PALSAR ScanSAR mode image observed on April 22, 2017, at 03:24 UTC near the Korean Peninsula. The white arrows represent the wind direction, derived from ECMWF reanalysis model data.

Fig. 9 shows the relationship between the estimated wind speed and stability in the MABL. To calculate the stability, the 2-m air temperature data from the ECMWF reanalysis and the SST from NOAA AVHRR were used. When the air temperature was higher than the SST, the MABL was stable. However, when the SST was higher than the air temperature, the MABL was unstable. The wind speed was lower over the stable MABL than the unstable MABL. In other words, as the MABL becomes more destabilized, higher momentum can be transferred, wind stress increases, and surface winds are amplified; the reverse is also true [1,13,14].

The stability of the MABL affected not only the wind speed, but also the wind direction. As shown in Fig. 8, the wind passing over the warm-core eddy changed direction. Previous studies demonstrated that as the MABL became more destabilized, air–sea momentum was more effectively transmitted, which increased the wind stress and decreased the veering angle of the surface winds; the reverse was also true [2,14]. Moreover, the effect of stability in the MABL on the wind field instantly occurred within a small spatial scale of less than 25 km [15].

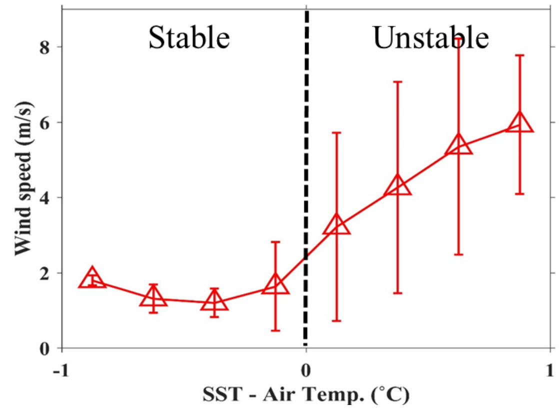

Fig. 9. Wind speed variations with respect to air-sea temperature differences (SST minus air temperature) (°C), where the red error bars represent the standard deviation of wind speeds for each bin.

5. CONCLUSION

In this study, we applied the adaptive threshold method to detect and remove ships from ALOS-2 PALSAR data. To retrieve the sea surface wind, the L-band GMF 2009 algorithm was applied to preprocessed ALOS-2 PALSAR data. To assess the estimated sea surface winds, we used 45 stripmap fine mode images. The accuracy of the sea surface winds had an RMSE of approximately 2.11 m s−1, bias of −1.16 m s−1, and standard deviation of 1.78 m s−1. As the wind speed increased, the L-band GMF 2009 tended to underestimate. In terms of the sea area, the underestimation was strongest in the EJS, and weakest in the Yellow Sea; however, the Yellow Sea showed the highest standard deviation compared with the other areas. Because the Yellow Sea has a shallow water depth and strong tidal currents, the wind speed is generally overestimated; however, in the ALOS-2 PALSAR data, the overestimation due to these characteristics alleviated the underestimation in the L-band GMF 2009. Thus, the characteristics of the Yellow Sea caused a large standard deviation and uncertainty for the sea surface wind derived from ALOS-2 PALSAR.

To investigate air-sea interactions in the MABL, we used SST data from the NOAA AVHRR, chl-a data from COMS/GOCI, SSHA from AVISO, air temperature from the ECMWF reanalysis model data, and sea surface wind derived from ALOS-2 PALSAR ScanSAR mode images. Based on the spatial distribution of SST and SSHA, we found that a warm-core eddy was located over the EJS on April 22, 2017. The influence of the stability of the MABL on the wind field was revealed by the differences between the SST and air temperature. In the warm-core eddy, an algal bloom occurred with a high chl-a concentration above 5 mg m-3. As the MABL became more destabilized, it amplified the magnitude of surface winds, and vice versa. The change in wind speed also affected the wind direction.

This study examined the estimation of wind using the ALOS-2 PALSAR by assessing its accuracy. Furthermore, this study addressed the importance of ALOS-2 PALSAR data to understand the wind field and its role in air-sea interactions, which are related to physical forcing and low-level ecosystem responses. We expect that ALOS-2 PALSAR data will continue to contribute to coastal marine studies using high-resolution wind data.

6. REFERENCES

[1] Kim, T. S., Park, K. A., Li, X., and Hong, S., "SAR-derived wind fields at the coastal region in the East/Japan Sea and relation to coastal upwelling," *International journal of remote sensing*, 35(11-12), 3947-3965, 2014.

[2] Kim, T. S., Park, K. A., Li, X., Mouche, A. A., Chapron, B., and Lee, M., "Observation of Wind Direction Change on the Sea Surface Temperature Front Using High-Resolution Full Polarimetric SAR Data," *IEEE Journal of Selected Topics in Applied Earth Observations and Remote Sensing*, 10(6), 2599-2607, 2017.

[3] Jang, J. C., Park, K. A., Mouche, A. A., Chapron, B., and Lee, J. H, "Validation of sea surface wind from sentinel-1A/B SAR data in the coastal regions of the korean peninsula," *IEEE Journal of Selected Topics in Applied Earth Observations and Remote Sensing*, 12(7), 2513-2529, 2019.

[4] Park, K. A., Woo, H. J., and Ryu, J. H., "Spatial scales of mesoscale eddies from GOCI Chlorophyll-a concentration images in the East/Japan Sea," *Ocean Science Journal*, 47(3), 347-358, 2012.

[5] Ballarotta, M., Ubelmann, C., Pujol, M. I., Taburet, G., Fournier, F., Legeais, J. F., Faugere, Y., Delepoulle, A., Chelton, D., Dibarboure, G., and Picot, N., "On the resolutions of ocean altimetry maps;" *Ocean Science*, 15(4), 1091-1109, 2019.

[6] Shimada, M., M. Watanabe, T. Moriyama, T. Tadono, M. Minamisawa, and Higuchi, R., "PALSAR Radiometric and Geometric Calibration," *Journal of the Remote Sensing Society of Japan*, 27(4), 308–328, 2007.

[7] Shimada, M., O. Isoguchi, T. Tadono, and Isono, K., "PALSAR Radiometric and Geometric Calibration," *IEEE Transactions on Geoscience and Remote Sensing*, 47(12), 3915–3932, 2009.

[8] JAXA EORC, "ALOS-2 First Year Operation Results, Ver. Mar. 23, 2017," JAXA Library. March 23, 2017. (Accessed on March 23, 2022. https://www.eorc.jaxa.jp/ALOS-2/calval/CalibrationFactors_PALSAR2_v20170323.pdf)

[9] Isoguchi, O. and Shimada, M., "An L-band Ocean Geophysical Model Function Derived from PALSAR," *IEEE Transactions on Geoscience and Remote Sensing*, 47(7), 1925–1936, 2009.

[10] Jang, J. C., Park, K. A., and Isoguchi, O., "Characteristics of environmental factors contributing to ALOS-2 PALSAR wind speed errors," *International Journal of Remote Sensing*, 41(15), 5695-5725, 2020.

[11] Isoguchi, O. and Shimada, M., "Detection of Wind Fields from PALSAR-2," Paper presented at the *Geoscience and Remote Sensing Symposium (IGARSS), 2016 IEEE International*, Beijing, China. 2209–2211, 2016.

[12] Laiolo, L., McInnes, A. S., Matear, R., and Doblin, M. A., "Key drivers of seasonal plankton dynamics in cyclonic and anticyclonic eddies off east Australia," *Frontiers in Marine Science*, 3, 155, 2016.

[13] Johannessen, J. A., Shuchman, R. A., Digranes, G., Lyzenga, D. R., Wackerman, C., Johannessen, O. M., and Vachon, P. W., "Coastal ocean fronts and eddies imaged with ERS 1 synthetic aperture radar," *Journal of Geophysical Research: Oceans*, 101(C3), 6651-6667, 1996.

[14] Park, K. A., Cornillon, P., and Codiga, D. L., "Modification of surface winds near ocean fronts: Effects of Gulf Stream rings on scatterometer (QuikSCAT, NSCAT) wind observations," *Journal of Geophysical Research: Oceans*, 111(C3), 2006.

[15] Park, K. A. and Cornillon, P. C., "Stability‐induced modification of sea surface winds over Gulf Stream rings," *Geophysical research letters*, 29(24), 64-1, 2002.

3.12 Resources related research

INVESTIGATION OF NATURAL SURFACES BY USING DIFFERENT SAR MISSIONS FOR RISK AND WATER RESOURCES MANAGEMENT

PI No.: ER2A2N062

Simone Pettinato[1], Alessandro Lapini, Emanuele Santi, Simonetta Paloscia, Giacomo Fontanelli, Andrea Garzelli, [2]

[1] Institute of Applied Physics–National Research Council of Italy (IFAC–CNR)
[2] Department of Information Engineering and Mathematics, University of Siena, 53100 Siena, Italy

1. INTRODUCTION

Multifrequency synthetic aperture radar (SAR) images from ALOS/PALSAR, ENVISAT/ASAR and Cosmo ‐ SkyMed sensors were studied for forest classification in a test area in Central Italy (San Rossore), where detailed in ‐ situ measurements were available. A preliminary discrimination of the main land cover classes and forest types was carried out by exploiting the synergy among L ‐ , C ‐ and X ‐ bands and different polarizations. SAR data were preliminarily inspected to assess the capabilities of discriminating forest from non ‐ forest and separating broadleaf from coniferous forests. The temporal average backscattering coefficient ($\sigma°$) was computed for each sensor ‐ polarization pair and labeled on a pixel basis according to the reference map. Several classification methods based on the machine learning framework were applied and validated considering different features, in order to highlight the contribution of bands and polarizations, as well as to assess the classifiers' performance. The experimental results indicate that the different surface types are best identified by using all bands, followed by joint L ‐ and X ‐ bands. In the former case, the best overall average accuracy (83.1%) is achieved by random forest classification. Finally, the classification maps on class edges are discussed to highlight the misclassification errors.

2. TEST AREA AND INPUT DATA

The investigation was carried out in a forest area in Central Italy, where ground measurements,meteorological information and other ancillary data were available. The natural park of San Rossore (43.72°N, 10.30°E) is a protected flat area of about 4800 ha located along the coast of Tuscany Region. The area is covered by forests and pastures; forests are dominated mainly by Mediterranean pines (Pinus pinaster Ait. and Pinus pinea L.) and deciduous broadleaf (i.e., Quercus robur L., Fraxinus subsp. oxycarpa M. Bieb. ex Wild, Ulmus laevis Miller, Alnus glutinosa (L.) Gaertner, etc.). The ground truth is represented by the forest type map produced by 'Dimensione Ricerca Ecologia Ambiente', DREAM (2003) [1]. The original classification map was provided at the 1:15000 scale and was derived from field observations collected in the whole Park. According to the definition used by the Tuscany Regional authority, forests correspond to areas having a minimum extension of 2000 m 2, a length greater than 20 m, and tree cover must be greater than 20%. Unfortunately, evergreen broadleaf forests (dominated by Holm oak, Quercus ilex L.) cover only a marginal area (0.2%) of the whole Park, thus, it was not possible to separate them to coniferous and deciduous broadleaf forests. Logging activities had an interested part of the forest area since 2009; therefore, a preliminary check was done to exclude these areas from the training and the test

phases. Felled areas were identified using a Landsat TM of 2009 and Google Earth images of 2010. Additional conventional measurements were carried out on 72 forest stands covered by three forest species groups: Mediterranean pines, holm oak and deciduous trees, whose area ranged from 1 to 170 ha [2]

A series of SAR images, listed in Table 1, was collected at L-(ALOS/PALSAR), C-(ENVISAT/ASAR) and X-(COSMO ‐ SkyMed) bands in 2009 and 2010 across different seasons and by using different modality of observation. The original (range, azimuth) resolution of the PALSAR, ASAR and COSMO ‐ SkyMed images were (9.3 m, 6.1 m), (7.8 m, 4.0 m) and (1.1 m, 1.9 m), in that order. Furthermore, the images are characterized by different incidence angle, polarization, acquisition mode and daily time acquisition, as reported in Table 1

Table 1 SAR images available in the test area of San Rossore.

Group	Sensor	Date	Time (UTC)	Inc. Ang.	Pol.
1	PALSAR	28/02/2009	21:43:00	38	HH
	ASAR	26/02/2009	09:38:29	23	VV
	CSK2	06/03/2009	05:13:15	33	HH
2	PALSAR	07/06/2009	21:03:08	22	Full-pol
	ASAR	26/05/2009	20:59:38	23	VV
	CSK2	25/05/2009	05:12:24	33	HH
3	PALSAR	29/06/2009	21:41:48	38	HH/HV
	ASAR	27/06/2009	09:35:57	23	VV
	CSK2	25/05/2009	05:12:24	33	HH
4	PALSAR	16/07/2009	21:44:03	38	HH/HV
	ASAR	16/07/2009	09:38:31	23	VV
	CSK2	13/08/2009	05:11:29	33	HH
5	PALSAR	29/09/2009	21:42:14	38	HH/HV

	ASAR	24/09/2009	09:38:26	23	VV	IMS
	CSK2	29/08/2009	05:11:29	33	HH	Himage
6	PALSAR	16/10/2009	21:44:25	38	HH/HV	FBD
	ASAR	13/10/2009	20:59:34	23	VV	IMS
	CSK	*N/A	*	*		*
7	PALSAR	30/12/2009	21:42:15	38	HH	FBS
	ASAR	22/12/2009	20:59:34	23	VV	IMS
	CSK3	20/12/2009	05:10:04	34	HH	Himage
8	PALSAR	16/01/2010	21:44:22	38	HH	FBS
	ASAR	10/01/2010	21:02:24	23	VV	IMS
	CSK2	20/01/2010	05:09:38	33	HH	Himage
9	PALSAR	14/02/2010	21:42:06	38	HH	FBS
	ASAR	11/02/2010	21:02:24	23	VV	IMS
	CSK2	21/02/2010	05:09:15	33	HH	Himage
10	PALSAR	01/04/2010	21:41:07	38	HH	FBS
	ASAR	03/04/2010	09:35:32	23	VV	IMS
	CSK3	25/03/2010	05:08:25	33	HH	Himage
11	PALSAR	18/04/2010	21:23:47	38	HH	FBS
	ASAR	22/04/2010	09:38:20	23	VV	IMS
	CSK	*N/A	*	*		*
12	PALSAR	19/07/2010	21:42:52	38	HH/HV	FBD
	ASAR	20/07/2010	20:59:36	23	VV	IMS
	CSK3	01/08/2010	05:07:28	34	HH	Himage

3. METHODS

This investigation aims at evaluating the use of the available SAR data for discriminating forest from non‐forest land covers and separating broadleaved from coniferous forest types.

The classification of the test site was carried out by using the following supervised classification methods belonging to the machine learning framework:

- Random forest (RF);
- AdaBoost with decision trees (AB);
- K‐nearest neighbors (kNN);
- Feed forward artificial neural networks (FF‐ANNs);
- Support vector machines (SVM);

Quadratic discriminant (QD).

Random forest (RF) is a classification method belonging to the ensemble learning methods [3]. Ensemble classifiers perform decisions by aggregating the classification results coming from several weak classifiers. In RF, the weak classifiers are decision trees [4] and predictions are performed by the majority, i.e., the predicted class is the most voted by all the weak classifiers. Decision trees are trained by randomly drawing with replacement a subset of training data (bagging). The RF algorithm has been demonstrated to reduce both the bias and the overfitting with respect to decision trees, as well as making unnecessary the pruning phase [5]. Two main parameters must be set in RF: the number of features in the random subset at each node and the number of decision trees [6]. All these aspects, as well as a contained computation burden (compared, for instance, to SVM) and outperforming classification results, have contributed to make RF very popular in the study of land cover, too (see, for instance, [5–9]). Boosting algorithms generally refer to the method that combines weak classifiers to get a strong classifier [10]. AdaBoost with decision trees (AB) [11] is a boosting ensemble classification method whose prediction relies on a weighted mean of the outputs of several weaker decision trees (the higher the weight, the more reliable the decision tree). The iterative training algorithm selects a decision tree at each step, in order to minimize a cost function, and update the weights. This process has been shown to improve the overall performance under some optimality measure [12]. AdaBoost has been already considered in the remote sensing literature, e.g., for tree detection [13], land cover classification in tropical regions [14] and land cover classification carried out on hyperspectral images [15]. Nevertheless, the main drawbacks of AB are its sensitivity to outliers and the number of hyperparameters to be optimized in order to improve the classification performance. The K‐nearest neighbors (KNN) algorithm is another popular classification method [16]. In KNN, the training dataset corresponds to a set of labeled points in the space of features. The prediction is performed by only considering the classes of the k training samples that are closest to test sample, according to a given metric. There are many strategies to perform this decision, e.g., majority vote, weighted distance [17] or by using Dempster–Schafer theory [18]. An integration of KNN and SVM has been also proposed [19]. The basic KNN algorithm usually attains suboptimal classification performance compared to other more recent methods and can be memory intensive for a high number of features. Nevertheless, due its plain logic and configuration (the main parameter is the number of neighbor k), it has been thoroughly used as benchmark in the remote sensing community [9,20,21]. An algorithm based on feed forward artificial neural networks (FF‐ANNs) has been also considered for the comparison. FF‐ANN is conceived for establishing non‐linear relationships between inputs and outputs [22] and therefore cannot be regarded as a classification algorithm strictly speaking. However, they can be applied to almost any kind of input–output relationships and their ability in solving non‐linear problems has been largely proven [23]. FF‐ANN is composed of a given number of interconnected neurons, distributed in one or more hidden layers, that receive data, perform simple operations (usually additions and products) and propagate the results. The FF‐ANN training is based on the back propagation (BP) learning rule, which is a gradient descendent algorithm aimed at minimizing iteratively the mean square error (MSE) between the network output and the target value. As a main disadvantage, FF‐ANN is sensitive to outliers: a training representative of the testing conditions is therefore mandatory for obtaining satisfactory results [24].In this study, FF‐ANN was adapted to act as classifiers by simply rounding the obtained outputs to the closest integer. Another popular algorithm for classification is represented by support vector machine

(SVM). In SVM, the space of features is divided in subspaces by means of hyperplanes, named decision planes, and the prediction is performed according to the subspace that the test point belongs to (see, for instance, [25]). The decision planes are computed during the training phase searching for the maximum margin, according to some distance function. SVM have been also extended to deal with nonlinear separation hypersurfaces [25,26], allowing us to map the features in a higher‐dimensional feature space through some nonlinear mapping and formulating a linear classification problem in that feature space by means of kernel functions. SVM‐based methods are very common due to their good classification performance (see, for instance, [37,6,9,19,20]). As a drawback, SVM may require a fine tuning of many hyperparameters to obtain the optimal result. Furthermore, the training of SVM classifiers is performed by means of quadratic programming optimization routines [24]; thus, the training time is usually higher than, for instance, RF. The quadratic discriminant classifier (QD) pertains to the discriminant analysis framework [27]. In QD, data samples are assumed to be generated according to a Gaussian mixture distribution. The mean and the covariance matrix of each component are estimated by using the training data set belonging to the corresponding class. The prediction is performed by computing the posterior probability that the test sample belongs to each class and selecting the class for which the maximum is attained. Despite of the simplistic statistical hypothesis, QD can often deal with complex data models, exhibiting a competitive classification performance [28,29]. Furthermore, the training and decision phases are usually extremely fast

4. RESULTS

Classifiers were compared by means of a 10‐folds cross‐validation, where at each round the 10% of the dataset was used as training set and the remaining 90% for validation. In the training phase, five‐fold cross‐validation was adopted to optimize the hyperparameters of the classifiers. To investigate the contribution of different bands and polarizations, seven scenarios were tested. For each scenario, only a subset of classification stack's components was considered for training and validation. The indexes of the scenarios and the related components follows:

1. PALSAR HH + PALSAR HV;
2. CSK2 HH;
3. ASAR VV;
4. PALSAR HH + PALSAR HV + CSK2 HH;
5. PALSAR HH + PALSAR HV + ASAR VV;
6. CSK2 HH + ASAR VV;
7. PALSAR HH + PALSAR HV + CSK2 HH + ASAR VV.

Each scenario was trained and validated. The confusion matrices were subsequently computed over the overall 10 validation sets, in order to assess and compare the prediction capabilities among classifiers. The predicted and the ground truth classes are reported in rows and columns, respectively. The scores are normalized to 100% on each column (up to rounding error), such that the main diagonal and off‐diagonal entries report the sensitivity and the misclassification rate, respectively. In Table 4, the confusion matrix obtained in the scenario 1 is shown. Almost all classifiers exhibited the highest sensitivity for the non‐forest class, whereas the worst misclassification was between broadleaf and coniferous. This result confirms that L‐band data were more useful to discriminate forest and non‐forest rather than different forest types. As to scenario 2, whose results are reported in Table 5, the sensitivity was remarkably unbalanced toward the discrimination of forest types for all classifier, whereas they show very poor performance for the non‐forest type. Similar conclusions could be drawn by observing Table 6, where the results for scenario 3 are reported. A noticeable sensitivity balancing was obtained in scenario 4, as reported in Table 7. As to the forest type, four classifiers out of six exhibited sensitivity greater than 80% for both classes, whereas it ranged between 70% and 80% for the non‐forest class. This trend was also observed in the scenario 5 (see Table 8), even though the sensitivity values were slightly lower (about less 1%–2%). The joint use of band C‐ and X‐ (scenario 6, Table 9), on the contrary, did not provide enough information to discriminate the non‐forest class and the sensitivity of classifiers drops of about 50%‐ 70% with respect to the previous scenario. In Table 10, the results of scenario 7 are reported. By comparison with scenario 4 (Table 7), no remarkable trend emerged in terms of sensitivity or misclassification rate. In order to summarize the comparison, the average accuracies computed on the 10 folds, as well as the standard deviations, are reported in Table 9. RF classification achieved the best overall result (83.1 ± 0.1) and led in six out of seven scenarios. AB performed very closely to RF and both classification methods exhibited very low variance in all scenarios. KNN joins RF as to the best overall result, but the former suffered of poorer results in Scenario 2, 3 and 6. Moreover, some of the classifiers trained in the Scenario 2 resulted strongly biased towards forest classes, which was reflected in the higher standard deviations of the accuracy. A similar irregular pattern was exhibited by the SVM classifiers. FF‐ANN and QD sub‐optimally scored with respect to the best ones, even though no remarkable variability emerged across different realizations. All classification methods consistently attained their best in the scenario 7, that is, when all available data were used; the second‐best result was observed for the joint use of L‐ and X‐bands. Furthermore, the accuracies of all classifiers were remarkably above the 36.4% lower bound threshold, which corresponded to the accuracy of the trivial random assignment based on pixels' prior distribution. The average computational times of the tested classification methods are reported in Table 10. The computer simulations were carried out in MATLAB

R2019b, on an Intel(R) Core(TM) i7 - 8700 CPU @ 3.20GHz, 32 GB RAM, operating system Xubuntu 19.04 and exploiting six parallel processing. The time spent for the hyperparameters optimization was included and it varied according to several parameters, such as the i) dimensionality of predictors, ii) separability of classes, iii) number of parameters and the iv) stopping criterion of the optimization routines. It must be pointed out that, despite of a relatively fast training phase, KNN classifiers are more memory and processor intensive during the prediction phase, significantly being the slowest with respect to the other classification methods. For a visual evaluation, the classification maps obtained with RF are presented in Figure 1, considering three different scenarios. In scenario 1 (Figure 1a), identification between coniferous and broad leaf was scarce, whereas the non - forest areas were almost correctly identified as blue areas. Conversely, the classification map of scenario 2 (Figure 1b) shows a better discrimination between coniferous (red areas) and broadleaf (green) forests. In scenario 4 (Figure 1c), the improvement in the classification result combining L - and X - band was clear.

Table 2 Confusion matrices in the scenario 1 (PALSAR HH + PALSAR HV) for the classes coniferous, broadleaf and non - forest areas

	RF			AB			KNN		
	Ground Truth (%)			Ground Truth (%)			Ground Truth (%)		
Coniferous	71.9	25.9	8.8	72.2	26.2	8.7	68.8	27.6	9.0
Broadleaf	25.9	70.2	13.3	25.6	70.0	13.3	28.4	68.0	14.4
Non-forest	2.2	3.9	78.0	2.2	3.9	78.0	2.7	4.4	76.6
	FF-ANN			SVM			QD		
	Ground Truth (%)			Ground Truth (%)			Ground Truth (%)		
Coniferous	72.8	27.9	6.0	71.0	26.1	6.8	77.1	38.1	6.2
Broadleaf	25.6	67.7	16.4	27.3	70.7	17.5	19.7	56.7	13.1
Non-forest	1.6	4.4	77.5	1.7	3.2	75.7	3.2	5.3	80.7

Table 3 Confusion matrices in the scenario 2 (CSK2 HH) for the classes coniferous, broadleaf and non - forest area.

	RF			AB			KNN		
	Ground Truth (%)			Ground Truth (%)			Ground Truth (%)		
Coniferous	83.3	14.7	59.8	82.9	14.4	59.4	62.0	13.1	49.7
Broadleaf	15.4	85.2	30.1	15.7	85.5	30.5	12.3	63.7	23.0
Non-forest	1.3	0.1	10.0	1.4	0.1	10.2	25.7	23.2	27.3
	FF-ANN			SVM			QD		
	Ground Truth (%)			Ground Truth (%)			Ground Truth (%)		
Coniferous	76.7	10.1	51.5	61.2	20.5	52.5	87.4	18.1	67.9
Broadleaf	22.6	89.8	40.6	19.1	59.7	27.7	12.4	81.8	26.6
Non-forest	0.6	0.1	7.9	19.8	19.8	19.7	0.2	0.1	5.5

Table 4 Confusion matrices in the scenario 3 (ASAR VV) for the classes coniferous, broadleaf and non - forest area.

	RF			AB			KNN		
	Ground Truth (%)			Ground Truth (%)			Ground Truth (%)		
Coniferous	82.2	15.5	58.8	82.1	15.3	58.7	64.4	17.9	47.1
Broadleaf	17.8	83.4	36.3	17.9	83.6	36.6	19.3	70.4	35.1
Non-forest	0.0	1.1	4.9	0.0	1.1	4.8	16.3	11.7	17.8
	FF-ANN			SVM			QD		
	Ground Truth (%)			Ground Truth (%)			Ground Truth (%)		
Coniferous	81.6	14.8	58.2	83.2	16.5	59.7	82.2	15.4	58.8
Broadleaf	18.4	84.0	36.8	16.8	83.5	40.3	17.8	84.1	38.1
Non-forest	0.0	1.1	4.9	0.0	0.0	0.0	0.0	0.4	3.1

Table 5 Confusion matrices in the scenario 4 (PALSAR HH + PALSAR HV + CSK2 HH) for the classes coniferous, broadleaf and non - forest area.

	RF			AB			KNN		
	Ground Truth (%)			Ground Truth (%)			Ground Truth (%)		
Coniferous	83.6	13.1	10.5	83.2	12.8	10.5	83.4	13.3	10.7
Broadleaf	14.7	83.4	12.3	15.1	83.6	12.5	14.8	83.1	12.4
Non-forest	1.7	3.5	77.2	1.7	3.6	77.0	1.7	3.6	77.0
	FF-ANN			SVM			QD		
	Ground Truth (%)			Ground Truth (%)			Ground Truth (%)		
Coniferous	83.0	13.8	8.5	84.2	13.7	11.1	86.1	17.1	9.9
Broadleaf	16.0	82.2	15.6	14.2	83.0	14.2	11.2	78.4	11.2
Non-forest	1.0	4.1	75.9	1.6	3.4	74.7	2.7	4.4	78.8

Table 6 Confusion matrices in the scenario 5 (PALSAR HH + PALSAR HV + ASAR VV) for the classes coniferous, broadleaf and non - forest area.

	RF			AB			KNN		
	Ground Truth (%)			Ground Truth (%)			Ground Truth (%)		
Coniferous	81.3	13.6	10.9	81.2	13.5	10.8	81.5	14.0	11.2
Broadleaf	16.6	83.1	11.4	16.6	83.1	11.5	16.4	82.6	11.6
Non-forest	2.1	3.3	77.8	2.2	3.4	77.7	2.1	3.3	77.2
	FF-ANN			SVM			QD		
	Ground Truth (%)			Ground Truth (%)			Ground Truth (%)		
Coniferous	81.0	14.6	8.4	80.4	12.8	10.6	82.3	15.5	9.9
Broadleaf	17.7	81.9	16.2	17.6	83.7	12.7	14.9	80.1	10.8
Non-forest	1.3	3.5	75.4	2.0	3.5	76.6	2.8	4.4	79.4

Table 7 Confusion matrices in the scenario 6 (CSK2 + ASAR VV) for the classes coniferous, broadleaf and non - forest area.

	RF			AB			KNN		
	Ground Truth (%)			Ground Truth (%)			Ground Truth (%)		
Coniferous	82.7	12.9	50.6	82.6	12.7	50.6	76.3	13.8	46.8
Broadleaf	14.7	85.5	25.1	14.8	85.7	25.2	15.5	81.7	24.8
Non-forest	2.6	1.7	24.3	2.6	1.6	24.2	8.2	4.5	28.4
	FF-ANN			SVM			QD		
	Ground Truth (%)			Ground Truth (%)			Ground Truth (%)		
Coniferous	79.0	12.8	43.1	85.6	15.0	60.8	85.0	14.8	55.2
Broadleaf	20.1	86.0	36.2	13.4	81.9	29.4	13.3	83.1	23.8
Non-forest	0.9	1.2	20.7	0.9	3.1	9.8	1.7	2.1	21.0

Table 8 Confusion matrices in the scenario 7 (the PALSAR HH + PALSAR HV + CSK2 + ASAR VV)

for the classes coniferous, broadleaf and non‐forest area.

	RF			AB			KNN		
	Ground Truth (%)			Ground Truth (%)			Ground Truth (%)		
Coniferous	84.6	12.6	10.6	84.3	12.5	10.5	84.8	12.6	11.0
Broadleaf	13.6	84.1	11.3	13.9	84.1	11.5	13.7	84.3	11.6
Non-forest	1.8	3.4	78.1	1.8	3.4	78.0	1.6	3.2	77.4
	FF-ANN			SVM			QD		
	Ground Truth (%)			Ground Truth (%)			Ground Truth (%)		
Coniferous	84.5	14.2	8.5	83.9	12.2	10.9	85.6	15.1	10.8
Broadleaf	14.5	81.9	15.1	14.4	84.3	13.1	12.3	80.3	11.8
Non-forest	1.0	3.9	76.4	1.7	3.4	76.0	2.1	4.6	77.4

Table 9 Average and standard deviation of the accuracy of the classifiers for each tested scenario (abbreviations are used for sake of clarity). The best values for scenario are highlighted in bold.

Scenario	RF	AB	KNN	FF-ANN	SVM	QD
PALSAR	72.3 ± 0.1	**72.4 ± 0.1**	70.0 ± 0.3	71.6 ± 0.1	71.8 ± 0.1	69.4 ± 0.6
CSK2	**70.0 ± 0.0**	**70.0 ± 0.1**	56.0 ± 19.8	68.9 ± 0.1	52.6 ± 21.8	69.3 ± 0.1
ASAR	**67.8 ± 0.0**	**67.8 ± 0.0**	57.9 ± 3.3	**67.8 ± 0.0**	67.3 ± 0.0	**67.8 ± 0.0**
PALSAR + CSK2	**82.3 ± 0.1**	82.2 ± 0.1	82.1 ± 0.1	81.3 ± 0.1	81.8 ± 0.0	81.5 ± 0.1
PALSAR + ASAR	**81.4 ± 0.1**	81.3 ± 0.1	81.1 ± 0.1	80.3 ± 0.1	81.1 ± 0.0	80.8 ± 0.1
CSK2 + ASAR	**72.6 ± 0.1**	**72.6 ± 0.0**	69.3 ± 0.2	70.7 ± 0.2	69.5 ± 3.6	71.9 ± 0.1
PALSAR + CSK2 + ASAR	**83.1 ± 0.1**	83.0 ± 0.1	**83.1 ± 0.1**	81.9 ± 0.1	82.5 ± 0.0	81.8 ± 0.1

Table 10 Average computational times (s) of the training phase for different classification methods,including the hyperparameters optimization, as a function of the Scenario. Six parallel processing was used.

Scenario	RF	AB	KNN	FF-ANN	SVM	QD
1	175	219	27	45	190	<1
2	76	90	25	30	332	<1
3	79	107	26	43	129	<1
4	143	143	28	123	163	<1
5	191	169	28	145	186	<1
6	191	148	24	84	237	<1
7	215	180	27	201	121	<1

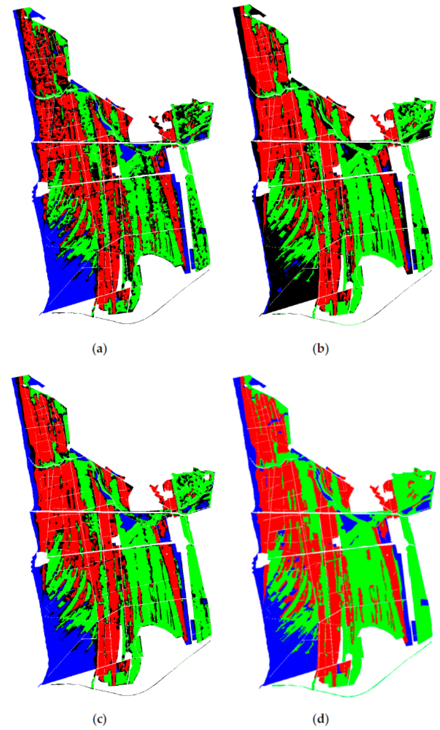

Figure 1 Classification maps of San Rossore test site obtained with random forest by using (a)PALSAR HH + PALSAR HV; (b) CSK HH and (c) PALSAR HH + PALSAR HV + CSK HH. (d) Reference forest classification map produced by DREAM [27]. Legend: Red: coniferous (correctlyclassified), Green: broadleaf (correctly classified), Blue: non‐forest (correctly classified), Black:misclassified.

5. CONCLUSIONS

The application of multi‐frequency SAR images to the study of heterogeneous Mediterranean forests, which have not been so far extensively investigated by using microwave remote sensing methods, have been adopted. The role of L‐, C‐ and X‐bands in land classification has been analyzed by applying several machine learning classification methods to data coming from different combinations of sensors and polarization. The joint use of multi‐frequency and multi‐polarization SAR data was shown to improve the classification of heterogeneous Mediterranean forests, allowing the separation of forest areas from non‐forest ones, as well as the identification of broadleaf and coniferous classes inside the forest class. The overall accuracy exceeded 80% when integrating both L‐ and X‐band contributions for almost all considered classifiers; instead, it was significantly lower when considering separately L‐ and X‐band. Furthermore, more homogeneous sensitivity across bands was achieved in the former case. By comparison, the contribution of C‐band had emerged to be of secondary importance. Random forest classification and support vector machines are two popular classification methods that were tested among others. In our results, the former had shown the best accuracy for all almost the considered scenarios and it was confirmed a powerful tool for classification purposes. The latter, on the contrary, was shown to suffer of unbalanced sensitivity among classes in some scenarios; this behavior could be also motived by the consistent number of hyperparameters that must be tuned to achieve optimality, which is an intrinsic limit of this algorithm with respect to random forest. This research could be also interesting in view of the OptiSAR Constellation mission, devoted to the Earth surface observation by means of spaceborne optical, L‐ and X‐band SAR sensors, with the aim of developing consistent applications in environmental, hazard and safety monitoring. This research was published in [30]

6. REFERENCES

[1] DREAM. Tenuta di San Rossore; Note illustrative della carta forestale e della fruizione turistica; D.R.E.Am. Italia Soc. Coop. Agr., Poppi, Italy; 2003.

[2] Corona, P.; Chirici, G.; Marchetti, M. Forest ecosystem inventory and monitoring as a framework for terrestrial natural renewable resource survey programmes. Plant Biosyst. Int. J. Deal. All Asp. Plant Biol. 2002, 136, 69–82.

[3] Breiman, L. Random Forests. Mach. Learn. 2001, 45, 5–32.

[4]. Quinlan, J.R. Combining Instance‐based and Model‐based Learning. In Proceedings of the Tenth International Conference on International Conference on Machine Learning, Amherst, MA, USA, 27–29 June 1993; Morgan Kaufmann Publishers Inc.: San Francisco, CA, USA, 1993; pp. 236–243.

[5]. Pal, M. Random forest classifier for remote sensing classification. Int. J. Remote Sens. 2005, 26, 217–222.

[6]. Camargo, F.F.; Sano, E.E.; Almeida, C.M.; Mura, J.C.; Almeida, T. A Comparative Assessment of Machine‐Learning Techniques for Land Use and Land Cover Classification of the Brazilian Tropical Savanna Using ALOS‐2/PALSAR‐2 Polarimetric Images. Remote Sens. 2019, 11, 1600.

[7] Yu, Y.; Li, M.; Fu, Y. Forest type identification by random forest classification combined with SPOT and multitemporal SAR data. J. For. Res. 2018, 29, 1407–1414.

[8] Marrs, J.; Ni‐Meister, W. Machine Learning Techniques for Tree Species Classification Using Co‐Registered LiDAR and Hyperspectral Data. Remote Sens. 2019, 11, 819.

[9] Hartling, S.; Sagan, V.; Sidike, P.; Maimaitijiang, M.; Carron, J. Urban Tree Species Classification Using a WorldView‐2/3 and LiDAR Data Fusion Approach and Deep Learning. Sensors 2019, 19, 1284.

[10] Schapire, R.E. The strength of weak learnability. Mach. Learn. 1990, 5, 197–227.

[11] Freund, Y.; Schapire, R.E. A Decision‐Theoretic Generalization of On‐Line Learning and an Application to Boosting. J. Comput. Syst. Sci. 1997, 55, 119–139.

[12] Yao, W.; Wei, Y. Detection of 3‐D Individual Trees in Urban Areas by Combining Airborne LiDAR Data and Imagery. IEEE Geosci. Remote Sens. Lett. 2013, 10, 1355–1359.

[13] Shiraishi, T.; Motohka, T.; Thapa, R.B.; Watanabe, M.; Shimada, M. Comparative Assessment of Supervised Classifiers for Land Use‐ Land Cover Classification in a Tropical Region Using Time‐Series PALSAR Mosaic Data. IEEE J. Sel. Top. Appl. Earth Obs. Remote Sens. 2014, 7, 1186–1199.

[14] Stavrakoudis, D.G.; Galidaki, G.N.; Gitas, I.Z.; Theocharis, J.B. A Genetic Fuzzy‐Rule‐Based Classifier for Land Cover Classification from Hyperspectral Imagery. IEEE Trans. Geosci. Remote Sens. 2012, 50, 130–148.

[15] Fix, E.; Hodges, J.L. Discriminatory Analysis. Nonparametric Discrimination: Consistency Properties. Int. Stat. Rev. Rev. Int. De Stat. 1989, 57, 238.

[16] Dudani, S.A. The Distance‐Weighted k‐Nearest‐Neighbor Rule. IEEE Trans. Syst. Man Cybern. 1976, SMC‐6, 325–327.

[17] Zhu, H.W.; Basir, O. An adaptive fuzzy evidential nearest neighbor formulation for classifying remote sensing images. IEEE Trans. Geosci. Remote Sens. 2005, 43, 1874–1889.

[18] Blanzieri, E.; Melgani, F. Nearest Neighbor Classification of Remote Sensing Images with the Maximal Margin Principle. IEEE Trans. Geosci. Remote Sens. 2008, 46, 1804–1811.

[19] Ndikumana, E.; Ho Tong Minh, D.; Baghdadi, N.; Courault, D.; Hossard, L. Deep Recurrent Neural Network for Agricultural Classification using multitemporal SAR Sentinel‐1 for Camargue, France. Remote Sens. 2018, 10, 1217.

[20] Carpenter, G.A.; Gjaja, M.N.; Gopal, S.; Woodcock, C.E. ART neural networks for remote sensing:Vegetation classification from Landsat TM and terrain data. IEEE Trans. Geosci. Remote Sens. 1997, 35, 308–325.

[21]. Hornik, K.; Stinchcombe, M.; White, H. Multilayer feedforward networks are universal approximators. Neural Netw. 1989, 2, 359–366.

[22] Linden; Kindermann Inversion of multilayer nets. In Proceedings of the International Joint Conference on Neural Networks, Washington, DC, USA, 1989; Volume 2, pp. 425–430.

[23] Santi, E.; Paloscia, S.; Pettinato, S.; Fontanelli, G. Application of artificial neural networks for the soil moisture retrieval from active and passive microwave spaceborne sensors. Int. J. Appl. Earth Obs. Geoinf. 2016, 48, 61–73.

[24] Vapnik, V.N. The Nature of Statistical Learning Theory; Springer: New York, NY, USA, 2000; ISBN 978‐1‐4757‐3264‐1.

[25] Boser, B.E.; Guyon, I.M.; Vapnik, V.N. A training algorithm for optimal margin classifiers. In Proceedings of the fifth Annual Workshop on Computational Learning Theory—COLT ’92, Pittsburgh, PA, USA, 27–29 July

1992; ACM Press: New York, NY, USA, 1992; pp. 144–152.
[26] Melgani, F.; Bruzzone, L. Classification of hyperspectral remote sensing images with support vector machines. IEEE Trans. Geosci. Remote Sens. 2004, 42, 1778–1790.
[27] Fisher, R.A. The Use of Multiple Measurements in Taxonomic Problems. Ann. Eugen. 1936, 7, 179–188.
[28] Bandos, T.V.; Bruzzone, L.; Camps‐Valls, G. Classification of Hyperspectral Images with Regularized Linear Discriminant Analysis. IEEE Trans. Geosci. Remote Sens. 2009, 47, 862–873.
[29] Bioucas‐Dias, J.M.; Plaza, A.; Camps‐Valls, G.; Scheunders, P.; Nasrabadi, N.; Chanussot, J. Hyperspectral Remote Sensing Data Analysis and Future Challenges. IEEE Geosci. Remote Sens. Mag. 2013, 1, 6–36.
[30] Lapini, A., Pettinato, S., Santi, E., Paloscia, S., Fontanelli, G., & Garzelli, A. (2020). Comparison of Machine Learning Methods Applied to SAR Images for Forest Classification in Mediterranean Areas. Remote. Sens., 12, 369.

INTEGRATION OF ALOS-2 AND SENTINEL-1 DATA FOR MONITORING OF FAST DEFORMATION CAUSED UNDERGROUND COAL EXPLOITATION IN UPPER SILESIAN COAL BASINS

PI No.: ER2A2N206

Kamila Pawluszek-Filipiak [1], Andrzej Borkowski[1]

[1] Insitute of Geodesy and Geoinformatics, Wroclaw University of Environmental and Life Sciences

1. INTRODUCTION

As was described in the project proposal, monitoring mining deformation is necessary to legislative requirements, predict subsidence, maximize of coal extraction and risk and environmental monitoring [1]. Mining monitoring conducted by traditional monitoring techniques as field survey using levels, total stations or GPS are labour-intensive and time-consuming when the study regions become large. Hence, the monitoring is usually constrained to very localized areas. Mining measurements on the levelling lines are generally performed one per year or sometimes even rarely Moreover, these techniques are point-by-point basis, thus, the spatial extent is not enough to assist in understanding the mechanism involved in ground subsidence [2].

Thus, Satellite Synthetic Aperture Radar Interferometry (InSAR), like any other remote sensing technique, captured considerable attention in subsidence monitoring by providing measurements of ground deformation. Many application of Sentinel-1 data have been demonstrated for subsidence or deformation monitoring [3]. However, for deformation with high deformation gradient, as well as in the vegetated areas, this data are not appropriate [4]. Therefore, the idea of the this project was **synergetic integration of ALOS-2 and Sentinel-1 data in order to measure the whole deformation range from mm/yr up to m/yr in the areas of active coal exploitation**.

Through, traditional DInSAR exploits single interferometric SAR pairs, the accuracy of this technique is limited by factors related to spatial and temporal decorrelation, signal delay as a result of atmospheric artefacts as well as orbital or topographic errors. In order to overcome abovementioned limitations, different techniques which exploit time series interferometric SAR analysis (TS-InSAR) have been proposed such as Persistent scattered interferometry (PSInSAR) or Small Baseline Subset [5-7]. **However, due to the limited number of ALOS-2 SAR images (5) in the GPortal, application of the PSInSAR approach was not possible.** Therefore, only one possible option was integration of ALOS-2 and Sentinel-1 by on the level of DInSAR processing.

From another point of view, by considering the high availability of ALOS-1 data, additional integration was made in term of time. More specifically long lime series monitoring of the mining areas by using various SAR sensors. It was carried out in the area of the Mieroszewskich palace where some crack exists which was deduced to be an effect of the mining activity in the past.

Taking into account such a valuable culture heritage, it is very important to answer the question what is causing the palace damages and in the authors opinion, satellite radar interferometry will be very helpful tool.

To investigate this issue we applied various SAR dataset to check the history of the deformation is this areas.

-Firstly, we will utilized ALOS-1 data from 2007-2011 to check if during this time, significant deformation occur in the area of interest, PSInSAR approach will be used for such purpose.

-Secondly we will apply available archive data from TerraSAR-X satellite from 2011-07-05 to 2013-01-27 to estimate deformation by using PSInSAR approach - Thirdly, we will utilized Sentinel-1 ascending and descending data for the period of 2014-2020 to estimate deformation by using PSInSAR approach.

-Finally, we will utilize TerraSAR-X images for the year of 1-04-2019 up 4-04.2021.This results was utilized as a

2. STUDY AREAS

First study area is Rydułtowy mine in the Upper Silesian Coal Basin, which is used as case study in appendixes A-B. Second study case is area of the Mieroszewskich Palace which is presented in the appendix C.

CASE STUDY 2

The Rydułtowy mine is the oldest active mine in the Upper Silesian Coal Basin (USCB) in Poland. The USCB is one of the largest hard coal mining areas in Europe. The Rydułtowy mine is located in the southwest part of the USCB (Figure 1-Appendix A,B) and covers approximately 46 km^2. The average daily production of the mine ranges between 9,000 and 9,500 t/day and the extraction depth reaches 800 - 1200 m. This area was investigated during the EPOS-PL project, which allowed the purchase of five passive corner reflectors (CRs) and placed them in the area of interest. EPOS-PL is the Polish implementation of the European Plate Observing System (EPOS) initiative, which aims at the integration of existing and newly created research infrastructures to facilitate the use of multidisciplinary data and products in the field of Earth sciences in Europe.

CASE STUDY 2
Mieroszewskich Palace building is a baroque-classicist building erected in 1702 as a symbol of the position and rank of the Mieroszewskich family in the Duchy of Siewier, it is a typical 18th-century noble residence modeled on French palaces. It is a late baroque, one-story palace, with a mansard roof, two-bay, with an enfilade arrangement of rooms. After renovation in 1958, the building was turned into a Children and Youth Culture Center. He performed this role until the 1970s. From the mid-1960s, the management of the Museum in Będzin, together with the Provincial Conservator of Monuments, made efforts to change its function and start comprehensive conservation of the entire palace and park complex. In March 1982, after years of efforts and work carried out by the Monuments Conservation Studios in Krakow, the USCB Museum in Będzin presented stylish 18th and 19th-century interiors to the visitors to the palace opening. The interior design of the eighteenth-century interiors is complemented by fireplaces, stylish furniture, artistic craftsmanship and a collection of portrait and landscape paintings from the eighteenth - nineteenth centuries. The palace interiors also exhibit works by artists from USCB and archaeological and ethnographic collections.

3.METHODOLOGY

As was mentioned in the introduction section, ALOS data have been used in two aspect. First aspect utilized ALOS-2 data altogether with Sentinel-1 by the integrated DInSAR approach to appropriate estimate deformation form the active mining exploitation. Methodology flowchart is attached in the appendix A and B.
Second aspect was made by the integration of the ALOS-1 data altogether with other SAR mission for the long term monitoring post mining area in the Mieroszewskich Palace. For that aspect we utilized PSInSAR approach to facilitate mm-level accuracy. Also it was possible due to the availability of the bigger amount of SAR Scenes (at least 20 is needed for the PSInSAR calculations). All utilized data are presented in the Appendix C.

4. RESULTS

Integration of the DInSAR results from ALOS-2 and Sentinel-1 by using various strategies which are deeply described in the appendix A-B, are presented in the following table. As can be observed , the best results are received for the integration option 2D+1D, for the Sentinel-1 and ALOS-2 data.

	Integration and decomposition			
	Sentinel-1 only		Sentinel and ALOS-2	
Deformation component	3D	2D+1D	3D	**2D+1D**
Vertical [m]	0.065	0.038	0.052	**0.032**
Easting [m]	0.046	0.031	0.038	**0.018**
Northing [m]	0.572	0.034	0.288	**0.024**

The results of the second aspect are presented in the figure 1 in the appendix C. As can be observed, in each cases there were no characteristic basins which can suggest that cracks detected in the Mieroszewickich palace are the source of the post mining activity. Integration of ALOS-1, TerraSAR-X and Senitnel-1 data allow for the long time investigation of the mining and post mining areas.

5. DISCUSSION

Achieved results of ALOS-2 and Sentinel-1 data indicated the positive value of the additional to freely available Sentinel-1 data for the proper estimation of the vertical and horizontal deformation component. Unfortunately, in the areas of the study only 5 ALOS-2 data were available. Thanks to the long wavelength of the ALOS-2 mission, coherence was still enough to carry out the satellite interferometry by using conventional DInSAR approach. Unfortunately this amount of data is not enough for PSInSAR approach, therefore this method could not be applied. Nevertheless, it is foreseen that in another case studies where more ALOS-2 data is available, the results of the Sentinel- and ALOS-2 data integration will be much more accurate. Especially, when at least 20 ALOS-2 images are available, PSInSAR approach can be utilized which is known for its better performance.
Additionally, results of the Appendix c- integration of various sensors in the case of the long time monitoring by taking advantage of various time of the imaging of various satellites allows to answer many question about the surrounding environment. Thanks to the various mission it was possible to cover approximately time span of 10 years, which is very beneficial and unavailable with another geodetic measurement techniques.

6.CONCLUSIONS

In each of the investigated aspect ALOS missions proved to be beneficial for monitoring of mining and post mining areas. Benefits comes from longer wavelength of the ALOS SAR sensor applied in that mission. Additionally, ALOS-1 mission is beneficial in application in long term monitoring of infrastructures in the mining areas.
Unfortunately, in the mining area of USCB, ALOS-2 data availability is very limited. This makes impossibility to apply more sophisticated time series interferometric techniques as well as limits the revisiting time of the SAR measurements.

6. REFERENCES

[1] M. Przyłucka, G. Herrera, M. Graniczny, D. Colombo and Béjar-Pizarro, M. (2015). „Combination of conventional and advanced DInSAR to monitor very fast mining subsidence with TerraSAR-X data: Bytom City (Poland)". *Remote Sensing*, 7(5), 5300-5328.

[2] K. Pawluszek-Filipiak and A. Borkowski (2020). „Integration of DInSAR and SBAS Techniques to determine mining-related deformations using sentinel-1 data: The case study of Rydułtowy mine in Poland". *Remote Sensing*, 12(2), 242.

[3] K. Pawluszek-Filipiak and A. Borkowski (2021). „Monitoring mining-induced subsidence by integrating differential radar interferometry and persistent scatterer techniques". *European Journal of Remote Sensing*, 54(sup1), 18-30.

[4] Z. Du, L. Ge, X. Li, and A. H. M. Ng, (2016). "Subsidence monitoring over the Southern Coalfield, Australia using both L-Band and C-Band SAR time series analysis." *Remote Sensing*, 8(7), 543.doi: 10.3390/rs8070543

[5] P. Berardino, G. Fornaro, R. Lanari and E. Sansosti,. (2002). "A new algorithm for surface deformation monitoring based on small baseline differential SAR interferograms." *IEEE Transactions on Geoscience and Remote Sensing*, 40(11), 2375-2383, doi: 10.1109/TGRS.2002.803792

[6] A. Ferretti, C. Prati, and F. Rocca, F. (2001). "Permanent scatterers in SAR interferometry." *IEEE Transactions on geoscience and remote sensing*, 39(1), 8-20.

[7] C. Colesanti, A. Ferretti A, C. Prati and Rocca, F. (2003). "Monitoring landslides and tectonic motions with the Permanent Scatterers Technique." *Engineering geology*, 68(1-2), 3-14.

RESENTATION AT THE INTERNATIONAL CONFERENCES

Results achieved within the 2nd Research Announcement on the Earth Observations (EO-RA2) were or will be selected on the following international meetings and conferences.

[1] The Joint PI Meeting of JAXA Earth Observation Missions FY2020. "An attempt to estimate horizontal and vertical displacements over the underground minig using DInSAR in the area of Rydułtowy mine, Poland". *Authors: Kamila Pawluszek-Filipiak; Natalia Wielgocka, Damian Tondaś, Andrzej Borkowski*

[2] 1st EPOS+ national conference, 25th of March, 2021 "The use of satellite radar interferometry for the determination and prediction of land surface deformation in mining areas", authors: *Kamila Pawłuszek – Filipiak, Krzysztof Stasch, Maya Ilieva, Andrzej Borkowski, Przemysław Tymków, Paweł Bogusławski, Natalia Wielgocka, Mateusz Karpina*

[3] ISPRS congress Nicea 2022."Assessing the effect of ALOS-2 data utilization on the accuracy of estimation vertical and horizontal deformation components in the area of hard coal mining exploitation in Poland by using differential synthetic aperture radar interferometry." *Authors: Kamila Pawluszek-Filipiak; Natalia Wielgocka, Damian Tondaś, Andrzej Borkowski*

APPENDIX

Appendix A: conference paper from ISPRS congress in Nice which presents the integration of 5 scenes of ALOS-2 data with the data of the Senitnel-1 for the year of 2019.

Appendix B: poster form the Joint PI Meeting of JAXA Earth Observation Missions FY2020

Appendix C: document/paper draft in which integration of the ALOS data was made in terms of time. More specifically, various SAR data have bed utilized in order to evaluate the if the mining deformation existed in the investigated study case.

3.13 Polarimetry and interferometry

INSARにおける電離層および中性大気遅延効果の補正手法高精度化に関する研究

PI No.: ER2A2N001
木下 陽平 [1]

[1] 筑波大学システム情報系

1. INTRODUCTION

合成開口レーダー干渉法（InSAR）は面的かつ高精度（cm オーダー）・高空間分解能（数 m から数十 m）に地表面変位を観測できる宇宙測地技術の一つであり、これまでに地球科学および工学分野において数多くの研究成果を挙げてきた（例えば[1-3]）。しかしながら、観測にマイクロ波を用いる InSAR は GNSS 同様に地球大気による大気伝搬遅延効果を受けるため、観測量には地表面変位の寄与の他に大気による見かけの変位が重畳し、地表面変位検出精度を数 cm 程度のレベルに制限している [4]。この大気遅延に対する補正手法の開発研究はこれまでに数多くなされており、現在代表的な補正手法には、電離層遅延に対しては Range Split-Spectrum Method (SSM; [5])、中性大気遅延に対しては数値気象モデルの出力データを用いた補正手法（e.g.[6]）がある。電離層補正については SSM により高精度に補正できることが複数の研究で報告されているものの（e.g. [7]）、中性大気遅延補正についてはいまだ十分な補正効果を実現しているとは言い難く、さらなる研究が求められている。

本研究では、主に中性大気遅延補正を対象に、従来にない新たな補正手法を提案し、その補正効果を検証した。具体的には、GNSS の天頂遅延量（ZTD）データと水平遅延勾配データを用いた補正手法を開発し、ALOS-2 の ScanSAR データを用いて補正効果の検証を行なった。加えて関連研究として、InSAR で推定した可降水量および天頂遅延量観測の精度評価を GNSS と比較することで行なった。電離層補正については SSM の補正精度を定量的に評価したので、その結果についても報告する。

2. GNSS 天頂遅延量と遅延勾配を用いた INSAR 大気遅延補正モデルの開発

本研究では、Arief and Heki [8] にて提案された天頂湿潤遅延量（ZWD）の格子面復元手法を応用して、ZTD の面的分布を復元することにより InSAR 補正モデルの構築を行なった。本手法の基本的な理論・構成は [8] と同様であるが、以下の点について本研究独自の変更を行なった。

- InSAR 中性大気遅延は乾燥・湿潤遅延の両方が含まれるため、使用・推定する物理量を ZWD から ZTD に変更した。
- 使用する観測点を海岸線付近のみではなく、使用可能な全ての観測点を使用した。
- InSAR 遅延遅延で顕著よく知られている成層遅延効果（Stratified delay component）を精度良く推定するため、ZTD の標高依存効果について 1 次関数を組み込むことでモデル化した。
- ZTD 復元の際の観測方程式には ZTD のスケールハイトが必要であるため、本研究ではラジオゾンデデータを用いて推定した。

これらの変更により、InSAR 大気遅延効果をより高精度に推定することを図った。補正モデルの入力データにはネバダ大学測地研究室（NGL）が公開している 5 分間隔 PPP 解析の結果を使用した [9]。国土地理院が公開している 3 時間間隔の天頂遅延量データと比較してより InSAR 観測時刻に近い時刻の観測データを使用でき、天頂遅延分布の高い再現性が期待できる。

開発した補正モデルの検証用データには、L バンド SAR 衛星の ALOS-2/PALSAR-2 ScanSAR（WD1）データを使用した。観測領域は関東平野周辺で、パスおよびフレームは 17-2900 である（Fig. 1）。干渉処理には RINC ver.0.41（[10]）を使用し、高精度軌道情報と SRTM 1 arc-second DEM を用いて軌道縞および地形縞をシミュレートした。ALOS-2/PALSAR-2 は長波長の L-band であり電離層の影響が大きいことが知られている。本研究では SSM により電離層起源の位相擾乱（正確には分散性の遅延効果）を補正した。SSM による補正効果の検証結果は 3 章に記載している。なお解析期間中（2016 年 1 月から 2020 年 4 月）に茨城県北部にて 2016 年 12 月 23 日に M6.3 の地震が発生している（Fig. 1 内の黄色の星印）。この地震による地表面変位の影響を避けるため、この日を含む干渉ペアは使用していない。

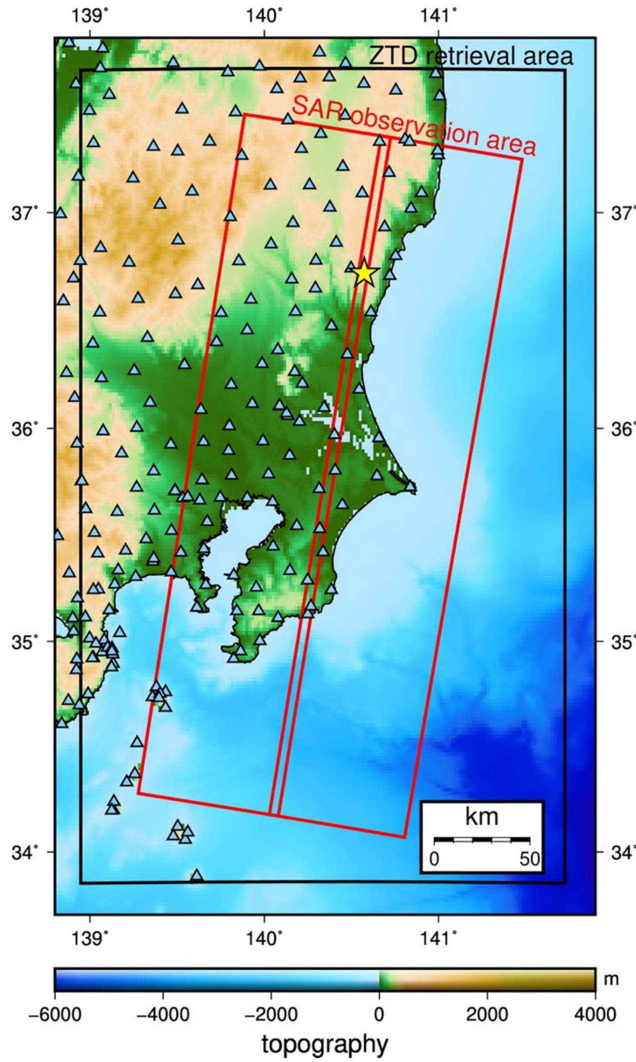

Fig. 1 Geographic condition in this study. The contour color map shows the topography. Black and red rectangles represent the area of the gridded ZTD model and the ALOS-2 SAR coverage, respectively. Triangles colored in light blue represent locations of GNSS stations. The yellow star symbol represents the earthquake epicenter with the Japan Meteorological Agency's magnitude of 6.3 occurred on 28 December 2016.

まずはラジオゾンデによるスケールハイトの推定結果について述べる。ラジオゾンデデータには日本国内で定期観測が実施されている 16 観測点全ての利用可能な観測データを使用した。使用したデータの観測期間は 2011 年から 2020 年の 10 年間である。観測データから各高度での ZTD を計算し、地表面での ZTD が 1/e 倍になる高度を、指数関数 fitting により求め、全期間の平均値を求めた。結果的に ZTD スケールハイトの推定値は 6930.8±389.2 m となった。以後、本研究では 7000 m を ZTD スケールハイトとして使用した。

次に ZTD の面的分布推定の結果について述べる。推定した ZTD の面的分布が元の ZTD ポイントデータをどの程度再現できているか、それぞれの差分を取ることで検証した。なお ZTD の面的分布復元についての概要図は Fig. 2 に示している。比較検証の結果、復元した ZTD とオリジナルの ZTD データとの残差の平均および標準偏差は 0.14±2.89 mm となり、2000 から 3000 mm のオーダーを持つ ZTD の復元制度としては十分高い結果であった。

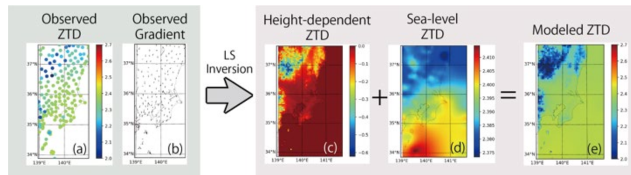

Fig. 2 A brief example of the processing flow in the gridded ZTD retrieval.

Table. 2 Statistics of the gridded ZTD retrieval result.

Date	mean of residual (mm)	STD of residual (mm)
2016/01/23	0.09	2.03
2016/03/19	0.06	2.98
2016/04/30	0.12	2.52
2016/07/23	0.18	2.79
2016/12/24	0.08	2.48
2017/04/15	0.15	3.78
2017/05/13	0.12	2.79
2017/09/30	0.15	3.39
2017/10/14	0.14	3.18
2017/12/23	0.10	2.45
2018/04/14	0.12	2.73
2018/09/29	0.18	3.26
2018/12/22	0.23	3.45
2019/09/28	0.22	3.37
2019/12/21	0.14	2.72
2020/04/11	0.10	2.40
Average	0.14	2.89

InSAR データへ適用・補正した結果、従来の中世大気遅延補正手法と比較して本研究で開発した補正手法は高い補正効果を示した。一例として Fig. 3 に補正適用前後の InSAR 画像を示す。Fig. 3 で用いた InSAR 画像は 2016 年 3 月 19 日と 2016 年 4 月 30 日に撮像された SAR 画像を用いており、観測間隔が短い（42 日間）ため、高い干渉性（コヒーレンス）を示しておりかつ地表面変位の影響も含まれていない可能性が高い。元々のオリジナル InSAR 画像（Fig. 3a）では主に東西方向に長周期の位相変化が 2 サイクルほど見えており顕著であるものの、SSM による電離層補正を適用することで概ね補正できている（Fig. 3b）。しかし電離層補正のみでは北西-南東方向にかけての長周期の位相変化が残っており、電離層補正のみでは補正が十分ではないことも視認できる。この電離層補正済み InSAR 画像に本研究で開発した GNSS ベースの補正モデルを適用した結果を Fig. 3c に示す。GNSS ベースの補正により、Fig. 3b では残っていた北西-南東方向の位相変化は概ね補

正・除去されており、補正後 InSAR 画像には数 km スケールの大気遅延ノイズが散見されるというレベルにまで補正できている。Fig. 3 では比較のために、気象庁メソスケールモデル（MSM）による補正および近年公開された GACOS モデル（[6]）による補正を適用した InSAR 画像を Fig. 3d および Fig. 3e にそれぞれ示している。目視でも確認できるように、MSM および GACOS による補正では GNSS ベースの補正に比べ大きな位相変化が残っており、GNSS ベースの補正がこれら従来の補正手法より効果的に補正を実現していることが分かる。

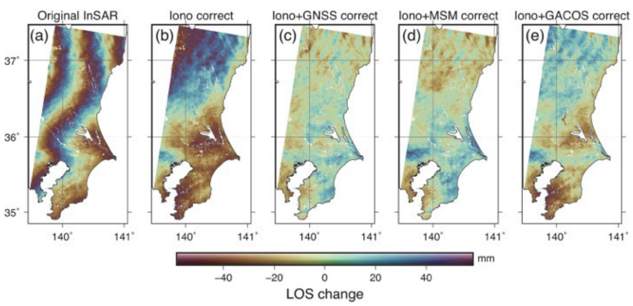

Fig. 3 (a) An original wrapped interferogram of 19 March 2016 and 30 April 2016 over Kanto region. No corrections were applied in this image. (b) An interferogram that the ionospheric correction was applied to the interferogram (a). (c-e) Phase residuals corrected for the GNSS-based, MSM, and GACOS delay model, respectively. The model phase was subtracted from (b).

上述の補正手法を、38 の InSAR 画像に適用した結果を Fig. 4 に示す。Fig. 4 は InSAR 画像における位相の標準偏差について、補正前後の値をそれぞれ縦軸・横軸として図示した散布図である。Fig. 4 には GNSS ベースの補正結果（Fig. 4 の青丸）に加え、MSM による補正（Fig. 4 の赤四角）、GACOS による補正（Fig. 4 の緑三角）も図示している。Fig. 4 から、ほぼ全ての InSAR 画像に対して GNSS による補正の効果が最も高いことが見て取れる。38 ペアのうち 2 ペアのみ、GNSS による補正適用で位相の標準偏差が増加した（適切に補正できなかった）ペアがあるものの、統計的には十分な補正効果を示した。位相の標準偏差は 38 ペアの平均で 35.02 mm から 23.16 mm へと約 34%低減できている。MSM および GACOS による補正では補正適用により平均で 26.04 mm（約 26%）および 29.31 mm（約 16%）の低減となり、統計的にも GNSS による補正が優れていることが分かった。遅延補正効果の距離依存性についても、Fig. 5 に示すセミバリオグラムから、主に距離 50 km 以上の範囲で大気遅延補正がよく機能している様子が見て取れる。セミバリオグラム（Fig. 5b）においても、GNSS による補正が他の補正手法と比べてより高い補正効果を示していることが見て取れる。

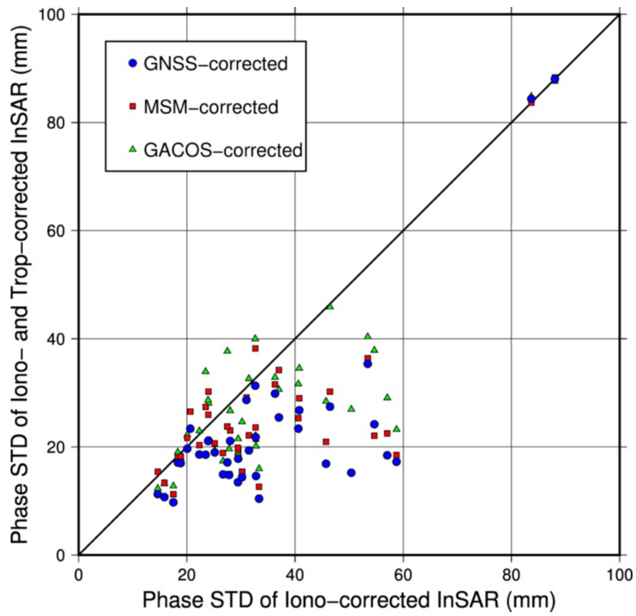

Fig. 4 Phase standard deviation differences from ionosphere-corrected interferograms (shown in Figure 6) against interferograms corrected by the SSM and neutral atmospheric delay models. Each dot represents the single interferogram. Blue circles, red rectangles, and green triangles represent interferogram phase standard deviations corrected by the GNSS-based delay model, the MSM, and the GACOS, respectively.

これらの結果から、本研究で開発した GNSS 観測（ZTD と遅延勾配データ）に基づく InSAR 中性大気遅延補正モデルは、従来の補正手法を上回る補正効果を示しており、大気遅延補正に対して有効な補正手法の一つとなることが期待できる。ただし本研究で開発した補正手法の短所として、GNSS 観測データを利用できない地域においてはそもそも補正の適用ができないことが挙げられる。これは稠密 GNSS 観測網（GEONET）が展開されている日本国内においては問題とならないものの、アフリカや東南アジアなど一部地域においては大きな問題となる。この点を克服するためには、GNSS 地上観測点を増加させることの他に、例えば GACOS のように全球数値気象モデルの出力データを融合利用するなどモデルそのものの改良が有効であると考える。

本章で報告した研究の成果は、執筆時点（2022 年 3 月 31 日）において国際学術誌に論文原稿を投稿済みであり、現在改訂稿の査読中である。

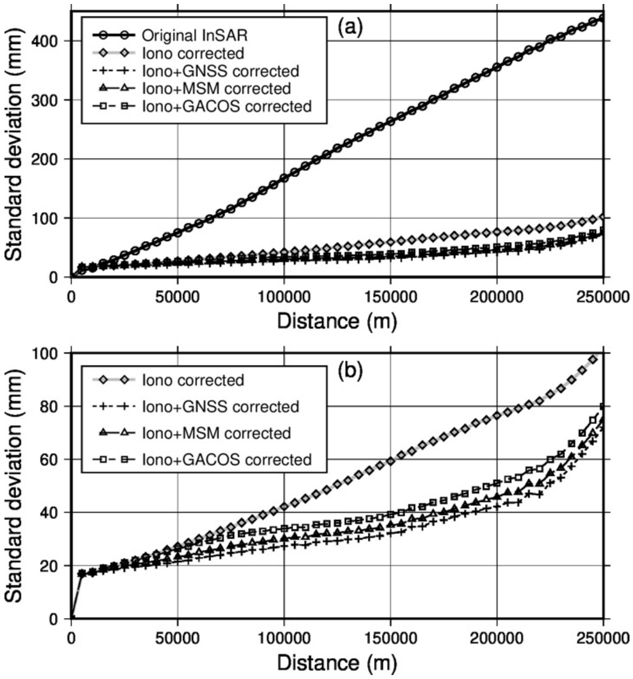

Fig. 5 (a) A figure representing phase standard deviations as a function of distance. Circles with a solid bold black line is derived from interferograms without any corrections, diamonds with dashed black line is from ionosphere- corrected interferograms, plus symbols, triangles, rectangles with dashed lines are from interferograms with the GNSS-based correction, the MSM correction, and the GACOS correction, respectively. (b) Enlarged view of (a) to focus the difference between three neutral atmospheric delay correction models. The original interferogram is omitted in (b).

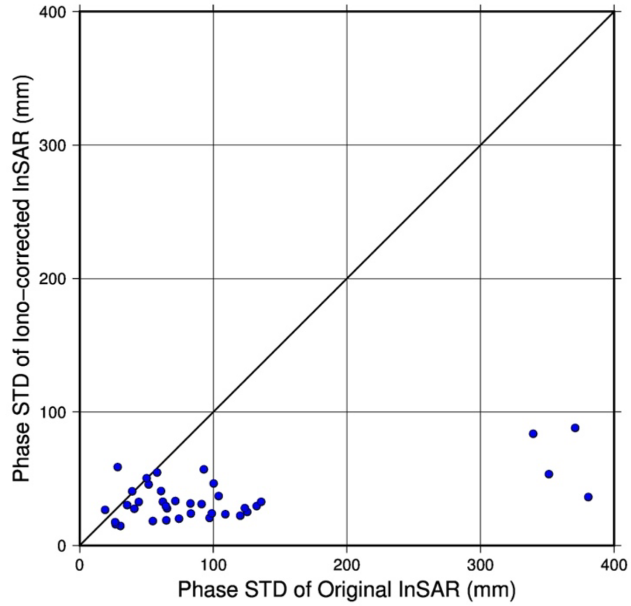

Fig. 6 Phase standard deviation differences from original interferograms against ionosphere-corrected interferograms. Each dot represents the single interferogram.

3. SSM による L-BAND INSAR 電離層補正効果の検証

本章では 2 章の研究において使用した ALOS-2/PALSAR-2 ScanSAR 干渉画像に対し、SSM による電離層補正をした結果を報告する。

Fig. 4 と同様に、位相の標準偏差を電離層補正前と後で計算し、それぞれ縦軸・横軸に標準偏差を設定して図示した散布図が Fig. 6 である。Fig. 6 より、SSM による電離層補正は ScanSAR データに対して非常に有効であることが分かる。使用した全 InSAR データについての位相の標準偏差の平均は、補正前の 102.87 mm から補正適用により 35.02 mm に低減し、これは約 66%の位相擾乱を補正できたことを示している。先行研究において本研究のように SSM による電離層補正の統計的・定量的な評価をした研究は見かけていないため、本研究で示した統計的評価結果は世界初のものと考えられる。

4. L-BAND INSAR による大気観測の精度評価

本研究では InSAR 大気遅延と同じ物理量を観測できる GNSS ZTD データを利用して、InSAR 大気観測に対する精度評価を行なった。この研究は、2 章で開発した GNSS を用いた遅延補正手法の開発において、GNSS 大気遅延観測データの有効性を検証することに寄与している。本研究はすでにオープンジャーナル”Remote Sensing”に原著論文（[11]）として掲載されており、本報告書にも参考資料として添付しているため、詳細は割愛する。

本研究では ALOS-2/PALSAR-2 の SM1 モードで得られた InSAR 画像から天頂遅延量（ZTD）および可降水量（PWV）を推定し、GNSS から得られる同観測量と比較をすることで InSAR ZTD, PWV の GNSS に対する相対的観測精度を求めた。また先行研究による GNSS ZTD, PWV の絶対誤差の数値と誤差伝播理論を用いて、InSAR ZTD, PWV の絶対誤差（観測精度）も推定した。対象地域には日本国内の 4 地域（北関東、関東西部、大阪、九州南部）を選定し、ZTD から PWV 計算の際の変換係数は AMeDAS 地上気象観測データから推定している。GNSS のデータには 2 章同様にネバダ大学測地研究室が公開している PPP 解析データを利用した。また全ての InSAR 画像は事前に SSM により電離層補正を適用している。

まず GNSS との比較の結果を示す。4 つの地域それぞれでの InSAR と GNSS での ZTD の残渣を Fig. 7 にヒストグラムで示す。この図から ZTD 残渣の分布は正規分布に近い形を示しており、電離層の取り残

しなどによる bias や skew は小さいことが分かる。利用可能な InSAR 画像および GNSS 観測点数の違いから、地域によって正規分布モデルの fitting 精度に違いが見られるものの、概ねよい一致を示した。Fig. 8 には 4 地域すべての ZTD 残差をまとめた結果を示している。こちらの図からも、ZTD 残差の分布は正規分布に従っていることが見て取れる。統計的な数値の結果は、InSAR ZTD の GNSS からみた相対誤差は標準偏差で 7.36 mm となった。InSAR ZTD を推定する時点で、推定値全体の offset を GNSS により補正しているため、平均（bias）はゼロである。この結果から誤差伝播理論を用いて絶対誤差（精度）を評価したところ、InSAR ZTD の絶対誤差は 18.03 mm、InSAR PWV の絶対誤差は 2.96 mm となった。この結果は他の PWV 観測手段と比較してもそれほど悪くはない観測精度と言える（Fig. 9）。

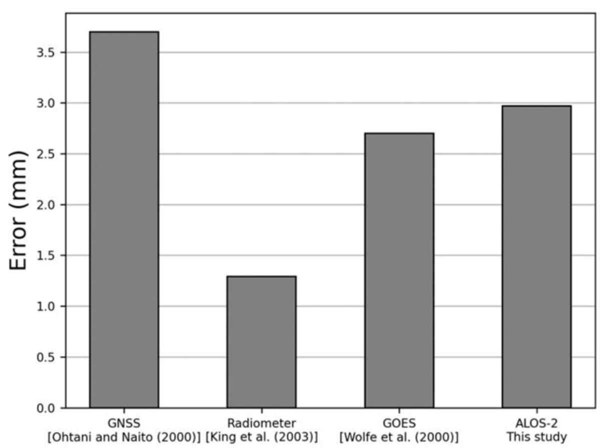

Fig. 9 Absolute errors of PWV observations.

5. まとめ

本研究では InSAR 大気遅延効果を対象に、1) GNSS 観測データに基づく InSAR 中性大気遅延補正モデルの開発と検証、2) SSM による電離層補正の補正効果の統計的検証、そして 3) GNSS と InSAR の ZTD および PWV 観測の比較を通じた観測精度の評価を実施した。いずれの研究においても良好な結果を得ており、4 章の研究についてはすでに国際学術誌”Remote Sensing”へ原著論文として掲載済み、2 章の研究についても国際学術誌に改訂稿査読中である。

6. REFERENCES

[1] D. Massonnet, M. Rossi, C. Carmona, F. Adragna, G. Peltzer, K. Feigl, and T. Rabaute “The displacement field of the Landers earthquake mapped by radar interferometry” *Nature*, 364(6433), 138-142, 1993.

[2] Y. Takada, and Y. Fukushima, “Volcanic subsidence triggered by the 2011 Tohoku earthquake in Japan” *Nature Geoscience*, 6(8), 637-641, 2013.

[3] M. P. Poland, and H. A. Zebker, “Volcano geodesy using InSAR in 2020: the past and next decades” *Bull. Volcanol.,* 84(27), 2022.

[4] H. A. Zebker, P. A. Rosen, and S. Hensley, “Atmospheric effects in interferometric synthetic aperture radar surface deformation and topographic maps” *J. Geophys. Res. Solid Earth*, 102(B4), 7547-7563, 1997.

[5] G. Gomba, A. Parizzi, F. De Zan, M. Eineder, and R. Bamler, “Toward operational compensation of ionospheric effects in SAR interferograms: The split-spectrum method” *IEEE Transactions on Geoscience and Remote Sensing*, 54(3), 1446-1461, 2015.

[6] C. Yu, Z. Li, N. T. Penna, and P. Crippa, “Generic atmospheric correction model for interferometric synthetic aperture radar observations” *J. Geophys. Res. Solid Earth*, 123(10), 9202-9222, 2018.

[7] M. Furuya, T. Suzuki, J. Maeda, and K. Heki, “Midlatitude sporadic-E episodes viewed by L-band split-spectrum InSAR,” *Earth Planets Space*, 69(1), 1–10, 2017.

[8] S. Arief and K. Heki, “GNSS meteorology for disastrous rainfalls in 2017–2019 summer in SW Japan: a new approach utilizing atmospheric delay gradients,” *Front. Earth Sci.*, 8, 2020.

[9] G. Blewitt, W. C. Hammond, and C. Kreemer, “Harnessing the GPS data explosion for interdisciplinary science,” *Eos*, 99, 2018.

[10] T. Ozawa, E. Fujita, and H. Ueda, “Crustal deformation associated with the 2016 Kumamoto Earthquake and its effect on the magma system of Aso volcano,” *Earth Planets Space*, 68(1), 1–15, 2016.

[11] K. Matsuzawa, and Y. Kinoshita, “Error Evaluation of L-Band InSAR Precipitable Water Vapor Measurements by Comparison with GNSS Observations in Japan”. *Remote Sens.* 13(4866), 2021.

APPENDIX

[1] K. Matsuzawa, and Y. Kinoshita, “Error Evaluation of L-Band InSAR Precipitable Water Vapor Measurements by Comparison with GNSS Observations in Japan”. *Remote Sens.* 13(4866), 2021.

MOMENT AND STRAIN ACCUMULATION RATE ALONG THE SAN ANDREAS FAULT SYSTEM FROM INSAR AND GPS (EO-RA2)

PI No.: ER2A2N015

Xiaohua Xu[1], David Sandwell[2], Bridget Smith-Konter[3], Yuri Fialko[2], Xiaopeng Tong[4], Christopher Crosby[5], Paul Wessel[3], Eric Fielding[6], Zhen Liu[6], Cunren Liang[7], Roland Burgmann[8], [9]Manoochehr Shirzaei, and [10]Alejandro Gonzalez

[1] University of Texas at Austin
[2] University of California at San Diego
[3] University of Hawaii at Manoa
[4] China Earthquake Administration
[5] UNAVCO
[6] Jet Propulsion Laboratory/Caltech
[7] Peking University
[8] University of California, Berkeley
[9] Verginia Tech University
[10] CICESE

1. INTRODUCTION

The original objective of this proposal was to continue our research on understanding of seismic moment and stress accumulation rate along the San Andreas Fault System using InSAR observations from ALOS-2, Sentinel-1 and GNSS measurements. It was written in November 2018 as a backup plan to the research objective, since we did not know whether the prior RA6 proposal (PI NO.: 3071) will be extended. After we received the announcement that the prior RA6 proposal will be extended, we decided that the data quota from this proposal will be mainly used for advancing the development of processing approaches in GMTSAR related to ALOS-1 and ALOS-2 data. The results will further ensure the goals described in RA6 3071, the original form of this proposal and any future proposals under JAXA RA programs.

2. DEVELOPMENTS AND RESULTS

Phase gradient estimator for ALOS-1 / ALOS-2

We developed the phase gradient estimator original for detection of small changes associated with earthquake ruptures. The phase gradient approach is able to reveal small motions that are localized to nearby cracks or faults next to the main rupture [1]. Fig.1 shows the basic theory why taking a phase gradient will help the detection of small changes. The top plot shows the simulated deformation from an earthquake rupture in unwrapped and wrapped forms at C-band. Without further help, the small crack at -5km away from the fault will not be identified. The middle plot shows after taking the gradient, the motion from this crack shows up nicely. Despite the effectiveness in detecting small changes, taking the phase gradient will magnify noise, making this technique inapplicable in cases of loss of coherence. Usually, this can be addressed with stacking multiple acquisitions together thus the noise level is reduced. The bottom plot of Fig.1 gives an example how stacking could help reduce the noise in the phase gradient measurement.

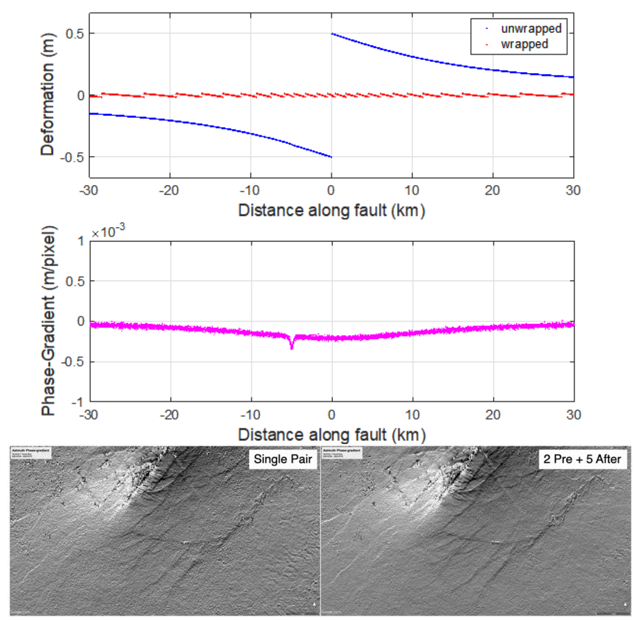

Fig. 1 Phase gradient approach

With this approach, we were able to reveal hundreds of small fractures next to the rupture region of the 2019 Ridgecrest earthquakes (Fig.2 top) [2-3]. We used kinematic slip model derived from ALOS-2 and Sentinel-1 InSAR measurements, ALOS-2 Multi-Aperture Interferometry, GNSS and optical offset estimates, to calculate the stress and strain release from this earthquake and found that the nearby faults with backward motion are consistent with compliant fault deformation, while the faults with forward motion are likely frictional slip [2]. These findings indicate the release of shallow strain may be much more distributed than scientists have believed.

Note the very straight lines are burst discontinuities caused by azimuthal motion from the earthquake rupture.

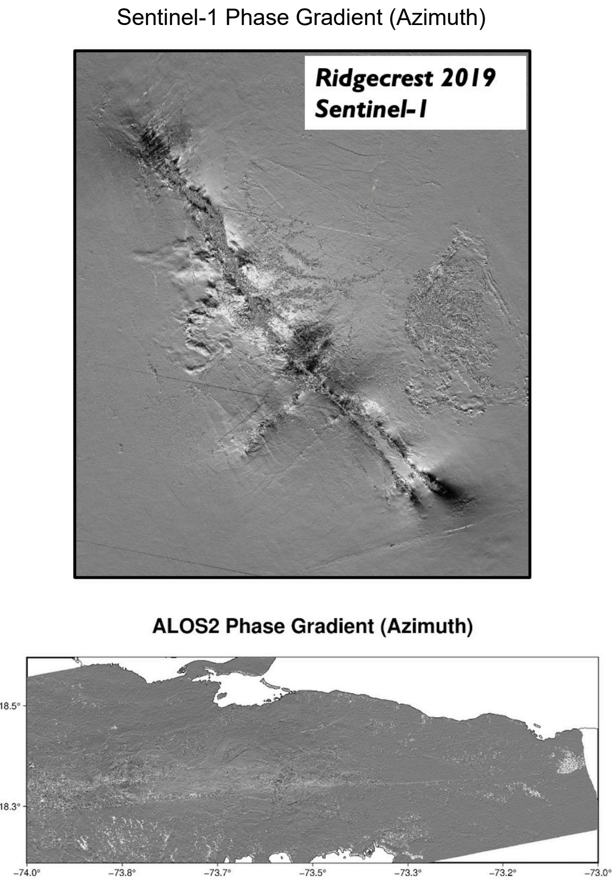

Fig. 2 Phase gradient results from Sentinel-1 for Ridgecrest earthquake (top) and Haiti Earthquake (bottom)

We experimented similar analysis over the recent 2021 Haiti earthquake, but the decorrelation from the heavy vegetation is too strong over the tropical region and even with stacking, the resulting phase gradient map is filled with noise. We then built an estimator of phase gradient for the ALOS-2 Stripmap data over the rupture region, considering that the L-band data is less subject to decorrelation noise from vegetation. Despite the strong noise, the deformation associated with some nearby faults showed up nicely with just a single pair of interferogram. The post-seismic creep toward the east is also detected by this technique. We also tried on the ScanSAR data but the quality of phase gradient maps is not as great, which could be due to the narrower range bandwidth of the data. This result could have been much better if there are more ALOS-2 Stripmap data acquired over the area. A paper that discusses these results is lead by a student at UCSD and is under preparation.

Ionosphere estimator for ALOS-1 / ALOS-2

We developed the ionospheric phase estimator in GMTSAR following several prior publications [4-7]. The overall idea is to bandpass the radar measurements in the ranging direction thus the dispersion of the electromagnetic beam through electron content could be used as a diagnostic of the volume of electron content itself [4]. ALOS satellites are acquiring data at L-band, which is subject to much stronger (wavelength squared) ionospheric delay than radar at smaller wavelengths. Over the duration of this proposal, we first implemented the ionospheric correction for ALOS-1 raw and SLC data and validated the effectiveness of our approach with prior publications (Fig.3). Following that, we further implemented and automated the ionospheric phase estimation in GMTSAR for ALOS-2 Stripmap and ScanSAR data (Fig.4) [8]. For both figures, the left column is the original data, the middle column is the estimated ionospheric phase and the right plot is the corrected phase. These implementations will help reduce the artifacts of radar phase from propagation delay through the ionosphere and help the deformation analysis. Eventually we would like to build a time-series similar to prior studies [9-10] and build a robust strain rate map combining measurements from Sentinel-1, ALOS-2, GNSS and the future NISAR data.

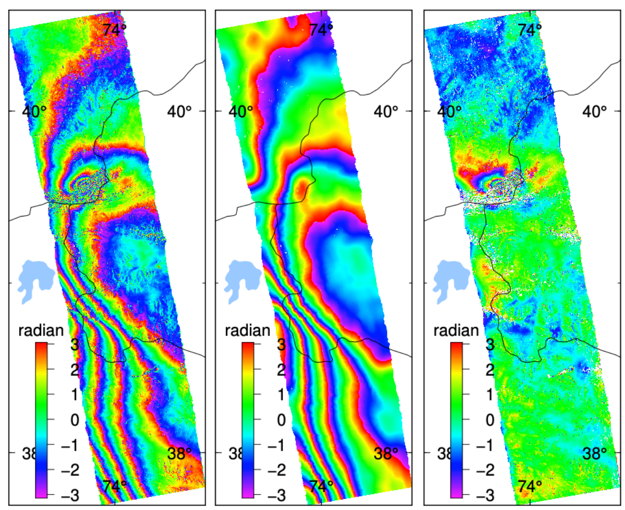

Fig. 3 Ionospheric phase estimation for ALOS-1 data

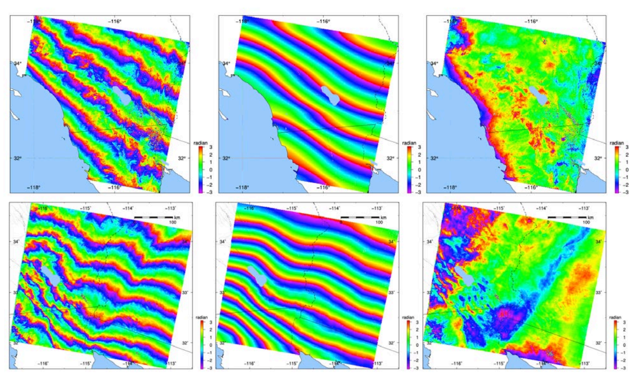

Fig. 4 Ionospheric phase estimation for ALOS-2 data

Multi-Aperture Interferometry Processor

We implemented and automated the multi-aperture interferometry processor for ALOS-1 and ALOS-2 data into GMTSAR. The processor band-passes the Single-Look Complex images in the azimuth direction and forms double difference interferograms for measurement of deformation along the track direction. This processor was used to map the azimuthal motion associated with the 2019 Ridgecrest earthquakes [2]. Adding this information helped reveal the smaller amplitude of rupture over the fault junction of the conjugate ruptures. It is noted that this measurement is subject to very short wavelength ionospheric perturbations, where the ionosphere gradient approach [7] may not fully capture the variabilities within such small scales. It is yet to be explored how such artifacts could be mitigated.

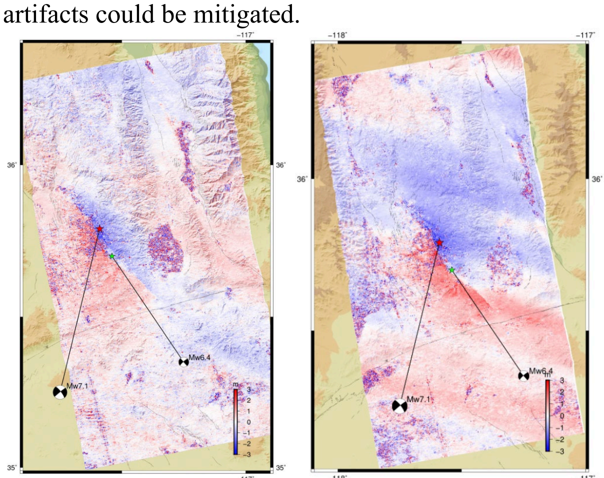

Fig. 5 MAI interferograms for the Ridgecrest earthquakes

3. CONCLUSIONS AND FUTURE TASKS

We have made a number of ALOS-1/ALOS-2 processing modules available to the general public through GMTSAR. These advancements will help in mapping deformation, detecting changes and mitigating the artifacts from ionospheric delays. We hope to further cooperate with JAXA scientists to benchmark some of these modules and make ALOS-2 and potentially the furture ALOS-4 data usage more accessible to the radar interferometry community.

4. REFERENCES

[1] Sandwell, D. T., & Price, E. J. (1998). Phase gradient approach to stacking interferograms. *Journal of Geophysical Research: Solid Earth*, *103*(B12), 30183-30204.

[2] Xu, X., Sandwell, D. T., Ward, L. A., Milliner, C. W., Smith-Konter, B. R., Fang, P., & Bock, Y. (2020). Surface deformation associated with fractures near the 2019 Ridgecrest earthquake sequence. *Science*, *370*(6516), 605-608.

[3] Xu, X., Sandwell, D. T., & Smith-Konter, B. (2020). Coseismic displacements and surface fractures from Sentinel-1 InSAR: 2019 Ridgecrest earthquakes. *Seismological Research Letters*, *91*(4), 1979-1985.

[4] Meyer, F. J., & Nicoll, J. (2008, July). The impact of the ionosphere on interferometric SAR processing. In *IGARSS 2008-2008 IEEE International Geoscience and Remote Sensing Symposium* (Vol. 2, pp. II-391). IEEE.

[5] Gomba, G., Parizzi, A., De Zan, F., Eineder, M., & Bamler, R. (2015). Toward operational compensation of ionospheric effects in SAR interferograms: The split-spectrum method. *IEEE Transactions on Geoscience and Remote Sensing*, *54*(3), 1446-1461.

[6] Fattahi, H., Simons, M., & Agram, P. (2017). InSAR time-series estimation of the ionospheric phase delay: An extension of the split range-spectrum technique. *IEEE Transactions on Geoscience and Remote Sensing*, *55*(10), 5984-5996.

[7] Liang, C., & Fielding, E. J. (2017). Measuring azimuth deformation with L-band ALOS-2 ScanSAR interferometry. *IEEE Transactions on Geoscience and Remote Sensing*, *55*(5), 2725-2738.

[8] Xu, X. and Sandwell, D.T., 2019. Toward absolute phase change recovery with InSAR: Correcting for earth tides and phase unwrapping ambiguities. IEEE Transactions on Geoscience and Remote Sensing, 58(1), pp.726-733.

[9] Tong, X., Sandwell, D. T., & Smith-Konter, B. (2013). High-resolution interseismic velocity data along the San Andreas Fault from GPS and InSAR. *Journal of Geophysical Research: Solid Earth*, *118*(1), 369-389.

[10] Xu, X., Sandwell, D. T., Klein, E., & Bock, Y. (2021). Integrated Sentinel-1 InSAR and GNSS Time-Series Along the San Andreas Fault System. *Journal of Geophysical Research: Solid Earth*, *126*(11), e2021JB022579.

APPENDIX

From PI:

[1] Xu, X., Sandwell, D. T., Ward, L. A., Milliner, C. W., Smith-Konter, B. R., Fang, P., & Bock, Y. (2020). Surface deformation associated with fractures near the 2019 Ridgecrest earthquake sequence. *Science*, *370*(6516), 605-608.

[2] Xu, X. and Sandwell, D.T., 2019. Toward absolute phase change recovery with InSAR: Correcting for earth tides and phase unwrapping ambiguities. IEEE Transactions on Geoscience and Remote Sensing, 58(1), pp.726-733.

[4] Sepúlveda, I., Haase, J.S., Carvajal, M., Xu, X. and Liu, P.L., 2020. Modeling the sources of the 2018 Palu, Indonesia, tsunami using videos from social media. *Journal of Geophysical Research: Solid Earth*, *125*(3), p.e2019JB018675.

[5] Ward, L.A., Smith-Konter, B.R., Xu, X. and Sandwell, D.T., 2021. Seismic Moment Accumulation Response to Lateral Crustal Variations of the San Andreas Fault System. Journal of Geophysical Research: Solid Earth, 126(4), p.e2020JB021208.

From other Co-Is (may not be complete):
[1] Fielding, E.J., Liu, Z., Stephenson, O.L., Zhong, M., Liang, C., Moore, A., Yun, S.H. and Simons, M., 2020. Surface deformation related to the 2019 M w 7.1 and 6.4 Ridgecrest earthquakes in California from GPS, SAR interferometry, and SAR pixel offsets. *Seismological Research Letters*, *91*(4), pp.2035-2046.
[2] Liang, C., Liu, Z., Fielding, E.J. and Bürgmann, R., 2018. InSAR time series analysis of L-band wide-swath SAR data acquired by ALOS-2. IEEE Transactions on Geoscience and Remote Sensing, 56(8), pp.4492-4506.
[3] Ross ZE, Idini B, Jia Z, Stephenson OL, Zhong M, Wang X, Zhan Z, Simons M, Fielding EJ, Yun SH, Hauksson E. Hierarchical interlocked orthogonal faulting in the 2019 Ridgecrest earthquake sequence. Science. 2019 Oct 18;366(6463):346-51.
[4] Tong, X., Sandwell, D.T. and Schmidt, D.A., 2018. Surface creep rate and moment accumulation rate along the Aceh segment of the Sumatran fault from L-band ALOS-1/PALSAR-1 observations. Geophysical Research Letters, 45(8), pp.3404-3412.
[5] Jin, Z., Fialko, Y., Zubovich, A., & Schöne, T. (2021). Lithospheric deformation due to the 2015 M7. 2 Sarez (Pamir) earthquake constrained by 5 years of space geodetic observations. *Journal of Geophysical Research: Solid Earth*, e2021JB022461.

A FINE DEFORMATION VELOCITY ACROSS THE LIJIANG-XIAOJINHE FAULT IN SOUTHWESTERN CHINA INVERTED JOINTLY FROM INSAR AND GPS OBSERVATION

PI No.: ER2A2N025

Xiaogang Song [1], Pengcheng Sha[1]

[1] State Key Laboratory of Earthquake Dynamics, Institute of Geology, China Earthquake Administration, Beijing, 100029, China

1. INTRODUCTION

Measurement of surface velocity field due to tectonic deformation provides an important constraint in geodynamic models, and a method to improve the evaluation of earthquake potential. The increase in spatial and temporal coverage of geodetic images such as those provided by Interferometric Synthetic Aperture Radar (InSAR) motivates us to better quantify the evolution of tectonic deformation and strain accumulation associated with crustal faulting.

The Chuandian block is located in southwestern corner of the Tibetan Plateau, and is one of the most seismically active areas in China. The Lijiang–Xiaojinhe Fault is a major transverse fault that divides the Chuandian block into southeastern and northwestern parts. Formation of the Lijiang-Xiaojinhe Fault may be due to other tectonic processes which have nothing to do with the slip transferring between the Xianshuihe and the Xiaojiang faults. The internal faults in the Chuandian block often control formation of Quaternary sedimentary basins and lakes. Large to medium size earthquakes frequently occur on those internal faults, and especially the Lijiang–Xiaojinhe Fault is the largest one among them. The fault itself consists of two discrete segments: the northeast trending Lijiang Fault and the north–south trending Xiaojinhe Fault. Trenches on the Lijiang Fault indicate three paleo-earthquakes in the Holocene at 7940-7210 a BP, 4740-4050 a BP and 1830-1540 a BP, respectively. Large earthquakes appear to fit the quasi-periodic model with the recurrence interval of ~3000yr and the estimated magnitude 7.5 [1]. On the western part of Lijiang Fault, the geological studies indicate that its quaternary left slip rate is 2.4-4.5mm/yr with small shortening rate of 0.6mm/a. Unfortunately, they did not report left-slip feature along the Xiaojinhe Fault [2-3]. The modern left-slip rate derived from GPS is no more than 3 mm/yr, and there also exist shortening [4-5]. These above studies reveal that the Lijiang-Xiaojinhe fault play an important role in the crustal deformation of the Sichuan-Yunnan region and it has the potential for generating big earthquake.

In this study, we want to know: how is the slip distributed locally along each segment of the Lijiang–Xiaojinhe Fault currently? What is its current strain accumulation rate, and how does individual segments interact with each other? Sparse GPS and geological data are not detailed enough to fully answer these questions. InSAR provides spatially dense maps of surface deformation at the kilometre scale over length scales of 100s of km, which benefit the achievement of our goal. With the launching of ALOS-2 satellite, L-band PALSAR-2 onboard provide us a good opportunity to carry out tectonic deformation observation with fine resolution in those heavily vegetated area like the Lijiang–Xiaojinhe Fault, the geographical focus of my proposal.

We seek to use PALSAR and PALSAR-2 data acquired between 2006 and 2021 to map an overall picture of the deformation velocity and strain fields across the whole Lijiang–Xiaojinhe Fault zone, which provide detailed constraints both on the slip rate of each segment and on the temporal and spatial evolution of the strain accumulation over the period the data spanned, examining the behavior of the fault movement, and looking for changes in the rates of movement on them. Our results will make significant contributions to the general understanding of how the active Lijiang–Xiaojinhe Fault accommodate the tectonic strain, and the interaction between its sub-parts, as well as providing critical first-order data for the assessment and mitigation of seismic hazard within this tectonically active area.

2. TECTONIC SETTING

The Lijiang-Xiaojinhe fault zone is an NE trending active tectonic belt within the Sichuan-Yunnan rhombic block, with a total length of 360km. The Sichuan-Yunnan rhombic block is obliquely cut into two secondary blocks： the Northwest Sichuan and central Yunnan subblocks. It is a reverse sinistral strike slip active fault with a high angle dipping to NW [6]. Many earthquakes with magnitude $\geq$ 6 occurred in this area in history, and the largest earthquake was the M7.5 Lijiang earthquake in 1996. The largest earthquake occurred on the Xiaojinhe fault was the M6 Yanyuan-Ninglang earthquake in 1976 [7] (Figure 1).

Many studies presented evidences that this fault system is still active. Shen et al. [4] gave a left-lateral strike slipping rate of 3mm/yr for the Lijiang-Xiaojinhe fault by analyzing the GPS data. Taking the GPS velocity field as the constraint, Wang Yanzhao et al. [8] inverted for the present-day segmented slip rate of the fault by using the least square method. The northeastern segment is a left-lateral strike-slip fault, with a small strike slip rate of 0.8 ± 1.5 mm/yr and a tensional rate of 2.4 ± 1.7 mm/yr; The middle segment is mainly left-lateral strike-slip, with a rate of 5.4 ± 1.2 mm/yr; The southwestern segment is dominated by compressing and thrust faulting, with a rate of 2.3 ± 1.8 mm/yr. In addition, the vertical components of leveling and GPS observation show that there are obvious differences in the vertical movement of the crust on both sides of the Lijiang-Xiaojinhe fault zone [9-10]. There exists a 50km seismic gap between the 1976 M6 and M6.7 Yanyuan-Ninglang earthquake rupture zone (Figure 1). In terms of the tectonic scale, fault activity and seismic activity, it is considered that the tectonic setting of the Lijiang-xiaojinhe fault zone is complex with strong tectonic activity.

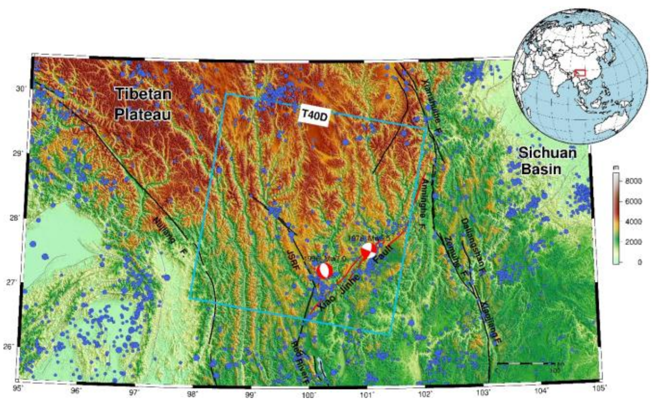

Fig. 1 Tectonic map of main active faults in Sichuan-Yunnan region. Fault traces are superimposed on SRTM DEM, blue dots indicate the seismicity (M>4) in history from USGS. The Global Centroid Moment Tensor (GCMT) focal mechanisms of the 1978 Mw 6.5 and 1996 Mw 7.0 Lijiang earthquakes are shown in red. T40D refers to the descending ALOS/PALSAR track is marked by cyan rectangle box, red lines indicate the Lijiang-xiaojinhe fault, active faults are shown in grey lines. JSRF: Jinshajiang Fault.

3. INSAR VELOCITY FROM ALOS-2 DATA

3.1 SAR data

The descending ALOS-2/PALSAR-2 ScanSAR data (350km×350km, track number: 40) from Japan Aerospace Exploration Agency (JAXA) was used to extract the deformation signal with time span from September 2014 to September 2019. The footprint is about 350km×350km, covering an area from 98E to 102E (as shown in Figure 1). A total number of 30 SAR acquisitions were used to form interferometric pairs (as shown in Figure 2).

In order to save data processing time and reducing unwrapping error, we choose to process only the three sub-strips on the right of the ScanSAR data that completely cover the fault deformation zone. To construct a redundant small-baseline network, a vertical orbit baseline threshold of 300m and a time baseline threshold of 2 years were used to generate 221 interferometric pairs. The interferometrc baseline network connects all SAR images to ensure the redundancy of the network. Due to the complex terrain, heavy vegetation coverage and more rainfall in Sichuan-Yunnan region, it is hard to maintain the coherence of interferograms in mountainous areas. Therefore, to avoid the impact of low coherence on the subsequent time series analysis, 41 long-time baseline (> 3.5 years) interference pairs with high coherence were chosen to form the final network, which connect as many images as possible (Figure 2). The first and the second acquisitions are excluded because of low coherence of the interferograms including them. The interferometric processing of SAR images were implemented by using the Gamma software [11], with 2 and 10 looks for multi-looking in range and azimuth respectively to improve the calculation efficiency and reduce the noise.

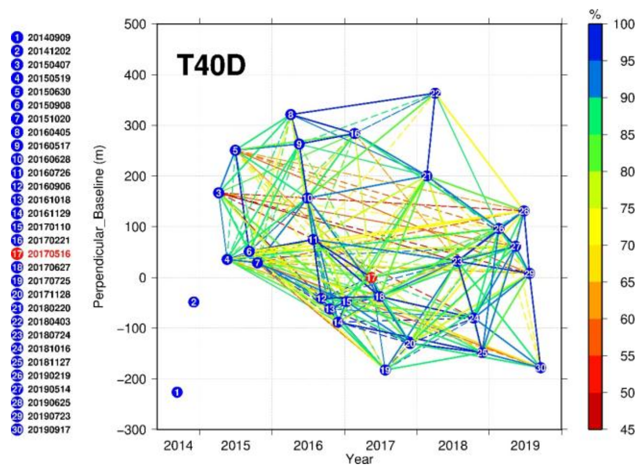

Fig. 2 Perpendicular and temporal baseline network plot on descending track T40D. The dates listed on the left are SAR acquisitions corresponding to the labeled blue circles, the red circles mark the master images, coherence color bar listed on the right. The lines present the interferometric pairs coloured according to the coherence. The solid lines are selected interferograms with best coherence, and dashed lines are dropped interferograms.

3.2 Error correction

A numerical weather model GACOS (A Generic Atmospheric Correction Online Service for InSAR) was used to correct atmospheric errors in interferograms in this study. It is proved that GACOS is useful in correcting the topography-dependent atmospheric effect. Before atmospheric correction, we need to remove the orbital error. Considering strong coupling between the long wavelength tectonic signal and orbital ramp, we need to define a "far field" to estimate the orbit phase [12], in which the phase gradient caused by tectonic activity is small. A quadratic polynomial is used to fit the orbital ramp using only phase measurements 30 km or further from the fault on both side to avoid the effect of the near-fault gradient in ground deformation. It is worth noting that the long wavelength component ionospheric phase delay is also removed in orbital correction. Then the distribution map of vertical stratified atmospheric delay error in the study area is reconstructed by using the GACOS data to correct the topography-dependent atmospheric error in interferograms. From figure 3, we can see that the topography-dependent atmospheric signal in interferograms is estimated effectively, and the interferogram after atmospheric correction is significantly improved. In acmospheric correction, we found that atmospheric phase in this area shows seasonal fluctuations. Interferograms whose master and slave image was acquired in the different season show much more serious stratified effect than those with the master and slave image from the same season. Therefore, we prefer to choose interferometric pairs in the same season when selecting interferograms for time-series analysis.

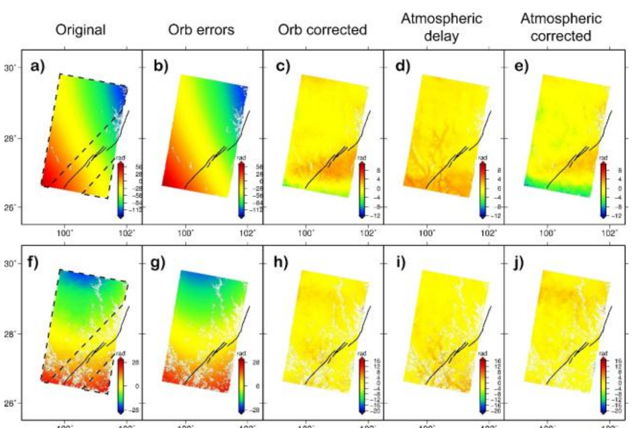

Fig. 3 Two examples of InSAR phase error correction for interferograms (20150407-20160405, 20150630-20190625). (a,f) Original unwrapped interferograms; (b,g) Estimates of quadratic orbital ramp errors; (c,h) Interferograms following orbital error correction; (d,i) Topography-dependent atmospheric delay derived from GACOS; (e,j) Atmospheric-corrected Interferograms. The black boxes in (a,f) are defined as "far-field" and are used to construct quadratic model in orbital correction.

3.3 InSAR ratemap and time-series deformation maps

Based on the interferometric network constructed above, the baseline construction problem discussed above, a least square method is used to solve for time series estimates of global and nonlinear deformation. Due only one interferometric network dataset used sets under baseline control, there is no matrix rank deficiency. We use Giant software to invert for the average deformation rate and cumulative changes in time of the Lijiang-xiaojinhe fault zone in the observation period. Through the least square method, the LOS observation value and its corresponding start and end dates in each interferogram are used to retrieve the incremental displacement relative to the reference time (the first image). The obtained velocity field of Lijiang-xiaojinhe fault zone is shown in Figure 4 (a), and the time series is shown in Figure 5.

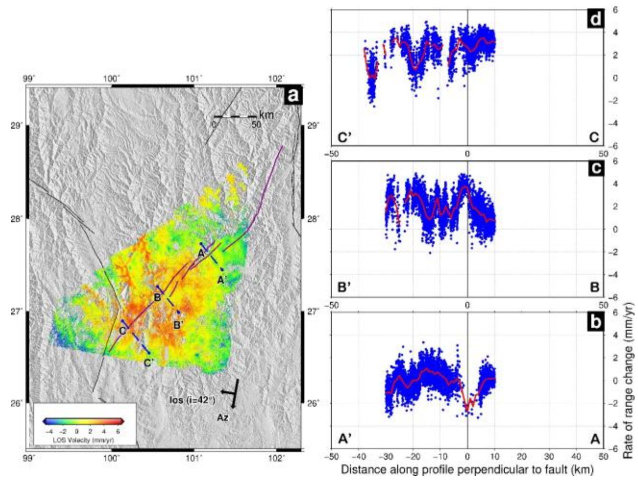

Fig.4 Mean LOS ratemap for track 40, produced from GAOCS corrected interferograms. Cold color (negative range change) is toward satellite, warm color (positive range change) corresponds to movement away from satellite. Profile AA', BB' and CC' correspond to figure b, c, d respectively.

4. INVERSION OF THE SLIP RATE AND LOCKING DEPTH

Based on the interseismic deformation field of Lijiang-Xiaojinhe fault zone we extracted above, the current fault activity for each segment of the fault could be evaluated by analyzing InSAR results. As shown in Figure 4 (a), we extracted the cross-fault profile in the northeastern section, middle section and southwestern section of Lijiang-Xiaojinhe fault, and inverted for the slip rate and locking depth for each section by using arctan screw dislocation model [13]. The results are shown in Table 1. As the "far field" away from the fault is contaminated by the atmospheric signal, the cross-fault profile we extracted are within the "near field". We can see that the ratemap and cross-fault profiles (Figure 4) show an obvious tectonic signal near the Xiaojinhe fault zone. Compared with the northeastern section with a small locking depth (3.7km), a big locking depth (12.4 and 15.8km was derived from cross-fault profile inversion for the middle and southwestern section respectively, which is consistency with GPS results [6]. We suggested there is a strong locking area in the central and southern section of the Xiaojinhe fault, which indicates that these two fault segments has an earthquake potential with the strain accumulating. In the northeastern section, the locking degree is shallower with a higher slip rate, which means it might be the existence of shallow creep.

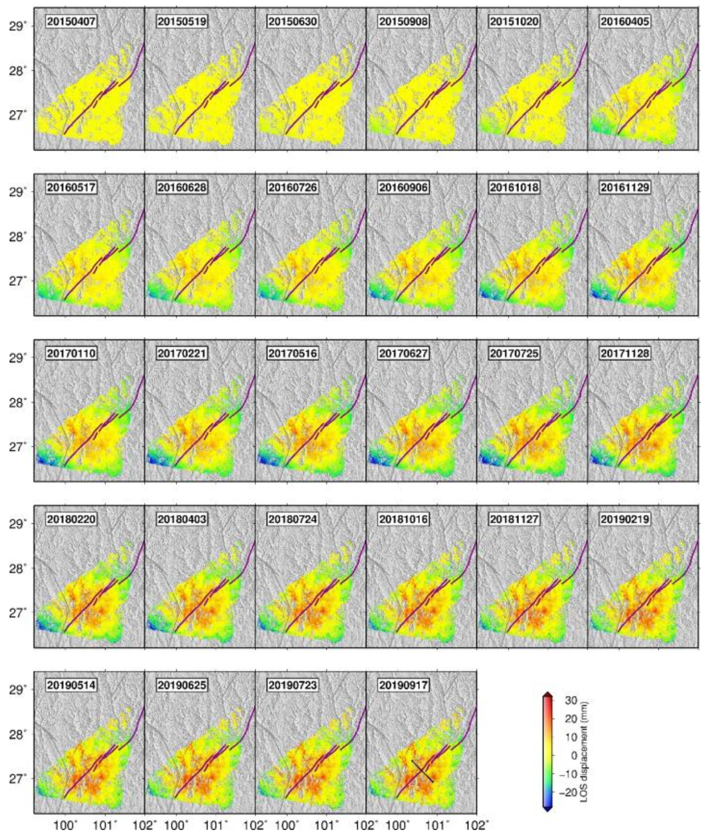

Fig.5 InSAR time series of the Lijiang-Xiaojinhe fault based on SBAS method. Line of sight (LOS) cumulative displacements are referenced to the first acquisition, 7 April 2015. Negative range change is toward satellite. Black line in the last snapshot indicates the location of profile shown in Figure 6.

Table 1 the slip rate and locking depth of three sections of the Lijiang-Xiaojinhe Fault

Profile ID	Fault segment	Slip rate (mm/a)	Locking depth (km)
AA’	Northeastern section	4.24	3.7
BB’	Middle section	3.41	12.4
CC’	Southwestern section	3.06	15.8

Figure 5 shows the time evolution of the LOS cumulative displacement maps on 28 acquisition dates. In the time series, we can see that the deformation evolution basically presents a linear accumulation, and the near-field displacement in the middle section of the Xiaojinhe fault reaches ~ 20mm (Figure 6).

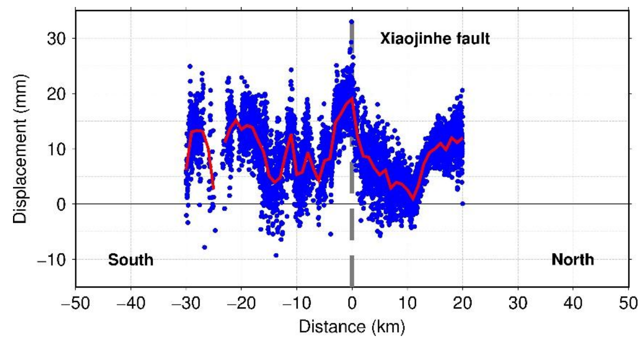

Fig.6 The cross-fault profiles of line of sight cumulative displacement across the middle of Xiaojinhe fault.

5. CONCLUSION

InSAR is an effective means to measure high-precision deformation of earth’s surface. The InSAR timeseries technology has been applied widely in monitoring trivial surface deformation and predicting geological disasters. 30 ALOS-2 ScanSAR images were processed to extract InSAR interseismic deformation field of the Lijiang-Xiaojinhe fault. GACOS was used to correct atmospheric error in interferograms. The profiles across the fault show a left-lateral strike slip movement on the fault which is coincidence with geological observation. The results from inverting the cross-fault profiles show the locking depth is deeper in middle and south segment, while it is shallower in north part with a high slip rate, which means it might be the existence of shallow creep.

6. ACKNOWLEDGMENTS

This work is supported jointly by the National Key R&D Program of China (NO. 2019YFC1509205) and the ALOS EO-RA2 project. All ALOS-2 data were provided and are copyrighted by the Japan Aerospace Exploration Agency (JAXA).

7. REFERENCES

[1] Ding R, Ren J J, Zhang S M, et al. Late Quaternary Paleoearthquakes on the Middle Segment of the Lijiang-Xiaojinghe Fault, Southeastern Tibet. Seismology & Geology, 2018, 40(3): 622-640 (in Chinese).

[2] Xiang H, Xu X W, Guo S, et al. Sinistral thrusting along the Lijiang-Xiaojinhe fault since Quaternary and its geologic-tectonic significance-Shielding effect of transverse structure of intracontinental active block[J]. Seismology and Geology, 2002, 24(2): 188-198(in Chinese).

[3] Xu X, Wen X, Zheng R, et al. Pattern of latest tectonic motion and its dynamics for active blocks in Sichuan-Yunnan region, China. Science in China Series D: Earth Sciences, 2003, 46(2): 210-226.

[4] Shen Z K, Lü J, Wang M, et al. Contemporary crustal deformation around the southeast borderland of the Tibetan Plateau[J]. Journal of Geophysical Research: Solid Earth, 2005, 110(B11).
[5] Zhang P Z. A review on active tectonics and deep crustal processes of the Western Sichuan region, eastern margin of the Tibetan Plateau[J]. Tectonophysics, 2013, 584: 7-22.
[6] LI Ning, ZHU Liangyu, LIU Lei, Study on Present-day Locking Degree and Seismic Hazard of the Lijiang-Xiaojinhe Fault Zone, Journal of Seismological Research, 2 : 244-250, 2018 (in Chinese).
[7] Li Le, Chen Qifu, Niu Fengling et al., Estimation of the slip rate of the Lijiang-Ninglang fault zone in deep from repeated earthquakes, Chinese Science Bulletin, 53(23):2925-2932, 2008 (in Chinese).
[8]Wang Yanzhao, Wang Enning, Shen Zhengkang et al., Inversion of the present-day slip rate of main faults in Sichuan-Yunnan region based on GPS data, SCIENCE CHINA Earth Sciences, 38(5):582-597, 2008 (in Chinese).
[9] Wang Qingliang, Cui Duxin, Wang Wenping et al., Study on the present vertical crustal movement in Western Sichuan, SCIENCE CHINA Earth Sciences, 38(5):598-610, 2008 (in Chinese).
[10] Liang S M, Gan W J, Shen Z K, et al. 2013. Three－dimensional Velocity Field of Present－day Crustal Motion of the Tibetan Plateau Derived from GPS Measurements. Journal of Geophysical Research, 118 (10):5722－5732.
[11]Werner, C.; Wegmüller, U.; Strozzi, T.; Wiesmann, A. GAMMA SAR and interferometric processing software. In Processing of the ERS-Envisat Symposium, Gothenburg, Sweden, 16-20 October 2000.
[12] Biggs, J., T. Wright, Z. Lu, and B. Parsons, Multi‐interferogram method for measuring interseismic deformation: Denali fault, Alaska, Geophys. J. Int., 170, 1165–1179, 2007.
[13] Savage, J. C., and R. O. Burford, Geodetic Determination of Relative Plate Motion in Central California, Journal of Geophysical Research, 78, 832–845, doi:10.1029/ JB078i005p00832, 1973.

THE CHARACTERISTICS AND EVOLUTION OF SURFACE DEFORMATION INDUCED BY AGRICULTURAL IRRIGATION IN THE JUNGGAR BASIN FROM THE INSAR MEASUREMENT

PI No.: ER2A2N038

Guangcai Feng [1,2], Lijia He[1,2], Yuedong Wang[1,2]

[1] Laboratory of Radar Remote Sensing, School of Geosciences and Info-Physics, Central South University, Changsha 410083, China

[2] Key Laboratory of Metallogenic Prediction of Nonferrous Metals and Geological Environment Monitoring, Central South University, Changsha 410083, China

1. INTRODUCTION

In this report, we firstly measured the coseismic surface displacements caused by the 2018 Palu earthquake using the InSAR data from both the ALOS-2 ascending and descending tracks. We then jointly used the sub-pixel correlation results of SAR and Sentinel-2 optical images to invert the 3D coseismic surface deformation field. Subsequently, we constrained the fault geometry and estimated the fault-slip distribution jointly using the SAR offsets in the near field and the InSAR LOS displacements in the far field.

Then we use the InSAR, multiple aperture InSAR (MAI) and pixel offset-tracking (POT) measurements from Sentinel-1 and ALOS-2 SAR data to obtain the coseismic displacement fields caused by the two largest earthquakes during the 2019 Ridgecrest sequence. We build a joint-event model constrained by four SAR image offsets and four InSAR LOS displacements that temporally covers both earthquakes. We use the joint-event model to simultaneously estimate the cumulative coseismic slip distribution of both events.

We also map the surface deformation of the southern Junggar Basin, China, using TS-InSAR method. To conduct comprehensive monitoring of regional-scale ground subsidence in JSOAA, we collected a total of 1116 SAR images covering the whole region of JSOAA from 2007 to 2020, including ALOS-1/PALSAR data of 13 ascending tracks and 29 frames (2007 - 2010) and Sentinel-1 data of 4 ascending tracks and 2 descending tracks (2015 - 2020). Among them, the ascending ALOS-1/PALSAR and ascending Sentinel-1 data achieved full coverage of JSOAA. Due to the short time coverage, the descending Sentinel-1 data in the western part of JSOAA is not processed. The coverage of all InSAR data used in this study is shown in Fig. 1.

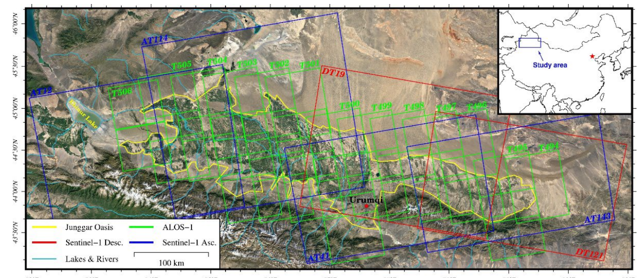

Fig. 1. Study area and InSAR data cover. The yellow line delineates the boundary of JSOAA. The green, blue, and red boxes show the coverage of the ALOS-1/PALSAR, ascending Sentinel-1, and descending Sentinel-1 data, respectively. The light blue lines mark the main surface runoff distribution around JSOAA.

2. ALOS/ALOS2 PALSAR DATA AND PROCESSING

2.1 Coseismic deformation measurement

The ALOS PALSAR platform provides data that are playing an important role in earthquake deformation and surface subsidence caused by agricultural irrigation. The SAR data are used in this project to create interferograms of coseismic deformation following the various earthquakes we researched. In addition to the data from this project, we also use lots of data from our S1A/B from ESA. The ALOS/PALSAR SAR data are processed from raw products with the conventional two-pass differential interferometry approach using the GAMMA software package. During the SAR data processing, all the FBD (Fine Beam Double Polarization) PALSAR data are oversampled to the resolution of the FBS (Fine Beam Single Polarization) mode. The 30m SRTM (DEM) is used to remove the phase component contributed by the topography. We apply a multi-look operation before phase unwrapping. We use the minimum cost flow algorithm (MCF) to unwrap each of the interferograms. In order to illustrate the finer structure of the displacement field and for ease of comparison, we rewrap the LOS displacement from both the PALSAR and S1A/B displacement products with the same fringe cycle of 11.8

cm. In order to obtain accurate coseismic deformation associated with the earthquake, the potential spurious phase contributions, e.g. topographic error phase, the ionosphere disturbance and atmosphere delays, and orbital errors need to be considered and mitigated. In some great earthquakes, coseismic deformation distortions related to ionosphere disturbance also need be considered. From the error analysis above, we conclude that the discontinuities are mainly due to orbital ramps although incidence angle variation can be potentially another reason.

2.2 TS-InSAR measurement for agricultural irrigation in the Junggar Basin

In this study, the L-band ALOS1/PALSAR data would be used to obtain the deformation information of the Junggar Basin from 2006 to 2011, and the data are processed by differential interference with GAMMA software. The image needs to be registered before the interference processing, and the registration accuracy between the two scene images is better than 0.1 pixels. The terrain phase in the interferogram is removed using the 1-arcsecond (~30m) Shuttle Radar Topography Mission (SRTM) data provided by United States Geological Survey (USGS). Since the ALOS1/PALSAR and orbital information of the L-band are not accurate enough, there is still obvious orbital residual phase in the differential interferogram after removing the flat phase and the terrain phase. In this project, a modified Goldstein filter would be used to reduce noise phases. In order to avoid or weaken the effect of low coherence regions (sea and isolated islands, etc.) on phase unwrapping, a mask with a coherence of less than 0.4 is masked. Finally, we used Phase unwrapping with Minimum Cost Flow (MCF) algorithm to unwrap pixel. In order to obtain more accurate deformation information, it is necessary to remove noise signals such as orbital errors, atmospheric delays, and the like. For orbital errors, the unwrapped phase can be removed by polynomial fitting.

The phase of each pixel in the interferogram can be expressed as:

$$\delta\phi_j(x,r) = \phi(t_B,x,r) - \phi(t_A,x,r) \approx \frac{4\pi}{\lambda}\Delta d + \frac{4\pi}{\lambda}\frac{B_{\perp j}\Delta z}{r\sin\theta} + \Delta\phi_{atm} + \Delta_{n_j} \qquad (1)$$

where $\delta\phi_j(x,r)$ is the phase of the interferogram, Δd is the cumulative deformation along line of sight (LOS) between the two moments of the same pixel point, Δz is the residue DEM error, $\Delta\phi_{atm}$ is the atmospheric delay phase, Δ_{n_j} is the phase noise. In order to find the low-frequency deformation component and the elevation residual, the equation (1) is transformed into a matrix form:

$$\begin{bmatrix} \frac{4\pi}{\lambda}\Delta t_1 & \frac{4\pi}{\lambda}\frac{B_{\perp 1}}{r\sin\theta} \\ \frac{4\pi}{\lambda}\Delta t_2 & \frac{4\pi}{\lambda}\frac{B_{\perp 2}}{r\sin\theta} \\ \vdots & \vdots \end{bmatrix} \begin{bmatrix} v \\ \Delta z \end{bmatrix} = \begin{bmatrix} \delta\phi_1 \\ \delta\phi_2 \\ \vdots \end{bmatrix} \qquad (2)$$

where v is the deformation rate. By solving the equation (2) by the least squares method, the average deformation rate and the elevation residual of each pixel point can be obtained, and the shape obtained at this time is a low-frequency deformation component. The obtained low-frequency deformation phase and elevation residual phase are removed from the original interferogram, then the high-frequency deformation phase, atmospheric phase and noise remain in the original interferogram, and then the singular value decomposition method is used in the interferogram. The residual phase is assigned to each scene image.

The SAR image in study area is seriously disturbed by the atmosphere, so atmospheric effects must be removed. The atmospheric phase is a low frequency signal in space and a high frequency signal in time. The noise is a high frequency signal in both time and space. Therefore, according to the temporal and spatial characteristics of the atmospheric phase and noise, the image of each scene is spatially low-pass filtered and high-pass filtered in time to remove atmospheric errors and noise. Then, the high-frequency deformation sequence is solved for the interferogram containing only the high-frequency deformation phase, and the final time deformation sequence can be obtained by adding the low frequency deformation back to the interferogram.

3. RESULTS

2018 Mw 7.5 Palu earthquake: For the 2018 Palu earthquake, we used the ascending Stripmap mode and the descending ScanSAR mode ALOS-2 images to map the coseismic deformation fields of this earthquake. These SAR images provide sufficient coverage of the entire rupture zone. There are also some C-band Sentinel-1 data in this area, but the L-band ALOS-2 data have obvious advantage in this case. We processed the ALOS-2 data using the GAMMA software (Werner et al., 2001). To increase the signal-to-noise ratio (SNR), both the ascending and descending interferograms were multi-looked to a ground resolution of about 80 m. The 90 m SRTM DEM was used to correct the topographic phase component. The interferograms were filtered by an improved Goldstein filter (Li et al., 2008). The polynomial fitting model was applied to mitigate the long wavelength orbital errors and the atmospheric delay associated with the ground topography. Finally, the interferograms were geocoded to the geographic WGS-84 coordinate system. The ascending and descending coseismic interferograms of the 2018 Palu earthquake are shown in Fig. 2.

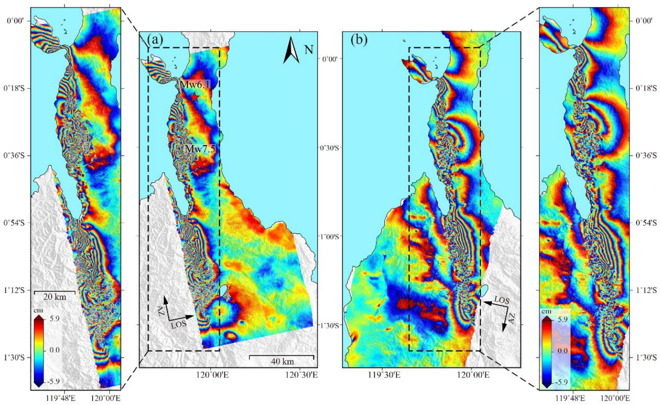

Fig. 2. Coseismic deformation fields of the 2018 Mw7.5 Palu earthquake derived from the ALOS-2 phase data.

For the 2018 Palu earthquake, the InSAR coseismic deformations near fault ruptures were not well observed due to the decorrelation caused by the great deformation gradient and the rugged terrain. We thus calculated the range and azimuth offsets for ascending and descending image pairs using the SAR pixel offset-tracking technique (Strozzi et al., 2002) (Fig. 3). Although the image offsets are much noisier than conventional InSAR observations, they can provide unambiguous range and azimuth displacements parallel and perpendicular to the LOS displacements, and can improve the near-field displacement measurement. We estimated the offset fields using almost square search patches of 50 × 100 pixels (range × azimuth) for the ALOS-2 Stripmap images (about 300 m × 300 m window size) and of 30 × 140 pixels for the ALOS-2 ScanSAR images (about 400 × 400 m window size). To maintain a pixel spacing of around 50 m for the two datasets, the offsets were estimated for every 5 pixels in range and 10 pixels in azimuth for the ALOS-2 Stripmap images, and for every 6 pixels in range and 28 pixels in azimuth for the ALOS-2 ScanSAR images.

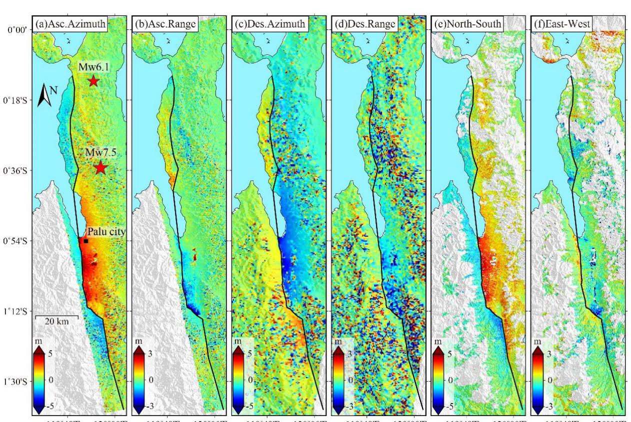

Fig. 3. ALOS-2 ascending (a) azimuth and (b) range offsets, ALOS-2 descending (c) azimuth and (d) range offsets, Sentinel-2 (e) north-south and (f) east-west components of the surface displacement of the 2018 Palu earthquake.

For the 2018 Palu earthquake, we obtained the multi-sight coseismic surface deformation fields of the 2018 Mw 7.5 Palu earthquake using InSAR, SAR and optical sub-pixel correlation technologies. These datasets provide valuable constraints for the fault geometry and fault slip on the Palu-Koro fault. we utilized the rectangular dislocation (Okada, 1992) in a homogeneous elastic half-space domain to simulate the coseismic displacements of the mainshock. The fast non-negative constrained least squares algorithm (Bro and Jong, 1997) was employed to solve for the strike-slip and dip-slip components on each fault segment (Fig. 4). The second-order Laplace smoothing constraint was used to minimize the abrupt variation of slip among the adjacent sub-fault patches (Jónsson et al., 2002). We utilized a three-segment fault model with variable strike angles and found that a newly discovered fault lies in the north of Palu city, and extends northward ~ 60 km. The best-fitting fault model fits the InSAR LOS displacements and SAR offsets well.

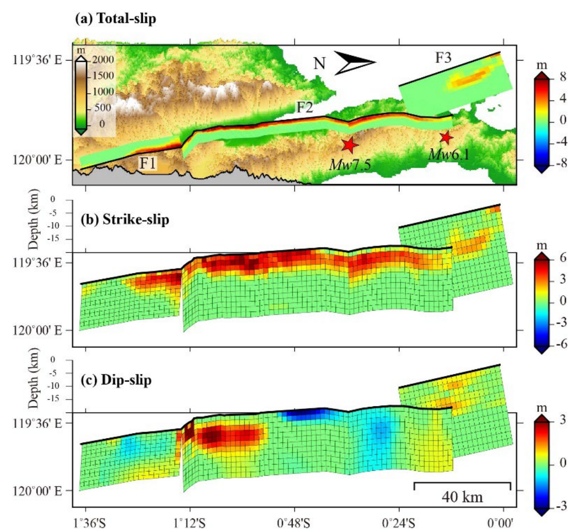

Fig. 4. (a) Total slip, (b) strike- and (c) dip-slip distributions of the 2018 Palu earthquake estimated from the joint inversion of InSAR and SAR datasets.

<u>**2019 Ridgecrest earthquake sequences:**</u> For the 2019 Ridgecrest earthquake sequence, we coregistrated two single look complex images with the assistance of DEM. A multi-looking operation of 30×8 and 6×32 (range × azimuth) was applied for Sentinel-1 and ALOS-2 interferograms, respectively. After minimizing the decorrelation noise with an improved Goldstein filter, the minimum cost flow method (Chen & Zebker, 2002) was used to unwrap interferometric phase by masking the areas with coherence value smaller than 0.4. The

ascending and descending coseismic interferograms of the 2019 Ridgecrest earthquake sequence are shown in Fig. 5.

For the 2019 Ridgecrest earthquake sequence, the POT and MAI methods have lower accuracy than the DInSAR method, but they can extract the deformation along the AT direction, which is crucial for interpreting geophysical phenomenon with large surface displacement such as earthquakes, glaciers, or volcanic movements. To measure the ground deformation by the POT method, the matching window size of 300×60 pixels and 40×185 pixels (range×azimuth) was utilized for Sentinel-1 and ALOS-2 data, respectively. The MAI procedure was applied to both the ALOS-2 and Sentinel-1 data, but only the azimuth result of the former was selected, because the latter has lower coherence. The sub-aperture interferograms were generated on the framework of the DInSAR process (Liang & Fielding, 2017). These two sub-aperture interferograms were then differenced to generate the azimuth deformation related phase maps, which would be further filtered to generate the final AT deformation. A directional filter was applied to the ascending ALOS-2 MAI interferogram to mitigate the influence of ionospheric disturbs. The POT and MAI measurements have similar spatial resolution with the DInSAR ones (Fig. 5).

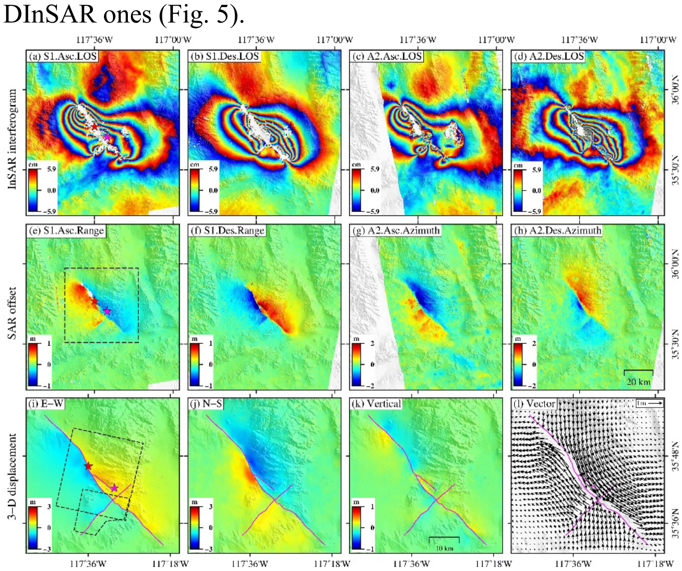

Fig. 5. Coseismic displacement fields of the 2019 Ridgecrest earthquake sequence obtained from the space-based geodetic data. (a) and (b) are the ascending and descending coseismic interferograms from Sentinel-1 images, respectively. (c) and (d) are the cumulative ascending and descending coseismic interferograms from ALOS-2 images, respectively. (e) and (f) show the cumulative ascending and descending coseismic POT range offsets from Sentinel-1 images, respectively. (g) and (h) are the cumulative ascending and descending coseismic MAI azimuth offsets from ALOS-2 images, respectively. (i-l) E-W, N-S and vertical components of the 3-D cumulative surface displacement as well as the horizontal offset vectors, respectively.

For the 2019 Ridgecrest earthquake sequence, we used the geodetic data, including four InSAR interferograms and four SAR image offsets, to estimate the coseismic slip distribution on the fault segments F1-F3 (Fig. 6). The geodetic moment on segment F2 determined by the joint-event inversion is 8.86×1018 N□m (Mw 6.60), almost 39% larger than that determined by the single inversion of the mainshock (5.40×1018 N□m; Mw 6.46), because a part of slip component between zones A and B of segment F1 is mapped into zone E during the joint-event inversion, leading to a slip amplitude of ~4 m in zone E in the joint-event slip model, almost twice that (~2 m) in the single slip model of the mainshock.

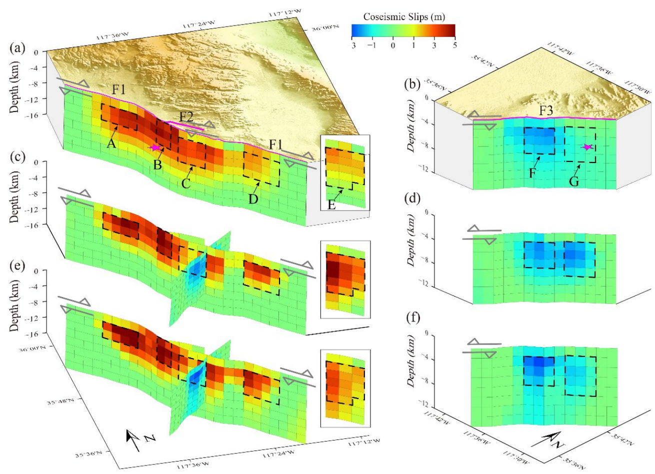

Fig. 6. Top view of the coseismic slip distributions of the 2019 Ridgecrest earthquake sequence. (a) and (b) show the single-event coseismic fault slip distributions induced by the mainshock and the foreshock, respectively. (c) and (e) show the joint-event and the combined-data coseismic fault slip distributions induced by the two events, respectively. (d) and (f) represent the slip component on segment F3 in (c) and (e), respectively. The two single-event slip models shown in (a) and (b) are inverted from the Planet-Lab optical and GPS datasets. The joint-event slip model shown in (c) is inverted from four SAR offsets and four InSAR LOS displacements. The combined-data slip model shown in (e) is inverted from all the used data.

__Surface subsidence of the southern Junggar basin:__ Using all the ALOS-1/PALSAR and Sentinel-1 data covering JSOAA, we obtained the regional-scale ground displacements along the LOS direction in JSOAA during 2007 - 2010 (Fig. 7(a)) and 2015 - 2020 (7(b-c)). As the results show, there are multiple settlement funnels in JSOAA. Compared with the corresponding optical images, the subsidence funnels (Fig.7 in closed dotted line) are consistent with the agricultural planting area in spatial scope and is positively correlated with the planting area and planting intensity, while negatively correlated with the distribution density of surface runoff. That is, the settlement funnels are more significant in areas with high planting intensity and insufficient surface water supply. The comparison between the ground subsidence from 2007 to 2010 and that from 2015 to 2020 shows that the spatial distribution range and magnitude of settlement funnels are expended and intensified. Many settlement funnels in the eastern part of JSOAA, where there was no settlement previously.

There were two independent settlement funnels distributed in this profile during 2007 - 2010. During 2015 - 2020, these two settlement funnels gradually expanded and approached, and merged into a large settlement funnel. The maximum accumulative settlement reached about 400 mm from 2007 to 2010, and about 500 mm from 2015 to 2020. The subsidence rate of the main subsidence area of the section remains unchanged.

Due to the low temporal resolution (⩾46 days) of ALOS-1/PALSAR data, the periodicity of ground deformation is not well represented during 2007 - 2010. However, Sentinel-1 data with higher temporal resolution (⩾12 days) can capture the periodic signals of ground deformation well. The subsidence occurred between March and September each year, and the deceleration of subsidence and uplift occurred from October to February. This is consistent with the exploitation and recharge of groundwater caused by seasonal agricultural irrigation in JSOAA. The results confirm the advantages and potential of Sentinel-1 data in monitoring regional-scale periodic ground deformation caused by groundwater extraction.

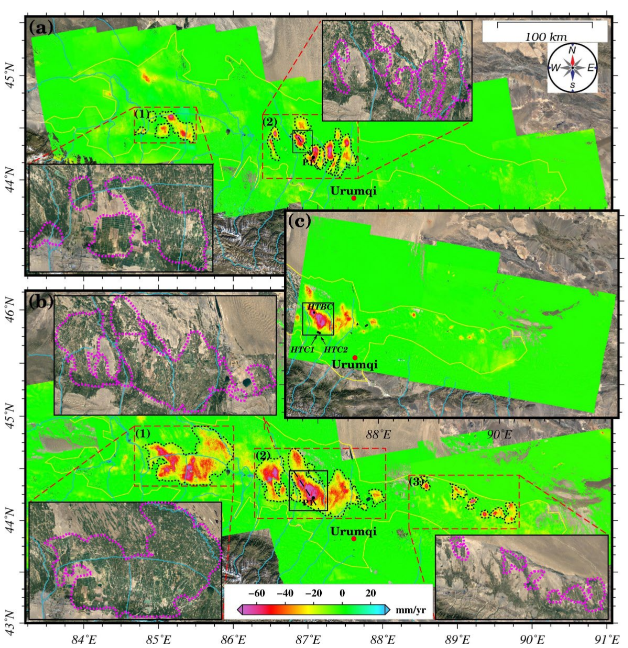

Fig.7 The mean displacement velocity along the LOS direction derived from (a) the ALOS-1/PALSAR ascending data, (b) Sentinel-1 ascending data, and (c) Sentinel-1 descending data. The closed black dotted lines delineate the main deformation zones. The black rectangle identifies the range of the regions selected for accurate verification of the results. The yellow line shows the scope of JSOAA. The light blue lines indicate the spatial distribution of surface runoff.

4. ACKNOWLEDGMENTS

We thank the JAXA PI project No. ER2A2N038 award, without their help and ALOS PALSAR data our work would not have been possible. In addition to the quota of data obtained through our PI project, we also benefited from a large number of PALSAR data and S1A/B data from the ESA. We thank the staff at the JAXA AUIG helpdesk and ESA user services offices for their help with providing and processing the data products. Part of this research was performed at the Central South University. The research presented in this report is supported in part by the Natural Science Foundation of China (42174039 and 41574005).

5. REFERENCES

[1] Werner, C., Wegmüller, U., Strozzi, T., Wiesmann, A., 2001. Gamma SAR and interferometric processing software. In Proceedings of the ers-envisat symposium, gothenburg, sweden (Vol. 1620, p. 1620).
[2] Li, Z. W., Ding, X. L., Huang, C., Zhu, J. J., Chen, Y. L., 2008. Improved filtering parameter determination for the Goldstein radar interferogram filter. ISPRS Journal of Photogrammetry and Remote Sensing, 63(6), 621-634. https://doi.org/10.1016/j.isprsjprs.2008.03.001.
[3] Chen, C. W., Zebker, H. A., 2002. Phase unwrapping for large SAR interferograms: Statistical segmentation and generalized network models. IEEE Transactions on Geoscience and Remote Sensing, 40(8), 1709-1719. http://doi.org/10.1109/TGRS.2002.802453.
[4] Strozzi, T., Luckman, A., Murray, T., Wegmuller, U., Werner, C. L., 2002. Glacier motion estimation using SAR offset-tracking procedures. IEEE Trans. Geosci. Remote Sens. 40(11), 2384-2391. https://doi.org/10.1109/TGRS.2002.805079.
[5] Okada, Y. (1992). Internal deformation due to shear and tensile faults in a half-space. Bulletin of the seismological society of America, 82(2), 1018-1040. https://doi.org/10.1785/BSSA0820021018.
[6] Bro, R., Jong, S., 1997. A fast non-negativity-constrained least squares algorithm. Journal of Chemometrics: A Journal of the Chemometrics Society, 11(5), 393-401. https://doi.org/10.1002/(SICI)1099-128X(199709/10)
[7] Jónsson, S., Zebker, H., Segall, P., Amelung, F., 2002. Fault slip distribution of the 1999 Mw 7.1 Hector Mine, California, earthquake, estimated from satellite radar and GPS measurements. Bulletin of the Seismological Society of America, 92(4), 1377-1389. https://doi.org/10.1785/0120000922.

APPENDIX

[1] He, L., Feng, G., Li, Z., Feng, Z., Gao, H., Wu, X. (2019). Source parameters and slip distribution of the 2018 Mw 7.5 Palu, Indonesia earthquake estimated from space-based geodesy. Tectonophysics, 772, 228216.
[2] He, L., Feng, G., Hu, J., Xu, W., Liu, J., Li, Z., ... & Lu, H. (2022). Surface Displacement and Source Model Separation of the Two Strongest Earthquakes During the 2019 Ridgecrest Sequence: Insights from InSAR, GPS, and Optical Data. Journal of Geophysical Research: Solid Earth, 127(2), e2021JB022779.

COMPREHENSIVE STUDY AND MONITORING OF GEODYNAMIC PROCESSES IN THE KURILE-KAMCHATKA SUBDUCTION ZONE BY JOINT INTERPRETATION OF SATELLITE SAR AND SURFACE DATA

FINAL REPORT OF
THE 2ND RESEARCH ANNOUNCEMENT ON
THE EARTH OBSERVATIONS(EO-RA2)

PI No.: ER2A2N075

Mikhailov V.[1], *Volkova M.* [1], *Timoshkina E.* [1], *Timofeeva V.*[1], *Dmitriev P.* [1],

[1] Schmidt Institute of physics of the Earth Russian academy of sciences

1. INTRODUCTION

Purpose of our project is further development and application of methods for studying and monitoring of active geodynamic processes in the Kuril-Kamchatka subduction zone (KKSZ). This area is very difficult for application of SAR technologies, but investigation and monitoring of geodynamic processes leading to major earthquakes, eruptions and tsunamis is an important issue for Society. Catastrophic earthquakes and tsunamis in KKZS can lead to loss of human lives and economic infrastructure in all countries of the pacific coast. Large volcanic eruptions disrupt domestic and international air-traffic for long time-periods.

Reason for addressing the problem is that in 2018 a new joint laboratory in Schmidt Institute of physics of the Earth Russian academy of sciences was created in cooperation with the Kamchatka Institute of Volcanology and Seismology and some other Institutions. The scientific leader of the project is Nikolay Shapiro, head of laboratory is PI of this project prof. Valentin Mikhailov.

The laboratory is aimed at extension of surface seismic and geodetic networks, collection and processing of big volume of information for studying volcanic and seismic processes, development of new technologies for joint analysis and interpretation of terrestrial and satellite geophysical data and their application for studying the geodynamics of subduction zones of the Russian Far East. Because of limited budget of the laboratory, we planned to restrict our study mostly by Sentinel 1A,B images, whenever ALOS images are often more efficient for DInSAR and PSInSAR studies of natural terrains in specific conditions of KKZS. Our research proposal supported by JAXA helped us considerably extending our study using both Sentinel and ALOS images, performing comparative application of different technologies of SAR data processing and interpretation.

The main research areas of the project are closely linked to activity of the created laboratory. Content of Research includes:

(1) Development of innovative methods for processing of SAR data efficient in specific conditions of KKZS.

(2) Application of SAR interferometry for studying and monitoring of volcanic and seismic events. For it, new surface data will be used as ground control for validation of SAR results and for joint inversion of surface and satellite data.

(3) Scientific and educational activities, including training of graduate students and organization of scientific field schools for students of Russian universities.

Innovative part of the project is in joint analysis and interpretation of SAR with big volume of data which now is collecting for the KKZS by new laboratory.

Let us consider the main results obtained in the frameworks of the EO-RA2 ER2A2N075 project.

2. A JOINT STUDY OF SEISMICITY AND SAR INTERFEROMETRY OBSERVATIONS FOR ASSESSING THE POSSIBILITY OF AN ERUPTION OF THE DORMANT BOLSHAYA UDINA VOLCANO

Seismicity began to be recorded in October 2017 around the dormant Bolshaya Udina Volcano (B. Udina in what follows) situated 10 km southeast of Plosky Tolbachik Volcano. Seismic tomography showed the existence of a long-lived magma chamber south of B. Udina in the area of the Tolud River. The chamber has its top at a depth of about 15 km, and may probably be connected to the Plosky Tolbachik plumbing system. Some authors related the observed resumption of seismic activity to a hypothetical emplacement of magma beneath the B. Udina volcanoes, pointing out a high likelihood of the resumption of volcanic activity.

In our study we examined data from permanent seismic stations showing a systematic displacement of the center of seismic energy southward from B. Udina from October 2017 through August 2019. The center characterizes the location of the volume that generates the bulk of seismicity. We used images of the Sentinel-1A satellite (wavelength 5.6 cm) taken from a descending orbit of track 60 during the period from June 7, 2017 through September 23, 2017 (10 images) and during the period from May 21, 2018 to September 30, 2018 (12 images) to determine time series and average velocities of displacement on the slopes of B. Udina. Persistent scatterers were only identified at the foot of B. Udina (Fig.1). An analysis of displacement time series for the surface of the volcano showed that the character of displacements in 2017 and 2018 on the southwestern and eastern slopes remained nearly the same, while the average rate of displacement on the northwestern slope decreased in 2018 [1]. We used three images of the ALOS-2 PALSAR-2 satellite (wavelength 23.5 cm) taken on October 4, 2016, June 13, 2016, and October 2, 2018 from an ascending orbit to construct interferograms, which characterize displacements for the time period between images. The displacements on both interferograms did not exceed a few centimeters, except for narrow zones confined to local relief forms (Fig.2). The deformations thus detected were most likely due to surface processes.

The deformed volumes related to pressure changes in the magma chamber at a depth of 5 km must have linear dimensions of 10–15 km, while the displacement areas detected in the satellite images are considerably smaller. These results suggested an alternative model that postulates the resumption of seismic activity to accompany the retreat and sinking of magma melt from B. Udina into the chamber in the Tolud River area as identified by tomographic techniques.

Hence we can conclude that, beginning mid-2016, no evidence for emplacement of magma material from the Tolud chamber lying in the middle and lower crust northward toward B. Udina was detected. The important fact to remember is that ground deformation did occur based on SAR data before eruptions of Kizimen, Kamchatka, Pl. Tolbachik (TFE-50), and Bezymianny.

The presence of a hydraulic connection between the Tolud River area and the area of fissure eruptions on Plosky Tolbachik is also corroborated by the fact both in 1975 and in 2012, a few days after massive lava flows began to be discharged, large earthquakes were occurring in the Tolud River area. The hydraulic connection described above makes B. Udina an unlikely location for the next eruption, because in that case magma would have to find a way upward through cooled, consolidated, and higher-lying (relative to Tolbachik Dol) rocks in the edifice of this dormant volcano. The results derived in the present study in combination with the previously observed facts suggest the inference that the dormant B. Udina volcano is an unlikely site for a new eruption.

Results were published in the paper submitted to “Volcanology and Seimology” Journal of Russian Academy of Sciences (indexed in Web-of-Science and Scopus) entitled “Joint study of seismicity and SAR interferometry data for evaluating a possible eruption of a non-active volcano Big Udina” authors S. Senyukov, V. Mikhailov et al. [1].

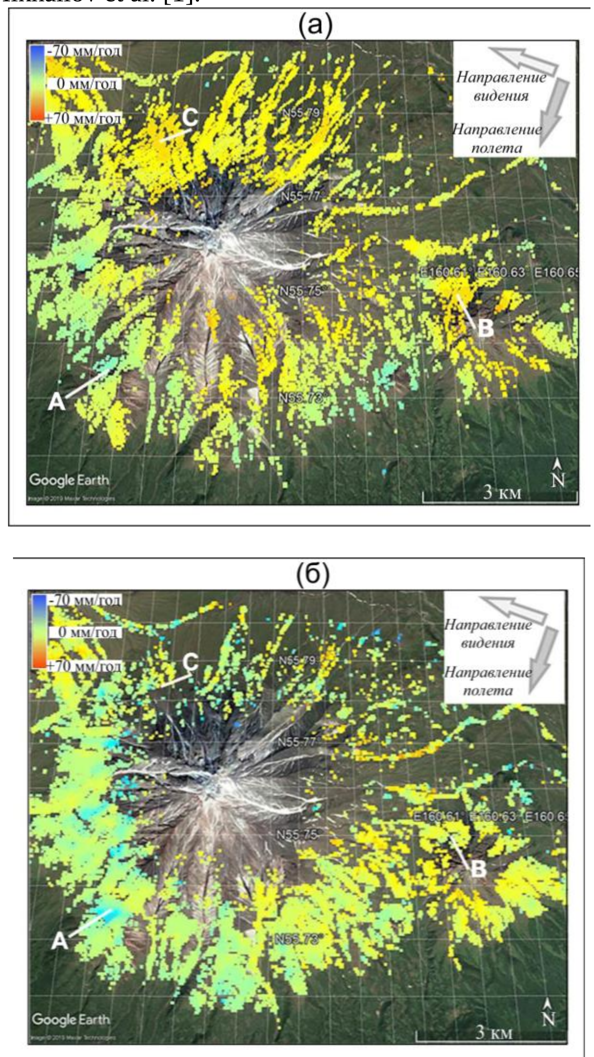

Fig. 1. The positions of persistent scatterers on the B. Udina slopes: survey period from June 7, 2017 to September 23, 2017 (a); survey period from May 21, 2018 to September 30, 2018 (b). The topographic background was based on an image at Google Earth. The color scale in the upper left corner represents average displacement rates between +70 and –70 mm/yr. The blue persistent scatterers were displaced away from the satellite. The flight direction and the line of sight are shown by arrows in the upper right corner.

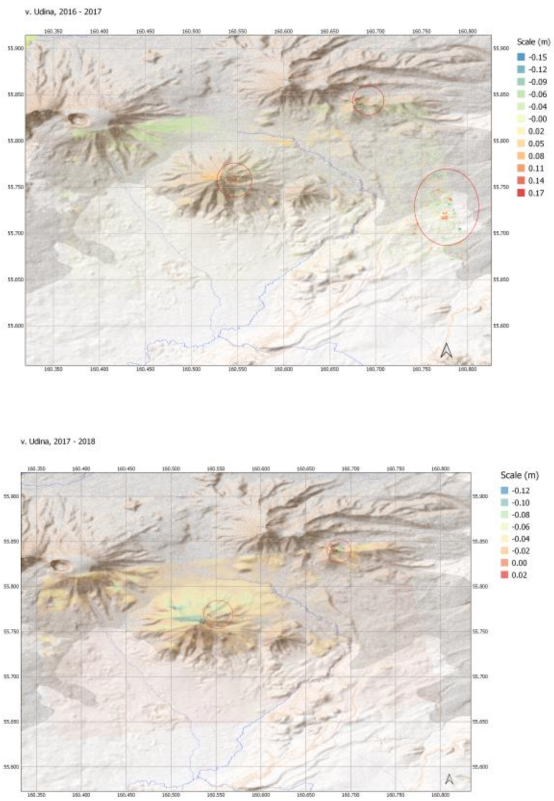

Fig. 2. Displacements in map view (meters) derived from paired interferograms based on ALOS-2 PALSAR-2 images for the periods from October 4, 2016 to June 13, 2017 (a) and from June 13, 2017 to October 2, 2018 (b). The red contours enclose areas with low (<0.35) coherence where displacement could not be determined with reliability. Negative values denote displacements from satellite, positive ones toward satellite.

3. ON THE CONNECTION BETWEEN THE 2008–2009 ACTIVATION OF THE KORYAKSKII VOLCANO AND DEEP MAGMATIC PROCESSES

The Koryakskii stratovolcano is located in the southern part of the Kamchatka Peninsula. It is the largest volcano in the Avachinskii–Koryakskii group of volcanoes (AKGV) located in the immediate vicinity of Petropavlovsk-Kamchatskii, the largest city of the peninsula. Studying the volcanic and seismic processes taking place in the AKGV region, the periods and causes of their activation, and eruption forecasting are critically important for people living in this most densely populated part of the peninsula.

The last activation of the Koryakskii volcano in 2008–2009 was accompanied by intense fumarolic and seismic activity. Volcanic activity peaked in March–April 2009 when ash plume rose to a height of 5.5 km and extended laterally over more than 600 km. To understand the dynamics of the volcanic processes and to forecast the further course of the events, it is relevant to establish whether the eruption was associated with a rise of magma to beneath the volcanic edifice or caused by fracturing of the volcano's basement and penetration of groundwater into a high temperature zone.

Based on the analysis of the images from the Japanese satellite ALOS-1 using satellite radar interferometry methods, the slope displacements of the Koryakskii volcano during its last activation have been estimated for the first time [2].

For the activation period of the Koryakskii volcano, we found seven ALOS-1 satellite images in the database of the Japan Aerospace Exploration Agency (JAXA). One image was rejected because of a long baseline and low coherence. The images map the ground surface as of June 21, 2006; August 16, 2007; May 18, 2008; October 6, 2009; May24, 2010; August 24, 2010, and October 9, 2010.

For the selected AKVG region, we calculated interferograms for different image pairs. The best results were from the image pair August 16, 2007 and October 6, 2009 the interval between which covers the entire eruption period. An important fact is that on the days of the survey, substantial territory of the slopes was free of snow cover.

The interferograms were calculated using the SARscape software with pixel averaging perpendicular to the orbit so that the resolution cell was as large as 14.98 × 12.29 m. Phase filtering was carried out by the Goldstein method. The interferometric coherence of the image pair is high for natural terrains (0.6). As the displacements are determined from the phase shift of the signals reflected from the same scatterer during the repeated imaging, the displacements on the interferogram are expressed in radians and wrapped modulo 2π. The absolute phase is determined by unwrapping, i.e., adding the number of full periods (2π multiples) corresponding to the path-length difference. To unwrap phase, we used minimum cost flow algorithm. After passing from radar coordinates to geographic coordinates, we constructed a map of displacements in m.

The displacements are determined in the line-of-sight direction. Their values on a selected area range from –33 (from the satellite) to 22 cm (towards the satellite). Assuming that displacements mainly occur in the vertical direction, then, with an average incidence angle of the satellite beam of 38.69°, the displacements in the directions towards the satellite should be multiplied by 1.28.

Areas of negative displacements are spotted on the slopes of all volcanoes on the image and can be primarily associated with erosion. Within the image there is only one area of the uplifts on the northwestern slope of the Koryakskii volcano around the 2008– 2009 eruption zone. The displacements increase from 9–15 cm at the foot to 20–22 cm towards to summit. Assuming that the displacements are purely vertical, we obtain that the displacements at the summit are above 28 cm.

We stress that the positive displacements on the northwestern slope of the Koryakskii volcano can barely be associated with the increase in the thickness of snow cover and glaciers in the vicinity of the summit or with the formation of a layer of ash deposits. According to the field data, the ashes, as a rule, had insignificant thickness and occurred as separate patches on the snow even at a small distance from the eruptive center. The cited work reports ash deposits with a thickness of a few cm. This is also clearly visible in many photo images presented on the Internet and in the articles. Moreover, it reported on melting of glaciers and on the formation of deep troughs in them due to the reduction of reflectivity of ice. These processes should have caused a surface to subside. Therefore, volcano surface uplifts with the amplitude up to 25 cm cannot be attributed to the formation of the ash layer.

The persistent ash emissions throughout the 2008– 2009 eruption and the analysis of seismicity indicate that magma could approach close to the volcano's surface. The total volume of the uplifts on the northwestern slope of the volcano (Fig. 3) is 1.3×10^6 m^3. In the Okada model of an dilating fault, this value is approximately equal to the volume of the opened space. This is very close to the estimate obtained by Gordeev and Droznin for the volume of magma (10^6 m^3) required whose cooling can provide the observed steam emission and to the value of opening of a fissure with a volume of 1.2×10^6 m^3 in the model. This indicates that the uplifts of the volcano slope just as the other observed processes are most likely to be associated with the intrusion of magma material.

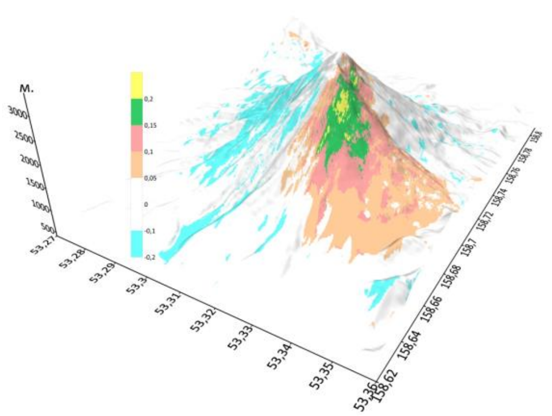

Fig. 3 Displacements (color scale in m) obtained from paired interferogram based on images of August 16, 2007 and October 6, 2009. Negative and positive values are displacements in the direction away from and towards the satellite. Shadow relief is based on SRTM DEM. Vertical scale is terrain elevations in m, horizontal scale is coordinates in degrees.

To interpret the displacement field we used the solution of Okada about surface deformation of an elastic half-space due to the displacement along a rectangular fault located in it. In the general case, the displacement vector includes three components: tensile (TS) reflecting extension, dip-slip (DS) component describing the up-dip or down-dip displacement along the fault plane, and a strike-slip (SS) component corresponding to the displacement along the strike. Application of this solution in our case is challenging because the solution is obtained for the displacements along a crack located in an elastic half-space with a horizontal free surface. Within the displacement region shown in Fig. 4, the terrain elevations vary from 1300 to 3450 m; therefore, the neglect of the real topography can lead to errors. To mitigate the terrain effect, we converted the displacement map into the local Cartesian coordinates and approximated the relief in the region with LOS above 10 cm by a plane. Then, the coordinate system was rotated around the Oz axis by an angle of 43.03° (the rotation direction is shown by red arrow in Fig. 4a) so that to make the Ox axis parallel to the projection of the approximating plane gradient vector onto the xOy plane (Fig. 4b). Within the displacement map, the heights of the approximating plane vary within 2.15 km and terrain elevations relative to this plane (Fig. 4b) range from –220 to 220 m.

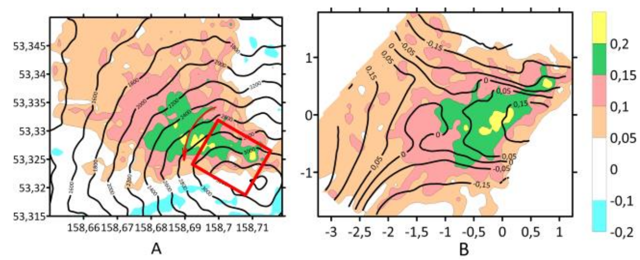

Fig. 4. Displacements in the direction towards satellite (color scale, m) on western and northwestern slope of Koryakskii volcano: (a) map in geographic coordinates, height in m. Red arrow is direction of rotation around Oz axis; (b) map in local Cartesian coordinates after subtraction of plane approximating local relief and rotation around the Oz axis. Isolines show height above approximating plane in m.

Next, the coordinate system was rotated by an angle of 27.3° around the Oy-axis so that the Oz-axis was perpendicular to the approximating plane. In the new coordinates, the plane approximating the relief coincides with the free surface of the elastic half-space and the deviations of the residual relief (Fig. 4b) prove to be small compared to a fracture depth. Now, as a distance from the fracture to the ground surface, in formulas of Okada we can either use the very distance to the approximating plane or to add to this distance the height of the local topography above this plane. Calculations have shown that with the heights of the local relief in the study region, this does not cause a significant change in the solution. After solving the inverse problem, the displacement field on the surface of the model is rotated back to the local coordinate system (Fig. 4b), and LOS displacement is calculated using the flight path azimuth and the incidence angle of radar beam (for ALOS-1 ascending track,–8.16° and 38.69°, respectively).

In the solution of Okada, a fracture is approximated by a rectangular element or a set of elements. We only considered a single rectangular element which ensures numerical stability of the inverse problem. A rectangular element is characterized by ten parameters. These are the three coordinates of the center of the lower edge of the rectangle; its dip and strike dimensions; the dip and strike angles; and the three components of the displacement vector (TS, DS, and SS). The displacement field on the surface is a linear function of the three components of the displacement vector; the dependence on the other parameters is nonlinear.

The size of the displacement region and the characteristic distance from the maximum to the half-maximum of the displacement field on the ground depend on the fracture depth and size. We selected the parameters of the rectangle based on the analysis results of seismic event distribution. The lower edge of the rectangular element was located at a depth of 0.5 km above sea level as suggested by the dimensions of the displacement region. The dip and strike dimensions were assumed to be 2.4 and 1.0 km, respectively. The dip angle was varied within 45–80°. The coordinates of the lower edge and the strike of the rectangle can be easily selected by shifting the maps of the calculated and measured displacement field relative to each other. We set the displacements along the fissure strike to be zero (SS = 0) and determined two components–extension (TS) and dip-slip displacement (DS)–by solving a system of linear equations.

The best fit of the LOS displacement field is achieved with the fissure dip angles in the interval from 45 and 60° (Fig. 5). In all models, the normal dip-slip displacement component is a few cm, i.e., zero within the accuracy. The extension at the dip angles 45°, 60° and 80° is 82, 71, and 64 cm, respectively. Thus, the volume of the injected material is 2.0×10^6, 1.7×10^6, and 1.5×10^6 m^3, respectively, which is consistent with the above data of other authors. The model with one rectangular fracture fairly well approximates the real displacement field; therefore, in our opinion, it was unreasonable to complicate the model.

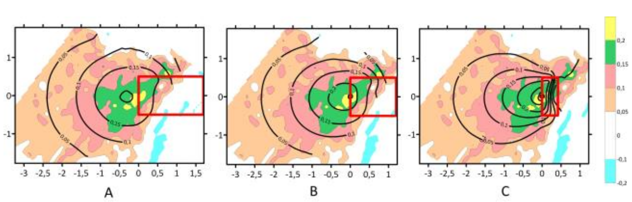

Fig. 5. Model of fissure in volcanic structure of Koryakskii volcano. Displacements in the LOS direction are shown by color (meters), isolines are the calculated LOS displacements in m: (a), (b), (c) models with dip angle 45°, 60°, and 80°. Red rectangle is projection of fissure on horizontal plane.

Hence we can conclude that:

1. The surface displacements of the Koryakskii volcano estimated by SAR interferometry are larger than 25 cm and cannot be explained by the ash layer formed during the eruption of 2008–2009. Slope processes and glacier melting should have produce displacements of the opposite sign. Therefore, as the most likely cause of the observed displacements, we should recognize the injection of magmatic material into the volcano structure. This is also suggested by the analysis of seismic catalogs and the results of thermal imaging studies.
2. A fissure model with a bottom edge at a depth of 0.5 km above sea level, a width of 1.0 km along the strike and 2.4 km along the dip, and a dip angle from 45° to 60° fairly well fits the displacements identified by SAR interferometry. Fissure volume is consistent with the estimates of other authors. We note that the depth of the fissure can be increased by 1 km with the corresponding reduction of its geometrical dimensions.
3. The obtained results support the hypothesis that the activation of the Koryakskii volcano was associated with the ascent of volcanic material and its injection, inter alia, into the volcanic structure of the volcano itself. Therefore, the processes taking place beneath the volcano can be threatening to the nearby localities and infrastructure and require continuous monitoring.

4. OTHER AREAS UNDER STUDY

1. Monitoring of Mutnovsky volcano situated close to the Petropavlovsk-Kamchatsky city and in the neighborhood of the largest hydrothermal power plant. Using the available ALOS-2 images (06/03/2017, 06/02/2018, 06/01/2019), paired interferograms and displacement maps for different time intervals were calculated. On the map of displacements based on images from 06/02/2018-06/01/2019 various changes are visible on the sides of the crater of Mutnovsky volcano, including subsidence on its western slope and inside the crater with amplitude from 4 to 8 cm. Since March-May 2018 a new lake within the crater of the volcano was formed. Active fumaroles were observed at this time on the sloped of the volcano, so this minor subsidence can highly likely be associated with snowmelt and/or glacier retreat.
2. Using ALOS-2 images from 2018- 2021 years, we are studying an intense volcanic activity on the Shiveluch volcano. This activity is increasing since 2018. Using the obtained displacements, we study the properties of the pyroclastic flow deposited after the powerful eruption on August 29, 2019 using thermo-mechanical model of its subsidence. From 2020 to 2021 years, the displacement amounted to -25 centimeters.
3. Using ALOS-2 images from 09 descending (2016/05/02, 2017/03/06, 2017/05/01) and 108 ascending (2016/07/30, 2017/07/29) tracks we are studying the

South Ozernoe earthquake that occurred on March 29, 2017 in the western part of the Bering Sea, the magnitude of the event was Mw = 6.6. In this study, the DInSAR technology was used. The ENVI SARscape and SNAP software packages with the built-in SNAPHU plugin were employed for the calculations. All possible pairs of ALOS-2 images covering the studied seismic event were analyzed. Additionally we calculated paired interferograms for Sentinel-1A images (since May 2016 till September 2017, 22 images all together) and compared the results. The interpretation of the obtained results is a non-trivial task. In the area under consideration at this time of the year, usually there is a thick snow cover, not necessarily dry. With the availability of geodesic data, it will be possible to build a model of the fault surface and conclude whether registered LOS displacements show displacements of the earth's surface or they dealt with displacements of the snow/ice cover.

APPENDIX

List of published papers related to ALOS EO-RA2

[1] Senyukov, S.L., Mikhailov, V.O., Nuzhdina, I.N. et al. A Joint Study of Seismicity and SAR Interferometry Observations for Assessing the Possibility of an Eruption of the Dormant Bolshaya Udina Volcano. J. Volcanolog. Seismol. 14, 305–317 (2020).

[2] Mikhailov V., Volkova M., Timoshkina E., Shapiro N., Smirnov V., 2021 On the Connection between the 2008-2009 Activation of the Koryakskii Volcano and Deep Magmatic Processes. Izv., Phys. Solid Earth 57(6), 819-824.

LANDSLIDE DEFORMATION MONITORING AND MECHANISM INVERSION REVEALED BY ADVANCED INSAR TECHNIQUES

PI No.: ER2A2N100

Yuanyuan Liu [1]

[1] Faculty of Geomatics, East China University of Technology, Nanchang, China

1. INTRODUCTION

Long-term multi-dimensional time series deformation monitoring is crucial for generating early warnings for active landslides and mitigating geohazards. Various advanced interferometric synthetic aperture radar (InSAR) methods have been widely applied to detect and monitor small-gradient landslide deformation. However, the InSAR observations were just limited to LOS ascending or descending direction, which could hardly reveal correct deformation characteristics when the landslide showed multi-dimensional deformation. Thus, a refined small baseline subsets (SBAS) method and multidimensional small baseline subset (MSBAS) InSAR technique were applied to characterize the landslide kinematics with multi-track synthetic aperture radar (SAR) images. Moreover, measuring the steep-gradient landslide deformation has posed certain challenges. An improved cross-platform SAR offset tracking method was proposed, which can not only estimate high-precision landslide deformation in two and three dimensions but also calculate long-term time series deformation over a decade using cross-platform SAR offset tracking measurements.

2. METHODS

2.1 Small Baseline Subsets (SBAS) InSAR

Due to the limited interferometric datasets from the ALOS PALSAR-2 satellite, the small baseline subsets (SBAS) InSAR technique [1] was applied to retrieve the landslide deformation. To obtain the DEM error and time series deformation, a refined SBAS-InSAR method was applied in our study, which divides the interferograms into high- and low-quality sets and estimates the parameters iteratively [2]. In general, a minimum cost flow (MCF) method with the aid of coherence is adopted to unwrap the interferogram [3]. However, the continuous motion of the Three Bears landslide makes it troublesome to produce effective long-duration (>70 days) interferograms. Therefore, a deformation model constructed from a stack of correctly-unwrapped short-duration interferograms was introduced and then subtracted from the original interferograms. Thus, we could maintain coherence and minimize the phase unwrapping error. After the residual interferometric phase was filtered and unwrapped, the subtracted deformation derived from the deformation model was added back into the residual unwrapped interferogram. This technique works well because it prevents the phase gradient of adjacent pixels exceeding π radian (5.9 cm for ALOS PALSAR-2). We carefully compared the new unwrapped interferograms with the original wrapped interferograms to ensure that no artifacts were introduced in this processing. Once the interferograms were successfully unwrapped, the time series deformation was retrieved by using either the least squares (LS) or a singular value decomposition (SVD) method.

2.2 Two-dimensional time series deformation inversion with multi-track SAR datasets

The SAR data from each independent track were processed using the above-mentioned SBAS method, so the InSAR observations were limited to LOS ascending or descending direction. The availability of ascending and descending ALOS PALSAR-2 measurements in the Three Bears landslide provides us with an opportunity to extend the displacement vectors to 2-D or 3-D [4]. Therefore, the east-west and vertical deformation components were simultaneously inverted by using a multidimensional small baseline subset (MSBAS) InSAR technique [5] by using multi-track synthetic aperture radar (SAR) images.

2.3 Multi-dimensional long-term time series inversion with improved cross-platform SAR offset tracking method

The proposed procedure focuses on the three shortcomings of traditional SAR offset tracking methods in the time series deformation mapping of slow-velocity landslides, especially in complex areas, such as rugged mountain areas, steep terrains, and non-homogenous targets. For the first solution, the ortho-rectification of the SAR images was added to remove topographic relief effects and achieve accurate co-registration of SAR images from identical and cross platforms. Second, adaptively varying windows were introduced into the cross-correlation computation to avoid the bias caused by non-homogenous samples in two image patches, thus improving the accuracy of the azimuth and slant-range offset measurements, particularly for offset pairs with longer spatial baselines. Third, high-quality offset pairs were optimally selected to design the network of deformation inversion based on the measurement uncertainties and the theory of optimization and design of geodetic networks. Fourth, the mathematical equation of two-dimensional (2D) deformation rates and time series inversion was established using the designed network, into which the M-estimator was introduced to restrain the outliers caused by low correlation. Next, the three dimensional (3D) deformation inversion based on the surface-parallel flow model [6] and the estimated 2D deformation were followed. The TLS algorithm was applied to estimate the 3D deformation rates and time series, given that random errors exist not only in the observations but also in the coefficient matrix (caused by inaccurate DEM).

3. DEFORMATION MONITORING OF THREE BEARS LANDSLIDE IN NORTHERN CALIFORNIA

The spatiotemporal deformation variations of the Three Bears landslide in northern California have not been systematically monitored and interpreted. In this study, we applied advanced time-series InSAR analysis methods to characterize the kinematics of the landslide covering two periods (2007-2011 and 2015-2017) with multi-track synthetic aperture radar images acquired from L-band ALOS PALSAR-1/2 satellites.

The annual LOS deformation rates derived from each independent SAR datasets are shown in Fig.1. It is worth noting that the positive values indicate the landslide motion toward the satellite sensor while the negative values represent the landslide motion away from the satellite sensor. As seen on the deformation maps, the large displacement mainly occurs in the eastern part of the Cedar Grove Ranch Earthflow, which is consistent with the active landslide identified by Zhao et al. [7]. Furthermore, the average ascending LOS deformation rates were almost similar to those of the descending LOS velocities during the period of 2015-2017, but the signs were the opposite, indicating that the landslide moved toward the satellite sensor in the descending tracks, but away from the sensor in the ascending tracks (Fig. 1c-f). These observations also suggest that the landslide displacements must be dominated by the horizontal motions. We can also see that the Three Bears landslide underwent strong movement with the deformation rate exceeding 300 mm/yr from 2007 to 2011, but the motions decreased to around 250 mm/yr from 2015 to 2017.

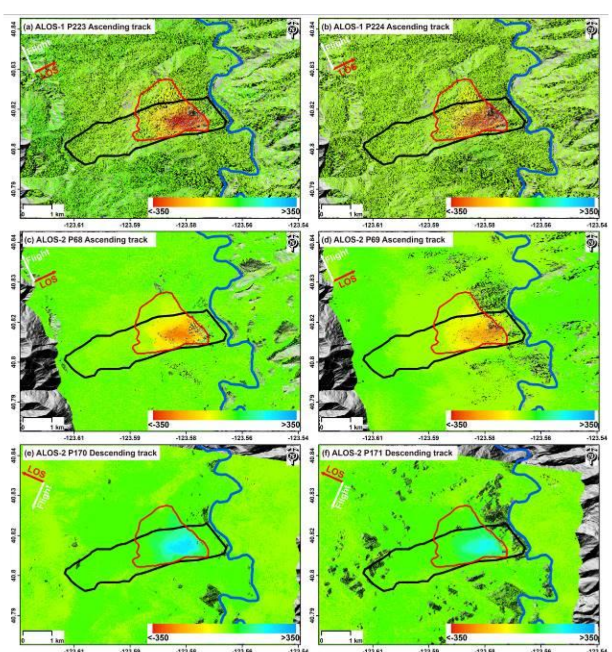

Fig. 1 Average LOS deformation rate maps of the Three Bears landslide calculated with L-band SAR datasets (unit: mm/yr). The figures in the first and second row show the results derived from ascending datasets: (a) P223 of ALOS PALSAR-1 (data period: 2007-2011), (b) P224 of ALOS PALSAR-1(data period: 2007-2011), (c) P68 of ALOS PALSAR-2 (data period: 2015-2017), and (d) P69 of ALOS PALSAR-2 (data period: 2014-2017). The figures in the third row show the results derived from descending datasets: (e) P170 of ALOS PALSAR-2 (data period: 2015-2017) and (f) P171 of ALOS PALSAR-2 (data period: 2015-2017).

Combining the results shown in Fig. 1c-f with the slope and aspect information derived from DEM data, it can be deduced that the Three Bears landslide primarily moved eastward horizontally. Since both ascending and descending ALOS PALSAR-2 data had the same time span from 2015 to 2017, we derived the east-west and vertical deformation components by using eight (six from P68 and two from P69) ascending interferograms and eighteen (fourteen from P170 and four from P171) descending interferograms. The two-dimensional time-series deformations of the active landslide are presented in Fig. 2 and Fig. 3, respectively. It can be seen that there was a continuous eastward movement of the landslide and obvious uneven deformation patterns were also visible during the whole monitoring period. The maximum cumulative east-west deformation from March 2015 to November 2017 could reach up to 1400 mm in Zone 1, but just 500 mm in Zone 2, and less than 300 mm in Zone 3. However, a different pattern and trend was seen in the cumulative vertical deformation. It can be seen from Fig. 3: (1) that the landslide in Zone 1 experienced continuous subsiding deformation during the whole period with a maximum cumulative displacement up to -500 mm; (2) The landslide in Zone 2 presented a relatively small movement before February 2017 with an average deformation rate of -20.4 mm/yr, but moved quickly after February 2017 with an average deformation rate of -44.1 mm/yr, where the maximum vertical displacement amounted to -200 mm; and (3) The landslide in Zone 3 showed less vertical movement than the other two zones with a maximum vertical displacement just up to -100 mm during the period of March 2015 to November 2017.

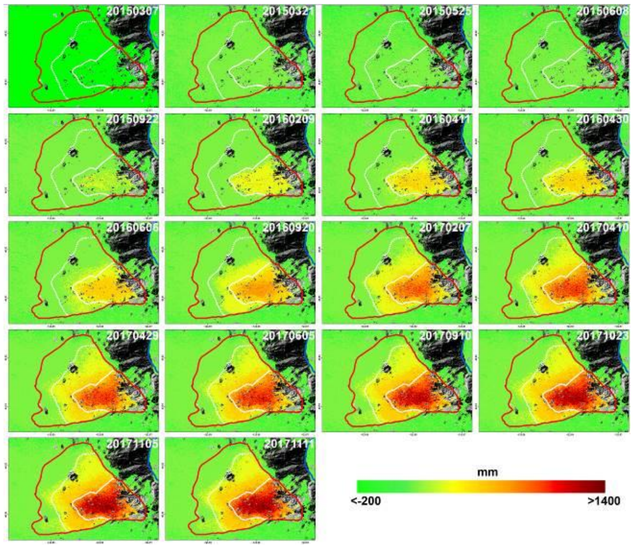

Fig. 2 Cumulative east–west deformation from March 7 2015 to November 11 2017 inverted by using ascending and descending ALOS PALSAR-2 satellite datasets. It is worth noting that the positive values indicate eastward movement while the negative values represent westward movement.

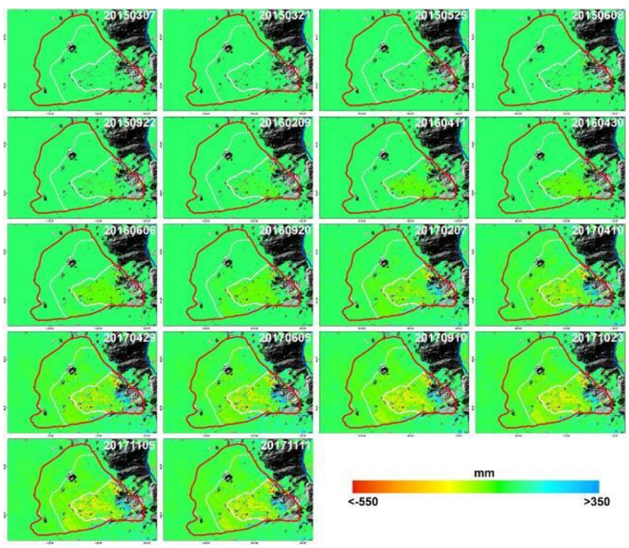

Fig. 3 Cumulative vertical deformation from March 7 2015 to November 11 2017 inverted by using ascending and descending ALOS PALSAR-2 satellite datasets.

4. LANDSLIDE DETECTION IN LINZHI, THE QINGHAI-TIBETAN PLATEAU OF CHINA USING LONG-WAVELENGTH ALOS PALSAR-2 SAR OBSERVATIONS

The Qinghai-Tibetan is a highland with the highest elevation and most complex geological setting in the world. Linzhi is located in the southeast of the Qinghai-Tibetan Plateau of China. For the purpose of disaster management and prevention, we used ALOS PALSAR-2 SAR images based on InSAR method to detect and map active landslides in the study area. The deformation rate map between 2016 and 2019 are shown in Fig. 4, where the positive values (blue color) indicate the motion toward the satellite, and the negative values (red color) indicate the motion away from the satellite. We can see that most regions of the study area are quite stable, and two concentrated areas of landslides were detected (see the red rectangles in Fig. 4), which are located in the northeast and southwest of the study area. The deformation rate of the two concentrated areas are highlighted in Fig. 5, we can see that a host of small-scale landslides were observed, which were driven by glacier movements and glacier avalanches. The results suggest that long-wavelength SAR images have unique advantages for detecting landslides in dense vegetation cover areas. However, serious decorrelation occurred in large glacier-covered areas duo to the large-gradient deformation, thus casing the phase measurements of SAR images failure. Therefore, we will apply the offset-tracking method based on SAR amplitude information to measure large-gradient deformation in future work.

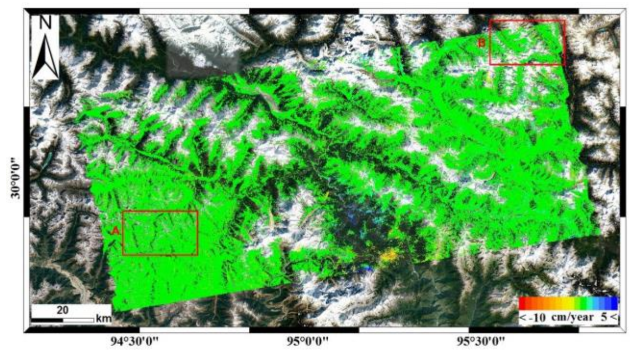

Fig. 4 The deformation rate map of Linzhi, China between 2016 and 2019 calculated with ALOS PALSAR-2 images.

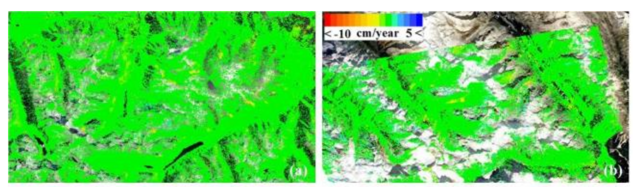

Fig. 5 Enlarged deformation rate maps of regions A (a) and B (b) marked in Fig. 4.

5. MULTI-DIMENSIONAL AND LONG-TERM TIME SERIES MONITORING OF THE LAOJINGBIAN LANDSLIDE, WUDONGDE RESERVOIR AREA (CHINA)

Using the cross-platform ALOS PALSAR-1 and ALOS PALSAR-2 images, we retrieved the long-term 2D deformation rates and time series of the Laojingbian landslide from August 2007 to May 2020. Then, we estimated the long-term 3D deformation rates and time series by using the 2D displacements and external DEM.

Fig. 6 shows the 2D annual deformation rates of the Laojingbian landslide during different periods. In Fig. 6(a), (c), and (e), the blue colors indicate that the pixels are moving along the flight direction of the satellites, while the blue colors in Fig. 6(b), (d), and (f) indicate that the landslide is moving away from the satellites. Furthermore, the landslide movements were simultaneously measured in both the azimuth and slant-range directions, suggesting that the Laojingbian landslide has 3D movement characteristics. The maximum deformation rates in the azimuth direction from August 2007 to March 2011, from September 2014 to May 2020, and from August 2007 to May 2020 were -0.9, -1.5 and -1.0 mm/year, respectively, and the corresponding deformation rates in the slant-range direction were -1.6, -2.6 and -1.7 m/year. The results suggest that the landslide movement in the slant-range direction is approximately 1.7 times that in the azimuth direction. The average slope aspect derived from DEM indicates that the Laojingbian landslide is oriented toward the east, which is nearly perpendicular to the flight directions (approximately $-10°$ from the north) of the ALOS PALSAR-1 and ALOS PALSAR-2 sensors. Thus, the observed landslide displacement mainly occurred in the slant-range direction. Moreover, the 2D deformation rates of the landslide increased with time, suggesting that the landslide may have been in the accelerated displacement stage during the observational period of the ALOS PALSAR-2 images.

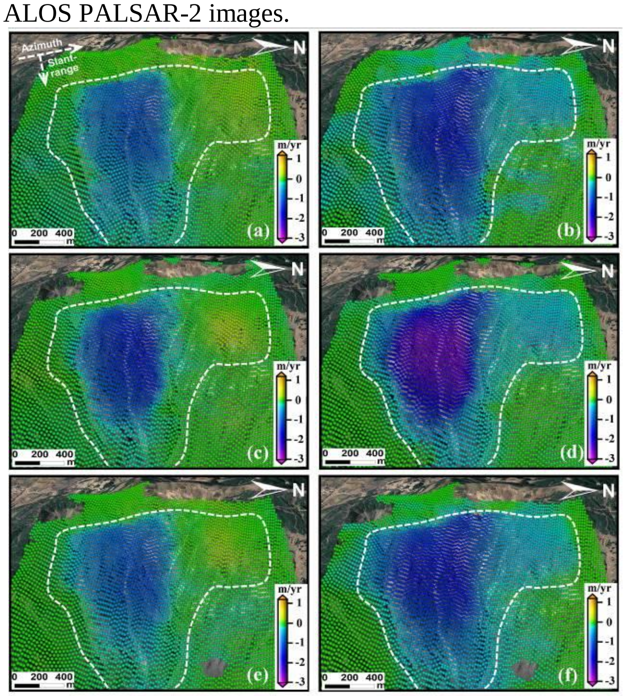

Fig. 6 2D long-term deformation rates in the azimuth and slant-range directions of the Laojingbian landslide retrieved with the ALOS PALSAR-1 and ALOS PALSAR-2 images. The white dashed lines indicate the unstable region. (a) and (b) are the deformation rates in the azimuth and slant-range directions, respectively, retrieved from the ALOS PALSAR-1 images between August 2007 and March 2011; (c) and (d) are the deformation rates in the azimuth and slant-range directions, respectively, retrieved from the ALOS PALSAR-2 images between September 2014 and May 2020; and (e) and (f) are the deformation rates in the azimuth and slant-range directions, respectively, retrieved from the cross-platform ALOS PALSAR-1 and ALOS PALSAR-2 images between August 2007 and May 2020.

On the basis of the estimated 2D displacements, the 3D long-term deformation rates and time series of the Laojingbian landslide were retrieved. Fig. 7 shows the 3D deformation rates in the north-south (N-S), east-west (E-W), and up-down (U-D) directions of the Laojingbian landslide from August 2007 to May 2020. The 3D deformation time series for P1-P6 are presented in Fig. 8. Negative values (blue) in the N-S deformation maps indicate northward landslide movement, negative values (blue) in the E-W deformation maps indicate eastward landslide movement, and negative values (blue colors) in the U-D deformation maps indicate downward landslide movement. As shown in Fig. 7 and Fig. 8, the 3D displacement fields clearly revealed the fine-scale spatiotemporal characteristics of the Laojingbian landslide, which can lead to a better understanding of the movement and failure mechanism of the slope in depth. The N-S deformation rates shown in Fig. 7(a), (d), and (g) highlight the landslide with both northern movement and southern movement, with the maximum deformation rates of -0.6, -0.9 and -0.6 m/year from August 2007 to March 2011, from September 2014 to May 2020, and from August 2007 to May 2020, respectively. The E-W deformation rates shown in Fig. 7(b), (e), and (h) suggest the eastward movement of the landslide, with maximum deformation rates of -2.5, -4.3 and -2.8 m/year from August 2007 to March 2011, from September 2014 to May 2020, and from August 2007 to May 2020, respectively. The U-D deformation rates presented in Fig. 7(c), (f), and (i) indicate only downward movement of the landslide, with deformation rates of -0.7, -1.2 and -0.8 m/year from August 2007 to March 2011, from September 2014 to May 2020, and from August 2007 to May 2020, respectively. The results revealed that the displacement in the E-W direction was much larger than those in the N-S and U-D directions, suggesting that the landslide movement was dominated by the E-W displacement. Similar to the 2D displacements, the displacements in the three directions increased with time, and the boundary of the active part of the landslide was clearly mapped by the 3D displacements.

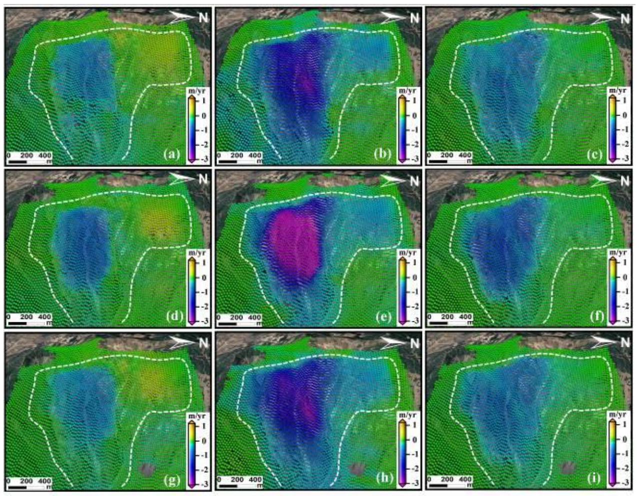

Fig. 7 Estimated 3D deformation rates in the north-south (N-S), east-west (E-W) and up-down (U-D) directions of the Laojingbian landslide. The white dashed lines indicate the unstable region. (a)-(c) are the deformation rates in the N-S, E-W and U-D directions, respectively, calculated with the ALOS PALSAR-1 images from August 2007 to March 2011; (d)-(f) are the deformation rates in the N-S, E-W and U-D directions, respectively, calculated with the ALOS PALSAR-2 images from September 2014 to May 2020; and (g)-(i) are the deformation rates in the N-S, E-W and U-D directions, respectively, calculated with the cross-platform ALOS PALSAR-1 and ALOS PALSAR-2 images from August 2007 to May 2020.

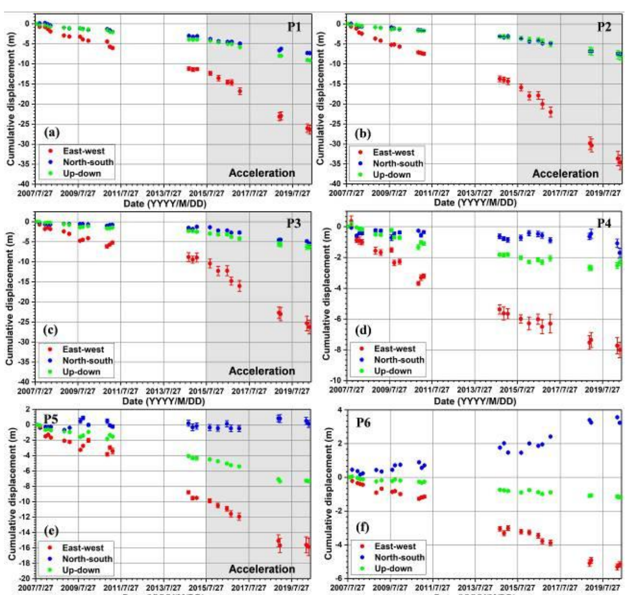

Fig. 8 Estimated 3D deformation time series of the Laojingbian landslide for P1-P6 from August 2007 to May 2020, retrieved with cross-platform ALOS PALSAR-1 and ALOS PALSAR-2 images.

6. REFERENCES

[1] P. Berardino, G. Fornaro, R. Lanari, and E. Sansosti, “A new algorithm for surface deformation monitoring based on small baseline differential SAR interferograms”, *IEEE Transactions on Geoscience and Remote Sensing*, vol. 40, no. 11, pp. 2375-2383, 2002.

[2] C.W.Lee, Z. Lu, H.S. Jung, J.S. Won, and D. Dzurisin, “Surface deformation of Augustine Volcano (Alaska), 1992–2005, from multiple-interferogram processing using a refined SBAS InSAR approach”, *In The 2006 eruption of Augustine Volcano, Alaska: U.S. Geological Survey Professional Paper 1769; Power, J.A., Coombs, M.L., Freymueller, J.T., Eds.; U.S. Geological Survey: Reston, VA, USA*, pp. 453-465, 2010.

[3] C.W. Chen, and H.A. Zebker, “Two-dimensional phase unwrapping with the use of statistical models for cost functions in nonlinear optimization”, *Journal of the Optical Society of America A*, vol. 18, no. 2, pp. 338-351, 2001.

[4] T.J. Wright, B.E. Parsons, and Z. Lu, “Toward mapping surface deformation in three dimensions using InSAR”, *Geophysical Research Letters*, vol. 31, pp. L01607, 2004.

[5] S. V. Samsonov, and N. d'Oreye, “Multidimensional small baseline subset (MSBAS) for two-dimensional deformation analysis: Case study Mexico City”, *Canadian Journal of Remote Sensing*, vol. *43*, no. 4, pp. 318-329, 2017.

[6] J. J. Mohr, N. Reeh, and S. N. Madsen, “Three-dimensional glacial flow and surface elevation measured with radar interferometry”, *Nature*, vol. 391, pp. 273-276, 1998.

[7] C. Zhao, Z. Lu, Q. Zhang, and J. de La Fuente, “Large-area landslide detection and monitoring with ALOS/PALSAR imagery data over Northern California and Southern Oregon”, USA. *Remote Sensing of Environment*, vol. 124, pp. 348-359, 2012.

APPENDIX

[1] Y. Liu, Z. Lu, C. Zhao, J. Kim, Q. Zhang, and J. de la Fuente, “Characterization of the Kinematics of Three Bears Landslide in Northern California Using L-band InSAR Observations”, *Remote Sensing*, vol. 11, no. 23, pp. 2726, 2019.

MULTI-TEMPORAL INSAR ANALYSIS OF HIGH-SPEED RAILWAY DEFORMATION IN BEIJING-TIANJIN-HEBEI REGION USING PALSAR-2

PI No.: ER2A2N115

Qingli Luo [1], Zhiyuan Yin [1]

[1] State key Laboratory of Precision Measuring Technology and Instruments, Tianjin University, No. 92, Weijin Road, Nankai District, Tianjin 300072, China

Abstract: Synthetic aperture radar interferometry (InSAR) is widely applied in ground subsidence monitoring. In this report, with ALOS PALSAR-2 data, we presented the first multi-temporal InSAR analysis of high-speed railway deformation located in the Beijing-Tianjin-Hebei region. 47 ALOS PALSAR-2 images were processed to extract the time series deformation results. The deformation trend along the high-speed railways located in the Beijing-Tianjin-Hebei region is analyzed. We also analyzed the subsidence centers along Beijing-Shanghai and Beijing-Tianjin intercity high-speed railways, respectively. These results show high potential for high speed railway subsidence monitoring with ALOS-2 data and the research provides a reference for further deformation monitoring along high-speed railway in the Beijing-Tianjin-Hebei region.

Keywords: ALOS PALSAR-2 data, InSAR, high-speed railway, deformation monitoring

1. INTRODUCTION

Land subsidence is one of the most serious geological hazards in the world. Three major regions affected by most serious land subsidence in China include the Yangtze River Delta, the North China Plain, and the Fence-Weihe basins [1]. The Beijing-Tianjin-Hebei region is located in North China Plain. The possible reasons of the serious land subsidence over these areas are the geological conditions, the soft clay coverage and the increasing underground water demand. Two main important high-speed railways are located in these areas and they are Beijing-Shanghai and Beijing-Tianjin intercity high-speed railways. The deformation along high-speed railways cause will bring risk on life security and economic loss.

Traditional monitoring methods include leveling, bedrock markers, stratified tables, and GLOBAL Positioning System (GPS) measurements [2]. Synthetic aperture radar interferometry (InSAR) makes it possible to monitor land subsidence accurately over a wide range and with short interval. The inherent limitations of InSAR were avoided by Multi-temporal InSAR (MT-INSAR) methods including permanent scatterers [3-4]. It can accurately extract the surface deformation information through multi-temporal InSAR data by looking for point-target scatter. Berardino et al.[6] proposed a small baseline method and it searched for distributed scatters [7]. More recently, methods have been proposed by exploring both types of the scatterers [8-10]. The detection of partially coherent targets has been detected by Quasi-PS (QPS) [11] technique. These different techniques can be optional methods for multi-temporal InSAR (MT-InSAR) analysis when applied to monitor deformation in diverse applications according to real conditions and restrictions.

One of the main drawback of SAR images is the low resolution. With the launch of new generation high-resolution SAR satellites, the level of details visible in SAR images increased dramatically [12]. ALOS PALSAR-2 can provide SAR data with global coverage and high resolution, and it has relatively high temporal and spatial coherence even in vegetated and forested areas.

To explore the potential ability for monitoring subsidence along high-speed railway, 47 ALOS PALSAR-2 images were processed and the results are presented in this report. The study area is located in Beijing-Tianjin-Hebei region and the datasets are collected from 2015 to 2021. The subsidence information was extracted by MT-InSAR method. Combined with the historical information of the study area, the subsidence centers along these two high-speed railways were analyzed. All of these results will provide reference for further monitoring planning along these two high-speed railways in the Beijing-Tianjin-Hebei region.

2. STUDY AREA AND DATASET

The study area is located in Beijing-Tianjin-Hebei region. Beijing-Shanghai and Beijing-Tianjin intercity high-speed railways are across this region. The geographic location of the study area is illustrated in Figure 1. Two high-speed railway are highlighted with red and green lines, respectively.

The study area includes part of Beijing, Tianjin, and Hebei provinces, and they are located in North China Plain. It is affected by most serious land subsidence in China. Beijing-Tianjin Inter-city railway (from 39.865068°N, 116.376120°E to 39.003333°N, 117.678745°E). The whole railway track is about 120 km and more than 130 pairs of trains are working along this railway. Beijing-Shanghai high-speed railway (from 39.750048°N, 116.299992°E to 39.151547°N, 117.075745°E). Beijing-Shanghai high-speed railway is across Beijing, Tianjin and Hebei, and several other provinces. The length of the whole track is 1318 km. The operation lasts 7 years and the total number of passengers achieved 82,000,000. The small deformation will cause large economic loss and threaten the safety of lives.

The available SAR datasets are composed of four frames of ALOS-2 L-band images. Four frames are 137-790, 137-780,137-770a, 137-770b, and 137-760, and they are marked with blue frames. The detail lists of each frame are listed in Table 1.

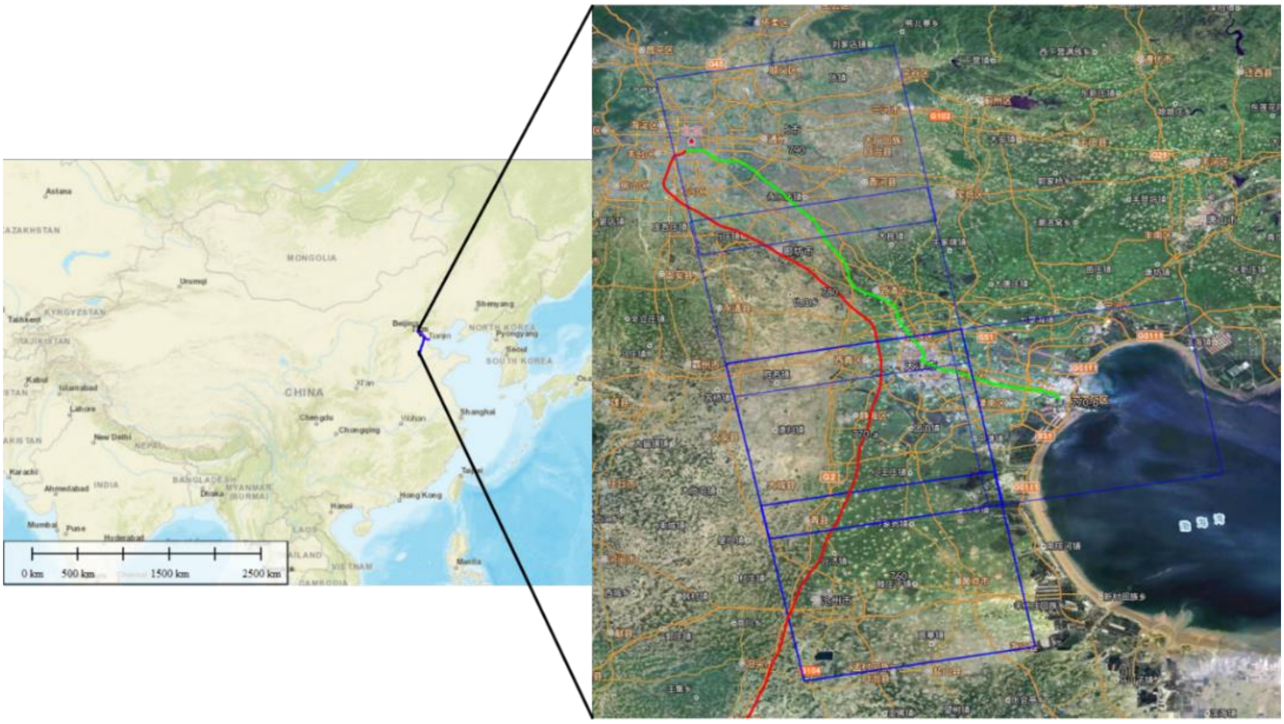

Fig. 1 Study area and PALSAR-2 data. The location of the study area is highlighted with the blue line on the map of China, which is zoomed and illustrated in the right inset, as shown by the red line and green line.

Table1 The acquisition date of the ALOS PALSAR-2 datasets

Frame 790		Frame 780	Frame 770A	Frame 770B	Frame 760
No.	Date	Date	Date	Date	Date
1	20150709	20150205	20150709	20150723	20150709
2	20150917	20150709	20150917	20151001	20150917
3	20151126	20150917	20151126	20151029	20151126
4	20160915	20151126	20160915	20151210	20160915
5	20161124	20160915	20161124	20160721	20161124
6	20170202	20161124	20170202	20160929	20170202
7	20170706	20170202	20170706	20161208	20181025
8	20171109	20170706	20181025	20181108	20190509
9	20181025	20181025	20190509	20190718	--
10	20190509	20190509	20210506	--	--

3. METHODOLOGY

QPS technique was applied to process the ALOS-2 dataset and it was implemented with the software SARPROZ [13]. For processing the ALOS PALSAR-2 datasets, the processing strategy is designed according to the spatial-temporal baseline distribution of the datasets, the number of images in the datasets, and the deformation situation of the study area. The whole processing can be divided into two sections and they are InSAR processing and MT-InSAR processing. We need to set the threshold of average spatial coherence during multi-baseline construction. In our processing, we select the threshold as 0.3. It means the baselines are constructed with triangulation network when the average spatial coherence is above 0.3. After calculating the atmosphere, the interference information of the image is used to calculate the deformation in the subsequent processing. All the QPS points are connected with a single reference point. The flow chart is illustrated as Fig. 2.

4. EXPERIMENTAL RESULTS

4.1 The whole subsidence analysis of the study area

According to the above processing, the average deformation velocity of the Beijing-Tianjin-Hebei region is extracted. The average deformation map of the whole study area located in Beijing-Tianjin-Hebei region is illustrated in Fig. 3(a). The average subsidence velocity ranges from -155 to 20 mm/a. As Fig. 3(a) shows, the deformation velocity in the northern region is much faster than that in the southern region. Several distinct subsiding centers formed in the northern region, while the deformation velocity was relatively slow in the southern region.

As shown in Fig. 3(b), there are two subsiding areas around Beijing city. They are located in Tongzhou district and Langfang city. The maximum subsidence velocity in Tongzhou district is more than 135 mm/a. The average subsidence velocity in Langfang city is relatively slower than that in Tongzhou district and it is about 113 mm/a.

Fig. 3(c) presents the enlarged average deformation map around Tianijn city. Three subsiding centers are located in Wuqing, Beichen, and Jinghai districts, respectively. The maximum subsidence velocity is 152mm/a, and it is located in Wangqingtuo Town of Beichen district. Geyucheng town, Yangfengang town, and Tangerli town are also located in Beichen district affected by serious subsidence. These areas are newly formed and monitored settlement centers in suburb of Tianjin. In jinhai district, Tuanbo town is one of the areas affected by serious subsidence, and the average subsidence velocity reaches 126mm/a.

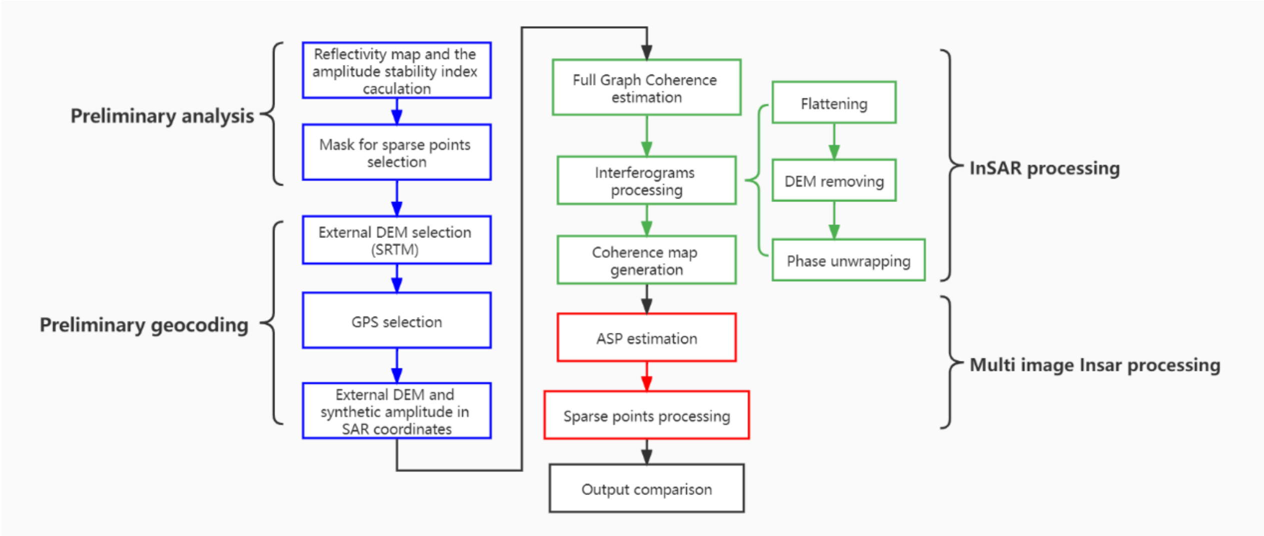

Fig. 2 The flow chart of data processing

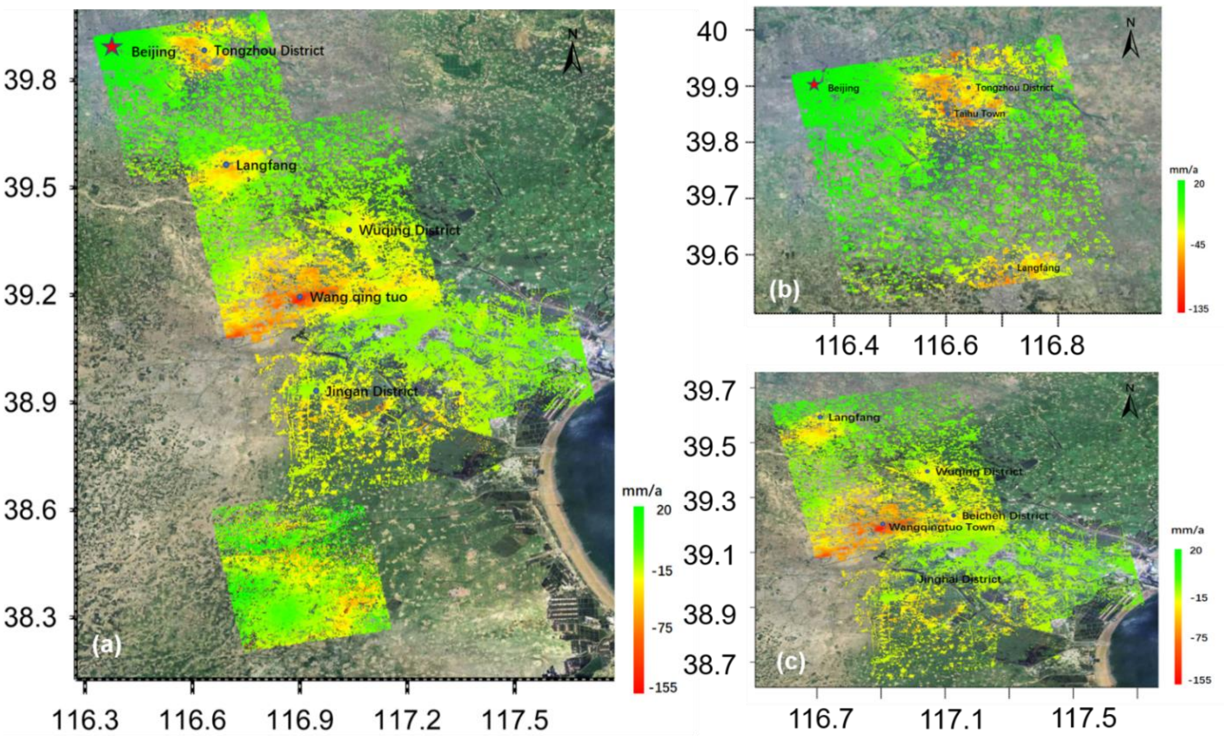

Fig. 3 The average deformation velocity map of the study area located in Beijing-Tianjin-Hebei area. (a) The whole average deformation map. (b) The enlarged average deformation velocity map around Beijing city. The two subsidence centers are located in Tongzhou district and Liangfang city. (c) The enlarged average deformation velocity map around Tianjin city. Three subsidence centers are located in Wuqing, Beichen, and Jinghai districts.

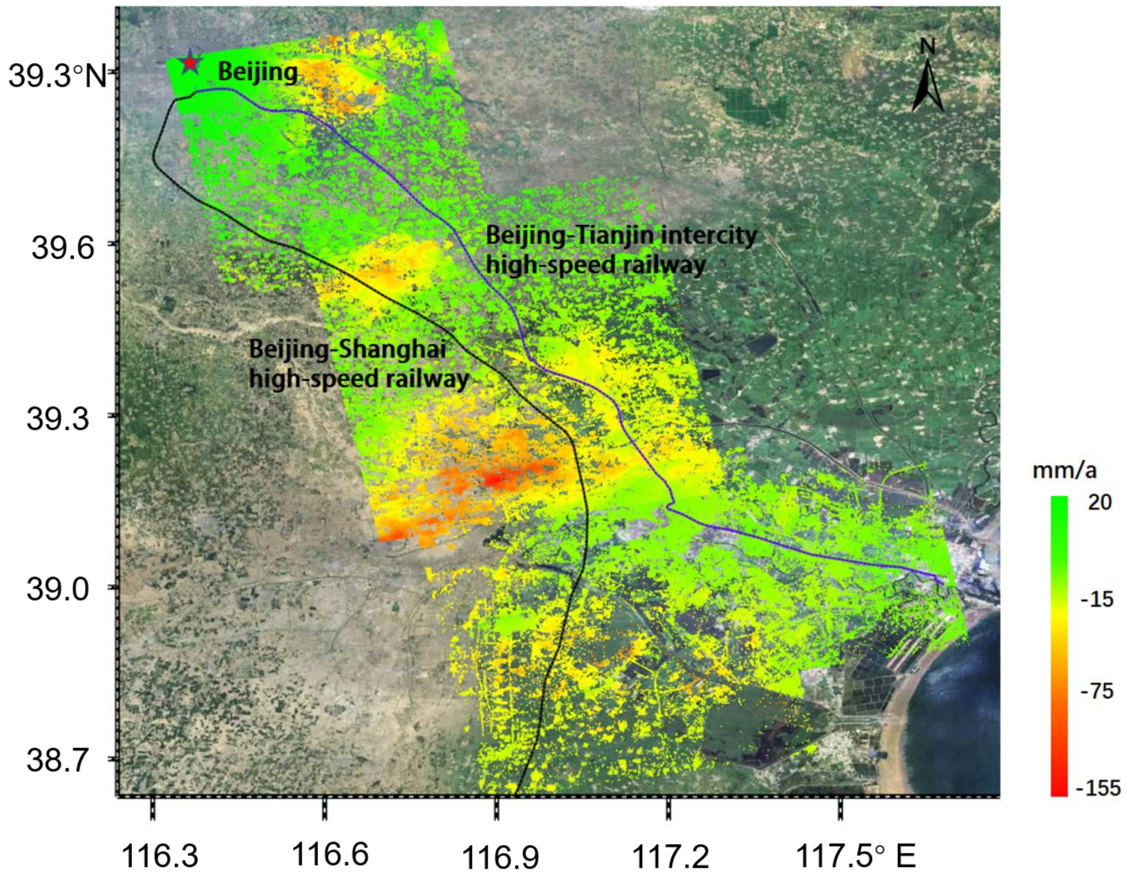

Fig. 4 The average deformation velocity map of Beijing-Tianjin intercity and Beijing-shanghai high-speed railway located in Beijing-Tianjin-Hebei Region. The locations of these two high-speed railways are highlighted with black and blue lines, respectively.

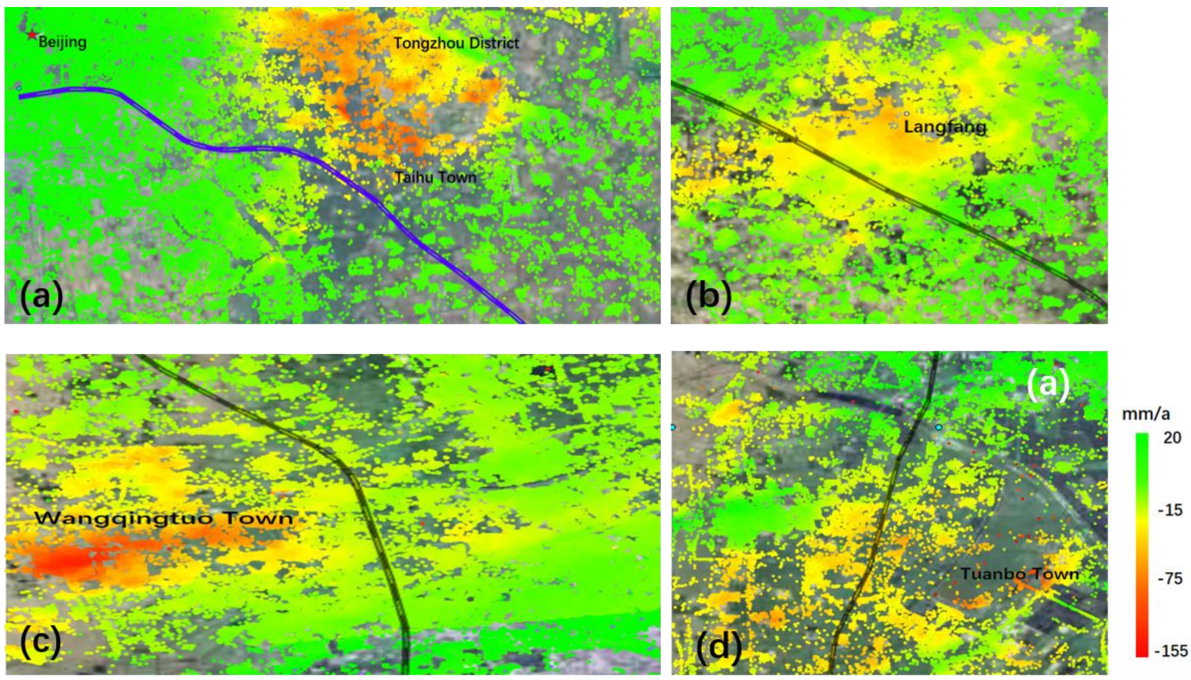

Fig. 5 The partially enlarged average deformation map of Beijing-Tianjin intercity and Beijing-shanghai high-speed railways. These two high-speed railways are highlighted with the blue and black lines, respectively. (a) The subsiding centers located in Tongzhou District. (b-d) present the subsiding centers located in Langfang city, Wangqingtuo and Tuanbo town, respectively.

4.2 Subsidence analysis along two high-speed railways

Beijing-shanghai and Beijing-Tianjin intercity railway are two high speed railway across this study area as illustrated in Fig. 4. These two high-speed railways are highlighted with the blue and black lines, respectively. Fig. 5 presents the partially enlarged average deformation velocity map of these two high-speed railways. Fig. 5(a) shows Beijing-Tianjin intercity railway is across the edges of the subsiding center with serious subsidence located in Tongzhou District. Beijing-Shanghai high-speed railway is across the subsiding centers located in Beichen, Jinhai district of Tianjin and Langfang city as illustrated in Fig. 5(b-d). The subsidence rate of these subsiding centers is more than -100mm/a. The safe operation of the two high-speed railways is possibly affected by these subsiding centers.

As shown in Fig. 5(a), the subsiding velocity in Tongzhou District is from -94 to -45 mm/a. Part of Beijing-Tianjin intercity railway pass through the edge of this subsidence center and it is most possibly affected by the subsidence of this area. The subsidence velocity of other sections along the railway is not obvious, which is around 20mm/a. Then, more attention should be paid on these areas with large spatial difference of deformation velocity.

Beijing-Shanghai high-speed railway is affected by the serious subsidence located in Langfang city, Wuqing, Beichen and Jinghai Districts in Tianjin. The subsidence center of Langfang is only 3 km away from the railway. And the defamation velocity ranges from -86 to -37 mm/a. The subsidence velocity in Wuqing District of Tianjin is around -107 to -70 mm/a. The maximum subsidence velocity in Beichen District is -135mm/a and the closest subsiding center is only 2km away from the railway. In Jinghai District, the subsidence velocity is from -120 to -75mm/a, nearly by Hai Industrial Park. The possible reasons for serious subsidence is due to over-extraction of groundwater caused by large population density and the developed industrial parks except for geological conditions [14-19].

5. CONCLUSION

In this paper, we exploited the potential ability for monitoring subsidence along high-speed railway with the use of multi-temporal SAR data from ALOS-2. The results are presents in Fig. 3, 4 and 5. These results proved that ALOS PALSAR-2 data has high potential ability for monitoring subsidence along high-speed railway. The main subsiding centers along Beijing-Tianjin intercity and Beijing Shanghai high-speed railways are detected clearly and they are located in Tongzhou district, Langfang city and Wuqing district, Beichen and Jinghai district, respectively. ALOS-2 data has longest wavelength and then it could provide high coherence data even within nearly one year. That provides us a chance to monitoring the subsidence within one year with the use of DINSAR alone. Also, it provides high density coherent targets in rural area, which couldnot be achieved by other satellites.

The drawbacks of MT-INSAR analysis for monitoring of subsidence along high-speed railway should be that the detected PS targets cannot be easily connected with the actual targets one by one. Moreover, there is a common case that no PS points can be actually detected on the target of your interest.

6. REFERENCES

[1] H.R. Yu, H.L. Gong, B.B. Chen, K.S. Liu. “ Research progress and reflection on ground subsidence in Beijing-Tianjin-Hebei region”.Science of Surveying and Mapping. 2020, 45(4)

[2] Y. Yang, S.M.Jia, Y. Luo. “Analysis and outlook of the land subsidence in Beijing”. Urban Geology, 2012, 7(2): 9-13.

[3] A. Ferretti, C. Prati and F. Rocca, "Permanent scatterers in SAR interferometry". IEEE 1999 International Geoscience and Remote Sensing Symposium. IGARSS'99 (Cat. No.99CH36293), 1999, pp. 1528-1530 vol.3, doi: 10.1109/IGARSS.1999.772008.

[4] A. Ferretti, C. Prati, “Nonlinear subsidence rate estimation using permanent scatterers in differential SAR interferometry”. IEEE Transactions on Geoscience & Remote Sensing, 2000, 38(5):2202-2212.

[5] A. Ferretti, G. Savio, R. Barzaghi, A. Borghi, S. Musazzi, F. Novali, C. Prati, F. Rocca, “Submillimeter accuracy of InSAR time series: Experimental validation”. IEEE Trans. Geosci.Remote Sens. 2007, 45, 1142–1153.

[6] P. Berardino, G. Fornaro, R. Lanari, E. Sansosti, “A new algorithm for surface deformation monitoring based on small baseline differential SAR interferograms”. IEEE Trans. Geosci. Remote Sens. 2002, 40, 2375–2383.

[7] A. Hooper, P. Segall, H. Zebker. “A New Method for Measuring Volcanic Deformation Using InSAR Persistent Scatterers”. AGU Fall Meeting Abstracts, 2004.

[8] A. Ferretti, A. Fumagalli, F. Novali, C. Prati, F. Rocca, A. Rucci, “A new algorithm forprocessing interferometric data-stacks: SqueeSAR”. IEEE Trans. Geosci.RemoteSens.2011,doi:10.1109/TGRS.2011.2124465.

[9] A. Hooper, “A multi-temporal InSAR method incorporating both persistent scatterer and small baseline approaches”. Geophys. Res. Lett. 2008, 35, doi:10.1029/2008GL034654.

[10] T. Li, G. Liu, H. Lin, H. Jia, R. Zhang, B. Yu, Q. Luo, “A hierarchical multi-temporal InSAR method for increasing the spatial density of deformation measurements”. Remote Sens. 2014, 6, 3349–3368.

[11] D. Perissin, W. Teng, “Repeat-pass SAR interferometry with partially coherent targets”. IEEE Trans. Geosci. Remote Sens. 2012, 50, 271–280

[12] J. Inglada, G. Mercier, “A new statistical similarity measure for change detection in multitemporal SAR images and its extension to multiscale change analysis. IEEE Trans”. Geosci. Remote Sens. 2007, 45, 1432–1445

[13] D. Perissin, 2009, “SARPROZ software manual” http://ihome.cuhk.edu.hk/~b122066/manual/index.html .

[14] Y. Jiang, Y. Yang, H. G. Wang and F. Tian, “Factors controlling land subsidence on the Beijing plain, Shanghai Land and Resources”, 2014. 35 (4): 130-133.

[15] G. P. Li and Q. M. Xi. “The study strategies of the Beijing population orderly organization under Beijing Tianjin and Hebei province collaborative development”. Population and Development. 2015 (2):28-33.

[16] K.C.Lei, Y. Luo, B.B. Chen. “Distribution characteristics and influence factors of land subsidence in Beijing area”. Geology in China, 2016, 43(6):2216-2225.

[17] C. Zhu, Y. Zhang, G.F. He, “In-situ tests of land subsidence caused by pumping in the Tianjin Binhai New

Area". Hydrogeology and Engineering Geology, 2018, 45(2):159-164.
[18] Y. Pan, J.G.Pan, H.L. Gong, "Research on the relationship between groundwater exploitation and subsidence in Tianjin Proper". Earth and Environment, 2004, 32 (2):36-39.
[19] Y. Yang, F.D. zheng, L.C. Liu, "Study on the correlation between groundwater level and ground subsidence in Beijing Plain area". Geotechnical Investigation and Surveying, 2013 (8): 44-48.
[20] J. Xiong. "Study on Influence of Groundwater Exploitation in the Tianjin Area on the Beijing-Shanghai High-speed Railway Roadbed Settlement". Chengdu: Southwest Jiaotong University, 2013.
[17] ZHU Can, ZHANG Yun, HE Guofeng, et al. In-situ tests of land subsidence caused by pumping in the Tianjin Binhai New Area[J]. Hydrogeology and Engineering Geology, 2018, 45(2):159-164.
[18] PAN Yun, PAN Jiangang, Gong Huili, et al. Research on the relationship between groundwater exploitation and subsidence in Tianjin Proper [J]. Earth and Environment, 2004, 32 (2):36-39.
[19] Yang Yong, ZHENG Fandong, LIU Licai, et al. Study on the correlation between groundwater level and ground subsidence in Beijing Plain area [J]. Geotechnical Investigation and Surveying, 2013 (8): 44-48
[20] XIONG Juan. Study on Influence of Groundwater Exploitation in the Tianjin Area on the Beijing-Shanghai High-speed Railway Roadbed Settlement. Chengdu: Southwest Jiaotong University, 2013:66

NEW APPLICATIONS OF ALOS-2/4 L-BAND SAR AND INSAR DATA OVER PERMAFROST REGIONS

PI No.: ER2A2N128

Franz Meyer, Simon Zwieback, Go Iwahana, Helene Genet [1]

[1] University of Alaska Fairbanks, Fairbanks, Alaska, USA

1. INTRODUCTION

Most ice-rich permafrost landscapes have undergone or will undergo substantial surface deformation in the coming century. Such thaw-induced deformation, or thermokarst, poses a hazard to communities, infrastructure, and national security in the rapidly warming Arctic. It also drives shifts in the geomorphic, hydrological, and biogeochemical functioning of permafrost landscapes, impacting slope stability, water resources and the global climate.

Accurate observations of surface deformation and state variables such as soil moisture are critical for improving our understanding of the Arctic. Within this project, we have developed new and refined existing applications of L-band SAR and InSAR.

This report summarizes our principal achievements and findings.

2. SURFACE DEFORMATION IN PERMAFROST-AFFECTED FLUVIAL LANDSCAPES

In regions of continuous permafrost, rivers and their floodplains are in a complex balance. Surface water can increase ground temperatures substantially. River water also promotes permafrost degradation adjacent to the channel. Floodplains are also prone to permafrost degradation due to enhanced energy transfer into the soils during and after a flood, the latter associated with disruption to the organic layer, sediment deposition and increased wetness. Equally, however, river floods are essential to floodplain aggradation following channel migration. The deposition of fine-grained sediment promotes increased vegetation cover, soil saturation and organic matter content. As the active layer thickness decreases, segregated and wedge ice accumulate over centuries to millennia. The concomitant increase in elevation in turn reduces flood frequency and contributes to ecological succession. Not only does flood-promoted aggradation of permafrost ground ice shape the hydrological and ecological functioning of these fluvial landscapes, but it also makes them sensitive to disturbance.

A major challenge for predicting permafrost terrain changes is their inherent variability. The variability is not restricted to differences between regions or flood events, as a single flood may induce contrasting patterns in elevation changes, post-flood subsidence and changes in vegetation and wetness.

This is due to variability in the drivers and controls of permafrost terrain changes. Drivers such as water temperature, shear stress, river ice abrasion and sediment deposition vary within the flood perimeter. Among the controls, we emphasize ground ice properties, vegetation cover and organic layer thickness, as they exert a fundamental and yet complex influence on the sensitivity of different geomorphic units to permafrost degradation. For instance, how does post-flood subsidence vary with floodplain age? Younger stabilized floodplains host less perennial ground ice, but the ground ice is also less protected. These complex interactions highlight the importance of monitoring permafrost terrain changes on the landscape scale, and they indicate that even a single event can further process understanding.

We studied permafrost terrain changes after the 2015 spring flood of the Sagavanirktok River near Deadhorse, on the Alaskan North Slope. Following extensive aufeis development, the river flooded various geomorphic units and 40-year-old infrastructure that had not been flooded before. The flood damaged infrastructure, most notably the Dalton highway, and breaches of impounded water led to localized ice-wedge washout due to thermal erosion. Conversely, the landscape-scale terrain changes remain unknown.

The subsidence estimated from ALOS-2 stripmap observations from 2015 (midsummer) to 2019 (end of summer) varied by more than 10 cm across the region (Fig. 1a). Half of the observations ranged from 0 to 3 cm (interquartile range). Such low values were found over most of the study region, irrespective of 2015 flood extent. Context is provided by the CALM active layer thickness observations, which varied by as little as 5 cm over this period. The lowest value was observed in 2018, when the thawing degree days (TDD) were 20-30% smaller than in the other years of the 2015-2019 period.

The largest multiannual subsidence of around 15 cm was observed at the throat of an inactive channel in the north of the study region that was flooded in 2015. Isolated hotspots with large subsidence of approximately 10 cm were observed in the inundated area west of the highway and on the abandoned floodplain in the south. Elevated subsidence estimated generally corresponded to large standard errors of 2-5 cm (Fig. 1b).

After summer 2016, the satellite observations shown in Fig. 1c indicate low levels of long-term subsidence. Between the end of summer 2016 and 2019, respectively, the estimates are less than 5 cm throughout.

We observed highly variable subsidence, both across and within geological units. Across units, age (a proxy for ice content) showed the expected positive association with subsidence (Fig. 2a). The between-unit differences were largely due to the tails of the subsidence distributions, with the largest subsidence in ice-rich inactive and abandoned floodplains. These results reinforce the notion that excess ground ice is a necessary but not a sufficient condition for thaw settlement.

Inundation during the 2015 spring flood was associated with elevated subsidence in the ice-rich units (Fig. 2). The association is not necessarily causal. Within a given unit, the inundated areas differed systematically in their age, their disturbance history, their drainage conditions, and thus likely in the profiles of organic matter and ground ice.

These confounding factors could have predisposed them to increased subsidence in a warm period such as 2015-2019, even in absence of a large flood. One potential causal factor is rapid thaw penetration during the flood. As stated above, soil temperature observations and thermal calculations suggest it was only a minor factor where the immediate geomorphic disturbance was limited.

Our work shows the importance of remote sensing for monitoring the disparate and highly variable terrain changes in permafrost-affected fluvial lanscapes. These landscapes are on the cusp of change, raising important questions about permafrost stability, water resources and habitat in the coming decades.

We expect the manuscript [1] to be published before the end of 2022.

3. HILLSLOPE TRANSPORT

Sediment flux and slope instability may be controlled by force balances within sloping saturated soils, which are widely thought to be predictable from topographic metrics (e.g., slope, drainage area). In addition to cohesion imparted by soil and vegetation, thawing ground ice as active layers deepen may also control spatial trends in slope stability. The distribution of ground ice, however, is poorly constrained and hard to predict. To address whether slope stability and surface displacements follow topographic predictions, we document drivers of permafrost sediment flux present on a landscape in western Alaska that range from creep, solifluction lobes, gullying, and catastrophic hillslope failures ranging in size from a few meters to tens of meters.

We quantify the timing and rate of surface movements using a multi-pronged, multi-scalar dataset including UAV surveys, DGPS, InSAR, and climate data. Despite clear visual evidence of downslope soil transport of solifluction lobes, the interannual movement of these features does not outpace displacement of soil in topographically smooth areas (horizontal displacement means: 7 cm/yr for lobes over two years vs 10 cm/yr in other landscape positions over one year).

Annual displacements are weakly related to slope and unrelated to drainage area or solar radiation. Timeseries of InSAR displacements show accelerated movement in late summer associated with intense rainfall. While mapped slope failures do cluster at slope-area thresholds, a simple slope stability model driven with hydraulic conductivities representative of throughflow in mineral and organic soil drastically over-predicts the occurrence of slope failures.

This mismatch implies permafrost hillslopes have unaccounted-for cohesion and/or throughflow pathways, perhaps modulated by vegetation, which stabilize slopes against high rainfall. Our results highlight the complexity of soil transport processes in arctic landscapes and underline the utility of using a range of synergistic data collection methods to observe multiple scales of landscape change.

We have presented preliminary results on this work at the AGU Fall Meeting [2]. We are currently working on two separate manuscripts.

4. IMPROVING DISPLACEMENT ESTIMATION

L-band SAR can be strongly affected by ionospheric Faraday rotation. In contrast to radiometric observables, the errors in repeat-pass InSAR observations and hence in deformation analysis are largely unknown.

We conducted a theoretical and data-driven study of ionospheric Faraday rotation. Even though we were not able to include ALOS-2 data in the final manuscript due to space constraints, we report here on the principal findings, summarized from the abstract of our published paper [3].

We find that the deformation error may reach 2 mm in the co-pol channels over a solar cycle. It can exceed 5 mm for intense solar maxima. The cross-pol channel is more susceptible to severe errors. We identify the leakage of polarimetric phase contributions into the interferometric phase as a dominant error source.

The polarimetric scattering characteristics induce a systematic dependence of the Faraday-induced deformation errors on land cover and topography. Also their temporal characteristics, with pronounced seasonal and quasi-decadal variability, predispose these systematic errors to be misinterpreted as deformation. While the relatively small magnitude of 1-2 mm is of limited concern in many applications, the persistence on semi- to multi-annual time scales compels attention when long-term deformation is to be estimated with millimetric accuracy. Phase errors induced by uncompensated Faraday rotation constitute a non-negligible source of bias in interferometric deformation measurements.

5. LAND SURFACE VARIABLES AND PROCESSES

We have pioneered the use of L-band SAR for estimating shrub biomass and shrub rainfall interception in the Arctic. The importance of these advances lies in the expansion of shrubs across tundra regions, which induces complex and poorly understood changes to the carbon, energy, water, and nutrient cycles.

Our analyses demonstrate the unexploited potential of L-band SAR observations from satellites for quantifying the impact of shrub expansion on Arctic ecosystem processes. Our most important findings are as follows.

Polarimetric L-band SAR showed strong sensitivity to shrub biomass and leaf area index across a gradient in shrub density and stature. SAR captured the high spatial variability of shrub characteristics on the catchment scale.

Rainfall interception can be modelled by integrating SAR with meteorological data. We validated our predictions using in-situ measurements.

With continued shrub expansion, L-band SAR is projected to become a critical tool for improved understanding of Arctic ecosystems. It provides critical constraints on the water, the carbon and energy balances. Future missions such as ALOS/4 NISAR as well as the combination with optical remote sensing offer the potential to greatly enhance shrub mapping and monitoring in the tundra.

This work has been published in Remote Sensing of Environment [4].

6. REFERENCES

[1] S. Zwieback, M.McClernan, M. Kanevskiy, H. Bergstedt, Q. Chang, T. Jorgenson, V. Romanvosky,
S. Walker, H. Toniolo, and F. Meyer, "Disparate permafrost terrain changes after a large flood observed from space," International Journal of Applied Earth Observation and Remote Sensing, in review.

[2] Rowland, J.C., Del Vecchio, J., Glade, R., Fratkin, M., Lathrop, E. and Zwieback, S., 2020, December. Patterns and rates of soil movement and shallow failures across several small watersheds on the Seward Peninsula, Alaska. In AGU Fall Meeting Abstracts (Vol. 2020, pp. C012-0011).

[3] Zwieback, S., & Meyer, F. J. (2021). Radar interferometric phase errors induced by Faraday rotation. IEEE Transactions on Geoscience and Remote Sensing.

[4] Chang, Q., Zwieback, S., DeVries, B., & Berg, A. (2022). Application of L-band SAR for mapping tundra shrub biomass, leaf area index, and rainfall interception. Remote Sensing of Environment, 268, 112747.

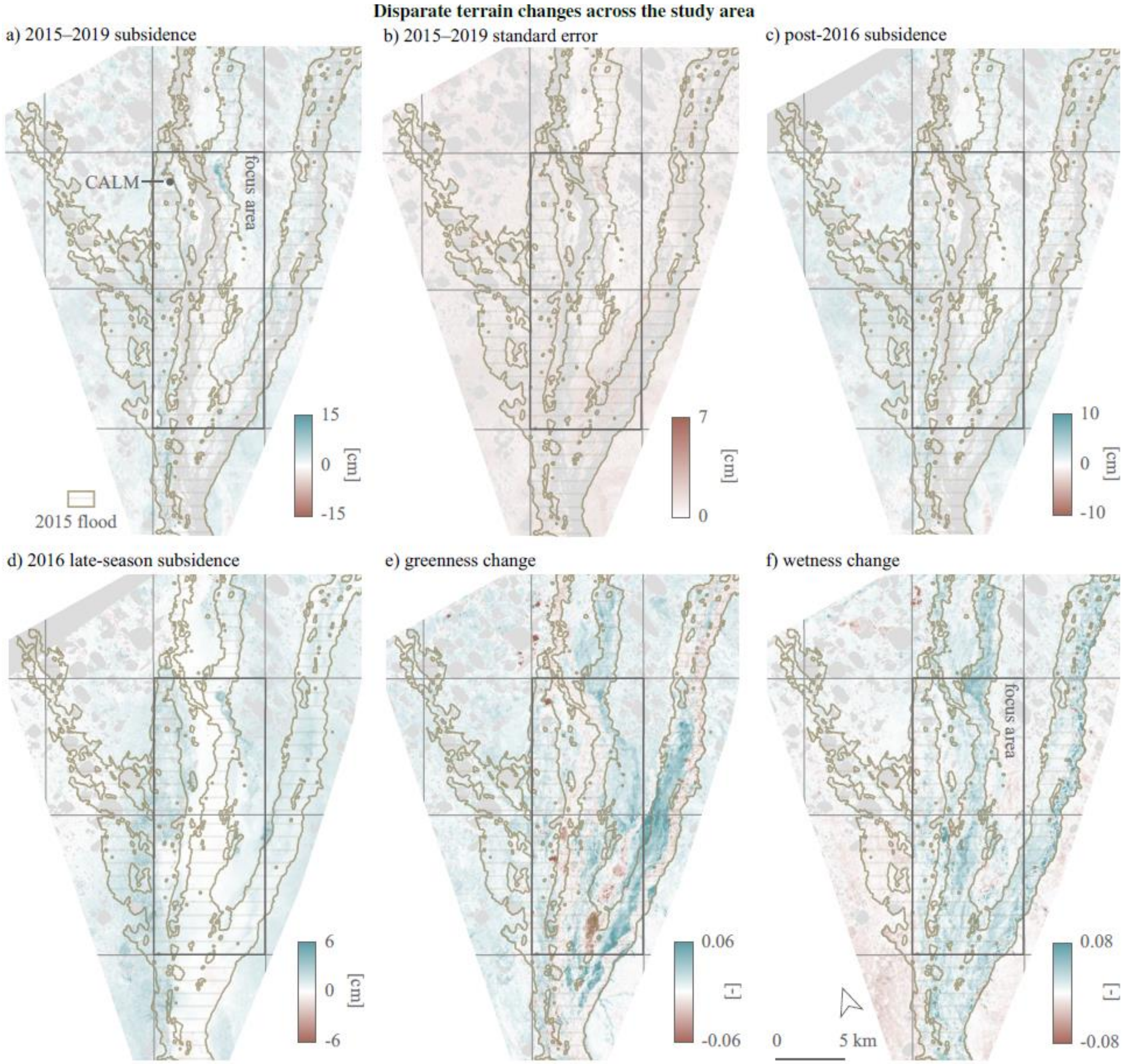

Figure 1. a-c) Estimates of post-flood subsidence and its standard error derived from ALOS-2 InSAR; d) late-season subsidence in 2016 from Sentinel 1; e--f) pre-flood to post-flood changes in greenness and wetness from Landsat-8, with positive signs corresponding to an increase. The 2015 flood extent is shown in yellow.

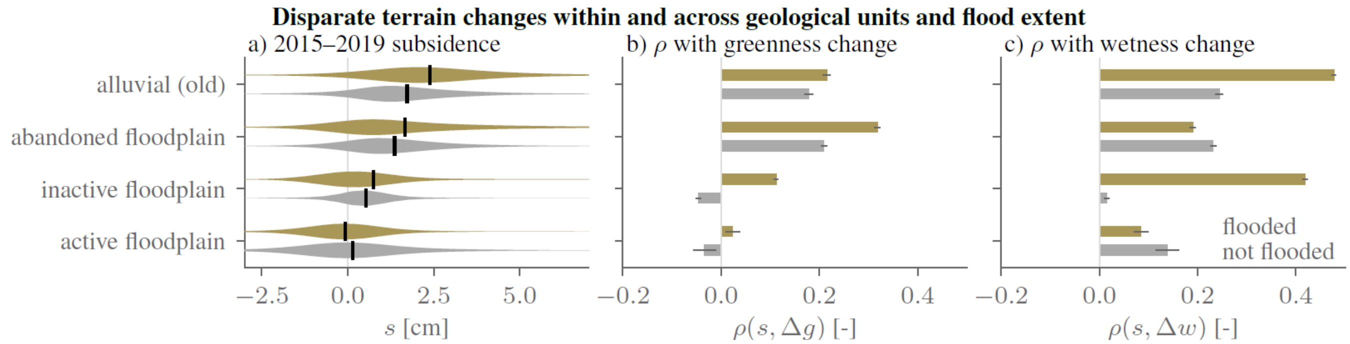

Figure 2. a) Kernel-density-based distribution of estimated 2015--2019 subsidence for the four dominant geological units in the focus region, stratified according to whether they were or were not inundated during the 2015 flood. The vertical line shows the mean.

複数衛星データの統合解析による広域環境変動と自然災害発生状況の関係分析

PI No.:ER2A2N153

中山裕則[1], *村瀬雅之*[1]

[1] 日本大学文理学部

1. はじめに

本研究では、これまでの RA(RA1)などで行ってきた日本と東アジアから中央アジアにかけての環境変動分析、自然災害発生とその被害状況の調査分析、災害発生要因の検討を、新たに複数の衛星データを適用して継続的に実施することを目指した。特に、これまで十分に解析ができなかった ALOS-2/PALSAR2 のデータも用いた地盤変動分析、地表被覆分析、環境変動分析などを行うことを目的とした。
対象地域は、洪水などの自然災害発生リスクの高い日本および東アジアと、環境変動の著しい東アジアから中央アジアにかけての領域であり、それぞれ地盤変動や地表被覆分類などを対象とした。各研究の概要、内容、結果を順に示す。

2. 研究の概要

本研究で目指した技術的な主なテーマは、SAR データを用いた干渉 SAR 適用による洪水発生リスクの高い地域における地盤変動の検出とその高度化、および SAR データ適用による地表被覆分析の高度化である。
干渉 SAR に関する研究の対象地域は、日本の関東平野中央部地域とベトナムのホーチミン市周辺地域とし、地表被覆分析については、乾燥化の懸念が高い中央アジアのバルハシ湖の南に位置するイリデルタ地域とした。これらの地域は、これまで複数の基礎的な研究を実施し、多くの既存情報を有している。
具体的に推進した研究テーマは以下の通りである。

1）関東平野中央部地域の長期的干渉 SAR 解析を適用した詳細地盤沈下検出の可能性
2）PSInSAR による関東平野中央部地域の地盤沈下検出とその要因検討
3）複数 SAR データを用いた PSInSAR による細密地盤変動検出の可能性とその適用
4）DInSAR 解析によるベトナム･ホーチミン市の地盤沈下モニタリング
5）SAR データを含む複数衛星データと DSM データによる中央アジアのバルハシ湖イリデルタの微地形分類

以下に研究の内容と結果について述べる。

3. 研究内容と結果

3.1 関東平野中央部地域の長期的干渉 SAR 解析を適用したに詳細地盤沈下検出の可能性[1]

(1)概要
関東平野中央部地域(特に埼玉県東部から東京都東部)では、1960 年代以降これまで高度成長期を中心に日本でも最大規模の地盤沈下が発生してきて、大規模洪水に伴う被害発生が懸念されている。現在、地盤沈下は緩やかになっているが、継続して進行は続いているとされる。しかし、その長期的な地盤沈下の推移や、最近の継続的な微小化した地盤沈下は十分に調べられていない。そのため、本研究では、まず、地上での水準測量成果を用いて過去約 60 年間の本地域の長期地盤沈下の傾向を把握し、次に、水準測量では明瞭には把握できない最近の沈下状況を干渉 SAR 解析で検出可能かどうかについて検討を行った。

(2)方法
以下の方法により解析、調査を行った。

a）対象地域である関東平野中央部地域の各自治体（東京都、埼玉県、千葉県、茨城県など）で作成、保管されている水準測量により作成された地盤変動図(主に紙媒体)を収集
b）収集された地盤変動図をデジタルデータに変換、編集し、長期的な地盤変動分布画像データを作成
c）作成された地盤変動分布データより、対象地域の地盤沈下域の面積及び体積(沈下量)を算出
d）地盤沈下の発生面積と沈下量の経年的な解析より、水準測量等による地盤沈下の推移を分析
e）地盤沈下量が微小化し、水準測量で十分な検出が難しくなった 1990 年代後半以降における干渉 SAR 解析の検討
f）2016 年から 2017 年を対象に欧州宇宙機関の Sentinel-1A/C-SAR データを収集
g）Sentinel-1A/C-SAR データを使用した干渉 SAR スタッキング処理による 2016 年から 2017 年の地盤変動量の検出の可能性を検討

(3)結果
本研究で得られた結果は以下の通りである。
①水準測量データによる 1960 年代から 2018 年までの約 60 年間における累積地盤変動分布(Fig.3.1-1)

より、この間の累積沈下量が 10cm 以上の地域は約 4000km^2 で、その体積は約 1.33km^3 と求められた。
②干渉 SAR スタッキング処理結果の LOS 変位量を鉛直方向の変動量に変換した結果(Fig.3.1-2)が示され、これと既存の水準測量成果との比較(Fig.3.1-3) を行い、両者の間には妥当な関係を示すことができた。
③衛星 SAR(C-SAR)データの干渉 SAR スタキング処理により、地上水準測量手法と比べてより詳細な微小地盤変動を検出する可能性が示唆された。
④さらに微小な変動量をより高精度に検出する干渉 SAR 解析手法の検討が考えらえた。

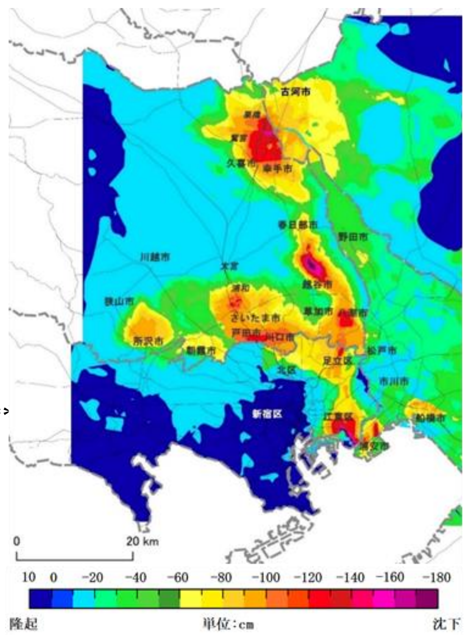

Fig.3.1-1 水準測量データに基づく過去約 60 年間の累積地盤変動分布

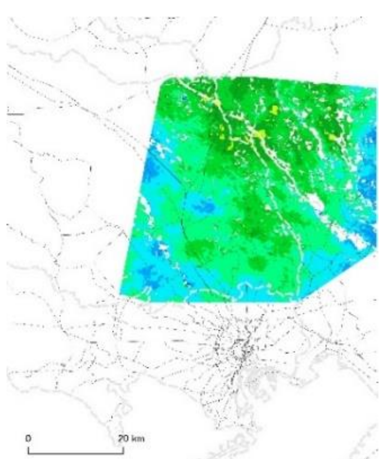

Fig.3.1-2 干渉 SAR スタッキング処理による鉛直方向の変動量に変換された地盤沈下分布

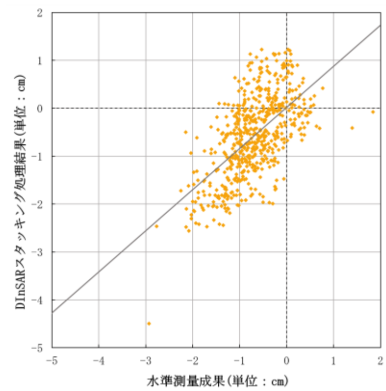

Fig.3.1-3 水準測量結果と干渉 SAR スタッキング処理結果による地盤変動量の比較結果

3.2 PSInSAR による関東平野中央部地域の地盤変動検出とその要因検討[2]

(1)概要

関東平野中央部地域では、水準測量により地盤沈下が続いていることが確認されており、その傾向は 1990 年代以降、微小に転じたこと、および水準測量や GNSS などの既存測量では点としての変動で、面的かつ詳細な地盤変動分布把握が難しい。さらに、衛星 SAR データによる干渉 SAR スタッキング処理では、さらに、より高精度な地盤変動検出のための解析手法適用の必要性が示された。このため、次のステップの研究として、解析期間内で恒久散乱体(PS)点を抽出し、その点の変動を時系列で追跡する PSInSAR 手法を新たに適用し、地盤変動(沈下)の検出を行った。また、検出された地盤変動量への影響要因にも言及した。

(2)方法

以下の方法により解析、調査を行った。

a) 引続き観測頻度が高く、データ入手が容易な 2016 年 12 月から 2019 年 1 月までの Sentinel-1A/C-SAR データを収集
b) 無償公開のソフトウェアの StaMPS を用いて PSInSAR 解析を実施し地盤変動の検出
c) 国土地理院の GNSS 成果(対象地域内の 3 地点)のデータと、PSInSAR による変動値の比較分析. 比較では、PSInSAR 処理による LOS 変位量を鉛直方向の変動量に変換.
d) 対象地域内のうち北部(栃木県野木原)付近における地盤変動と地下水位変動の関係を分析

(3)結果

本研究で得られた結果は以下の通りである。

①2017 年から 2018 年の約 2 年間で、Sentinel-1A/C-SAR データを用いた PSInSAR 解析により、対

象領域内のほぼ全域で 5mm/年以上の地盤沈下分布(水色～青色)が検出された(Fig.3.2-1)。

②国土地理院の GEONET (GNSS 連続観測システム)による年間変動量と、PSInSAR 処理結果の年間変動量の比較で、両者の絶対誤差は最小値 0.12mm/年、最大値 6.37mm/年が得られた(Fig.3.2-2)。

③PSInSAR の変動量と水準測量の変動量を点ベースで比較した結果、両者のほぼ妥当な関係が認められ、PSInSAR 解析による地盤変動抽出の有効性が示せた(Fig.3.2-3)

④対象領域内北部の野木原の地下水位観測所の月平均地下水位と PSInSAR による地盤変動の間に関係が認められ、地下水位の季節変動による地盤変動が確かめられた。

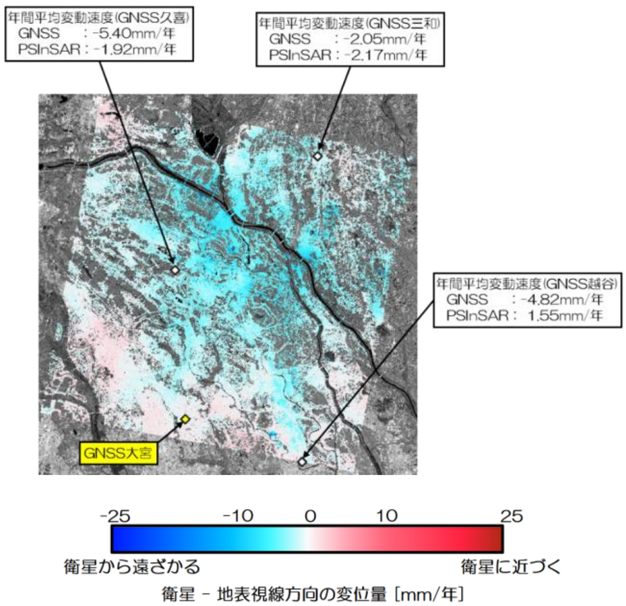

Fig.3.2-1 PSInSAR による 2017 年から 2018 年までの 2 年間における年間変動量分布

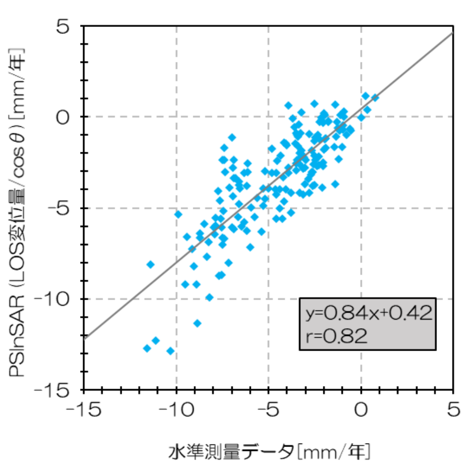

Fig.3.2-2 水準測量による地盤変動と PSInSAR による地盤変動の比較

3.3 複数 SAR データを用いた PSInSAR による細密地盤変動検出の可能性とその適用[3]

(1)概要

地盤沈下の進行により洪水発生とそれに伴う被害域拡大の懸念が高まっている地域は国内外にかかわらず多く認められている。首都圏に属する関東平野中央部地域もその代表であり、1990 年代以降、微小スケールになった地盤沈下の推移を面的かつ詳細に把握することは、防災などの観点から非常に重要である。

本研究では、PSInSAR の適用が、地盤沈下を詳細かつ面的に検出する可能性を示してきた。しかし、地盤沈下は数十年間継続しているため、長期的なモニタリングが必要である。一方で、SAR 搭載の各衛星の打上げ・運用は平均すれば数年間程度である。このため、地盤沈下の長期にわたる継続的なモニタリングのためには、複数の観測緒元の異なる衛星 SAR データの適用による解析が必要である。

ここでは、観測期間の異なる複数の SAR データごとに PSInSAR 解析を実施し、それらの解析結果を用いて、比較的長期間の地盤沈下把握の可能性について検討を目指した。また、異なる波長の SAR データによる PSInSAR 解析結果の特徴についても比較も行った。

(2)方法

以下の方法により解析、調査を行った。

a) 1997 年から 2005 年と、2016 年から 2020 年の期間の地盤変動を抽出するために、それぞれ ERS-2/SAR データおよび Sentinel-1A/SAR データを入手し、PSInSAR 解析を実施.

b) PSInSAR 解析データでは、国土地理院の GEONET (GNSS 連続観測システム) の季節変動が少ない観測点を参照点として適用し、干渉点以外の地域は B-スプライン補間法を適用して変動分布を内挿.

c) 2 期間の変動検出結果に基づき対象領域の地盤沈下傾向を分析.

d) 2016 年から 2020 年の期間における Sentinel-1A/SAR(C バンド)データと ALOS-2/PALSAR2(L バンド)データによる PSInSAR 解析に基づく地盤変動量を比較して、波長帯の異なる場合の地盤変動検出の特徴について分析.

(3)結果

本研究で得られた結果は以下の通りである。

①関東平野中央部地域において、ERS-2/SAR データの PSInSAR 解析による 1997 年から 2005 年までの年間変動量分布内挿画像(Fig.3.3-1)と、Sentinel-1A/C-SAR データの PSInSAR 解析による 2016 年から 2020 年までの年間変動量分布内挿画像(Fig.3.3-2)の比較によれば、1997 年から 2005

年の期間では、年間約 3～10 mm(部分的に最大年間約 13 mm)、2016 年から 2020 年では、年間約 2～7 mm(部分的に最大年間約 13 mm)の地盤沈下が検出されて、緩やかながら継続した地盤沈下を捉えることができた。

②国土地理院の標高(数値標高モデル)データ(Fig.3.3-3)を参照した、Fig.3.3-1 画像上の赤色線(X-X’、Y-Y’)上の年間変動量の比較(Fig.3.3-4)によれば、関東平野中央部地域内においては、低地や台地などの地形区分に関係なく明瞭な地盤沈下分布が確認できた。しかし、この要因分析には、ボーリングデータや地下水揚水量などのデータを参照した多角的な視点による分析が必要と考えられた。

③GEONET 点における PSInSAR と GNSS による(年間)変動量の比較によれば、両者の絶対誤差は最小値 0.10mm/年、最大値 2.54mm/年であり、ほぼ成果が妥当な結果であると考えられた。

④異なる波長、すなわち C バンド SAR と L バンド SAR データによる PSInSAR 解析結果(Fig.3.3-5 および Fig.3.3-6)の比較(Fig.3.3-7)では、両者間の関係は相関係数 r=0.65、回帰直線の傾きは 1.07 であった。また、長波長の L バンド SAR データでは C バンド SAR データよりも PS 点が約 3 倍多く検出された。このことから、例えば、東南アジアなどの植生の多い地域の地盤変動へ PSInSAR 解析を適用する場合、ALOS-2/PALSAR-2 データなどの長波長の SAR データの有効性が期待された。

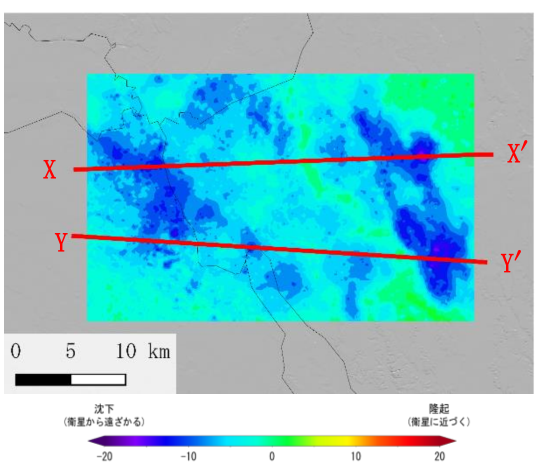

Fig.3.3-1 ERS-2/SAR データの PSInSAR 解析による地盤変動分布内挿画像[1997-2005]

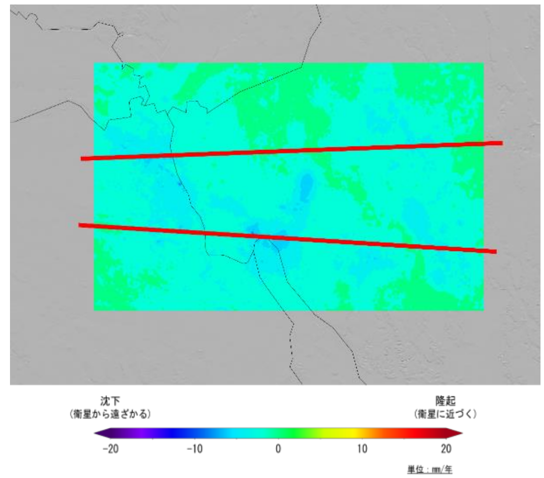

Fig.3.3-2 Sentinel-1A/C-SAR データの PSInSAR 解析による地盤変動分布内挿画像[2016-2020]

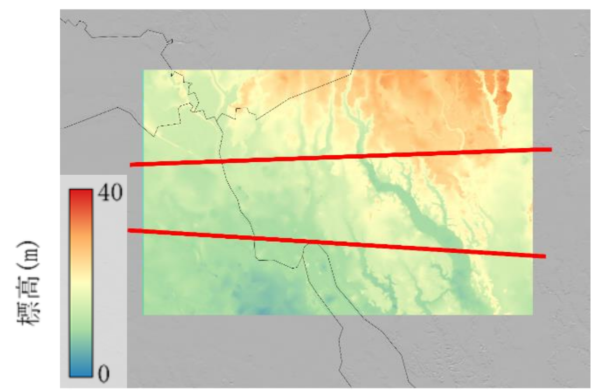

Fig.3.3-3 数値標高モデルによる標高分布

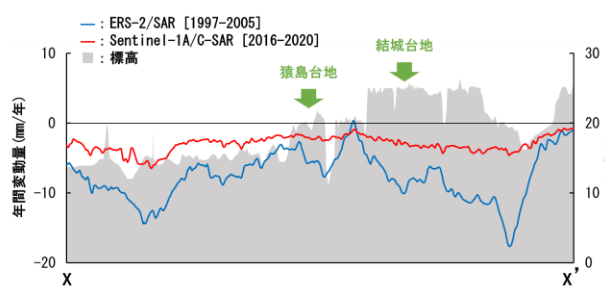

(a) X-X’ 区間

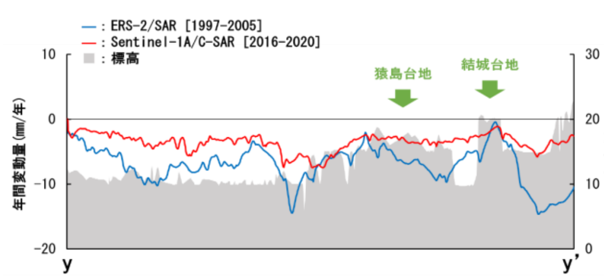

(b) Y-Y’ 区間

Fig.3.3-4 PSInSAR 解析による地盤変動分布内挿画像上の X-X’ と Y-Y’ における年間地盤変動量の分布

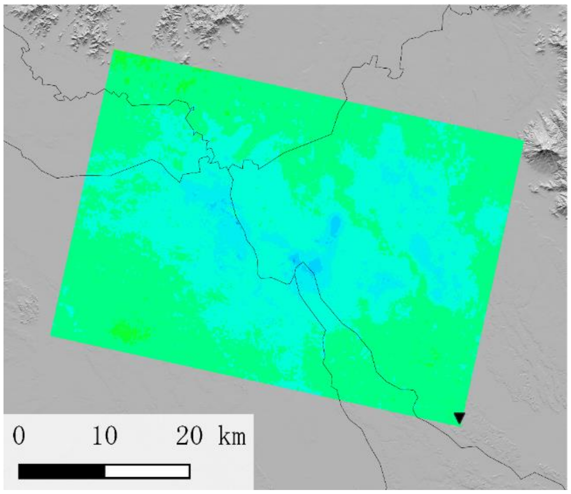

Fig.3.3-5 Sentinel-1A/SAR(C バンド)データの PSInSAR 解析による地盤変動分布内挿画像[2016-2020]

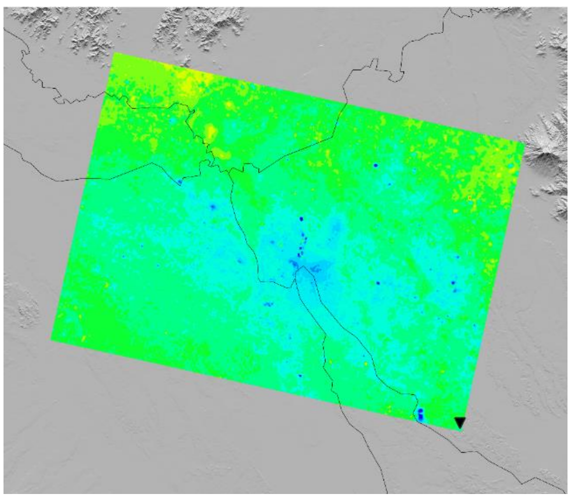

Fig.3.3-6 ALOS-2/PALSAR2(L バンド)データの PSInSAR 解析による地盤変動分布内挿画像[2016-2020]

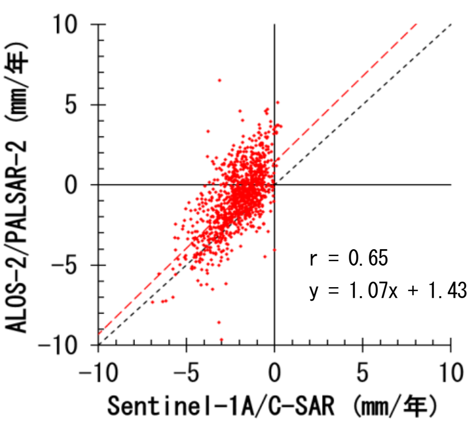

Fig.3.3-7 S Sentinel-1A/SAR(C バンド)と ALOS-2/PALSAR2(L バンド)の PSInSAR 解析による地盤変動の比較

3.4 DInSAR 解析によるベトナム・ホーチミン市の地盤沈下モニタリング

(1)概要

東南アジア諸国などの開発途上国においては、急速な経済成長に伴う地下水の過剰な汲み上げなどにより大都市とその周辺域において地盤沈下が進行し、その影響として社会インフラや住居などへの直接的な影響、水害による災害発生拡大のリスクが高くなっている。そのため、災害リスク管理の観点から、現在までのやや長期の地盤沈下を把握するとともに、今後も継続的に地盤変動モニタリングを行うことが必要とされている。

ここでは、地盤沈下が生じているとされるベトナムのホーチミン市とその周辺地域を対象とし、複数の衛星搭載 SAR データを用い、それぞれの DInSAR 解析結果により、過去数十年間のやや長期的な地盤変動の検出を行い、地盤沈下の傾向やその発生要因についての分析を試みた。

(2)方法

解析対象領域は Fig.3.4-1 の LANDSAT 画像内に赤枠で示したホーチミン市街地とその近郊地域を含む 27×36 kmの範囲である。モニタリング期間がやや長いため、使用したのは、約 12 年間に観測された JERS-1/SAR 、 ALOS/PALSAR 、 ALOS-2/PALSAR-2 および Sentinel-1A の 4 種類の衛星 SAR データである。それぞれ DInSAR 解析により、過去約 12 年間の地盤変動の分析を行い、地盤沈下の経年変化解析や平均沈下速度の算出、地盤沈下の傾向やその発生要因についての検討を試みた。

解析・調査の項目は以下のとおりである。

a) 12 年間における複数種類の SAR データと LANDSAT データの入手.
b) 各 SAR データによる時系列 DInSAR 解析.
c) 地盤変動域、地盤変動量、地盤変動速度などの分析.
d) LANDSAT データなどによる時系列土地被覆解析.
e) 地盤変動の要因と変動傾向の分析.

(3)結果

DInSAR 解析による過去約 12 年間の累積地盤変動(地盤沈下)分布画像(Fig.3.4-2)によると、ホーチミン市の市街域を取巻くように地盤沈下域が分布していることが明瞭に示された。そのうち最大の沈下量は 33 cmであった。一方で、Fig.3.4-3(12 年間の地盤隆起分布)のように、この同期間で、ホーチミン市街地の南西域で、約 4 cmの地盤の隆起分布も検出された。これらの地域を LANDSAT 画像や DSM データにより検討すると、地盤沈下地域は標高が相対的に低く、低湿な地域であること、地盤隆起パターン

の分布地域はやや標高の高い地域であることが分かった。P1ーP2 間(Fig. 3. 4-2 画像内)における過去 12 年間の地盤沈下量の推移を表したグラフ(Fig. 3. 4-4)よれば、地盤沈下量は年とともに徐々に緩やかになりつつあるが、現在も継続していることが明瞭に示された。

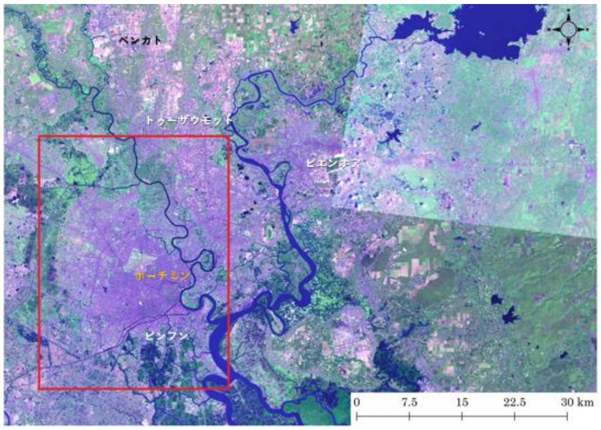

Fig.3.4-1 LANDSAT 画像に示した解析対象領域(赤枠内)

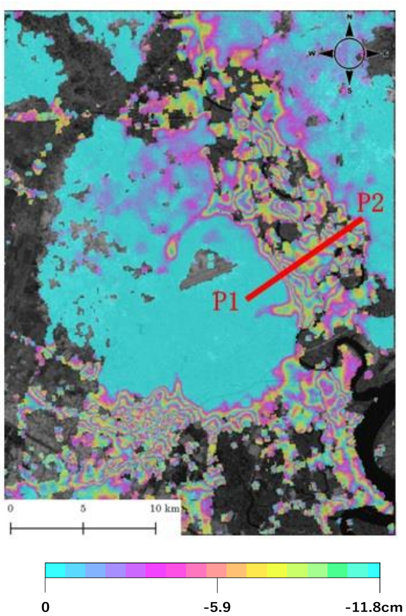

Fig.3.4-2 ALOS-2/PALSAR2 の DInSAR 解析による過去約 12 年間の地盤沈下分布

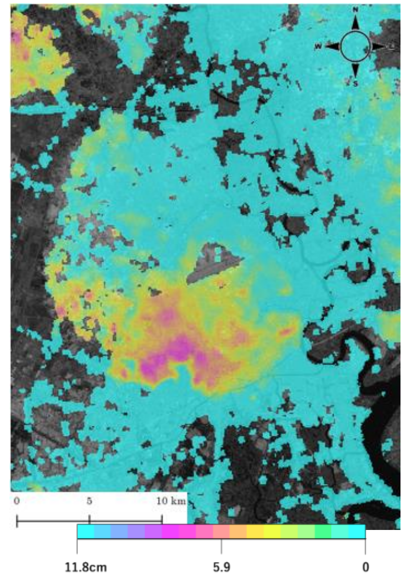

Fig. 3. 4-3 ALOS-2/PALSAR2 の DInSAR 解析による過去約 12 年間の地盤隆起分布

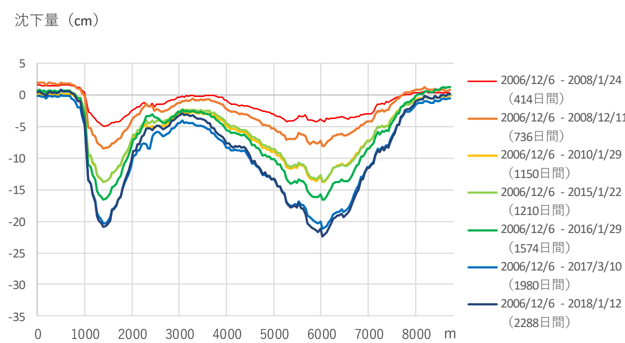

Fig. 3. 4-4 過去 12 年間の地盤変動(沈下)分布 (Fig. 3. 4-2 の P1-P2 間)

3. 5 複数衛星データと DSM データによる中央アジアのバルハシ湖イリデルタの微地形分類[4]

(1)概要

中央アジアの代表的な閉塞湖のバルハシ湖周辺地域は、過去 1〜2 万年頃に現在に比べ寒冷で湿潤であったことが示唆されている。このバルハシ湖に流入するイリ川河口の三角州には砂丘や段丘などの微地形が分布していて、湖岸沿いの微地形と共にその形成過程を調べることで、本地域の数千年から数万年スケールの気候変動とそれに伴う湖水位変動の把握が期待される。そのため、この微地形の既存成果に比べてより詳細な分類が複数の衛星データ、特に SAR データを統合して解析することができるかについて検討が必要であった。

ここでは、バルハシ湖に流入するイリ川河口付近のデルタ(三角州)を対象として、衛星光学センサデー

タや一般に公開された DSM データに加えて、SAR データを統合させた解析により、砂丘、段丘、旧河道などの地形情報抽出に基づく、より詳細な地形分布分類の可能性について検討を行った。

(2)方法

対象地域は、LANDSAT-8/OLI 集成画像 (Fig.3.5-1) のように、南からバルハシ湖の南西域へ流れ込むイリ川の中・下流部に広大なデルタ(三角州)が分布する。また、その周囲は砂丘地帯となっている。

一般公開され利用可能な DSM データとしては、いずれも 30m メッシュの ALOS 全球数値地表モデル(AW3D30)、ASTER 全球 3 次元地形モデル(GDEM)、Shuttle Radar Topography Mission (SRTM-1)があるが、対象地域内でこれらの各標高データ値の比較を行い、現地計測などによるバルハシ湖岸線沿いの標高値と最も差が少なく、異常値も少なくて、より微地形を表す AW3D30 を本解析に最適な DSM とした。この DSM データより、まず、砂丘などの微地形の地形斜面角、接峰面、接谷面などを算出し、そのデータ間の差分処理やフィルタリング処理などに基づき微地形分布の分類行った。次に、ALOS-2/PALSAR2 強度画像と NDVI ならびに NDWI データを参照しながら、より詳細な地形分類を行った。

解析・調査のステップは以下のとおりである。

a) LANDSAT-8/OLI データ、ALOS-2/PALSAR2 データ、既存 DSM データの収集入手.

b) DSM データの本解析のために最適なデータの評価・選定.

c) DSM データに対するフィルタリングおよび差分処理などによる砂丘分布特性の分類.

d) LANDSAT-8/OLI データによる正規化植生・水指標 (NDVI・NDWI) の算出に基づく現河床域の区分.

e) ALOS-2/PALSAR2 ScanSAR モードデータを統合したデルタ域の詳細地形分類とその結果の検討.

(3)結果

本研究で得られた結果は以下の通りである。

①分類処理に先立ち、現在、広く適用されている DSM データのうち、AW3D30、GDEM、SRTM-1 と現地計測データを参照して比較検討を行った結果、AW3D30(ALOS 全球数値地表モデル)が少なくとも微地形分類には最適であることを確認した。

②これまで行われてきた DSM(AW3D30)データに基づく砂丘、段丘などの微地形の地形斜面角の画像や地形の接峰面および接谷面ならびにそれらの差画像(Fig.3.5-2)に対し、新たに求めた NDVI ならびに NDWI データ(Fig.3.5-3)と、ALOS-2/PALSAR2 後方散乱強度データ(Fig.3.5-4)を統合させて分類を行った結果、これまでに比べより詳細な微地形分類データ(Fig.3.5-5)が求められた。

③新たな詳細微地形分布分類画像(Fig.3.5-6)により、イリデルタ内の砂丘の分布状況として、地形的に上位面から現河床(下位面)まで順に SD、TP、UB、LB、FP の 5 分類が可能であった。

④今後、各地形面の年代を調査することで、対象地域内の気候変化に伴う地形形成過程が明らかになると考えられた。

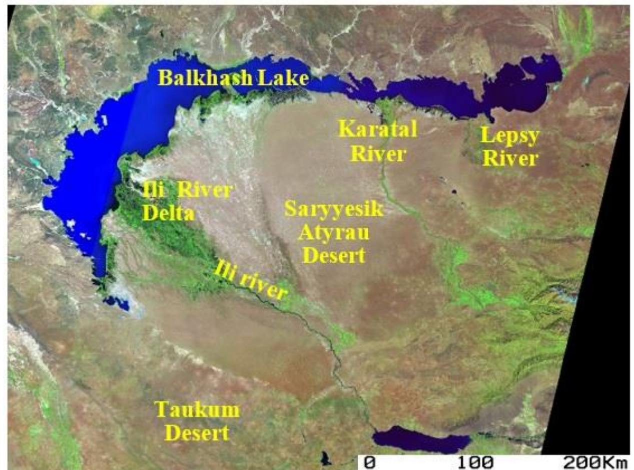

Fig.3.5-1 対象地域を表す LANDSAT-8/OLI モザイク画像

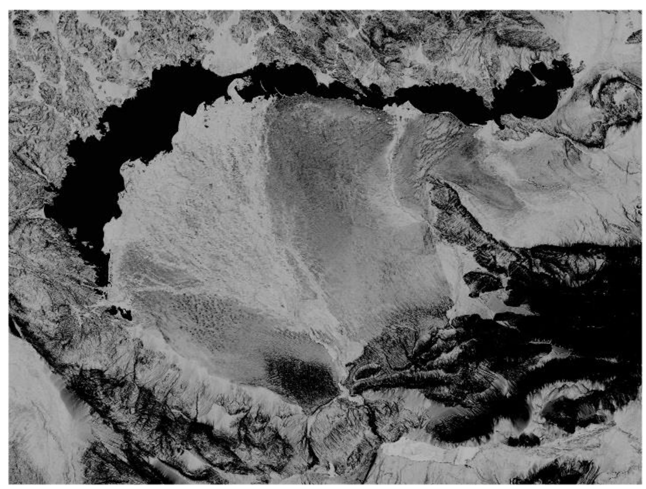

Fig.3.5-2 AW3D30 データに基づく接峰面と接谷面の差画像

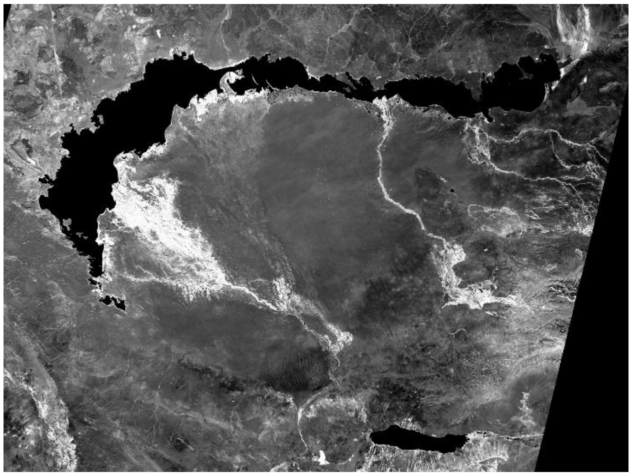

Fig.3.5-3 LANDSAT-8/OLI モザイク画像データより求められた NDWI 画像データ

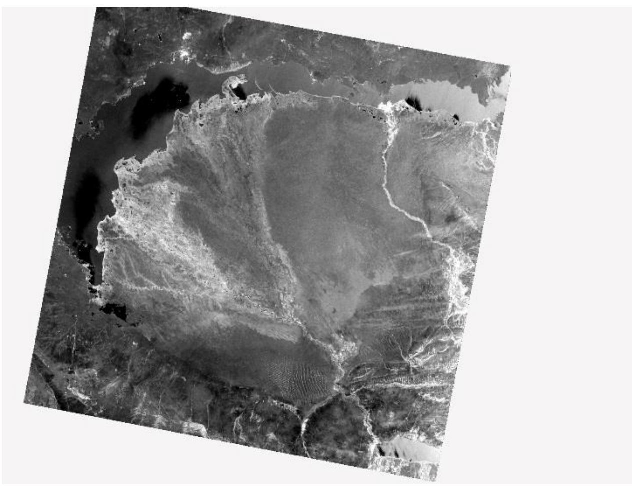

Fig.3.5-4 ALOS-2/PALSAR2 ScanSAR 後方散乱強度画像データ

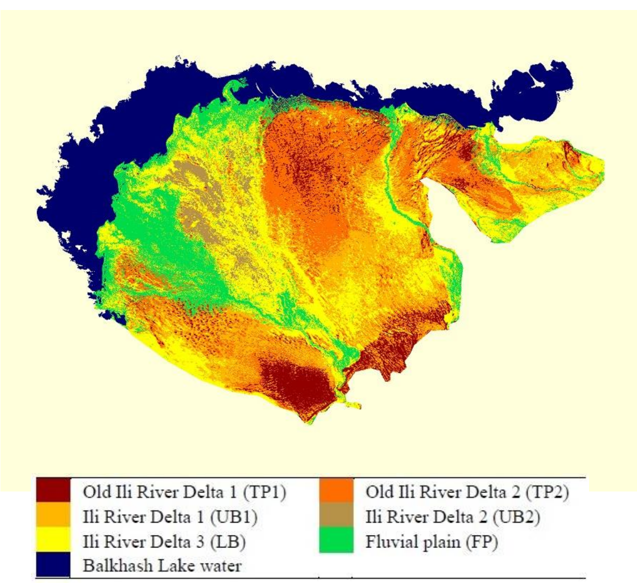

Fig.3.5-5 イリデルタ内の微地形分類画像

4. 研究のまとめ

本研究では、SAR データや光学センサデータなどの複数衛星データを組み合わせた解析により、洪水などの自然災害発生リスクに影響を及ぼす地盤変動(沈下)の検出と分析、その応用事例、さらには、長期の環境(機構)変動を反映した乾燥地域の微地形分布分類などについて検討を行った。その結果、以下の成果が得られた。

(1)地盤変動(沈下)の検出と分析については、複数の干渉 SAR 手法による解析結果の比較により、PSInSAR の適用で微小な地盤変動(沈下)の検出が可能であることを明瞭に示すことができ、今後もこの手法による継続的な地盤変動モニタリングの必要性が考えられた。

(2)雲や降雨の多い東南アジア(ベトナムの事例)における地盤変動については、DInSAR 手法の適用で明瞭な変動情報を示すことが確かめられた。

(3)長期の環境(気候)変動を反映した乾燥地域の微地形分布調査に関し、DSM データに光学センサデータによる正規化植生あるいは水指標データ、および SAR 後方散乱強度データを統合して解析ことで、より詳細な微地形分布の分類が可能であり、その結果の分析により、対象地域の過去からの長期におよぶ環境(気候)変動を分析することの可能性を示せた。

一方、検討項目として、以下のことも指摘された。

a)本研究では、干渉 SAR の解析に Sentinel の C バンド SAR データを多く用いたが、これは、「衛星が 2 機体制の運用で多くの観測データが取得されて、原則無償で入手可能」、「比較的広範囲(観測幅)を観測可能」、「既存研究で示された微小な変動の検出における C バンドの優位性」などによるものである[5]。

b)しかし、PSInSAR 解析のおける PS 点数については、PALSAR-2(L バンド)データの方が、C バンドに比べて多く(本研究の場合約 3 倍)検出され、より詳細な変動分布の把握の可能性が示せた。

c)微地形分布分類については、異なる偏波の SAR データの適用の可能性、今後打ち上げられる予定のより高空間分解能光学センサデータによる高精度な標高抽出が期待された。

5. 本研究の関連文献

(1) 本研究の発表関連文献

[1] 井鍋僚祐、中山裕則,″関東平野広域の長期地盤変動分析と干渉 SAR データによる地盤変動検出の高精度化の可能性,″ *日本大学文理学部自然科学研究所研究紀要,″* 第 56 号、日本大学文理学部自然科学研究所、pp.77-90、2021.

[2] 井鍋僚祐、中山裕則,″ PSInSAR 解析を適用した関東平野中央部の地盤変動の検出とその要因検

討,″(一社)日本リモートセンシング学会第 71 回（令和 3 年度秋季）学術講演会論文集、pp.159-160、2021.
[3] 井鍋僚祐、中山裕則,″複数衛星 SAR データによる PSInSAR 解析を適用した微小地盤変動の詳細検出の可能性 ―関東平野中央部における 1990 年代後半から 2020 年までを例として―,″(一社)日本リモートセンシング学会第 71 回（令和 3 年度秋季）学術講演会論文集、pp.159-160、2021.
[4] Yasunori Nakayama, Akio Sato, Kunihiko Endo, and Toshihiko Sugai,"A Classification of the Micro-topography in the Ili River Delta of Balkhash Lake by Satellite and DSM Data,"*Transactions of the Japan Society for Aeronautical and Space Sciences*," Aerospace Technology Japan, Vol.18, No.5, pp.159-164, 2020.

(2)本論の引用文献
[5]森下遊,″L バンドおよび C バンド SAR データによる PSI 結果の比較,″*測地学会誌*,” 第 61 巻 第 3 号、pp.157-166、2015.

MULTI-TEMPORAL INTERFEROMETRIC SAR DATA ANALYSIS FOR DISPLACEMENT MAPPING OF EARTHQUAKE AND URBAN AREAS

PI No.: PER2A2N190

Divya Sekhar Vaka[1], *Y. S. Rao*[1]

[1] Centre of Studies in Resources Engineering, Indian Institute of Technology Bombay, Mumbai, India.

1. INTRODUCTION

An earthquake of Mw 5.4 hit the Mirpur region in Pakistan on 24 September 2019 at 16.02 local time [1]. The event is a very strong earthquake with a maximum felt intensity of VII on a Modified Mercalli scale. The event severely damaged numerous buildings, roads, and bridges. Damage to the embankments resulted in the flooding of some villages alongside the canals. The seismic behavior in the Himalaya and its vicinity is a result of the continental collision between the Indian and Eurasian tectonic plates. The tectonic plates are converging at a rate of 4-5 cm/year with the Indian plate moving beneath the Eurasian plate. The Himalayan thrust zone mainly comprising of thrust fault zones such as the Main Central Thrust (MCT), Main Boundary Thrust (MBT), and the Main Frontal Fault (MFF) is seismically very active resulting in several moderate to high magnitude earthquakes every year.

As per USGS, the present Mw 5.4 Mirpur earthquake is a shallow event occurred at a depth of 11.5 km at 33.078° N, 73.794° E on a fault striking 352°, dipping 12° with a 164° rake angle [1]. The GCMT solution is different from the USGS solution, in which the earthquake happened at a depth of 14.7 km, on a fault striking 246°, dipping 10° with the epicenter at 32.83° N, 73.85° E. In this study, we use the DInSAR technique to map the coseismic surface deformation of the 2019 Mirpur earthquake using ALOS-2 stripmap data. We also derive source parameters corresponding to the earthquake using InSAR data.

2. DATA

The Japan Aerospace Exploration Agency's (JAXA) ALOS-2 satellite carries an L-band PALSAR instrument. The sensor acquires data in various modes (Spotlight, Stripmap and ScanSAR). The L-band ALOS-2 data are downloadable from the JAXA ALOS/ALOS-2 User Interface Gateway (AUIG2). In this study, we used two ascending pass images acquired on 22-07-2019 and 25-05-2020 to map coseismic surface displacement of the earthquake. The stripmap data are acquired with a swath width of 70 km at a spatial resolution of 9.1 × 5.3 m in range and azimuth respectively.

3. METHODOLOGY

We used the InSAR Scientific Computing Environment (ISCE) [2] for displacement map generation. The process starts with coregistration of master and slave SAR images. We used a 30 m Shuttle Radar Topography Mission (SRTM) mission digital elevation model (DEM) for topographic phase removal. The differential interferogram is then filtered using a Goldstein filter with a filter strength of 0.8. The interferogram is multilooked by a factor of 2 × 2 in range and azimuth to reduce the speckle noise and to improve the signal to noise (SNR) ratio. The phase is unwrapped using the Statistical Cost, Network Flow Algorithm for Phase Unwrapping (SNAPHU) software [3]. The unwrapped phase is geocoded at a 30 m pixel spacing and converted into line of sight (LOS) displacement.

The source parameters such as length, width, depth, dip, strike, strike-slip, dip-slip, location of the epicenter are necessary to understand the fault responsible for the earthquake. Here, we invert the InSAR coseismic interferogram using an elastic dislocation model for a uniform rectangular fault in an elastic half-space to determine the causative source parameters. We use the Steepest Descent Method (SDM) [4] for determining the geometry of the fault that triggered the earthquake. We downsample the displacement map to reduce the data points and improve the computational efficiency during the inversion.

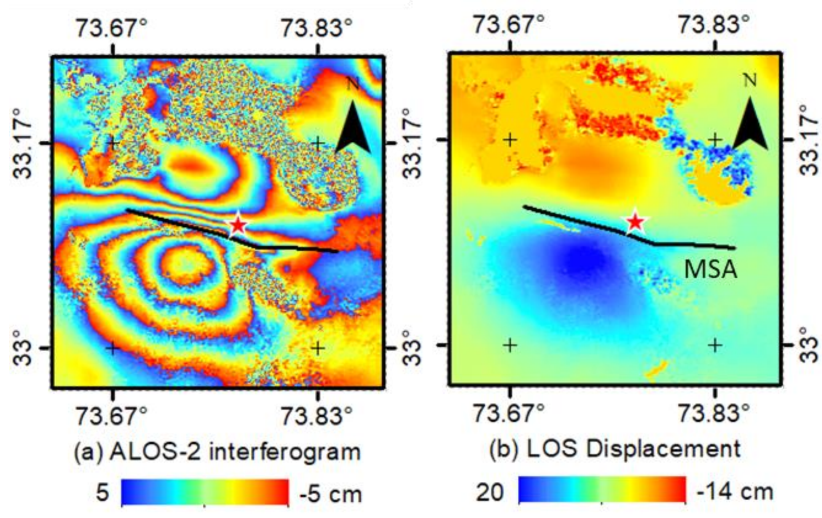

Fig 1 (a) ALOS-2 interferogram (b) LOS displacement

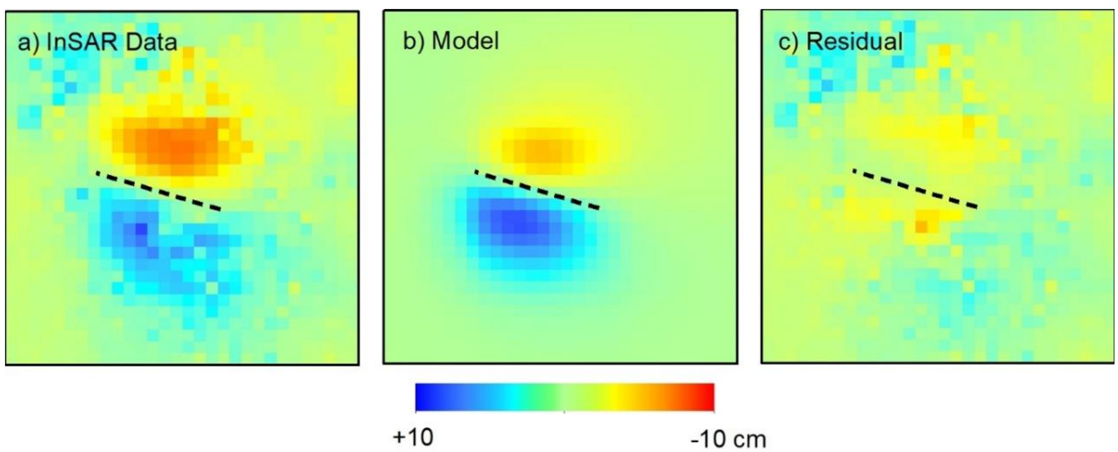

Fig 2. InSAR data, model, and residual. The dotted black line is the inferred fault.

4. COSEISMIC DEFORMATION

The coseismic interferograms and displacement maps shown in Fig 1 indicate two definite lobes of deformation corresponding to movement towards (+) and away (-) from the radar. The positive and negative LOS displacements corresponding to uplift and subsidence ranging from 20 cm to -14 cm respectively. The uplift is concentrated in the southwestern side of the MSA supporting the thrust nature of the causative fault. The deformed area is approximately 20 sq.km. Several decorrelated regions and phase discontinuities observed in the coseismic interferograms are a result of surface displacement due to shallow fault related folding in the epicentral region [5], [6].

5. COSEISMIC INVERSION

The optimal source parameters indicate a rectangular fault of length ~10 km and width ~5 km is responsible for the earthquake. The data, model and the residual are shown in Fig 2. Other parameters of the fault geometry are given in Table 1. The table indicates the source parameters of the earthquake with a correlation of 0.75 between the InSAR data and the model. The USGS and the GCMT values of the earthquake are also given for quick reference and understanding. The epicenter of the earthquake obtained from the model is close to the USGS solution. From the inversion result, it is clear that the earthquake occurred at a shallow depth of approximately 6 km. The causative fault is oriented nearly E-W with a strike angle of 279º. The dip and rake of the earthquake are 22.5º and 92.05º respectively. The depth of about 6 km is in good agreement with the depth of the Main Himalayan Thrust (MHT).

Table 1. Source parameters of the earthquake comparing with USGS and GCMT values.

Parameter	USGS	GCMT	Model
Longitude (deg)	73.79	73.85	73.76
Latitude (deg)	33.08	32.83	33.09
Length (km)	--	--	5.00
Width (km)	--	--	10.00
Depth (km)	11.50	14.70	6.10
Strike (deg)	352.00	246.00	279.40
Dip (deg) (Mean value)	12.00	10.00	22.50
Rake (deg) (Mean value)	164.00	--	92.05
Slip (m) (Mean value)	--	--	0.22
Magnitude	M 5.4	Mw 5.7	Mw 5.7
Data - Model correlation	--	--	0.75

6. CONCLUSIONS

The present study provides the coseismic displacement associated with the 2019 Mw 5.4 Mirpur earthquake. The displacement is spread around 20 sq.km. which damaged several buildings and infrastructure. The presence of minor amounts of strike-slip indicates that the earthquake also resulted in the horizontal motion of the ground surface. ALOS-2 images cover a larger timespan resulting in addition of postseismic deformation into the coseismic displacement. The postseismic deformation may be of different reasons such as after slip, viscoelastic or poroelastic relaxation etc. Therefore, the displacement values derived from ALOS-2 images are slightly greater compared to C-band results.

7. REFERENCES

[1] USGS, ‘M 5.4 - 7km SSE of New Mirpur, Pakistan’, 2019. https://earthquake.usgs.gov/earthquakes/eventpage/us60005mqp/executive (accessed Feb. 28, 2020).

[2] P. A. Rosen, E. Gurrola, G. F. Sacco, and H. Zebker, ‘The InSAR scientific computing environment’, in *EUSAR 2012; 9th European Conference on Synthetic Aperture Radar*, 2012, pp. 730–733.

[3] C. W. Chen and H. A. Zebker, ‘Two-dimensional phase unwrapping with use of statistical models for cost functions in nonlinear optimization’, *Journal of the Optical Society of America A*, vol. 18, no. 2, pp. 338–351, 2001, doi: https://doi.org/10.1364/JOSAA.18.000338.

[4] R. Wang, F. Diao, and A. Hoechner, ‘SDM-A geodetic inversion code incorporating with layered crust structure and curved fault geometry’, in *EGU General Assembly Conference Abstracts*, 2013, pp. EGU2013-2411.

[5] W. Feng *et al.*, ‘Geodetic constraints of the 2017 Mw7. 3 Sarpol Zahab, Iran earthquake and its implications on the structure and mechanics of the north-west Zagros thrust-fold belt’, *Geophysical Research Letters*, 2018, doi: https://doi.org/10.1029/2018GL078577.

[6] D. S. Vaka, Y. Rao, and A. Bhattacharya, ‘Surface Displacements of the 12 November 2017 Iran – Iraq Earthquake derived using SAR Interferometry’, *Geocarto International*, 2019, doi: 10.1080/10106049.2019.1618927.

Papers through the project:

Divya Sekhar Vaka and Y.S. Rao***, Surface displacements of 2019 Mirpur earthquake derived from ALOS-2 and Sentinel-1 InSAR data,*** The Joint PI Meeting of JAXA Earth Observation Missions FY2020 in January, 2021, Poster presentation.

Divya Sekhar Vaka and Y.S. Rao***, Effect of DEM error on DInSAR derived displacement accuracy,*** communicated to Geocarto International, 2021. Revising the paper.

OBSERVATION OF PEATLAND IN INDONESIA USING INTERFEROMETRY SAR

PI No.: ER2A2N201

Yessy Arvelyna[1]

[1] Remote Sensing Technology Center of Japan

1. INTRODUCTION

As the largest tropical peatland globally, peatland coverage in Indonesia is estimated about 24.67 million ha. Within this region, the coverage in Kalimantan and Sumatra are estimated about 8.4 million ha and 9.6 million ha, respectively. Major problems arise at peatland area such as deforestation, forest and land fires that contribute to peatland degradation. Triggered by ENSO, drought caused the peatland fires causing the release of oxidized products (CO, CH4, etc.), destructed environment and severely impacted the community health[1,2].

Therefore, effective method to observe the peatland surface change is necessary for peatland management and conservation measure to prevent degradation and to reduce peatland fire incidents. For the observation in tropical region, SAR image data analysis shows its effectiveness for wide area monitoring without cloud and smoke cover. Hence, interferometry SAR can provide the ground surface deformation with good resolution (in cm)[3]. This study applied the interferometry SAR analysis using PALSAR-2 data during 2015-2021 period for study area in Central Kalimantan and Riau Province, Indonesia. Differential of interferometry SAR (DInSAR) analysis and comparative study with field data are applied to observe ground surface fluctuation of peatland and the area before and after peatland fire. This study is done under collaborative research with JAXA (PI No. ER2A2N201) during FY2019-2021. The analysis results for each application are described.

2. DATA AND METHODS

PALSAR-2 L1.1 datasets mostly in dry season (between July to October) during 2015-2021 period for study area in Central Kalimantan and Riau Province were downloaded from JAXA AUIG2 and G-Portal platform (Table 1). Pair of PALSAR-2 datasets were processed using DInSAR method and time series of deformation processing were computed using the SBAS (Small BAseline Subset) DInSAR method of GAMMA software.
Optical data, i.e. ASTER, Sentinel-2, Landsat, KLHK's Land Cover map[4], LAPAN Fire Hotspot map[5], and BMKG's rain fall data were also observed to gather information on land cover, smoke cover during peatland forest fire, hotspot, rain fall, etc. Comparative studies are done between the derived DInSAR data and field data of the GWL and the GSL data from the SESAME project[6] in Central Kalimantan and bore field data at study area in Pulang Pisau, Central Kalimantan and Siak District, Riau Province. The bore field data consist of the peat depth and peat characteristics.

3. STUDY AREA

Observed study areas are located in peatland area as follow (Fig.1),

- Pulang Pisau District, Kalampangan District Matangai District, and Sebangau National Forest in southeast of Palangkaraya city, Central Kalimantan, where several ground water level (GWL) and ground surface level (GSL) stations installed (Station Taka-1 and Kalteng-1)[6]. In this area, peatland fires widely occurred in 2015-2016. In the classification of peatland from field data, the sites mainly drained peatland with peat depth average 3m and represent swamp shrub and secondary swamp forest on KLHK's Land Use Map 2019.

- Kampar Peninsula, Riau Province where wide coverage of peatland area exists with deep peat (>6m) and peat domes (>10m).

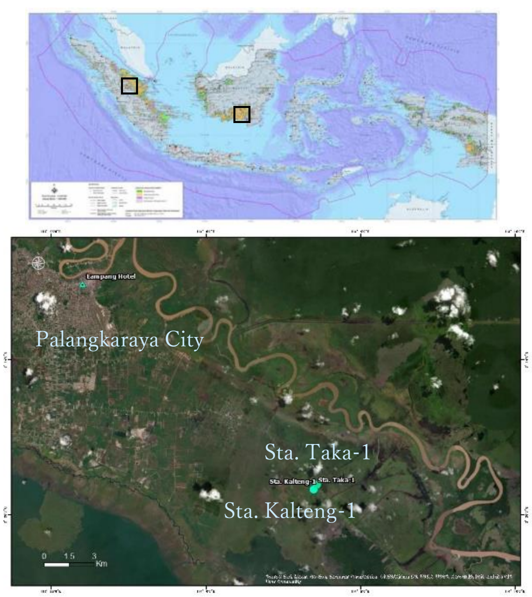

Fig. 1 Location of study area within box (top) and observation station in Central Kalimantan (bottom)

Table.1 List of PALSAR-2 data

No.	Date	Mode	Direction

Central Kalimantan Province			
1	2015/10/08	SM3	Ascending
2	2016/10/06		
3	2017/10/05		
4	2018/09/06		
5	2019/09/05		
6	2020/09/03		
7	2021/09/02		
Kampar Peninsula, Riau Province			
1	2015/02/14	SM3	Ascending
2	2015/09/26		
3	2016/07/16		
4	2016/09/24		
5	2016/12/03		
6	2017/07/15		
7	2018/08/25		
8	2019/08/24		
9	2020/08/22		
10	2021/08/21		

4. RESULTS AND DISCUSSION

4.1. The observation of peatland surface height variability

Peatland surface height variability for study sites in Central Kalimantan have been observed using Differential SAR Interferometry (DInSAR) analysis of PALSAR-2 data during 2015-2020 period. The comparative study with the GWL and GSL data from observed stations shows good correlation with the fluctuation direction of the GWL/GSL of field data from the SESAME project[6].

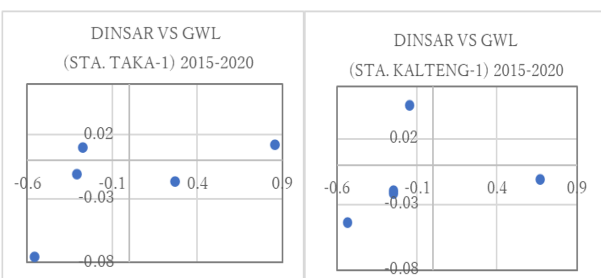

Fig. 2 Comparison of ground surface variability of peatland from DInSAR data and field data (GWL) at a) Sta. Taka-1 and 2) Sta. Kalteng-1

Table 2. The result of comparative study

Mode	Date	DINSAR vs GSL (cm)
Asc - SM2	150409	-2.6702
Asc - SM3	171005	2.1236
Asc - SM3	180906	0.1189
Asc - SM3	190905	-5.3484
Asc - SM3	200903	0.0599

The variability of peatland surface height affected by fluctuation of the ground water were observed by DInSAR analysis. The difference of peatland surface height variability between DInSAR analysis with the GSL data are about ±2.6cm for SM2 mode and ~±5.5cm for SM3 mode. The results were correlated with previous study that revealed the GWL data follows the GSL data in peatland area[3].

4.2. Peatland drought analysis in ENSO year

ENSO is the development of the El Niño Southern Oscillation in the Pacific Ocean and atmosphere involved extreme warm events for about 2 years and generated warm and dry climate in the Southeast Asia. The ENSO event in 2015 correlated with wide forest fires incidents at peatland areas in Indonesia and affected economy, social and resident's health of Indonesia and its neighbor countries from the haze cover[1]. As shown in Fig. 3, DInSAR analysis of PALSAR-2 data over Central Kalimantan during 2015-2020 period shown downward vertical movement from DInSAR data for observed stations in the ENSO year 2015-2016 (-2.8 cm to -4.2 cm) and 2018-2019 (-4.3 cm to -7.5 cm) during August - October period (dry season). While, the fluctuation of presumed stable areas were below -2 cm. Comparative study with field data shown that the GWL data at observed station marked the lowest level about -1.44 m on 2019/10/1. Although the lowest downward movement of ground surface of peatland area is shown in 2019, the forest fire incidents in this year occurred 0.5 times compared to 2015, which may indicate the impact of implementing new regulations on peatland management since 2016. The study results reveal that the fluctuation of DInSAR data derived from PALSAR-2 data correlated with the cycle of the ENSO year in Indonesia occurs every 2 years and peak every 4 years. Thus, the proposed analysis methods are useful to monitor the possibility of peatland forest fire areas that are shown amplified during the ENSO years.

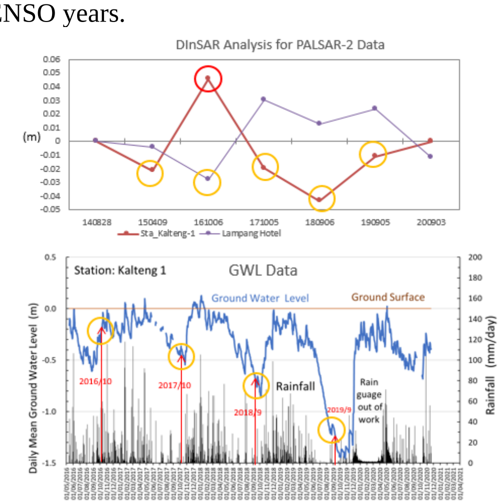

Fig. 3 DInSAR data of peatland area (Sta. Kalteng-1) on 2015/04, 2017/10, 2018/09 and 2019/09 (top) and the GWL data (bottom)

4.5. Peatland surface loss due to fires

DInSAR processing is applied on PALSAR-2 data pairs prior to and post fire incidents for selected fire hotspots with 80% level coincidence during 2015-2018 period. The DInSAR data analysis shows that the fluctuation of maximum height difference of peatland surface for T1-T9 hotspots on downward direction is about -2.9 cm before fire incidents and -23.5 cm after fire incidents suggesting the possibility of peat loss after fire. Peat loss is shown bigger at location around hotspot in barren land (Site 2). Higher rainfall data affected on fluctuation of peatland surface due to more water absorption, shown by smaller downward of DInSAR data for data pair at swamp shrub and secondary swamp forest. DInSAR analysis results on ALOS-2 data before/after fire incidents showed that peat loss after fire incidents could be derived using peatland surface height difference analysis[7].

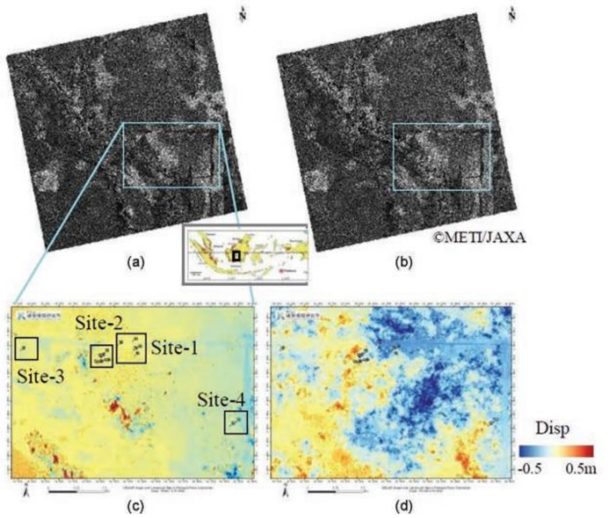

Fig. 4 PALSAR-2 pair data: (a) intensity image of master data (15/10/8) and (b) slave data (16/10/6), and (c) DInSAR image of study area at Pulang Pisau and Mantangai districts before the fire incident and (d) after the fire incident

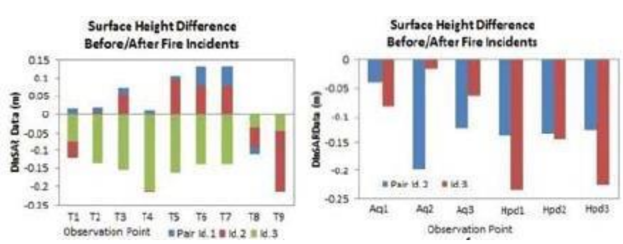

Fig. 5 Peatland surface height difference retrieved from DInSAR data before/after peatland fires

4.6. SBAS DInSAR analysis for peatland fire area

The SBAS DInSAR processing result of a series of PALSAR-2 data (8 scenes) for period 2015-2021 over Central Kalimantan is shown on Fig. 6. The retrieved time series of DInSAR data are located along deforestated areas and historical hotspots during 2015-2021 period (dark green represents vegetated area). Whilst, the areas that are not marked with hotspot, may have burned before 2015. Since SBAS method computed differential interferometry for the whole data pairs (each pair is defined with small baseline, i.e. less than 500m), high coherence data will be obtained from areas where surface deformation are mainly occurred. Thus, the time series SBAS DinSAR method can be used to delineate critical area such as from deforestated area and peatland fire area.

For hotspot with 80% probability (red marker in middle of Fig. 6), the preliminary result for the average of peatland surface fluctuation using SBAS DInSAR method is about -1.89 cm/year.

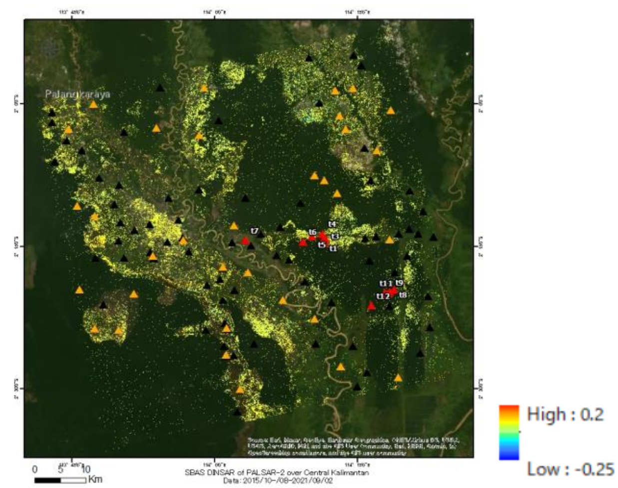

Fig. 6 SBAS DInSAR result for PALSAR-2 data (in m) overlay hotspot (▲: medium; orange: high probability; red: 80% probability, T1-T12) for period 2015-2021 over study area in Central Kalimantan

4.7. Peat dome analysis

The analysis of multi temporal intensity of PALSAR-2 data during 2015-2018 period over Kampar Peninsula, Riau Province shows that peat dome areas have lower backscattering about 0.067-0.22dB along vertical cross line. Maximum peat depth for these areas is about 14 m, while the bore data for non-peat dome area is about 6 m. DInSAR analysis results for PALSAR-2 data show large vertical fluctuation (~-40.5cm) in peat dome areas larger than non-peat dome areas (-27.8 cm) possibly due to higher moisture and bearing capacity[8].

4.8. Peatland subsidence analysis

Past study using DInSAR data analysis shows that peatland subsidence occurred by impact of agriculture activities such as palm plantation in West Kalimantan. The subsided areas were low in organic matter from laboratory test (Lost on Ignition method). It is considered to be affected by the decomposition process[9].

Recent study applied SBAS DInSAR method on PALSAR-2 data over study area in Central Kalimantan and Kampar Peninsula, Riau Province. The SBAS DInSAR data analysis results show the tendency of peatland subsidence at the areas with shallow peat thickness along coast, river, and canal possibly due to decomposition by water sedimentation transport. From 17 processed interferogram data for Kampar Peninsula, the average of deformation (subsidence) rate at study sites along coast is retrieved about 8.5 cm/year (Fig.7, box).

Fig. 7 SBAS DInSAR processing result (in m) for PALSAR-2 data over study area in Kampar Peninsula, Riau Province

5. CONCLUSION

The study results on the application of interferometry SAR to observe peatland area show that the proposed methods are useful for peatland fire monitoring, deep peat assessment and peatland subsidence observation. DInSAR analysis results on PALSAR-2 data before/after fire incidents showed that peat loss after fire incidents could be derived using peatland surface height difference analysis. The proposed methods can increase the accuracy of existing monitoring methods using optical satellite images, without limitation on the observation when clouds and smoke cover exist.

6. ACKNOWLEDGEMENT

Author would like to thank JAXA who provided ALOS-2 PALSAR-2 image data through the 2nd Earth Observation Collaborative Research (PI: ER2A2N201).

7. REFERENCES

[1] Nurbaya, S., Efransjah, Murniningtyas, S., Erwinsyah, and Damayanti, E.K.(Editors), "The State of Indonesia's Forests", Ministry of Environment and Forestry, Republic of Indonesia, Jakarta, p.36; 110, 234 pages, 2020.
[2] Vadrevu, K.P., Ohara, T. and Justice, C., "Air Pollution in Asia", *Environmental Pollution*, 12, 233–235, 2014.
[3] Arvelyna, Y., Takahashi, H., Osaki, M., Hirose, H. and Sato, T., "Monitoring of Peatland Surface Height Variability Using DInSAR Analysis on ALOS-2 PALSAR data and Field Observation of Ground Water/Surface Level Data, *The 64th Japan Remote Sensing Conference Proceeding*, pp. 111–112, Tokyo, Japan, 2018.
[4] WEBGIS of Ministry of Environment and Forestry Indonesia, http://webgis.menlhk.go.id:8080/kemenhut/index.php/en/map/interactive-map-2
[5] LAPAN Fire Hotspot, http://103.51.131.166/
[6] Takahashi, H., Shigenaga, Y., Hamada, Y., Osaki, M. and Setiadi, B., "Near-real time remote monitoring of ground-water/surface levels and warning to carbon loss from tropical peatlands in Indonesia", *The proceedings of the International Workshop on Forest Ecological Resources Security for Next Generation: Development and Routine Utilization of Forest Ecological Resources and their Domestication* (eds. Shiodera, S., Fujita, M., & Kobayashi, S.), pp. 80–90, Center for Southeast Asian Studies. Research Center, Kyoto University, Kyoto, 2018,
[7] Arvelyna Y., Takahashi, H., Indrayanti, L., Hayasaka, H., Vadrevu, K.P, Maryani, R., Osaki, M, Hirose, K., "Peatland Surface Loss due to Fires in Central Kalimantan, Indonesia – A Case Study Using Differential Interferometry SAR (DInSAR)", *Biomass Burning Mapping and Monitoring*, Edited by Vadrevu, P.K, Ohara, T., and Justice, C., Vol. I, pp. 77-90, 2021.
[8] Arvelyna, Y., Prayoto, R. Maryani, "Observation of peat dome and subsidence using DInSAR analysis on ALOS-2 PALSAR data (Study case: Kampar Peninsula, Central Sumatra)", *The 66th Japan Remote Sensing Conference Proceeding*, p.86-88, 2019.
[9] Arvelyna Y., Hirose, K., Anshari, G., Kunihiro, T., Koichi, H., and Yanto, R., "The Application of Interferometry SAR Data Analysis for Peatland and Land Use Monitoring in West Kalimantan", *The 59th Japan Remote Sensing Conference Proceeding*, Tokyo, Japan, pp.207-208, 2015.

APPENDIX

[1] Arvelyna, Y., Prayoto, R. Maryani, "Observation of peat dome and subsidence using DInSAR analysis on ALOS-2 PALSAR data (Study case: Kampar Peninsula, Central Sumatra)", *The 66th Japan Remote Sensing Conference Proceeding*, p.86-88, 2019.
[2] Arvelyna Y., Takahashi, H., Indrayanti, L., Hayasaka, H., Vadrevu, K.P, Maryani, R., Osaki, M, Hirose, K., "Peatland Surface Loss due to Fires in Central Kalimantan, Indonesia – A Case Study Using Differential Interferometry SAR (DInSAR)", *Biomass Burning Mapping and Monitoring*, Edited by Vadrevu, P.K, Ohara, T., and Justice, C., Vol. I, pp. 77-90, 2021
[3] Arvelyna, Y., Takahashi, H. Maryani, R., Osaki, M.," Peatland Monitoring using DInSAR of PALSAR-2 Data and Field Observation of Ground Water/Surface Level Data during the ENSO Year (Study case: Central Kalimantan, Indonesia)", *The 71th Japan Remote Sensing Conference Proceeding*, Tokyo, Japan, 2021.
[4] Arvelyna, Y, "The Achievement of the Observation of Peatland in Indonesia using Interferometry SAR", *JAXA PI Meeting*, Tokyo, Japan, 2022.

長期に蓄積されたSARデータを用いた複合的地表変動メカニズムの解明

PI No.: ER2A2N202
石塚 師也 [1]

[1] 京都大学 大学院工学研究科 都市社会工学専攻

1. 緒　言

干渉 SAR 解析は周期的に地表変動を面的に把握することができる技術として，地震や火山，地盤沈下，地すべり等の地表変動の把握に有効性を示している．また PS 干渉 SAR 解析や Small baseline subsets 解析に代表される干渉 SAR 時系列解析では，ミリメートルから 1 センチメートルの地表変動でも特定することが可能になりつつあり，変動モニタリング技術として，革新的な役割を果たしてきた．

研究代表者はこれまで，主に ALOS-2/PALSAR-2 や ALOS/PALSAR データを用いて，干渉 SAR 時系列解析の手法開発および適用を行ってきた．手法開発では，より推定精度を向上させるためのアルゴリズム開発を行い，適用研究では，地盤沈下や地すべり，地震や火山噴火に伴う地下水流動等を対象にしてきた．その結果，ミリメートル程度の地表変動が多くの地域で発生し，なおかつ種々の現象が複合的に関係して地表変動を生じていることを明らかとした．例えば，第 1 回地球観測研究公募を通じた研究では，2016 年熊本地震後に阿蘇カルデラ北西部で数 km の範囲で年間 5~6 cm ほどの局所的な地表変動が発生し，カルデラ内の熱水流動が地震によって促された可能性を示した[1]．このような複合的な地表変動は，至るところで発生していると考えられ，このような現象は，これまでには明らかとなっておらず，複合的な地球システムの理解に役立つとともに，我が国の国土強靭化に寄与すると考える．

また，近年では，Sentinel-1A, 1B に代表されるように，様々な SAR 衛星が打ち上げられ，データ利用可能となっている．多くの SAR 衛星は，ALOS-2 と異なる周波数帯，入射角，回帰日数で運用されている．そのため，これらのデータを相補的に用いることで，より詳細な地表変動の把握に役立つと考えられる．これは，ALOS-2/PALSAR-2 の実用性を高めることにも繋がると考えている．本研究は，長期にわたり蓄積された ALOS-2/PALSAR-2 および ALOS/PALSAR データを用いて，長期の地表変動を明らかにする．また，他国で運用されている異なる特徴をもつ SAR 衛星データを相補的に用いることで，地表変動現象をより詳細に理解できるか検討する．

特に本研究課題では，PS 干渉 SAR 解析を用いて，2016 年熊本地震の前と地震後の地表変動の時系列地表変動を推定し，地表変動のパターンにどのような違いがみられるか調べた．特に時系列のパターンによって，季節性の地表変動および長期的な地表変動成分を特定し，これらのパターンをもつ地域や大きさがどのように変化したかを明らかにした．対象は熊本地域とした（Fig. 1）．また，推定した地表変動と地下水位データを比較することで，地表変動と地下水位変化との関連性を明らかにした．干渉 SAR 時系列解析で得られた地表変動が地下水システムのモニタリングに有効であることはこれまでに示されているものの，地震による地下水システムの変化を干渉 SAR 時系列解析でモニタリングした事例はほとんどない．そのため，本研究は，地震を含めた地下水システムのモニタリングへの干渉 SAR 時系列解析の好例となると考えている．なお，本報告書の内容の多くは，[2]で論文発表を行っている．

2. 解析データおよび手法

本研究では，2016 年熊本地震前のデータとして，2007 年 1 月 7 日から 2011 年 3 月 5 日の間に南行軌道で取得された 19 シーンの ALOS/PALSAR データ（PATH/FRAME: 73/2960）を用いた．2016 年熊本地震後のデータとして，(1) 2016 年 4 月 18 日から 2018 年 12 月 10 日の間に南行軌道で所得された 28 シーンの ALOS-2/PALSAR-2 データ（PATH/FRAME: 23/2950, 23/2960），(2) 2016 年 7 月 1 日から 2018 年 12 月 10 日の間に南行軌道で取得された Sentinel-1 データ（PATH/FRAME: 163/483）および，(3) 2016 年 11 月 16 日から 2018 年 6 月 15 日の間に北行軌道で取得された Sentinel-1 データ（PATH/FRAME: 156/105）を用いた．南行軌道で取得された ALOS-2/PALSAR-2 データおよび Sentinel-1 データは，それぞれのデータから推定された地表変動が一致するかを確認することで，妥当性の検証を行った．また，北行軌道および南行軌道で取得された Sentinel-1 データは，2.5 次元解析により，準上下および準東西方向の地表変動を推定するために用いた．

本研究では，PS 干渉 SAR 解析を用いて時系列地表変動の推定を行った．PS 干渉 SAR 解析は，PS と呼ばれるマイクロ波の後方散乱強度および位相が安定しているピクセルのみを用いて地表変動を推定する手法である[3] [4]．また，PS 干渉 SAR 解析は，大気中でのマイクロ波伝播遅延の干渉位相への影響や数

値地形モデルの誤差による干渉位相への影響をとり除く戦略を有している．本研究では，差分干渉 SAR 画像を作成するために，Radar interferometry calculation tool [5]および GAMMA software [6]を用いた．PS 干渉 SAR 解析には，[7]および[8]でも用いられている自作のプログラムを用いた．
推定した地表変動の妥当性を検証するために，国土地理院が運用する GNSS 観測網である GEONET の F3 解を用いた．解析対象には，GEONET 観測点が 2 点（Kumamoto，Jonan）あり（Fig. 1b），1 点（Jonan）を基準点とし，残り 1 点（Kumamoto）の時系列地表変動と比較を行った．GNSS と PS 干渉 SAR 解析で得られた時系列地表変動を比較するため，GNSS の地表変動は衛星視線方向へ投影を行った．
PS 干渉 SAR 解析で推定された時系列地表変動の特徴を解釈するため，時系列地表変動モデルを用いた．本研究では，推定された時系列地表変動が 1 年の周期をもつ季節性の地表変動および長期的な地表変動で構成されるとした．季節性の地表変動は，季節性の地下水位変化に伴う地表変動を模擬しており，長期性の地表変動は，2016 年熊本地震に伴って発生した年周期をもたない地表変動を模擬した．この季節性の地表変動は，年周期のサイン関数でモデル化し，長期的な地表変動は指数関数でモデル化した．これらのモデルに含まれる変数は，最小二乗法で推定した．

3. 解析対象の概要

本研究の解析対象地域である熊本地域は，九州の中心部に位置し，豊富な地下水資源が存在することが知られている．地下水は阿蘇火山の西麗で涵養し，地形に沿って熊本地域に流入し，有明海に流出する．熊本地域の地表地質は，西部では主に沖積層で構成され，東部は主に阿蘇火砕堆積物で構成される（Fig. 1c）．帯水層は主にこの阿蘇火砕流堆積物で成ることが知られている．浅部の帯水層は比較的新しい火砕堆積物で構成されるが，深部の帯水層はより古い火砕堆積物で構成され，主に被圧帯水層である．浅部の堆積層の標高は，熊本地域東部の台地で約 0–200 m であり，西部の沖積平野では-50–0 m である．浅部および深部帯水層における地下水流動パターンは大よそ整合していると報告されている [9]．
2016 年熊本地震は，4 月 14 日（Mw 6.2）と 4 月 16 日（Mw 7.0）に日奈久断層帯および布田川断層帯で発生した（Fig. 1b）．この地震に伴って，地下水位変化が観測され，熊本中心部で地表面の亀裂が発生した箇所においては，地震後 30–45 日は，地下水位の低下が主に観測された．一方，熊本地域東部では，地下水位の継続的な上昇も観測された．[10] は，この熊本地域東部での地下水位上昇は，2016 年熊本地震に伴って阿蘇火山からの地下水放出量が増加したためと報告している．

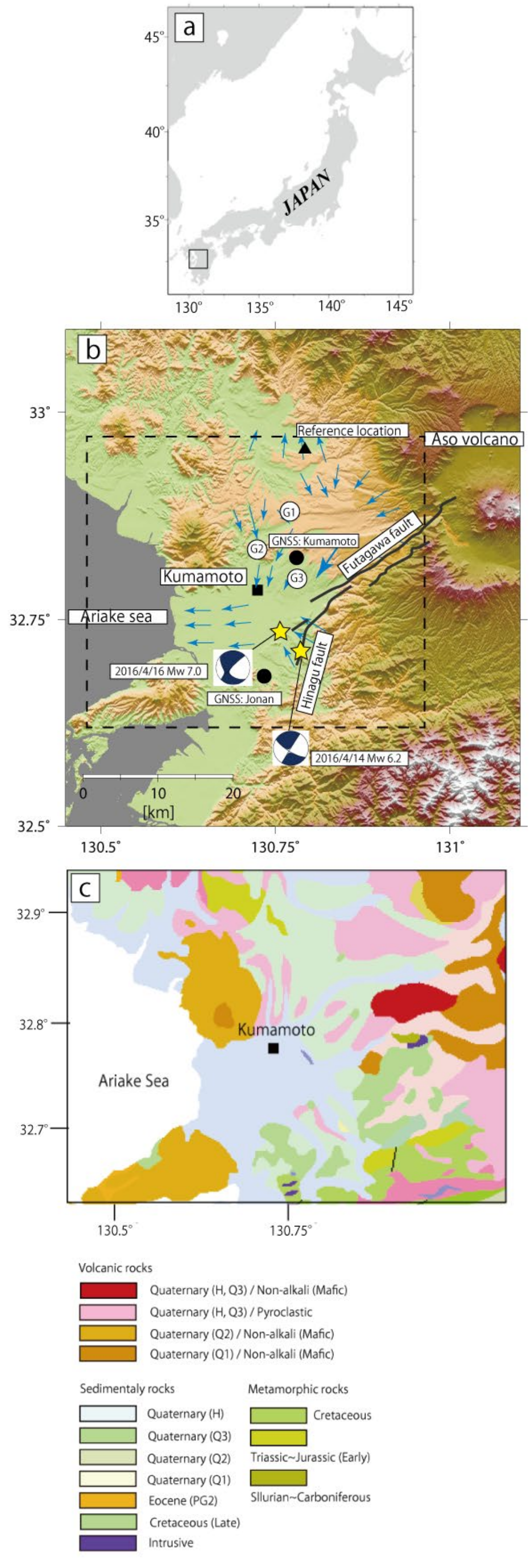

Fig. 1 (a) **解析対象範囲，(b) 対象地域の範囲（黒点線）および本地域における大よその地下水位流動方向（水色の矢印），2016 年熊本地震の震源位置（黄色星印）．(c) 対象地域における地表地質．**

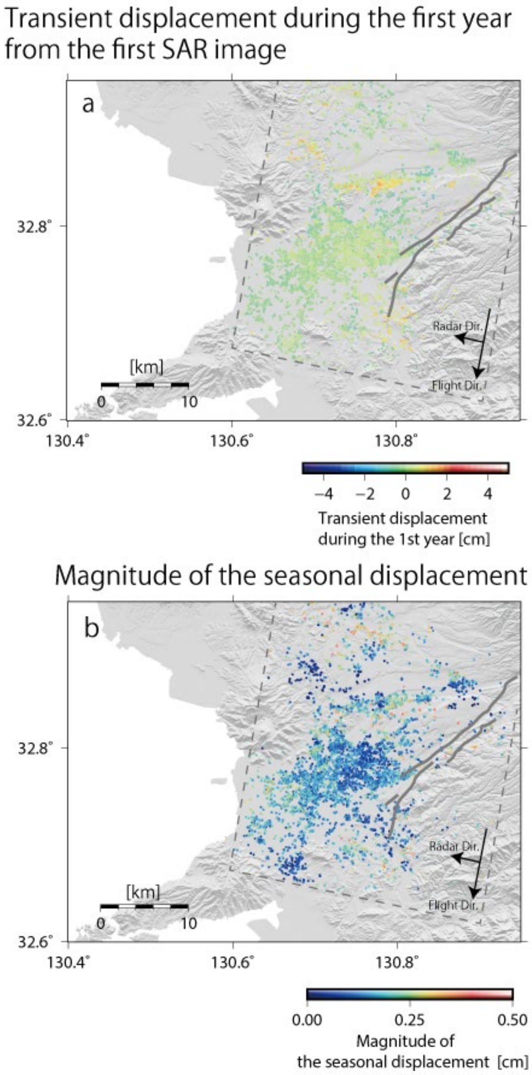

Fig. 2 **2007 年 1 月 7 日から 2011 年 3 月 5 日に南行軌道で取得された ALOS/PALSAR データによる地表変動．(a) 長期的な地表変動パターンの最初の 1 年間の変動量，(b) 季節的な地表変動の大きさ．**

4. 解析結果

2007 年 1 月–2011 年 3 月の PALSAR データを用いて解析した結果を Fig. 2 に示す．Fig. 2a は時間的に指数関数で表した地表変動モデルで得られた長期的な地表変動の最初の 1 年間における地表変動量であり，Fig. 2b はサイン関数で表した季節性の地表変動の大きさを表す．GNSS との比較においては，長期的な地表変動の誤差の絶対値は 0.30 cm であり，季節性地表変動の大きさの誤差の絶対値は 0.15 cm であった．

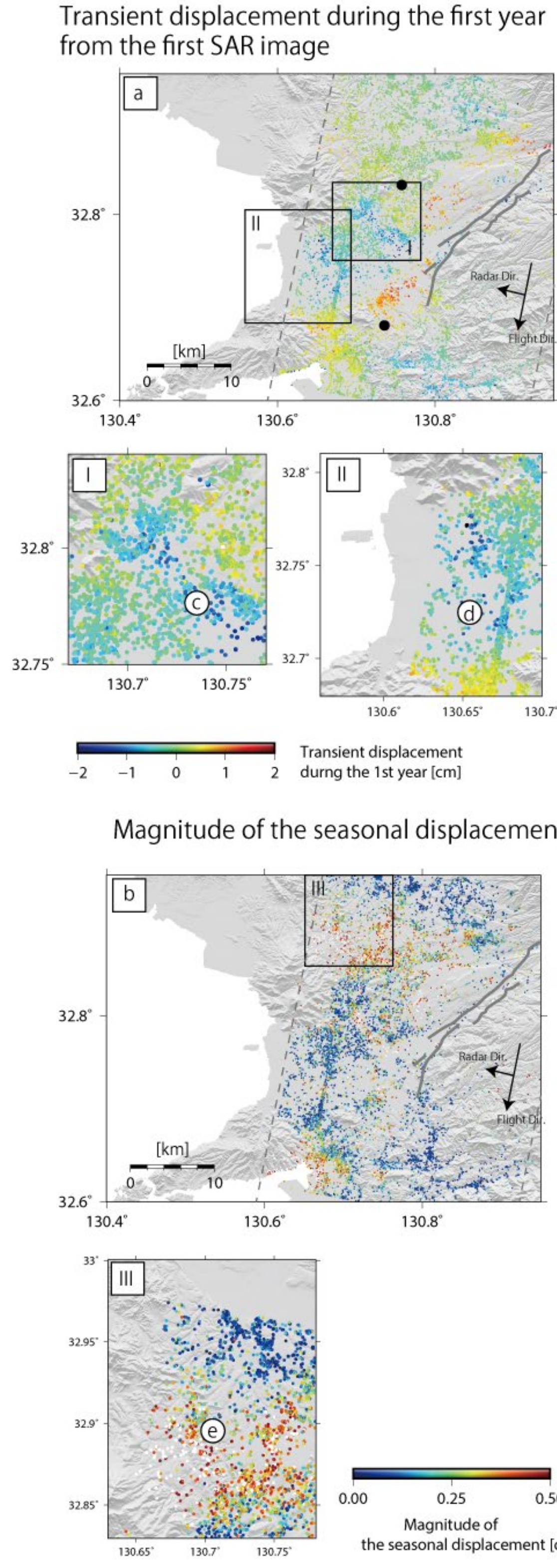

Fig. 3 **2016 年 4 月 18 日から 2018 年 12 月 10 日に南行軌道で取得された ALOS-2/PALSAR-2 データによる地表変動．(a) 長期的な地表変動パターンの最初の 1 年間の変動量，(b) 季節的な地表変動の大きさ．**

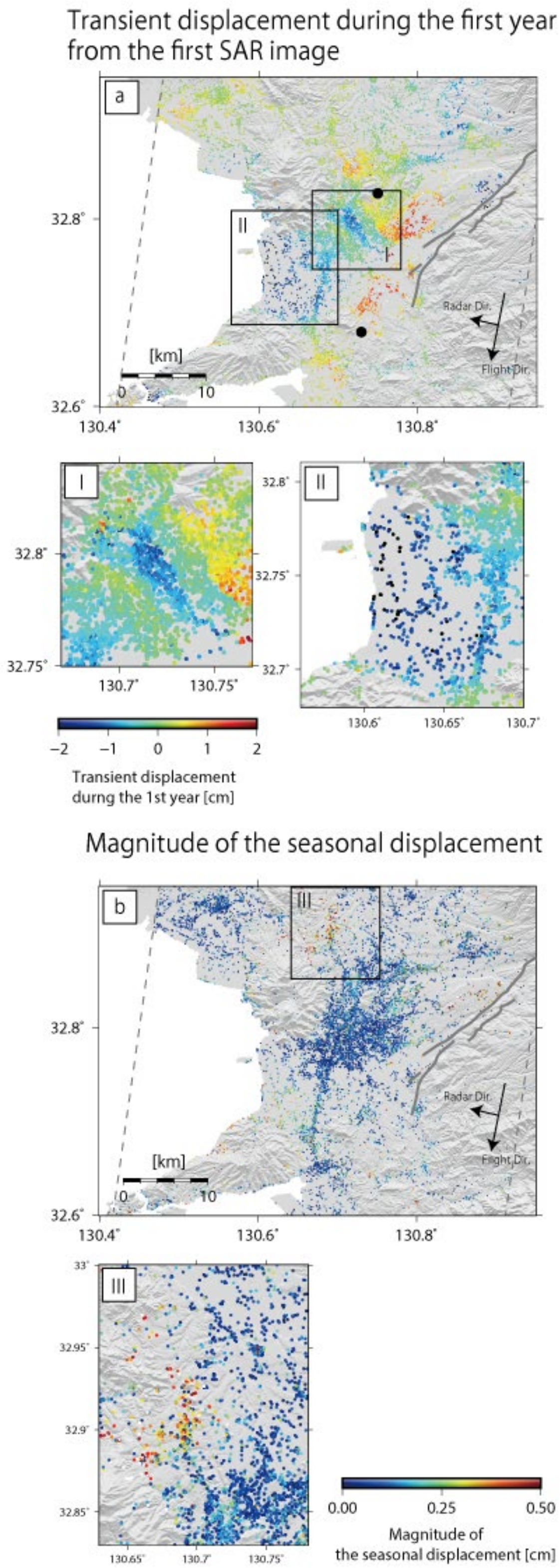

Fig. 4 2016 年 7 月 1 日から 2018 年 12 月 30 日に南行軌道で取得された Sentinel-1 データによる地表変動．(a) 長期的な地表変動パターンの最初の 1 年間の変動量，(b) 季節的な地表変動の大きさ．

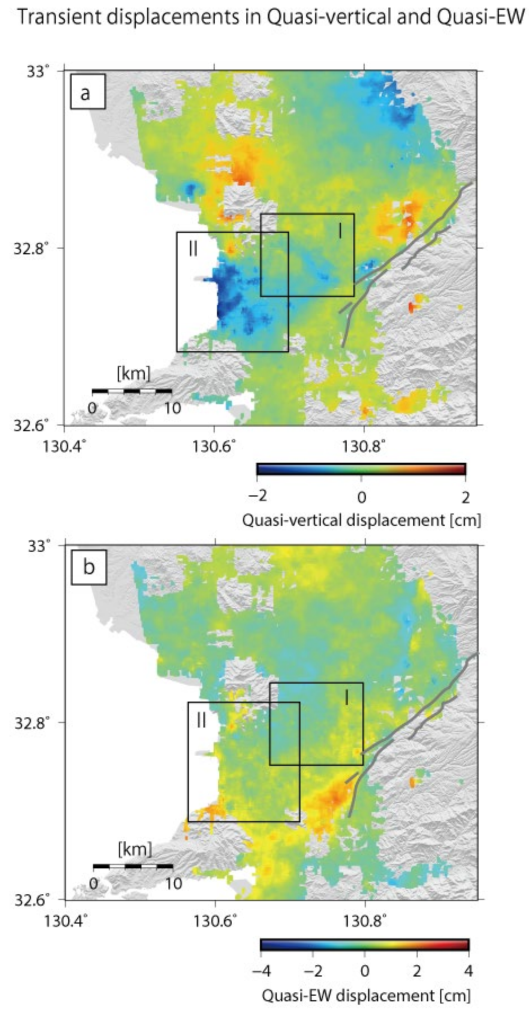

Fig. 5 Sentinel-1 の北行軌道と南行軌道のデータから得られた(a)準上下方向および(b)準東西方向の地表変動（長期的な地表変動パターンの最初の 1 年間の変動量）．

続いて，2016 年熊本地震後の長期的および季節性の地表変動量の傾向について議論を行う．Fig. 3a および 3b は 2016 年 4 月から 2018 年 12 月における PALSAR-2 の南行軌道で取得されたデータから得られた長期的な地表変動の最初の 1 年間における地表変動量と季節性の地表変動の大きさである．GNSS 観測点との比較を行ったところ，長期的な地表変動量の誤差の絶対値は 0.12 cm であり，季節性の地表変動量の誤差の絶対値は 0.072 cm であった．また，Sentinel-1 の南行軌道で得られたデータによる地表変動（長期的な地表変動の最初の 1 年間における変動量と季節性の地表変動の大きさ）を Fig. 4a および Fig. 4b に示す．GNSS で得られた地表変動量との比較では，長期的な地表変動量の誤差の絶対値は 0.19 cm であり，季節性の地表変動量の誤差の絶対値は 0.027 cm であった．

PALSAR-2 および Sentinel-1 の南行軌道から得られたデータの PS 干渉 SAR 解析結果は整合していることが分かる．長期的な地表変動量の傾向としては，布田川–日奈久断層帯の北部において衛星に向かう方向の地表変動が得られている．一方，解析地域の中央部周辺（Figs. 3 および 4 における I）および西部の海岸付近（Figs. 3 および 4 における II）では，両データともに衛星に遠ざかる方向の地表変動が推定されている．I における最初の 1 年間の地表変動量は約-1.1 cm（負の値は衛星から遠ざかる方向を示す）であり，II では約-2.0 cm であった．季節性の地表変動量においては，両データともに解析範囲の中央部および北部（Figs. 3 および 4 における III）において，約 0.5 cm の大きさで発生していることが分かった．

Sentinel-1 の南行軌道と北行軌道のデータから得られた長期的な地表変動の最初の 1 年間の変動量を用いて 2.5 次元解析を適用した結果を Fig. 5 に示す．本研究で用いた Sentinel-1 の北行軌道のデータの期間は 2016 年 11 月 16 日から 2018 年 6 月 15 日であり，本研究で用いた南行軌道のデータの全期間よりもやや短い．そのため，2.5 次元解析では，南行軌道においても 2016 年 11 月 22 日から 2018 年 6 月 9 日の間のデータの解析結果をもちいて，北行軌道のデータの期間と大よそ一致するようにした．Fig. 5 より，最初のデータは 2016 年熊本地震より 7 か月後であるが，上述の I および II における衛星から遠ざかる方向の変動が捉えられている．また，この衛星から遠ざかる方向の地表変動は，主に沈下方向の地表変動であることが，2.5 次元解析結果より分かった（Fig. 5）．また，布田川断層帯周辺の地表変動は，東西方向の地表変動も有することが分かった．

PALSAR-2 と Sentinel-1 の地表変動がどの程度整合しているか定量的に評価するため，観測された地表変動量が主に鉛直方向の成分である（準東西方向の地表変動の差の絶対値が 0.05 cm 以下である）地点において差を計算した．準東西方向の地表変動量は上述の 2.5 次元解析の結果を用いた．その結果，PALSAR-2 と Sentinel-1 の南行軌道のデータから推定された年間地表変動の差の平均は 0.55 cm であった．また，PALSAR-2 の南行軌道と Sentinel-1 北行軌道のデータの年間地表変動量の差の平均は 0. 54 cm であった．Sentinel-1 の南行軌道と Sentinel-1 の北行軌道のデータから得られた年間地表変動量の差の平均は 0.24 cm であった．この値は，[11] によるインドネシアバンドン平野における同様の比較が 0.75 cm であったことを考えると，よい精度で地表変動を推定できていると言える．また，本研究で議論を行う地表変動（例えば，Figs. 3, 4, 5 における I, II, III の変動）は誤差より十分に大きいと言える．

5. 地表変動から分かる地下水システムの変化

大規模な地震に伴い，地下水位が変化する事例はこれまでに多く報告されている [12] [13]．この地震に伴う地下水位の低下のメカニズムは，間隙水圧の変化 [14]や浸透性の変化 [15]，クラックの膨張 [16]等の複数要因が指摘されている．ただし，このような地下水位変化に起因する地表変動を捉えた事例は，間隙水圧の変化については，[14]や[17]などがあるが，それ以外については，浸透性の変化に伴う地下水位変化による地表変動の可能性を[8]で指摘しているのみであり，地震と地下水位変化，地表変動との相互作用について明らかになっていない点も多い．

2016 年熊本地震後の熊本地域の地表変動の一部は，[18]や[19]によって，下部地殻及び上部マントルの粘弾性変形により説明がされている．これは，地震による応力変化に伴って，下部地殻や上部マントルが粘弾性的に変形し，地表変動に表れるものである．これらの先行研究では，粘弾性変形をする深度は約 20–80 km と推定されている．本研究で捉えた局所的な地表変動（Figs. 3 および 4 における I, II, III）は数 km の空間スケールの地表変動であるため，広域に表れる粘弾性変形では説明がつかない．また，震源断層が地震後の非地震性のすべりを起こすことによって地表変動が発生することも知られているが，Figs. 3 および 4 の I, II, III での地表変動の空間パターンは震源断層の形状と合っていないため，このようなメカニズムでも説明が難しい．

一方，地下水位変化に伴う地表変動である蓋然性が高いと考えている．I の地域では，2016 年熊本地震の本震の地表変動の解析により，地表面の亀裂が捉えられている [20]．また，この亀裂が生じた場所において，4.74 m の地下水位の低下が観測されており，この地下水位の低下は，2.7×10^{7} m^{3} の体積量の地下水位が放出されたことが得られている [21]．本研究で沈下が観測された地域は，亀裂発生地域および地下水位が低下域と整合しており，地下水位の低下に伴う地表変動と解釈できる．

解析地域東部（II の地域）で推定された沈下域では，2016 年熊本地震後に地下水位が 1 m ほど上昇していることが分かっている．この沈下と地下水位の上昇は，液状化によって説明することができると考えられる．沈下が推定された地域では，2016 年熊本地震後に液状化に伴う噴砂が確認された地域である．

熊本地域の地下水位は季節性のパターンを示すことが知られている．降雨量は 6 月から 8 月ごろに増加し，地下水位も 6 月から 10 月ごろに増加の傾向を示す．本研究で捉えた季節性の地表変動（Figs. 3, 4 の III の地域）の周期は，地下水位の周期と大よそ一致しており，地下水位変化に伴う季節性の地表変動を捉えたものと考えられる．ALOS/PALSAR の解析では，この季節性の地表変動が十分に捉えられていない点を考えると，2016 年熊本地震以降にこの季

節性の地表変動が発生した可能性および ALOS/PALSAR の解析期間以降の本研究で解析を行っていない期間に季節性の地表変動が発生し始めた可能性がある．

6. まとめ

本研究では，ALOS/PALSAR，ALOS-2/PALSAR-2 および Sentinel-1 の SAR データを用いて，2007 年 1 月–2011 年 3 月および 2016 年 4 月–2018 年 12 月における熊本地域の地表変動をマッピングした．また，地下水位の変化と地表変動が関連することを示した．本研究の成果は，熊本地域の地下水モニタリングへの干渉 SAR 時系列解析のモニタリングの有効性を示すとともに，本手法が地震による地下水位変化への理解を深める点においても有効であることを示していると考えている．

謝辞

地下水位データについては，熊本地域の関係機関が観測したデータを日本地下水学会熊本地震と地下水調査研究グループによってとりまとめたものを利用しました．ここに記して感謝致します．

引用文献

[1] W. Yamada, K. Ishitsuka, T. Mogi, and M. Utsugi, "Surface displacements of Aso volcano after the 2016 Kumamoto earthquake based on SAR interferometry: implications for dynamic triggering of earthquake-volcano interactions", *Geophysical Journal International*, 218, 755-761, 2018.
[2] K. Ishitsuka, T. Tsuji, W. Lin, M. Kagabu, and J. Shimada, "Seasonal and transient surface displacements in the Kumamoto area, Japan, associated with the 2016 Kumamoto earthquake: implications for seismic-induced groundwater level change", *Earth Planets Space*, 72:144, 2020.
[3] A. Ferretti, C. Prati, and F. Rocca, "Nonlinear subsidence rate estimation using permanent scatterers in differential SAR interferometry" *IEEE Trans. Geosci. Remote Sens,* 38, 5, 2202-2212, 2000.
[4] A. Ferretti, C. Prati, F. Rocca, "Permanent Scatterers in SAR Interferometry" *IEEE Geosci. Remote Sens,* 39, 8–20, 2001.
[5] T. Ozawa, E. Fujita, and H. Ueda, "Crustal deformation associated with the 2016 Kumamoto earthquake and its effect on the magma system of Aso volcano" *Earth Planets Space*, 68,186, 2016.
[6] U. Wegmuller, and C.L. Werner, "GAMMA SAR processor and interferometry software" *Proc. 3rd ERS Symposium,* 1687-1692, 1997.
[7] K. Ishitsuka, and T. Matsuoka, "Accuracy evaluation of persistent scatterer interferometry using ALOS/PALSAR data: A case study of surface displacement in the Kujukuri Plain, Chiba Prefecture" *Journal of The Remote Sensing Society of Japan*, 36, 4, 328-337, 2016. (in Japanese with English abstract)
[8] K. Ishitsuka, T. Matsuoka, T. Nishimura, T. Tsuji, T. ElGharbawi, "Ground uplift related to permeability enhancement following the 2011 Tohoku earthquake in the Kanto plain, Japan", *Earth Planets Space*, 69:81, 2017.
[9] National Institute of Advanced Industrial Science and Technology (AIST)—Geological Survey of Japan (GSJ) (2014) Water Environment Map "Kumamoto area". (in Japanese)
[10] M. Kagabu, K. Ide, T. Hosono, K. Nakagawa, and J. Shimada, "Describing coseismic groundwater level rise using tank model in volcanic aquifers, Kumamoto, southern Japan", *Journal of Hydrology*, 124464, 2019.
[11] Z. Du, L. Ge, A.H.M. Ng, Q. Zhu, X. Yang, and L. Li, "Correlating the subsidence pattern and land use in Bandung, Indonesia with both Sentinel-1/2 and ALOS-2 satellite images", *Int. J. Appl. Earth Obs. Geoinformation*, 67, 54-68, 2018.
[12] D.R. Montgomery, M. Manga M, "Streamflow and water well responses to earthquakes", *Science*, 300, 2047-2049, 2003.
[13] M. Manga, I. Beresnev, E. E. Brodsky, J. E. Elkhoury, D. Elsworth, S.E. Ingebritsen, D.C. Mays, and C.Y. Wang, "Change in permeability caused by transient stresses: field observations, experiments, and mechanism", *Rev. Geophys*, 50, RG2004, 2012.
[14] S. Jonsson, P. Segall, R. Pedersen, and G. Bjornsson, "Post-earthquake ground movements correlated to pore-pressure transients", *Nature*, 424, 179-183, 2003.
[15] J.E. Elkhoury, E.E. Brodsky, D.C. Agnew, "Seismic waves increase permeability", *Nature*, 441, 1135-1138, 2006.
[16] R. H. Sibson, and J.V. Rowland, "Stress, fluid pressure and structural permeability in seismogenic crust, North island, New Zealand", *Geophysical Journal International*, 154, 2, 584-594, 2003.
[17] Y. Fialko, "Evidence of fluid-filled upper crust from observations of postseismic deformation due to the 1992 Mw7.3 Landers earthquake", *J. Geophys. Res.*, 109, B08401, 2004.
[18] J.D.P. Moore, H. Yu, C.H. Tang, T. Wang, S. Barbot, D. Peng, S. Masuti, J. Dauwels, Y.J. Hsu, V. Lambert, P. Nanjundiah, S. Wei, E. Lindsey, L. Feng, B. Shibazaki, "Imaging the distribution of transient viscosity after the 2016 Mw 7.1 Kumamoto earthquake", *Science*, 356, 163-167, 2017.
[19] F.F. Politz, T. Kobayashi, H. Yarai, B. Shibazaki, T. Matsumoto, "Viscoelastic lower crust and mantle relaxation following the 14-16 April 2016, Kumamoto, Japan, earthquake sequence", *Geophys. Res. Lett.*, 44, 8795-8803, 2017.
[20] S. Fujiwara, H. Yarai, T. Kobayashi, Y. Morishita, T. Nakano, B. Miyahara, H. Nakai, Y. Miura, H. Ueshiba, Y. Kakiage, H. Une, "Small-displacement linear surface ruptures of the 2016 Kumamoto earthquake sequence

detected by ALOS-2 SAR interferometry”, *Earth Planets Space*, 68:160, 2016.
[21] T. Hosono, C. Yamada, T. Shibata, Y. Tawara, C.Y. Wang, M. Manga, A.T.M.S. Rahman, J. Shimada, “Coseismic groundwater drawdown along crustal ruptures during the 2016 Mw 7.0 Kumamoto earthquake”, *Water Resource Research*, 55, 5891-5903, 2019.

3.14 Other

LONG-TERM DUAL-FREQUENCY SAR BACKSCATTER DYNAMICS OF A SALT FLAT IN NORTHERN CHILE

PI ER2A2N178

Matías Barber [1], Analía Delsouc [2]

[1] Quantitative Remote Sensing group, Institute of Astronomy and Space Physics, Buenos Aires, Argentina

[2] Hémera Centro de Observación de la Tierra, Facultad de Ciencias, Universidad Mayor, Santiago, Chile

1. INTRODUCTION

Detritical and evaporitic environments known as salt flats or salars evolve following physicochemical processes (crystal growing, precipitation, dissolution, others) that are not dominant or even present in other widely-studied environments such as soils, ice, and oceans.

This study is aimed to analyze the behavior of SAR backscattering over a highland salt flat using multitemporal analyses with Sentinel 1 (5.40 GHz, 5.55 cm) and ALOS 2/PALSAR 2 (1.23 GHz, 24,3 cm). Dual-frequency SAR images allow capturing information at different depths according to the wavelength of operation. Microwave response of halite crystal aggregates is linked to surface roughness of the salt crusts by means of the single-scattering surface-only model Integral Equation Model with multiple scattering at second order (IEM2Mc) and two-layer scattering model based on the second-order scattering solution of the Small Perturbation Model (SPM) in media with complex permittivity such as the brine-soil mixtures found in salars.

2. MATERIALS AND METHODS

2.1 Study Area

The Salar de Aguas Calientes Sur is a 476 km2 salt flat located in the high puna of northern Chilean Andes (67°41'16"W/23°58'27"S), at an altitude of approximately 4,000 m (Figure 1). The containing basin is endorheic and intra-volcanic. Overall, the northern and southern margins have shallow lakes. The most abundant evaporitic minerals found in the salt flat are gypsum and halite. To the west it is located the Salar de Capur and to the east the Laguna Tuyajto.

In Andes Highlands, geographical and climatic conditions are particular with two winter seasons per year (Altiplanic and austral winter), facing snow falls and strong winds. These features are underexplored with SAR in other salt flats.

Field observations and morphological analysis over the Salar de Aguas Calientes Sur were conducted on April 3, 2018 (Figure 2). Field observations showed highly heterogeneous pan crust environments that could be grouped into three different crust types.

The first is a hard crust (referred to as hard pan crust 1 (Figure 2(a)) formed primarily by gypsum, halite and detrital particles. It is characterized by an irregular concave shape, uplifted rims, and salt enrichments crystallized as granular forms and thin sheets covering the gypsum pan over the borders indicating that most of the time remains not flooded. These salts with granular form indicate that they were formed from evaporation and rise of brines by capillarity. This crust surface is rough over microwave scales from millimeter to centimeter such that of the sensors Sentinel 1 and ALOS 2.

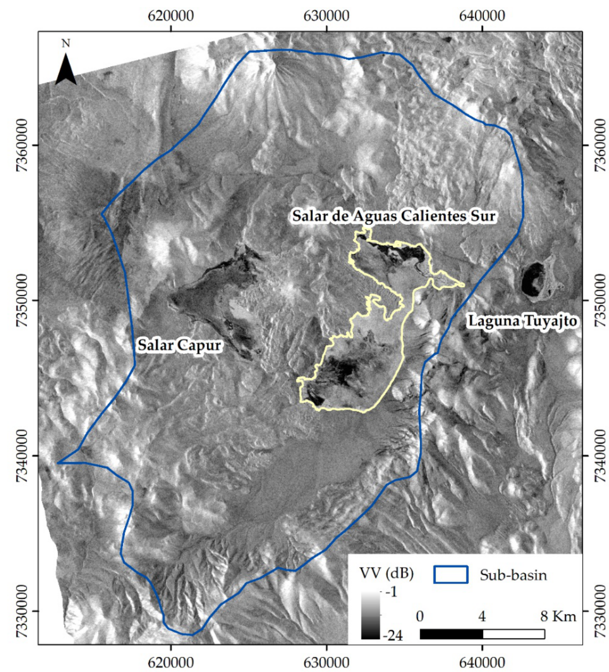

Figure 1: Sentinel 1B image, VV polarization in decibels (dB), acquired on April 3, 2018 over the study area. Location and boundary of the Aguas Calientes Sur salt flat is shown in light yellow.

The second crust type is referred to hard pan crust 2 (Figure 2(b)), and it is distributed along the east edge of the salt flat, formed by gypsum and halite containing cavities that indicate dissolution of salts due to infiltration and percolation of water causing loss of stiffness. The surface is somewhat soft, as can be noted from the footprint tracks left over as seen on the right in Figure 2(b).

A third salt crust with soft consistency is distributed over the northwest and southwest (Figure 2(c)). Almost flat with mud-crack polygons that contain a mixture of moistened salts, mainly halite, and some gypsum. The polygons indicate water loss after flooding events. This crust is over a lower part of the pan so that it is easily flooded. Its surface appeared smooth to microwave frequencies.

Towards the north and south of the salt flat, a few perennial lagoons are observed. The permanent inflow prevents them from drying out entirely by evaporation.

In the rest of the salt pan, the deposition of halite and gypsum crystals through evaporation and the following halite growth by the upward movement of capillary water plays an essential role in the temporal variability of the backscattered signal on the surface of the salt flat.

Figure 2: Types of salt crust observed in the field on April 3, 2018. (a) Upper panel: Hard pan crust 1, mixture of salts and sediments (rough surface); (b) Center panel: Hard pan crust 2 (gypsum and halite); (c) Bottom panel: Soft pan crust with contents of organic matter and thrust polygons by interaction with water.

2.2 Multitemporal SAR data

Sentinel 1A/B (C-band, 5.55 cm) and ALOS-2/PALSAR-2 (L-band, 23.4 cm) sensors provided the SAR imagery for this study. The former was acquired in Interferometric Wide Swath (IW) mode, level 1 processing, and Ground Range Detected (GRD) with a spatial resolution of 20 m x 22 m (range by azimuth) and a swath width of 250 km. The latter in StripMap (SM) Fine [10 m] mode with a spatial resolution of 10 m and a 70 km swath. The Sentinel 1 dataset encompasses five scenes per month from July 1, 2017 to December 29, 2018, in dual polarization (VV and VH) and ascending passes. In the same period, ALOS-2/PALSAR-2 dataset has three images in HH and HV polarization in ascending orbit.

For Sentinel 1, image processing started with usual preprocessing steps such as orbit correction and thermal noise removal. Then, Sentinel and ALOS images are radiometrically calibrated. Subsequently, a Refined Lee filter with a 7x7 pixel window was used to improve radiometric quality. Finally, the geometric terrain correction was applied by assigning the digital elevation model SRTM 1Sec HTG and bilinear interpolation, resulting in an image with a nominal pixel size of 10 m x 10 m. As a final product, output bands of backscattering coefficients σ^0 for Sentinel 1 (VV, VH) and ALOS-2/PALSAR-2 (HH, HV), along with their corresponding local incidence angle, were generated.

2.3 Microwave rough-surface scattering model

The Integral Equation Model with multiple scattering at second order for complex-permittivity media, referred to as IEM2Mc [Alvarez-Perez 2012] is the name given to an improved, enhanced version of the Integral Equation Model originally developed by Fung [Fung 1994] to describe rough-surface scattering in the field of radar remote sensing for Earth observation. Surface parameters for IEM2Mc are complex dielectric constant, surface standard deviation s, power spectrum and correlation length l. Research on dry salt lakes suggested that s/l~0.10 [Aly 2007, Lasne 2008, Liu 2016], with s on the millimeter scale. An exponential power spectrum is known to better fit natural surfaces [Barber16].

2.4 Microwave two-layer scattering model

In this work, the small perturbation method SPM will be used, which is based on solving Maxwell's equations in a perturbative way. A remarkable result is that, at second order perturbations, the SPM conserves energy [Johnson 1999, Demir 2003, Tsang 2004]. Furthermore, this model can be used both to solve the EM scattering problem only with a rough interface and in a layered medium. In the latter case, the scattering geometry includes volume scattering effects [Tabatabaeenejad 2006, Demir 2012]. A schematic view of the two-layer model is shown in Figure 3. Layer parameters are the same as the one surface case but adding the layer depth *d*.

Relative dielectric constant of primary constituents of dry lake saline soils are silicates (ε=5.90), halite (ε=4.48), and gypsum (ε=6.88) [Wadge 2003], all exhibiting a negligible imaginary part and a frequency-independent behavior in the microwave band [Ulaby et al., 2014, 4-8.1]. The dielectric loss in the media is entirely given by the brine under the dry lake floor through salts dissolved in the water therein. Salinity of the water is expressed in psu which is approximately equal to parts per thousand of solid salt in grams dissolved in 1 kg of solution.

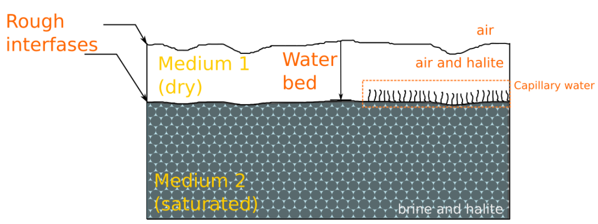

Fig. 3: Layer distribution within the salt flat volume.

Over the study area, subsurface brine salinity ranges between 2 and 45 psu as reported in 2013 by [Troncoso 2013]. A salinity of 66 psu was measured recently in the northern lake.

The brine layer within soil is a mixture consisting of solid particles and saline water allocated within soil's pores. A simple mixing model is used for modeling complex dielectric constants of saline soils. The dielectric constant of saline soil (ε_{ss}) was calculated using the dielectric values calculated for dry soil (ε_{ds}) and saline water (ε_{sw}) following [Ulaby et al., 2014], each weighted by its respective proportion of the combined mixture,

$$\varepsilon_{ss} = (1-\varphi)\varepsilon_{ds} + \varphi\varepsilon_{sw} \tag{1}$$

where φ is the medium's average porosity. Typical average porosity ranges 0.34-0.45 [Lasne 2008]. In Equation (1), ε_{sw} is a function of frequency, salinity and, to a lesser extent, soil temperature. Table 1 summarizes the computed dielectric constants for each layer at the two study frequencies.

TABLE 1. Dielectric constant of media modeled after Ulaby 2014.

Frequency [GHz]	Medium	Relative dielectric constant
5.40	1 (dry)	4.23+0i (lossless)
5.40	2 (saturated)	28.8+7.32i - 22.0+16.6i
1.23	1 (dry)	4.23+0i (lossless)
1.23	2 (saturated)	31.0+1.82i - 23.4+53.1i

4. RESULTS

4.1 Multitemporal analysis

Time series of Sentinel 1 VV-polarized and ALOS-2 σ^0 over the three crust types mentioned in Section 2.1 is shown in Figure 4. Precipitation information is also shown as a bar plot for rainfall and as occurrence instances for snowfall.

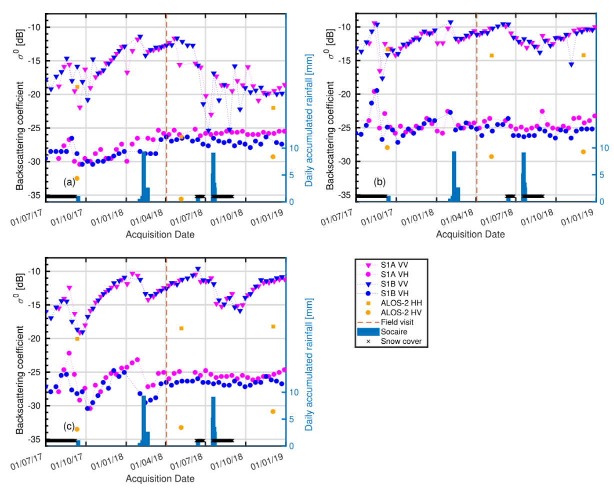

Fig. 4: Dual-frequency temporal backscattering observed over the salt pan. Sentinel 1A (magenta) and Sentinel 1B (blue) in ascending passes. VV polarization is indicated as triangles, and VH are circles. ALOS-2 is indicated with yellow markers. The vertical dashed line indicates field visit on April 3, 2018 (see Figure 2). (a) Soft pan crust, the local incidence angle is between 35.2°-35.4° (Sentinel) and 27.5°-28.4° (ALOS); (b) Hard pan crust 2, the local incidence angle is between 39.9°-40.1° (Sentinel) and 31.8°-32.0° (ALOS); (c) Hard pan crust 1, local incidence angle is between 39.2°-39.3° (ascending). Accumulated rainfall is shown as bars and snow occurrence is indicated as cross marks above the black x-ayis.

In this respect, Salar de Aguas Calientes Sur underwent an increase in the available water due to continuous snowfall events and some rainfalls from July to late September 2017. The availability of water and the evaporation that followed has driven the formation of crusts and henceforth the change in surface roughness detected at C-band. The rainfalls during February 2018 prevented σ^0 from further increasing. Over the dry period that followed, crust development resumed until late June 2018. A third cycle occurred during the dry period after October 2018.

Changes in the backscattered power showed different patterns depending on the salt pan spatial distribution and composition. For type 2 and type 1 hard crusts, Figure 4 (b) and (c), respectively, σ^0 increase-and-decrease pattern accounted for inter-annual wet and dry periods. This is more evident on the hard pan crust 1, where backscattering coefficient had a 10-dB-increase between the flooded and the well-developed crust surfaces in the five-month period from September 2017 to January 2018. On the other hand, for the soft pan crust, Figure 4(a), annual seasonality had little impact on σ^0.

In what follows, microwave rough-surface scattering from modeling is presented for hard and soft pan crust sites. Modeled against measured σ^0 is compared on dates when L- and C-band measurements are available.

4.2 Rough-surface analysis

Table 2 and 3 indicate σ^0 measurements for the rough, hard pan crust 1 and smooth, soft pan crust. Figures 5 and 6 show contour levels in dB modeled by IEM2Mc [Alvarez-Perez, 2012]. The contours are computed at approximated angles 31° and 28° at L-band and 39° and 35° at C-band. The combinations of σ^0 at L- and C-band for in May 2018 is well modeled by the single-scattering surface-only model, in accordance with a media with homogeneous profile at several cm depth. On the remaining dates, the salt pan condition is such that the scatters dominating the VV polarized σ^0 are at the top surface whereas those of HH are deeper.

4.3 Simulation study for two-layer model

Backscattering coefficients modeled by a two-layer SPM as a function of the normalized layer distance is shown in Figure 4. The periodic features are due to a coherent effect on the layer distance and enhanced responses occur at certain layer depths. Interestingly, certain combinations of depths result in HH at L-band close to VV at C-band. Therefore, sub-surface profiling with L-band is feasible (i.e. shallow water bed monitoring).

TABLE 2. σ^0 measurements for hard pan crust 1.

Date	Sensor (pol.)	Inc. angle (deg.)	σ^0 (dB)
11 Sept., 2017	ALOS 2 (HH)	30.9	**-20.0**
11 Sept., 2017	SENTINEL 1 (VV)	39.2	**-18.4**
7 May, 2018	ALOS 2 (HH)	30.9	**-18.5**
9 May, 2018	SENTINEL 1 (VV)	39.2	**-11.1**
3 Dec., 2018	ALOS 2 (HH)	30.9	**-18.2**
5 Dec., 2018	SENTINEL 1 (VV)	39.2	**-11.4**

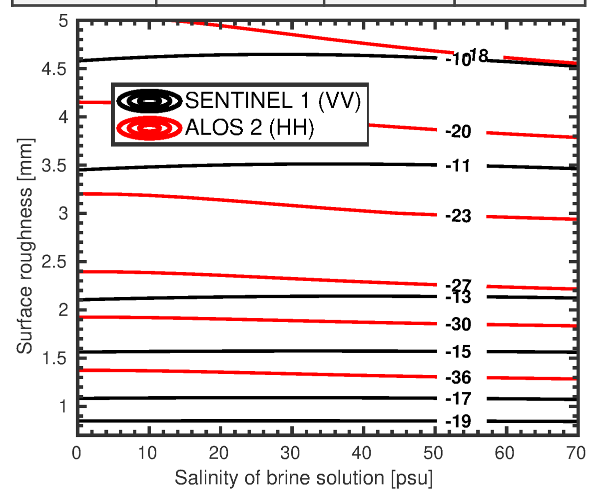

Figure 5: Contour levels in dB modeled by IEM2Mc for the hard pan crust. The contours are computed at approximated angles 31 and 28 at L-band and 39 and 35 at C-band.

TABLE 3. σ^0 measurements for soft pan crust 1.

Date	Sensor (pol.)	Inc. angle (deg.)	σ^0 (dB)
11 Sept., 2017	ALOS 2 (HH)	28.1	**-18.9**
11 Sept., 2017	SENTINEL 1 (VV)	35.1	**-15.6**
7 May, 2018	ALOS 2 (HH)	27.8	**-26.3**
9 May, 2018	SENTINEL 1 (VV)	35.3	**-11.8**
3 Dec., 2018	ALOS 2 (HH)	27.6	**-22.0**
5 Dec., 2018	SENTINEL 1 (VV)	35.1	**-18.6**

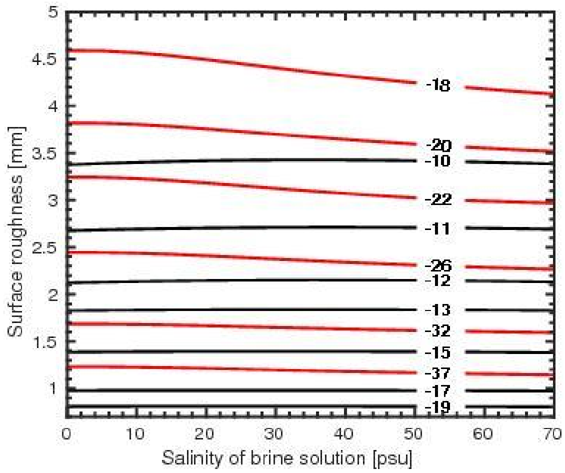

Figure 6: Contour levels in dB modeled by IEM2Mc for the soft pan crust. The contours are computed at approximated angles 31 and 28 at L-band and 39 and 35 at C-band.

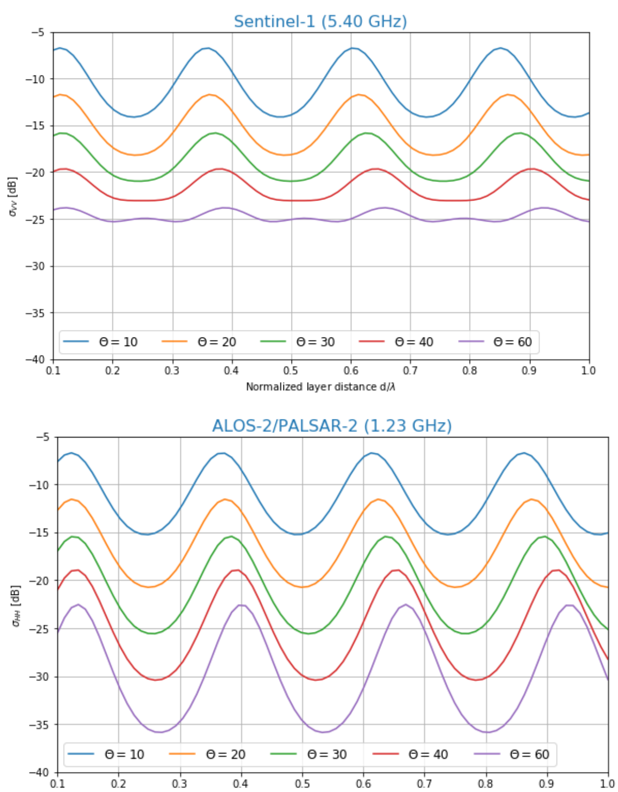

Fig. 4: Backscattering coefficients for C-band (5.40 GHz), VV-polarized (upper) and L-band (1.23 GHz) HH-polarized configuration at several incidence angles using a two-layer SPM.

5. FINAL REMARKS

Research on evaporitic environments can largely benefit from fully polarimetric data. L-band ALOS 2/PALSAR 2 measurements are combined along with that of C-band Sentinel 1A/B to study an evaporitic environment in an highland salar by means of its microwave response. Disregarding any scattering mechanism other than surface scattering, previous research has shown that C-band VV-polarized σ^0 has a strong dependence on surface roughness, whereas the scatters dominating the HH polarized σ^0 are located in the subsurface.

In a previous study [Barber & Delsouc, 2021], a single-scattering surface-only model showed its limitations to predict single-frequency (C-band) σ^0 measurements assuming that the dominant scatterers are located on the surface.

A two-layer composite model seemed better suited when dual-frequency microwave response of a salt flat is available. The uppermost layer might be of salt crusts whereas below it a brine-soil layer arises. However, further research is needed in this way. Due to continuous support from JAXA, this study will continue under a EO-RA2 contract on a salt flat in Northern Argentina.

6. REFERENCES

[Alvarez-Perez 2012] Alvarez-Perez, J. L., 2012. The IEM2M rough-surface scattering model for complex-permittivity scattering media. Waves in Random and Complex Media, 22(2), 207–233

[Aly 2007] Aly, Z.; Bonn, F.J.; Magagi, R. Analysis of the backscattering coefficient of salt-affected soils using modeling and RADARSAT-1 SAR data. IEEE Trans. Geosci. Remote Sens. 2007, 45, 332–341.

[Barber 2016] Barber, M. E., Grings, F. M., Álvarez Mozos, J., Piscitelli, M., Perna, P. A., Karszenbaum, H., 2016. Effects of Spatial Sampling Interval on Roughness Parameters and Microwave Backscatter over Agricultural Soil Surfaces. Remote Sensing, 8(6). https://www.mdpi.com/2072-4292/8/6/458.

[Barber & Delsouc 2021] Barber, M.; Delsouc, A; Pérez-Martínez, W.; Briceño-De-Urbaneja, I.; "Time series of salt crusts imaged by a dual polarization spaceborne Synthetic Aperture Radar (SAR) at C-band over an Andean Altiplano Salar of Northern Chile", LAGIRS 2020: 2020 Latin American GRSS & ISPRS Remote Sensing Conference, 22-26 Marzo 2020, Santiago, Chile, pp. 630-635, doi: 10.1109/LAGIRS48042.2020.9165684.

[Delsouc et al., 2020] Delsouc, A.; Barber, M.; Gallaud, A.; Grings, F.; Vidal-Páez, P.; Pérez-Martínez, W.; Briceño-De-Urbaneja, I. Seasonality Analysis of Sentinel-1 and ALOS-2/PALSAR-2 Backscattered Power over Salar de Aguas Calientes Sur, Chile. Remote Sens. 2020, 12, 941

[Demir 2003] M. A. Demir and J. T. Johnson, “Fourth-and higher-order small-perturbation solution for scattering from dielectric rough surfaces,” JOSA A, vol. 20, no. 12, pp. 2330–2337, 2003.

[Fung 1994] Fung, A. K., 1994. Microwave scattering and emission models and their applications. The Artech House remote sensing library, Artech House.

[Johnson 1999] J. T. Johnson, “Third-order small-perturbation method for scattering from dielectric rough surfaces,” JOSA A, vol. 16, no. 11, pp. 2720–2736, 1999.

[Lasne 2008] Lasne, Y.; Paillou, P.; Freeman, A.; Farr, T.; McDonald, K.C.; Ruffié, G.; Malézieux, J.-M.; Chapman, B.; Demontoux, F. Effect of salinity on the dielectric properties of geological materials: Implication for soil moisture detection by means of radar remote sensing. IEEE Trans. Geosci. Remote Sens. 2008, 46, 1674–1688.

[Liu 2016] Liu, C.-A.; Gong, H.; Shao, Y.; Yang, Z.; Liu, L.; Geng, Y. Recognition of salt crust types by means of PolSAR to reflect the fluctuation processes of an ancient lake in Lop Nur. Remote Sens. Environ. 2016, 175, 148–157.

[Paillou 2014] Paillou, P.; Sufyar, S.; Freeman, A. The Chott El Djerid, Tunisia: Observation and discussion of a SAR Phase signature over evaporitic soils. IEEE Trans. Geosci. Remote Sens. 2014, 52, 5798–5806

[Tabatabaeenejad 2006] A. Tabatabaeenejad and M. Moghaddam, “Bistatic scattering from three-dimensional layered rough surfaces,” IEEE Transactions on Geoscience and Remote Sensing, vol. 44, no. 8, pp. 2102–2114, 2006.

[Troncoso 2013] Troncoso, R.; Ercilla, O.; Carrasco, R.; Vivallo, W. Estudio del Potencial del Litio en Salares del Norte de Chile; Servicio Nacional de Geología y Minería: Santiago, Chile, 2013; p. 252.

[Tsang 2004 L. Tsang and J. A. Kong, Scattering of electromagnetic waves, advanced topics, vol. 26. John Wiley & Sons, 2004.

[Ulaby et al., 2014] Ulaby, F. T., Long, D., Blackwell, W., Elachi, C., Fung, A., Ruf, C., Sarabandi, K., van Zyl, J., Zebker, H., 2014. Microwave Radar and Radiometric Remote Sensing, University of Michigan Press: Ann Arbor, MI, USA, 2014

[Wadge 2003] Wadge, G.; Archer, D.J. Evaporation of groundwater from arid playas measured by C-band SAR. IEEE Trans. Geosci. Remote Sens. 2003, 41, 1641–1650. [CrossRef]